MECHANOCHEMICAL SYNTHESIS OF SUSTAINABLE HYDRAULIC CEMENTS

By

Faris Matalkah

A DISSERTATION

Submitted to
Michigan State University
in partial fulfillment of the requirements
for the degree of

Civil Engineering – Doctor of Philosophy

2017

ABSTRACT

MECHANOCHEMICAL SYNTHESIS OF SUSTAINABLE HYDRAULIC CEMENTS

By

Faris Matalkah

A mechanochemical approach was developed for synthesis of sustainable hydraulic cements based on the alkali aluminosilicate chemistry. This approach is energy-efficient with distinctly low carbon footprint; it also enables large-volume use of abundant wastes and carbon dioxide as raw materials. A theoretical framework was developed to explain the production process and the hydraulic mechanism of the alkali aluminosilicate cement. Refinement of the raw materials formulations and the processing conditions led to production of cements that meet or surpass standard requirements. The performance, cost, energy content and carbon footprint of the mechanochemically processed hydraulic cement were generally better than those of conventional Portland cement. The approach developed for production of alkali aluminosilicate cements is particularly effective in achieving significantly reduced carbon footprints by reducing the energy use in production of cement, avoiding chemical release of carbon dioxide, and making value-added use of CO_2 as a raw material. The scalability of the production process of the alkali aluminosilicate hydraulic cements was verified through integrated theoretical and pilot-scale experimental investigations. A methodical approach to concrete mix design with the alkali aluminosilicate cements was implemented, and was accompanied with experimental investigations of concrete materials of different mix designs prepared with either the alkali aluminosilicate cement or Portland cement. The trends in the effects of the concrete mix design parameters on its properties indicated that the popular mix design procedures developed for

Portland cement are generally compatible with the alkali aluminosilicate cement, which produces concrete materials of improved mechanical, physical and durability characteristics.

ACKNOWLEDGEMENTS

I would like to express my greatest gratitude to my advisor, Dr. Parviz Soroushian, for his consistent support and encouragement. I appreciate the support of the members of my PhD. guidance committee: Dr. Venkatesh Kodur, Dr. Roozbeh Dargazany and Dr. Susannah Dorfman. Throughout this research, I benefited from discussions with members of my research team, including Dr. Wenda Wu (scholar from Fuzhou University), Weerirsiri Rankothge (MSc. chemistry), Nalin Darsini (MSc. Chemistry) and other PhD and MS students working with Dr. Soroushian.

TABLE OF CONTENTS

LIST OF TABLES

LIST OF FIGURES

Chapter 1

Dissertation Overview

1.1 Motivation

Portland cement concrete is the most widely used man-made material; its consumption rate of 6 tons/yr for every living human being is exceeded only by water. Production of each ton of Portland cement releases close to one ton of carbon dioxide to the atmosphere, making it the third major source of anthropogenic carbon emissions. Portland cement production accounts for about 7% of carbon dioxide emissions and 3% of energy use worldwide [1-3]. The large carbon footprint and energy content of Portland cement are rooted in its particular chemistry (based on calcium silicates). Efforts to enhance the efficiency of Portland cement production without altering its chemistry have made relatively small contributions towards reduction of carbon emissions and energy use.

While carbon dioxide has been used to raise the rate of strength development of Portland cement concrete, this practice offers limited carbon uptake potential, is largely limited to the precast concrete market sector (requiring capital-intensive changes to production facilities), and (most importantly) compromises the long-term performance of concrete.

This research focused on development of a sustainable hydraulic cement chemistry via mechanochemical processing without resorting to elevated temperatures. The new cement chemistry is based on alkali aluminosilicates, which are prevalent in the earth crust, with significantly reduced carbon footprint and energy content when compared with Portland cement.

Alkali-activated aluminosilicates form via the dissolution of aluminosilicate precursors in an alkaline solution, which is followed by precipitation of inorganic (alkali aluminosilicate) polymeric binders [4]. These reactions occur at higher rates than ordinary Portland cement hydration reactions. The mechanisms governing the setting of alkali aluminosilicate cements (formation of monomers and initial hardening), and their subsequent hardening (formation of polymeric structures and improvement of mechanical properties) comprises the following steps: dissolution, transportation/orientation and polycondensation [4]. The extended 3D structure of alkali-activated aluminosilicate hydrates together with their relatively low content of chemically combined water, distinct molecular-scale pore structure, and robust chemistry explain their performance advantages over ordinary Portland cement hydrates. These advantages also allow for value-added use of abundant and market-limited industrial byproducts and carbon dioxide as raw materials in manufacturing of alkali aluminosilicate hydraulic cements. Hydration of the resulting cements (when processed in the presence of carbon dioxide) accompanies carbonation reactions which make important contributions towards the engineering properties of the resulting binder for concrete production.

The main thrust of this research is to devise preferred formulations of raw materials and mechanochemical processing conditions for achieving a desired balance of sustainability (including carbon uptake) and end product qualities which meet the performance-based requirements for hydraulic cement, and to scale-up the production process of this hydraulic cement and demonstrate its compatibility with field construction practices.

1.2 Summary of Research

This dissertation aims to devise a strategy for resolving the environmental and performance concerns with Portland cement which has been the dominant binder used in production of concrete for two centuries. A sustainable hydraulic cement chemistry based primarily on alkali aluminosilicates was developed using sustainable mechanochemical processing methods. The new cement was thoroughly characterized; the mechanical and durability aspects of its performance were evaluated and compared against those of conventional Portland cement. The research conducted for this dissertation is divided into eight main chapters. Each chapter has been prepared as a stand-alone paper written for submission to a peer-reviewed scientific journal with high impact factor in this field. Chapter 2 has been published in “Materials and Structures”. Chapters 3 has also been published in “Construction and Building Materials”, and Chapter 4 has been accepted for publication in the same journal. Chapters 5,6,7, 8 and 9 are currently under review. For convenience, the references from each chapter have been consolidated and appear at the end of the dissertation. The main chapters of the dissertation are summarized in the following.

1.2.1 Mechanochemical Synthesis of One-Part Alkali Aluminosilicate Hydraulic Cement

A novel approach was devised to synthesize a sustainable hydraulic cement based on alkali aluminosilicate chemistry via mechanochemical activation. This approach builds upon past work on activation of aluminosilicate precursors using alkaline solutions to produce inorganic binders for concrete construction. Recent efforts to develop one-part hydraulic cements based on the chemistry of alkali-activated aluminosilicates have resorted to high-temperature processing techniques which compromise the sustainability advantages of the system, and also require

curing at elevated temperatures. The mechanochemical process developed here takes place at room temperature, and yields a hydraulic cement that does not require addition of caustic solutions to render binding effects via room-temperature curing. Processing of this hydraulic cement takes place at room temperature; this advantage together with extensive use of recycled raw materials yield significant sustainability benefits. The (dry) raw materials used for mechanochemical processing of hydraulic cement included coal fly ash, quick lime, sodium hydroxide and Magnesium oxide. The mechanochemically processed hydraulic cement was evaluated through performance of tests concerned with their pH, heat of hydration, chemical composition, crystallinity and microstructure. The hydraulic cement was used to produce concrete materials cured at room temperature. The resulting concrete materials were found to provide desired levels of workability in fresh state and compressive strength after curing, which were comparable to those of Portland cement concrete. Investigations were also conducted on the hydration kinetics of the hydraulic cement and the microstructure of its hydrates in order to gain insight into its hydration process and the nature of hydration products.

1.2.2 Development of a Sustainable Hydraulic Cement That Meets Standard Requirements for General Use

A sustainable hydraulic cement was developed based primarily upon the alkali aluminosilicate chemistry. This cement employed largely coal fly ash, granulated ground blast furnace slag and natural feldspar as sources of aluminosilicates, with small concentrations of calcium oxide, sodium hydroxide and sodium silicate used as sources of alkalis and soluble silica. In addition, sodium tetraborate was incorporated into the cement formulation for set retardation. The dry raw materials were transformed into a hydraulic cement via input of mechanical energy using a

ball mill. Comprehensive experimental evaluation of the resultant hydraulic cement confirmed that it meets standard requirements for general use in concrete construction.

1.2.3 Freeze Thaw and Deicer Salt Scaling Resistance of Concrete Prepared with Alkali Aluminosilicate Cement

Concrete materials were prepared with the hybrid cement based primarily on the alkali aluminosilicate chemistry. Two aspects of concrete performance were emphasized and compared against those of Portland cement concrete: freeze-thaw durability, and deicer salt scaling resistance. Test results indicated that the concrete prepared with the hybrid cement produced excellent freeze-thaw durability; its dicer salt scaling resistance, however, was lower than that provided by Portland cement concrete. Efforts were made to improve the deicer salt scaling resistance of the hybrid cement concrete through refinement of the hybrid cement composition. The use of an air-entraining agent was found to enhance the deicer salt scaling resistance of the hybrid cement concrete. Modification of the hybrid cement chemistry with polyethylene glycol, tartaric acid, or a combination of sodium benzoate and triisopropanolamine was found to also improve the hybrid cement concrete resistance to deicer salt scaling with minimal effect on compressive strength.

1.2.4 Plastic Shrinkage Cracking and Bleeding of Concrete Materials Prepared with Alkali Aluminosilicate Cement

Cracking caused by internal and/or external restraint of shrinkage during construction and curing of concrete or in service adversely influences the long-term durability of the concrete-based infrastructure. This investigation focused on early-age surface cracking of concrete caused by internal restraint of plastic shrinkage in a hybrid cement which embodies key elements of alkali-

activated aluminosilicate chemistry. This class of cement differs from Portland cement in terms of surface qualities; bleeding was measured as a factor that could be a factor in plastic shrinkage cracking and other aspects of the exposed surface qualities of concrete produced with this class of cement. Rheological tests were also performed to gain further insight into factors which influence the early-age performance of the hybrid cement paste. Portland cement was used as control for comparative assessment of the hybrid cement performance. The hybrid cement concrete provided desired resistance to plastic shrinkage cracking. Its bleeding less than that of Portland cement concrete. The viscosity and yield stress of the hybrid cement paste were relatively high when compared with the Portland cement paste. The test data produced on the bleeding and rheological attributes of the hybrid cement concrete were used to explain its desired resistance to plastic shrinkage cracking.

1.2.5 Acid Resistance and Corrosion Protection Potential of Concrete Materials Prepared with Alkali Aluminosilicate Cement

An experimental investigation was conducted on two key aspects of the durability characteristics of concrete materials prepared with an alkali aluminosilicate hydraulic cement and with Portland cement, both cured at room temperature. The durability characteristics evaluated concerned the acid resistance of concrete, and its ability to protect the embedded reinforcing steel against corrosion under wet-dry cycles. Acid resistance was evaluated through monitoring of mass and strength change over time under acid attack, visual observations, and scanning electron microscopy (SEM). Corrosion resistance was evaluated through measurement of the corrosion potential, visual observations and scanning electron microscopy. The acid resistance and

corrosion protection potential of the concrete prepared with the alkali aluminosilicate cement were found to be superior to those of Portland cement concrete.

1.2.6 Carbon Dioxide Integration into Alkali Aluminosilicate Cement Particles for Achievement of Improved Properties

Alkali aluminosilicate cement developed using ground granulated blast furnace slag was produced mechanochemically in the presence of lime and sodium hydroxide. Processing of this cement in a carbon dioxide environment led to the incorporation of carbon dioxide into the resultant hydraulic cement as metastable carbonate complexes. The hydration reactions of cement were complemented with formation of crystalline carbonates; the resultant hydrates and carbonates made synergistic contributions towards the binding effects and stability of the inorganic binder. Analytical chemistry and physical test methods were performed on cements and their hydrates in order to understand the form of carbon dioxide in their corresponding structures. The test results indicated that carbon dioxide was integrated into the cement particles in metastable form, which formed carbonate crystallites integrated with the amorphous hydrates in the course of hydration of cement. This phenomenon led to significant improvements in the mechanical properties of the resulting binder.

1.2.7 Scaled-Up Production of an Alkali Aluminosilicate Hydraulic Cement in the Presence of Carbon Dioxide for Concrete Construction

Scalability of the mechanochemical processing of an alkali aluminosilicate hydraulic cement was investigated. Mechanochemical processing of this cement is performed in the presence of carbon dioxide for carbon capture in the course of cement production. Pilot-scale studies were performed in a power plant where the flue gas resulting from combustion of natural gas was used

as a dilute source of carbon dioxide. A theoretical framework was established to guide scale-up of the mechanochemical approach to processing of hydraulic cement. The resulting cement was used for industrial-scale production of concrete that was used in a field construction project. The project outcomes validated the scalability of the mechanochemical approach to production of alkali aluminosilicate hydraulic cement. The potential for selective capture of carbon dioxide from combustion emissions in the course of mechanochemical processing of the hydraulic cement was verified. The resulting hydraulic cement was found to be compatible with conventional methods of concrete mix design and industrial-scale production. Concrete materials produced with the mechanochemically processed hydraulic cement were found to be compatible with conventional field construction practices. Comparative studies indicated that the alkali aluminosilicate cement produced at pilot scale offers distinctly low carbon footprint and energy content at reduced cost when compared with ordinary Portland cement.

1.2.8 Theoretical Evaluation of The Fate of Captured Carbon Dioxide in Hydraulic Cements

Thermodynamic models were developed in order to simulate the hydration reactions that take place during curing of alkali aluminosilicate hydraulic cements with different carbon dioxide contents. The resulting models were used to identify the phases that from upon concurrent hydration and carbonation reactions. A theoretical framework was also established based on thermodynamic and diffusion principles to explain the mechanochemical capture and value-added use of carbon dioxide in hydraulic cements based on alkali aluminosilicate chemistry.

Chapter 2

Mechanochemical Synthesis of One-Part Alkali Aluminosilicate Hydraulic Cement

2.1 Introduction

An alternative cementitious binder, occasionally referred to as (two-part) "geopolymer", obtained by alkali-activation of an aluminosilicate precursor (e.g., metakaolin or ground granulated blast furnace slag), has been considered as a substitute for the hydrated Portland cement binder. Geopolymers are conventionally produced via activation of a solid aluminosilicate powder using alkali hydroxide/alkali silicate solutions [5-7]. Geopolymerization involves polycondnsation reaction of aluminosilicate oxide (geopolymer precursor) with alkalis, yielding inorganic polymers (alkali aluminosilicate hydrates) with 3D crosslinked chain structures [8] . The complex mineralogy of by-product precursors (e.g., slag or fly ash) could prompt simultaneous hydration reactions, which incorporate calcium silicate hydrate (C-S-H) and calcium hydroxide into the core geopolymer structure. Despite the superior mechanical and durability properties of geopolymers, there are some drawbacks with the two-part nature of their formulation [9]. The use of alkaline solutions limits the commercial prospects of this technology due to the corrosive (and viscous) nature of the required alkaline solutions [10]. Fresh geopolymer mixtures could also experience rapid stiffening (e.g., in the presence of high-calcium fly ash as an aluminosilicate precursor) [11] , which is not compatible with mainstream construction practices. The one-part hydraulic cement developed in this project seeks to overcome these drawbacks of two-part geopolymers while providing (or even enhancing) their sustainability and performance advantages.

Several investigations have been undertaken for developing methods of synthesizing one-part alkali aluminosilicate-based hydraulic cements. The more elaborate methods of synthesizing one-part geopolymer cements involve thermal activation of raw materials (including aluminosilicate precursors and alkalis). For example, albite has been activated thermally in the presence of solid alkalis (sodium hydroxide or sodium carbonate) at about 1000^{o}C [12]. The resulting one-part hydraulic cements provide viable rates of compressive strength development and final compressive strengths. Another investigation prepared one-part geopolymer cement via calcination of low-quality aluminosilicates in the presence of alkali hydroxides, which led to almost complete conversion of all aluminum sites into tetrahedral coordination and extensive chemical linking between Si–O_4 and Al–O_4 tetrahedra. The resulting powder could, upon addition of water, undergo polycondensation and formation of an amorphous geopolymer matrix. Although the resulting geopolymer paste exhibited spectroscopic parameters similar to conventional geopolymers, its compressive strength was relatively low [13]. Another example involved thermal treatment of low-quality kaolinite in the presence of alkalis [14]. It was found that nepheline and glassy phase sodium aluminosilicate are generated during heat treatment of blends of kaolinite and alkalis; hydration of this cement (at curing temperature of 80^{o}C) yielded P-zeolite. These particular one-part geopolymer cements yielded reasonable levels of dry compressive strength; their moisture resistant, however, was a concern. The methods used so far for production of one-part geopolymer cements employ relatively high alkali contents and also high processing temperatures, which compromise their economics and sustainability. A recent work in this field synthesized on-part geopolymer cement through thermal activation of red mud blended with silica fume at about 25 wt.% to improve the long-term strength of the

binder by optimizing the Al/Si ratio to enhance the stability of the geopolymer structure [15]. Even though the resulting geopolymer binder reached viable compressive strengths, use of high-temperature processing and relatively high concentrations of silica fume compromised the sustainability and economics of this approach. Another approach followed for production of one-part geopolymer cement involves simple blending of the dry caustic activator and the aluminosilicate precursor. A recent example involves blending of rice husk ash with sodium aluminate [16]. The resulting cement required curing at elevated temperature to yield viable levels of early-age compressive strength. At later ages, however, a drop in compressive strength was observed. The high cost of sodium aluminate is another drawback of this approach.

Effects of mechanical activation on coal fly ash and geopolymers incorporating the ash have been investigated [17]. It was found that mechanical activation reduces the particle size, changes the particle shape, and increases the reactivity of coal fly ash. The two-part geopolymer prepared using the mechanically activated fly ash cured at room temperature showed up to 80% increase in compressive strength when compared with that prepared with as-received fly ash. Work has also been reported on mechanochemical activation of natural pozzolans for use as precursors in geopolymer [18]. Ball milling of volcanic ash of relatively low reactivity induced some changes in the mineralogical composition of ash by reducing its degree of crystallinity. The rate of geopolymerization was found to increase with increasing duration of ball milling. Both these investigations view mechanical activation as a way of improving the source materials (precursors) for production of two-part geopolymer. The work reported here focuses on production of a one-part geopolymer cement via mechanochemical processing of blends of raw materials.

A novel approach was developed in this investigation in order to produce economically viable and sustainable one-part geopolymer cements (with relatively low carbon footprint and energy content). This approach employed mechanochemical processing at room temperature in order to transform the raw materials into hydraulic (geopolymer) cement. The raw materials comprised aluminosilicate precursors and sources of alkaline earth and alkali metal cations; mechanochemical processing of these raw materials was accomplished via simple ball-milling of their blends. The milling action incorporates alkali and alkaline earth metal cations into the aluminosilicate structure by disrupting the aluminosilicate bonds. Through this process, the presence of alkalis facilitates mechanochemical activation of the aluminosilicate precursor. In addition, incorporation of the alkali metal cations into the aluminosilicate structure makes the resultant hydraulic cement less caustic. Mechanochemical processing of raw materials yields hydraulic cement particles which embody soluble sources of aluminum, silicon, alkali and alkaline earth metals, which can undergo through-solution reactions to yield alkali aluminosilicate hydrate binders with viable performance characteristics.

2.2 Mechanochemical Processing

Mechanochemistry describes the chemical and physicochemical transformation of substance induced by mechanical energy [19]. This phenomenon is generally caused by simple milling operations (in ball mills, planetary mills, etc.) at room temperature and atmospheric pressure [20]. In particular, mechanochemistry deals with the physico-chemical transformations and chemical reactions affecting substances following the administration of mechanical energy. As mills represent typical energy suppliers, grinding and co-grinding are the common processes inducing mechanochemical transformations [21].

The mechanochemical processing approach adopted in this work seeks to activate aluminosilicate precursors such as coal fly ash (in the presence of alkaline compounds) to produce one-part alkali aluminosilicate hydraulic cements. This approach emphasizes compounding and activation of the blend of coal fly ash and supplementary materials by input of mechanical energy. The supplementary materials primarily introduce additional alkaline earth and/or alkali metal cations to destabilize the aluminosilicate constituent of the coal fly ash, facilitating their mechanochemical disordering/depolymerization and compounding to form a reactive alkaline earth/alkali metal aluminosilicate with desired hydraulic qualities. The resulting hydraulic cement can be processed into concrete using equipment and practices commonly applied to Portland cement, which is a major advantage for large-scale transition of the technology to construction markets.

The mechanochemical activation process is schematically depicted in Figure 1 . Control of the dissolution rates of the glassy phases present in coal fly ash can be achieved by optimizing the addition of readily available network-breaking cations (Ca^{2+}, Mg^{2+}, Na^{+}, K^{+}) during mechanochemical synthesis. The presence of alkaline earth cations in a glassy phase also produces an increased tendency toward framework disordering, including the formation of a small concentration of (weak, reactive) Al–O–Al bonds [22]. Divalent alkaline earth cations enhance dissolution when compared with monovalent alkali cations, enabling glasses to show different dissolution rates according to composition [9].

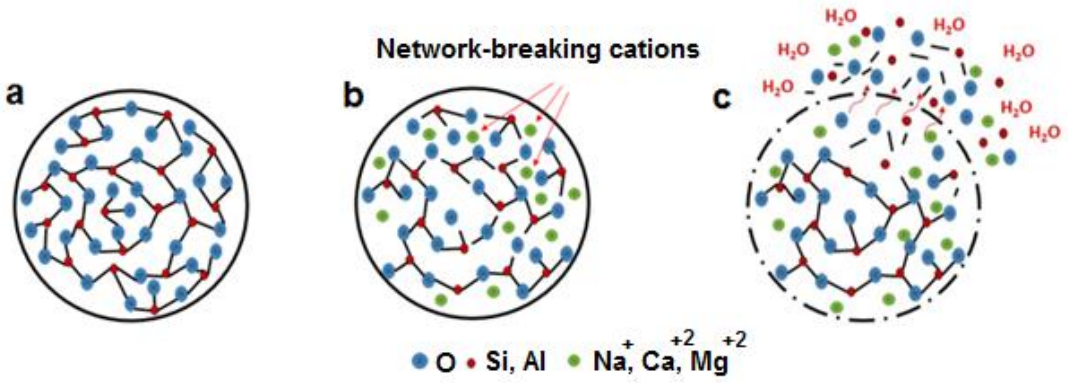

Figure 1. Schematics of mechanochemical transformation and hydration of aluminosilicate precursors and alkaline activators into hydraulic cement.

Four initial steps in hydration of an aluminosilicate-based hydraulic cement can be identified as: (a) ion-exchange; (b) hydrolysis; (c) network breakdown; and (d) release of Si and Al. These dissolution and breakdown phenomena, which occur with simple addition of water, prompt subsequent speciation, gelation, reorganization and polymerization processes which yield the solid alkali aluminosilicate hydrate-based binder [23]. The hydraulic cement particle has an amorphous aluminosilicate structure containing both monovalent and divalent network-modifying cations. Dissolution of this glassy structure occurs at the moderately high pH generated upon partial release of alkali cations to the solution; this step resembles that observed under acidic conditions as it is initiated by ion exchange of H^+ for Na^+ or Ca^{2+}. The difference between Na^+ and Ca^{2+} largely derives from the greater damage to glass structure induced by removal of a divalent versus a monovalent cation. The network breakdown process during glass transition is largely controlled by the surface-charging behavior. Some glasses show synchronous release of Si and Al while others leach one component preferentially – this is strongly dependent on the specific glassy phase used and also the leaching environment. The presence of alkaline earth cations in a glass also gives an increased tendency toward framework disorder, including the

formation of a small concentration of (weak, reactive) Al-O-Al bonds, as well as a non-bridging oxygen atom content higher than is strictly required by stoichiometry. An optimal glassy phase, or combination of glassy phases, would allow for tailored control of alkali activation, including workability, set time, strength development profile and durability [9].

2.3 Materials and Methods

2.3.1 Materials

The coal fly ash used in this study is a dry fly ash obtained from a power plant operated by the Lansing Board of Water & Light in Lansing, Michigan. The chemical composition of the fly ash, determined by x-ray fluorescence (XRF) spectroscopy, comprised 43.1% SiO_2, 14.3% CaO, 23.3% Al_2O_3, 1.7% K_2O and 0.9% N_2O and with LOI of 1.7%. Figure 2 shows the XRD spectrum for the as-received coal fly ash used in this study. The coal fly ash was found to be highly amorphous. Three main crystalline mineral phases were detected in the fly ash, namely quartz (SiO_2), mullite ($3Al_2O_32SiO_2$), and calcite ($CaCO_3$). Laboratory grade sodium hydroxide, reactive MgO and quick lime (CaO) were purchased in powder form with 97-98% purity from Sigma Aldrich

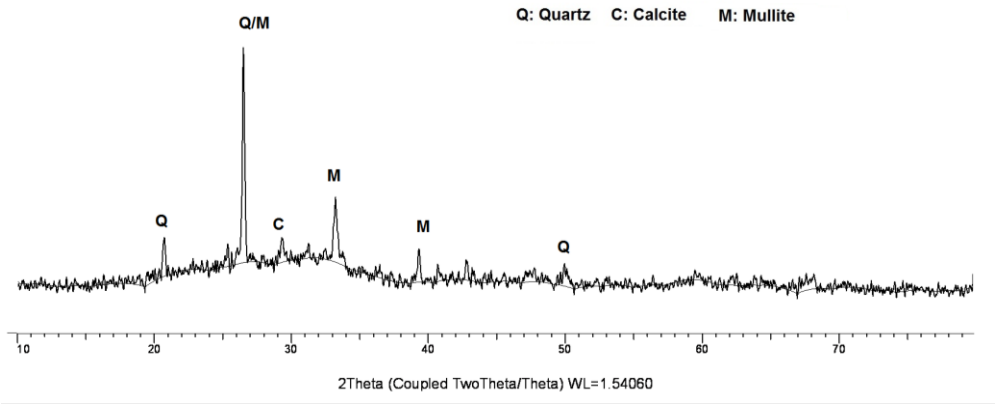

Figure 2. XRD patterns of the coal fly ash used in this investigation

Granite aggregate with 8.5 mm maximum particle size was used as coarse aggregate. Natural sand was used as fine aggregate with 0.15 to 4.75 mm size range.

2.3.2 Methods

The hydraulic cements considered in this investigation were formulated around coal fly ash. The formulation comprised coal fly ash: quick lime: MgO: NaOH at 75: 14: 5:6 weight ratios. This blend was selected, via trial experimental studies, to produce a desired balance of strength, set time and moisture stability. The blends of raw materials were mechanochemically processed through ball-milling in a ceramic jar (5.6 L) with solid-to-steel ball ratio of 1:10. Five different steel ball sizes were used as shown in Table 1. The speed of rotation was chosen to be in the range where milling media experiences "cascade" action, that is, the balls gain enough energy to get up to a certain height and fall, hitting other balls and the particles of powder at an angle of 45 to 60 degrees above the horizontal. The critical speed (rpm) was calculated as: $n_C = 42.29/\sqrt{d}$, where d is the internal diameter of the milling jar (in meters) [24]. Dry grinding was performed at about 75% of the critical speed. The mill was filled with balls and materials to 40-60 % of its volume. Ball-milling was carried out over a 2-hours period.

Table 1. Steel ball sizes and mass percentages.

	Ball size, mm				
	50	25	20	9.5	5
Mass, %	20	20	30	20	10

The resulting hydraulic cements were evaluated through experimental investigation of concrete materials incorporating them. The base concrete mix design considered in this experimental work is presented in Table 2.

A 20 Quart planetary mixer (Hobart A-200) was used to prepare the geopolymer concrete mix. The hydraulic cement was added first to the mixer, and mixed for about 1 minute at medium speed. Water was then added to the dry cement, and mixing was continued for 30 seconds. Fine

and coarse aggregates were added subsequently, followed by 3 minutes of mixing to produce a homogeneous fresh concrete mix.

Table 2. Mix design of hydraulic cement concrete materials.

Material	Quantity, Kg/m^3
Hydraulic cement	320
Fine aggregate	750
Coarse aggregate	1070
Water-to -cement ratio	0.4

The fresh mix workability was measured per ASTM C230 flow table test method. Initial and final set times were measured per ASTM C191 using the Vicat needle apparatus. The amount of water mixed with cement in the set time test was selected to produce the normal consistency per ASTM C187.

The specimens prepared for compressive strength testing were 50 mm cubes. The fresh mix was placed inside molds, and consolidated via external vibration at medium speed for 3 minutes. The molded specimens were kept in sealed condition, and were demolded after 24 hours. They were then subjected to room-temperature curing which was accomplished by simply sealing the specimens and storing them at room temperature until different test ages.

Another set of specimens was prepared with the same raw materials and proportions, which were milled separately and then blended during mixing of concrete. This separate milling was performed to demonstrate that the mechanochemical effects induced by combined milling of raw materials is key to successful processing of hydraulic cement.

The Particle size distribution was evaluated using a HORIBA LA-920 laser particle size analyzer. This test was performed on 0.5 gram of powder dispersed in a water-based solution of sodium

hexametaphosphate ((NaPO3)13·Na2O) in a glass vial by gently shaking the vial for 1 hour. The Blaine fineness of the hydraulic cement powder as well as that of the raw materials milled separately were measured using the air-permeability apparatus per ASTM C204. The pH of hydraulic cement in solution was evaluated by adding the cement to deionized water at 1 wt.% concentration in a vial. A pH meter (Extech pH 110) was used to determine the pH of solutions versus time.

The heat of hydration of hydraulic cement was measured using the calorimetry test method (I-cal 2000 HPC). For this purpose, the cementitious material was mixed with sufficient amount of water (defined by a w/c ratio that gives the normal consistency) by hand for 1 minute. The fresh paste was then placed inside the calorimeter, and heat release was monitored over 20 hours. The microstructure of hydrates was evaluated via scanning electron microscopy using a JEOL JSM-6610LV scanning electron microscope. Compression tests were performed on a Forney test equipment with 2,227 kN force capacity. EDX analyses were also conducted in the course of scanning electron microscopy. The mineralogy of cement paste was assessed via x-ray diffraction (XRD) using a Bruker D8 daVinci diffractometer equipped with Cu x-ray radiation operating at 40 kV and 40 mA.

2.4 Results and Discussion

2.4.1 Particle Size Analysis and Blaine Fineness

The particle size distributions for the as-received coal fly ash, blend of raw materials milled separately, and the hydraulic cement subjected to mechanochemical processing are presented in Figure 3. The milling action caused some reduction of the ash particle size. The median (D_{50}) values of particle size for the as-received coal fly ash, blend of raw materials milled separately,

and the hydraulic cements subjected to mechanochemical processing were 12.3, 7.9 and 8.1 µm, respectively. Milling of the raw materials separately or together produced comparable results as far as the particle size distribution is concerned. The differences in their reactivity and hydration qualities can thus be attributed to the mechanochemical phenomena induced during combined milling of raw materials rather than the commutation effects of milling.

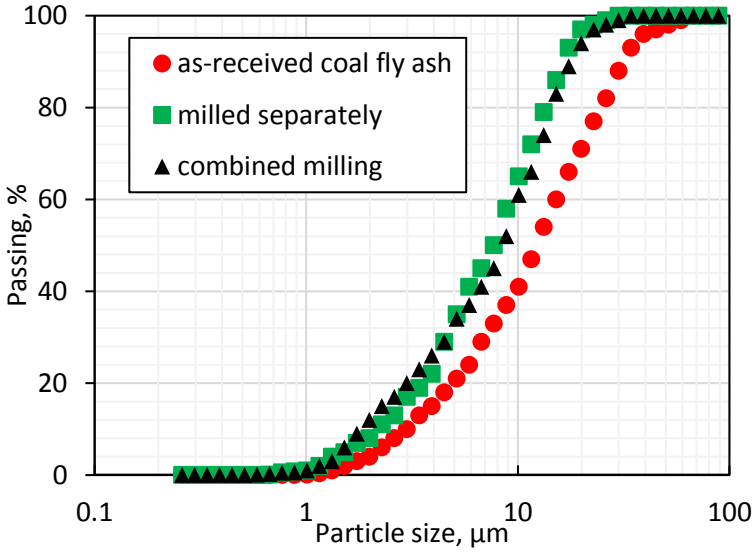

Figure 3. Particle size distributions of the as-received fly ash, blended raw materials milled separately, and the mechanochemically activated hydraulic cement.

Table 3 compares the measured values of Blaine fineness for the as-received coal fly ash, blend of raw materials milled separately, and the hydraulic cement subjected to mechanochemical processing. Milling the raw materials separately or together (in the case of mechanochemical processing) causes a rise in fineness. Milling the raw materials separately or together, on the other hand, has a relatively small effect on the fineness of the resultant powder.

Table 3. Specific surface area results (Blaine fineness), cm^2/g

As-received coal fly ash	Milled separately	Combined milling
2130	3182	2977

2.4.2 pH

Figure 4 compares the pH values in a dilute solution versus time for the blend of raw materials that were milled separately, and the mechanochemically processed hydraulic cements milled in air. The blend of raw materials milled separately exhibits higher alkalinity at all times. The mechanochemically activated hydraulic cement exhibits lower alkalinity than the blend of raw materials that were milled separately, which supports the hypothesis that the alkali and alkaline earth metal cations were diffused into ash particles during mechanochemical processing. The rate of pH rise is also lower for the mechanochemically processed hydraulic cement, which could be due to the slower release of alkali and alkaline earth metal cations incorporated into cement particles when compared with those available as separate particles.

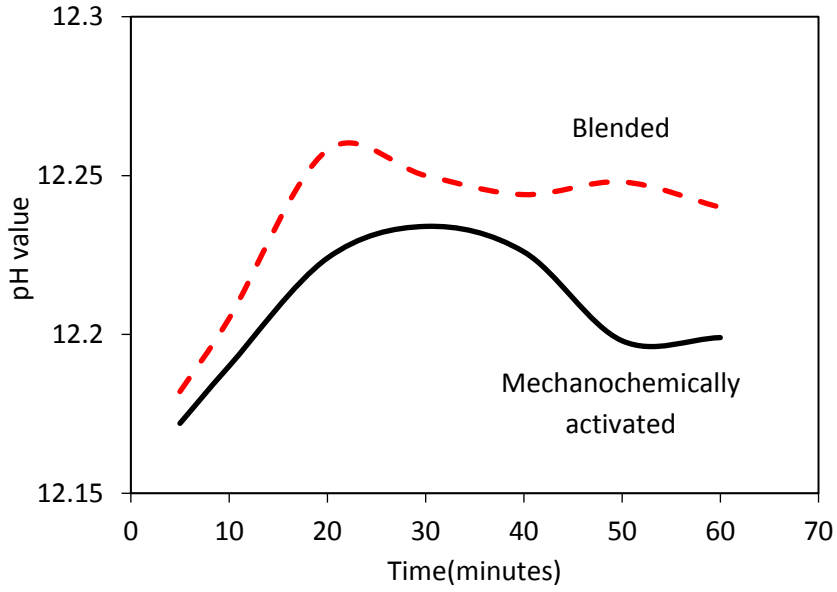

Figure 4. pH values versus time for the blend of raw materials milled separately versus hydraulic cements subjected to mechanochemical processing.

2.4.3 Heat of Hydration

The heat of hydration of hydraulic cement reflects upon the intensity of exothermic reactions at each point in time. Figure 5 presents the rates of heat release versus time for mechanochemically

processed hydraulic cements. An exothermic peak (a) appears immediately when water is mixed with cement, which can be attributed to the instant absorption of solution on the surface of cement particles, dissolution of the highly soluble components (e.g. NaOH), and hydration of CaO. The exothermic peak (b) is significantly higher than that of (a) implying that the alkaline solution is more intensively adsorbed, and OH^- anions begin attacking the Si-O and Al-O bonds [25]. The rapid declining of peak (a) could be due to the slowing down of wetting process and the initially slow reactions. After peak (a) declined for about 130 min, the second exothermic peak (b) appeared, suggesting drastic breakdown of the geopolymer cement particles in combination with the formation of a few of alumina/silica-hydroxyl species and oligomers such as $OSi(OH)_3^-$, $Al(OH)_4^-$, $(OH)_3$-Si–O-Al-$(OH)_3$ etc [26]. The polymerization process is exothermic, and becomes the main factor governing heat evolution (see peak (c), mainly beginning at 170 min). After about 900 min, the process goes into a thermally steady stage, during which the freshly formed gels are probably transformed into larger networks by local reorganization.

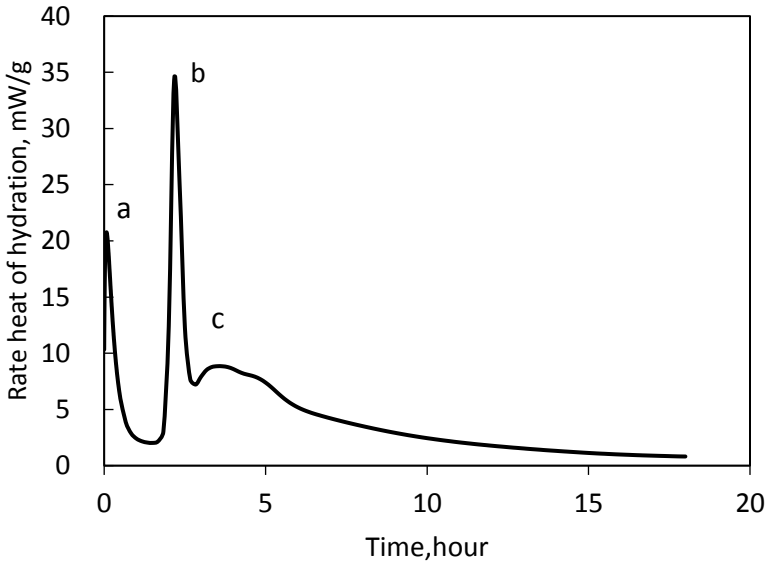

Figure 5. Rate of heat release versus time for the fly ash-based hydraulic cement

2.4.4 Workability and Set Time

The flow table and set time test results are presented in Table 4. The mix incorporating one-part geopolymer (hydraulic) cement used in this investigation provides static and dynamic flow (workability) attributes which are comparable to those offered by normal (Portland cement) concrete. Static and dynamic flows reflect upon the yield strength and viscosity of fresh mixtures. The relatively high rate of setting is a characteristic feature of geopolymer concrete versus normal Portland cement concrete. The initial and final set times of one part-based hydraulic geopolymer cement suits many concrete construction applications.

Table 4. Workability and set time test results.

Flow (cm)		Setting Time (min)	
Static	Dynamic	Initial	Final
54	82	38	210

2.4.5 Compressive Strength

Figure 6 compares the compressive strength test results for concrete materials prepared with the three systems introduced earlier. Residual strengths were measured after immersion of concrete specimens in tap water for 48 hours at room temperature. Concrete specimens made with the cement comprising raw materials milled separately provided the lowest compressive strengths at all ages compared with those made with hydraulic cements processed mechanochemically. For the cement comprised raw materials milled separately (without mechanochemical effects), the resulting concrete materials were not stable upon immersion in water. Mechanochemically processed hydraulic cements, on the other hand, produced moisture-resistant concrete materials. The concrete prepared using cement with raw materials milled separately exhibited decreasing levels of compressive strength with time.

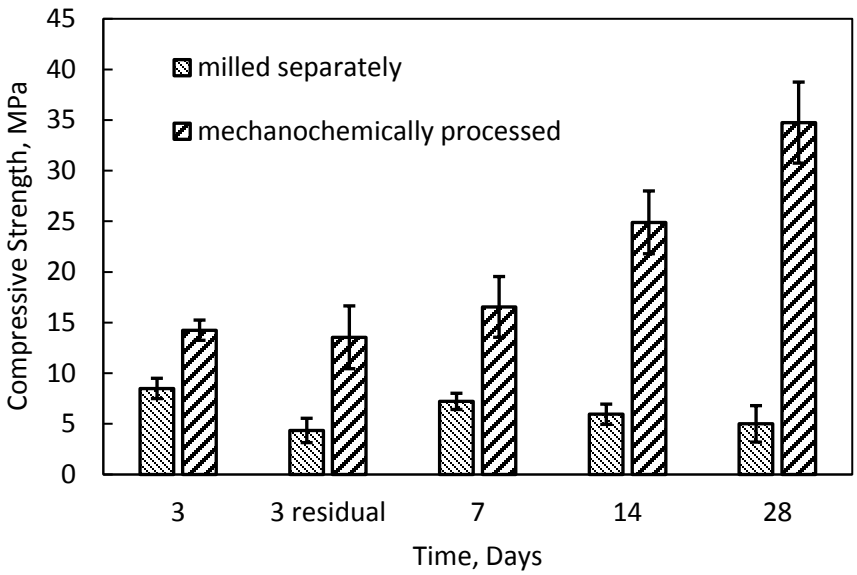

Figure 6. Compressive strength test results (mean values and 95% confidence intervals).

Figure 7 shows the surface appearances of concrete specimens made with different hydraulic cement types after 7 days of room-temperature curing in sealed condition. Specimens made with a cement comprising the raw materials milled separately exhibited surface cracking and swelling, which explain the drop in compressive strength with time. These trends may have been caused by expansive phenomena associated with delayed hydration reactions (e.g., those of residual MgO and free lime remaining after initial hardening of the paste) that form crystals in a solid medium, or by formation of highly hydrophilic compounds which imbibe water and swell. It should be noted that the solubility of calcium compounds decreases with increasing pH, which could lead to delayed formation of calcium hydroxide crystals [27]; this is a possible explanation for the swelling and cracking tendencies observed when the raw materials were milled separately. The XRD data presented later point at the presence of MgO crystals (periclase) in hydrated cement paste, the delayed hydration of which could be the cause of unsoundness.

(a) Milled separately (b) Combined milling

Figure 7. Surface appearances after 7 days of room-temperature curing for concrete specimens made with cements comprising raw materials milled separately (a) and processed mechanochemically via combined milling of raw materials (b).

2.4.6 Microstructure and Chemical Structure

Figure 8 compares SEM images of fly ash particles prior to and after mechanochemical. Surface changes can be observed on particles after mechanochemical processing, which could be interpreted as buildup of mechanochemically produced compounds on fly ash particles. Buildup of matter on the spherical fly ash particle is a distinct feature observed in Figure 8b, which has been attributed to mechanochemical effects. While some fly ash particles are known to incorporate smaller fly ash particles within their core, one cannot rule out that some products of mechanochemical reaction or even raw materials have been incorporated into the core of ash particle during milling. Figure 9 present the EDX spectra obtained at the surfaces of raw fly ash particles and the mechanochemically processed fly ash-based geopolymer cement. Mechanochemical processing of fly ash via milling with other raw materials into a one-part hydraulic cement has raised the Ca concentration (noting that CaO is a raw material milled with fly ash). The Na concentration, however, remained unchanged. This finding indicates that the matter built-up on fly ash particles is not the sodium hydroxide (another raw material milled with fly ash). This finding could also be used to explain the reduced pH of the one-part geopolymer

cement subjected to mechanochemical processing (via milling of blended raw materials); the absence of Na on the surface could reduce its availability to the solution.

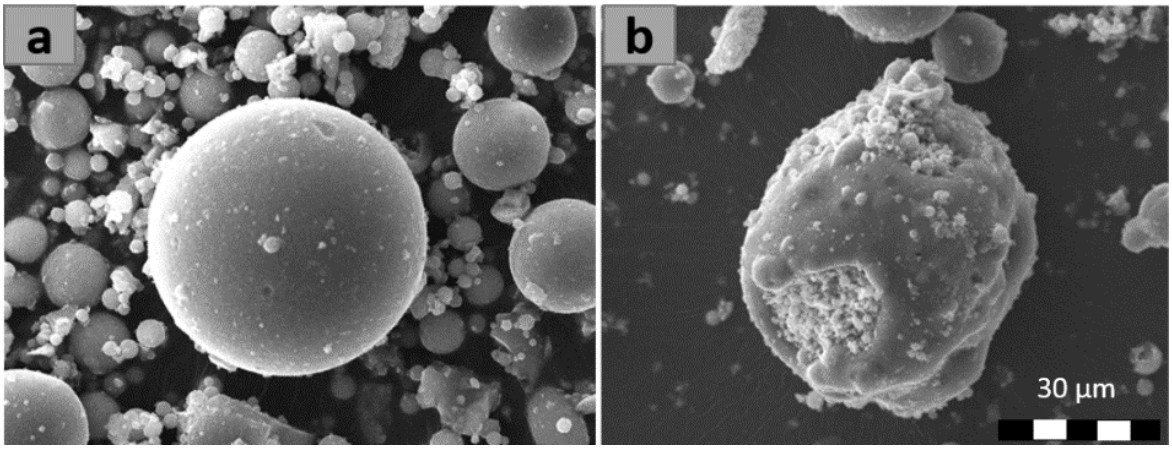

Figure 8. SEM images of particles of (a) fly ash; (b) fly ash-based hydraulic cement processed mechanochemically.

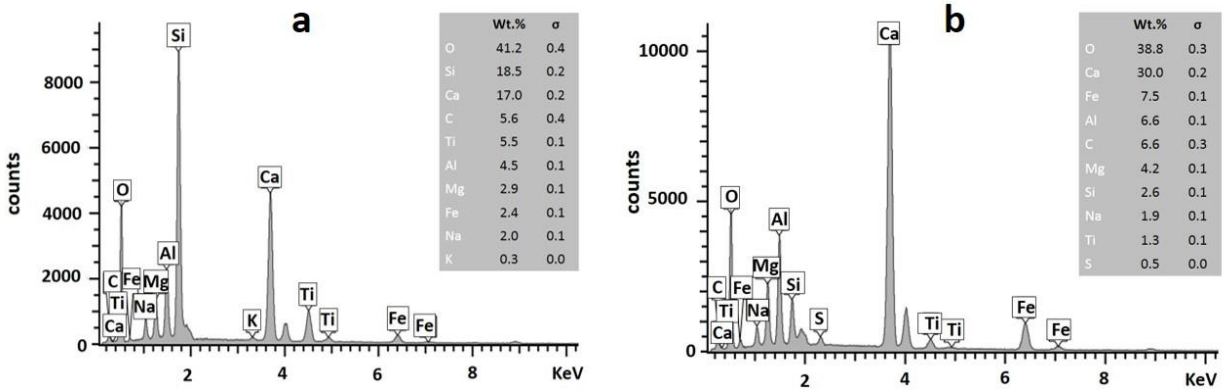

Figure 9. EDX spectra of (a) coal fly ash and (b) mechanochemically processed geopolymer cement.

Figure 10 shows SEM images of hydrated pastes for the three types of cements considered here. Cracks and microcracks can be clearly seen in the paste of cement made with raw materials milled separately; unreacted fly ash particle can also be detected in this image. With hydraulic cements subjected to mechanochemical processing, hydrated pastes do not exhibit a granular morphology or any sign of cracking (except for minor microcracking which could have been caused by preparation of specimens in vacuum); instead, the hydrated gel seem to have formed. While one

could argue that cracks could be formed due to drying shrinkage under vacuum when the specimens are being prepared for scanning electron microscopy, the fact that all specimens have been subjected to vacuum and some exhibit notable cracking supports the above findings.

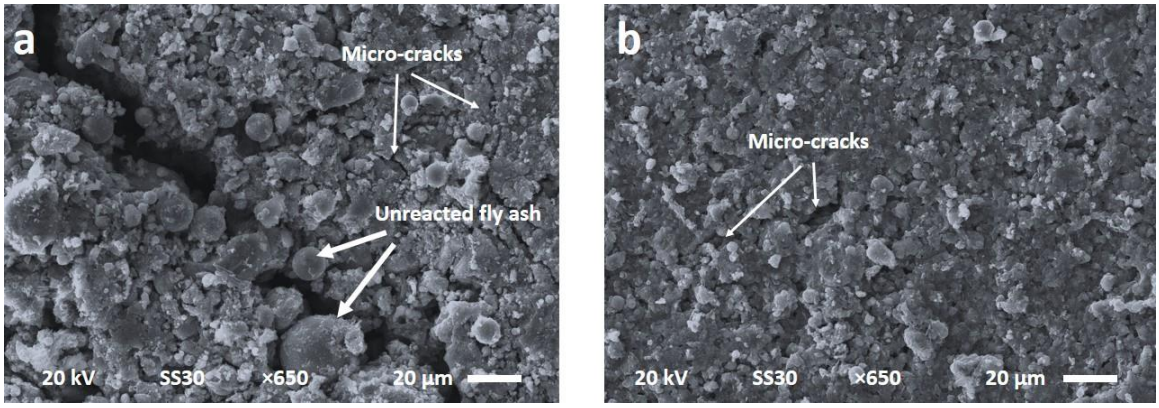

Figure 10. SEM images of hydrated cement paste for (a) cement made with raw materials milled separately; (b) hydraulic cement processed mechanochemically via combined milling of raw materials.

Figure 11 compares the XRD spectra for geopolymer pastes at 7 days of age made with cements comprising raw materials milled separately or processed mechanochemically via combined milling of raw materials. The paste made with the raw materials milled separately shows Portlandite $Ca(OH)_2$ peaks at angles at 2θ=18, 34, 46 and 51°. The presence of calcium hydroxide peaks could explain the swelling and surface cracking tendency observed in the paste made of raw materials milled separately. Mechanochemical processing of raw materials (by milling their blend) produces pastes which do not exhibit the Portlandite peak, suggesting that the calcium has been incorporated into other (probably amorphous) compounds with improved stability and binding effects. More investigations into the chemical structure of this one-part geopolymer cement hydrates are warranted. Solid-state NMR could be a powerful tool for resolving this structure.

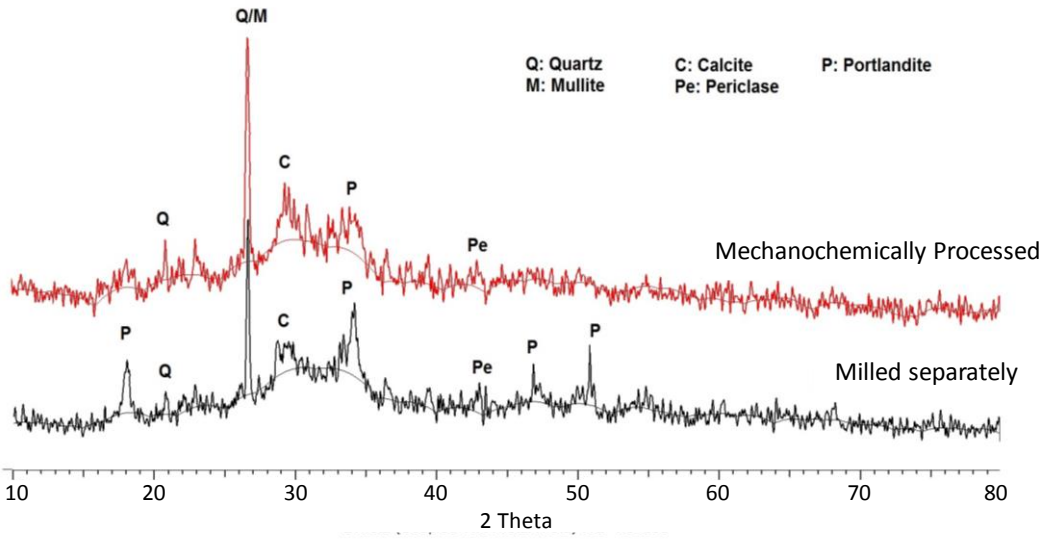

Figure 11. X-ray diffraction results for geopolymer paste made with cements comprising raw materials milled separately and processed mechanochemically via combined milling of raw materials.

2.5 Conclusions

- A new class of hydraulic cement was developed with the objective of realizing significant environmental and performance benefits when compared with conventional Portland cement. The new cement relies primarily upon alkali aluminosilicate hydrates to render binding effects, in lieu of the calcium silicate hydrate produced upon hydration of Portland cement.
- Mechanochemical effects rendered by simple milling of blends of raw materials were used to transform coal fly ash into hydraulic cement. This required supplementing the chemistry of coal fly ash as an aluminosilicate precursor with relatively small concentrations of compounds incorporating alkali/alkaline earth metal cations. The mechanochemical effects are hypothesized to produce a disordered aluminosilicate framework embodying alkaline earth and/or alkali metal cations.

- Addition of alkaline compounds enhanced the process of destabilizing the aluminosilicate structures with input of mechanical energy. This explains why milling of the blend of raw materials produced hydraulic cements with improved performance when compared with separately milled raw materials that were blended after milling.
- Microstructural, chemical and crystallographic investigations of hydraulic cements provided support for the role of mechanochemical phenomena in production of hydraulic cements with controlled rates of hydration reactions. Calorimetry studies highlighted the steps involved in hydration reactions of alkali aluminosilicate-based hydraulic cements.
- The simple approach to processing and the extensive use of recycled materials provide the new hydraulic cement with important sustainability and economic advantages. These attributes of the viable properties of the new hydraulic cement point at its commercial potential. Further investigations into the chemical structure of the hydraulic cement, and more comprehensive assessment of the engineering properties of the cement and its hydrates are warranted. Concrete materials made with the new hydraulic cement should also be thoroughly characterized in an effort to verify its ability to meet performance requirements in different fields of application.

Chapter 3

Synthesis and Characterization of Alkali Aluminosilicate Hydraulic Cement that Meets Standard Requirements for General Use

3.1 Introduction

Portland cement has been the predominant inorganic binder for production of concrete and other construction applications for several decades. Important improvements have been made in the efficiency of cement manufacturing, which has had quantitative effects on the energy use and carbon emissions associated with production of cement. In spite of these improvements, cement manufacturing is still a major source of anthropogenic CO_2 emissions and energy consumption worldwide [28]

The chemistry and the prevalent manufacturing features of Portland cement have remained essentially unchanged for several decades [29]. The cement industry has made significant investments in existing manufacturing plants, and has developed thorough know-how of the Portland cement chemistry, processing and performance. In recent decades, we have observed development of a chemical admixtures industry that is largely centered around the Portland cement chemistry, and has brought about significant improvements in concrete performance[30, 31]. These circumstances together with some highly desired features of Portland cement have created a strong inertia against fundamental changes in the chemistry and manufacturing process of cement. Portland cement benefits from the use of raw materials that are available abundantly across diverse geographic areas. In addition, the existing approach to manufacturing of Portland cement yields an end product that reliably and cost-effectively meets the

performance requirements relevant to the use of Portland cement in concrete construction and other applications.

The demands for improvement of the sustainability and some performance attributes of Portland cement have been on the rise. The significant energy content and carbon footprint of Portland cement, and the position of Portland cement concrete as the most widely used material of construction have prompted efforts to develop alternative hydraulic cements with significantly improved sustainability [9, 32]. Efforts towards development of alternative hydraulic cements are also driven by the growing need to enhance the service life and life-cycle economy of the concrete-based infrastructure [33].

In response to need for hydraulic cements that offer qualitative advantages over Portland cement in terms of sustainability and durability, the cement industry has developed performance-based ASTM standards that do not impose chemical constraints on hydraulic cements [34]. This initiative, however, has not yet led to breakthrough developments, and the performance-based standards have not been adopted and specified widely by agencies that own and manage infrastructure systems [35]. It should be noted that a number of alternative hydraulic cement chemistries are available commercially for niche applications. Examples include rapid-hardening hydraulic cements based on calcium aluminate, calcium sulfoaluminate and magnesium phosphate chemistries [36]. The performance and economics of these specialty hydraulic cements, however, do not allow their broad use in normal concrete construction.

Efforts have been undertaken in recent years towards development of “one-part” alkali aluminosilicate cements that, similar to Portland cement, undergo hydration reactions upon addition of water. These hydraulic cements are produced by heating of a blend of aluminosilicate

precursors (albite, kaolin, etc.) and alkalis [12-14]. The resulting hydraulic cements produced, upon hydration, inorganic binders with viable strength levels. This is a new field of development, and some key aspects of alkali aluminosilicate-based hydraulic cements require further improvement. For example, some of these hydraulic cements lack adequate stability in the presence of moisture. Efforts have been made to use lower-cost sources of alkalis for production of one-part alkali aluminosilicate cement. These hydraulic cements undergo hydration reactions in a more alkaline environment than Portland cement. Red mud (or red sludge) is a potential source of low-cost alkalis. It is a highly alkaline (with high concentrations of NaOH and $NaAlO_2$) byproduct of aluminum production, which comprises clay, silt, sand, Fe_2O_3 and Al_2O_3 [15]. Red mud is generated at an annual rate of about 77 million tons; it is a hazardous waste with serious disposal problem in the mining industry. Since alkali aluminosilicate hydrates provide significant hazardous waste immobilization qualities, red mud has been considered as a source of alkalis in development of hydraulic cements. This was accomplished via thermal processing of red mud and rice husk ash; the resultant hydraulic cement, upon hydration, produced moderate levels of compressive strength [15]. Simple blending of raw materials has also been used as a means of producing a one part hydraulic cement based on alkali aluminosilicate chemistry [16]. This approach, however, retains the caustic nature of the alkaline raw materials, and can suddenly release excess heat upon addition of water to the cement. The affinity of alkaline constituents for water could also limit their shelf life in air. Experimental results indicated that curing at elevated temperatures was required to yield viable levels of early-age compressive strength. At later ages, a drop in compressive strength was observed. More recent investigations have produced one-part formulations by blending either coal fly ash and sodium silicate or rice hull

ash and sodium aluminate to achieve viable compressive strengths with room-temperature curing [37, 38]. The caustic nature of cement, limited shelf life, and sudden release of excess heat upon addition of water would still be the drawbacks of these cements. Simple mixing of dry raw materials without chemically integrating the alkalis into the aluminosilicate structure (which also enhances the activity of the aluminosilicate precursor) is not a viable approach to production of hydraulic cements based on alkali aluminosilicate chemistry.

Efforts to develop one-part hydraulic cements based on the alkali aluminosilicate chemistry have been largely focused on the mechanical properties produced upon hydration. The dimensional and chemical stability, weathering and moisture resistance, microstructure and other properties of the hydration products of these cements have not been investigated. More efforts are needed to understand and improve the chemical composition of these cements, the effectiveness and efficiency of transforming the blends of raw materials into a hydraulic cement, and to thoroughly characterize these cements in order to qualify them based on performance-based standards developed for hydraulic cements which use general use in concrete production. The primary performance-based standard used in this development work was ASTM C1157 (Standard Performance Specification for Hydraulic Cement) [39].

ASTM C1157 allows for unrestricted use of raw materials and processing methods to produce innovative hydraulic cements [39]. ASTM 1157 also contains optional requirements that are not available under other specifications. The ASTM C1157 requirements are largely based on the performance limits of ASTM C150 (Standard Specification for Portland Cement) [40] and ASTM C595 (Standard Specification for Blended Hydraulic Cements) [41], the traditional cement specifications that contain a combination of prescriptive and performance limits. In ASTM C1157,

cements are classified into six types according to their intended use: GU for general construction, HE for high early strength, MS for moderate sulfate resistance, HS for high sulfate resistance, MH for moderate heat generation, and LH for low heat generation [39]. The focus of this investigation is on development of a new hydraulic cement that meets the general use (GU) hydraulic cement requirements.

ASTM C1157 represents a shift away from prescriptive specifications that dictate composition restrictions. Instead, the emphasis is on the ability of cement to perform. For the tricalcium aluminate (C_3A) content of Type II or V cement is prescriptively limited to control sulfate resistance. In ASTM C 1157, assurance of sulfate resistance of Type MS or HS cement is determined by testing (ASTM C1012) mortar bars made with the cement [42]. Laboratory tests, and not chemical analyses, are used as predictors for various aspects of performance. Some key performance specifications considered in this project were: (i) compressive strength development with time; (ii) heat of hydration, and initial and final set times; (iii) expansion tendencies due to alkali-silica reaction; (iv) change in length correlating with autoclave soundness; and (v) expansion of mortar bar immersed in lime-saturated water. Scanning electron microscopy, thermogravimetry, calorimetry and x-ray diffraction techniques were employed to gain more insight into the hydration mechanisms and the resultant microstructure of the new hydraulic cements.

The end product of this development effort is a hydraulic cement that meets standard requirements and is also compatible with the mainstream mix design and construction practices used with normal Portland cement concrete. These features, combined with sustainability and

some important performance advantages of the new hydraulic cement, facilitate its transition to concrete construction markets.

3.2 Materials and Methods

3.2.1 Materials and Their Characteristics

The aluminosilicate precursors used in this process were coal fly ash, ground granulated blast furnace slag, and albite. The (dry) alkalis used as raw materials were sodium hydroxide, sodium silicate, and calcium oxide. Sodium tetra-borate (Borax) was also added to the cement formulation to retard its set time [43, 44]. The weight ratios of raw materials used for production of an alkali aluminosilicate-based hydraulic cement are presented in Table 5. A predecessor for this formulation was devised to balance the Si, Al, Na and Ca molar ratios to enable formation of viable alkali aluminosilicate hydrates. The base formulation was then refined via trial-and-adjustment experimental studies to produce a desired balance of fresh mix workability, set time, strength development characteristics, and moisture resistance.

Table 5. Proportions of the raw materials used for production of an alkali aluminosilicate-based hydraulic cement.

	Fly ash	Slag	Albite	Na_2SiO_3	NaOH	CaO	Borax
Weight, %	45	25	15	7	3	4	1

The coal fly ash was supplied by the Lansing Board of Water and Light (Michigan) with mean particle size of 10.9 µm. The GGBF slag used in this study is iron slag powder (Nucem100) obtained from Lafarge-Holcim. This slag has a specific gravity of 2.90 and a bulk density of 1,225 kg/m3. Albite was used as a natural source of silica, alumina and sodium; it was purchased from Sister's Rocks (Westminster, Colorado). Albite was received as aggregates of 2-5 cm particle size

with 97-99% purity; these coarser particles were washed and crushed to 2-4 mm size prior to use in the process.

Table 6 presents the chemical compositions, determined by x-ray fluorescence (XRF) spectroscopy, of the aluminosilicate precursors (coal fly ash, slag and albite) used to prepare the hydraulic cement. The coal fly ash used here had silica and alumina contents totaling at 66.4 wt.%, with 19.3% calcium oxide content. It also incorporated some alkali metal cations. In the case of slag, silica and calcium oxides constituted about 75% of the total mass, and the weight ratio of silica to calcium oxide was close to 1. The alkali metal content of this slag was relatively low (<1 wt.%). Albite comprised primarily of silica (69.1 wt.%) and alumina (17.1 wt.%). The sodium oxide content of this albite was relatively high, approaching 10 wt.%.

Table 6. Chemical compositions (wt.%) of the coal fly ash, slag and albite used as raw materials for production of cement.

	SiO_2	CaO	Al_2O_3	Fe_2O_3	K_2O	Na_2O	MgO
Coal fly ash	43.05	19.30	23.33	7.82	1.72	0.90	1.43
Slag	37.53	40.78	9.54	0.47	0.21	0.25	10.85
Albite	69.1	0.18	17.1	0.10	0.21	9.87	0.10

The X-ray diffraction patterns for the coal fly ash, slag and albite used in this investigation are presented in Figure 12. The coal fly ash was found to be largely amorphous with two main crystalline mineral phases, namely quartz (SiO_2) and mullite ($3Al_2O_3.2SiO_2$). The crystalline phase quartz in coal fly ash is less reactive than the other ash constituents. It is, however, found to provide some chemical reactivity in an alkaline environment [45], and once finely ground, can provide nucleation sites for dispersed formation of the hydration products. The presence of quartz has been reported to enhance the rate of hydration reactions at early age [46]. The XRD

pattern for the slag points at its predominantly glassy state, with peaks associated with crystalline akermanite ($2CaO.MgO_3.SiO_2$) identified. Albite, on the other hand, exhibits a highly crystalline structure with sharp peaks pointing at the presence of albite ($Na(AlSi_3O_8)$) and small concentrations of microcline ($K(AlSi_3O_8)$).

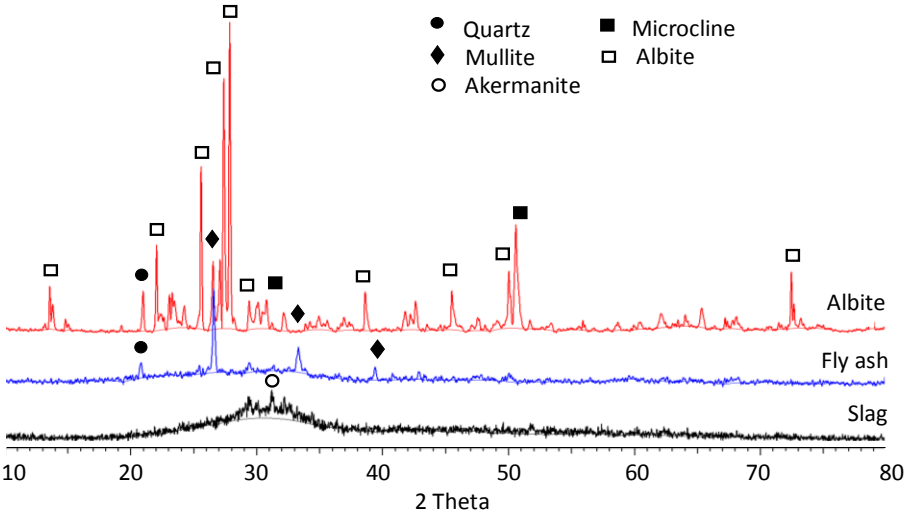

Figure 12. XRD Patterns of the coal fly ash, slag and albite used in this investigation.

Laboratory grade sodium hydroxide, sodium silicate, quick lime (CaO) and sodium tetra-borate were purchased in powder form at 97-98% purity from Sigma Aldrich.

The raw materials introduced above were processed via milling to produce a hydraulic cement. The milling process is described elsewhere [47]. The resultant hydraulic cement is an alkali aluminosilicate of constituents capable of forming hydrates upon addition of water.

Portland cement (Type I) was used in this investigation as the control cement against which the new hydraulic cement (alkali aluminosilicate cement) was evaluated. The chemical composition and Blaine fineness of the alkali aluminosilicate cement is compared with those of Type I Portland cement in Table 7. When compared with Portland cement, the alkali aluminosilicate cement incorporates lower CaO and higher SiO_2, Al_2O_3 and Na_2O contents.

Table 7. The chemical composition (wt.%) and Blaine fineness (BF) of the new alkali aluminosilicate cement (AAS) and Type I Portland cement.

	SiO_2	CaO	Al_2O_3	Fe_2O_3	MgO	K_2O	Na_2O	SO_3	BF, cm^2/g
AAS cement	35.2	28.1	13.6	4.03	3.73	1.14	8.89	0.53	3960
Portland cement	20.1	64.2	5.31	2.86	2.65	0.10	0.02	2.14	3870

The X-ray diffraction pattern of the alkali aluminosilicate cement is presented in Figure 13. The quartz (SiO_2) peaks identified in this pattern could come from coal fly ash. Sodium and potassium aluminosilicate, albite and anorthoclase $(Na,K)AlSi_3O_8$ peaks were also detected in the alkali aluminosilicate cement. Quick lime (CaO) and calcium silicate carbonates (spurrite, $Ca_5(SiO_4)_2CO_3$) were also found in the alkali aluminosilicate cement. A broad hump appeared within the 2θ range of 20 to 40°, which points at the presence of amorphous compounds in this cement.

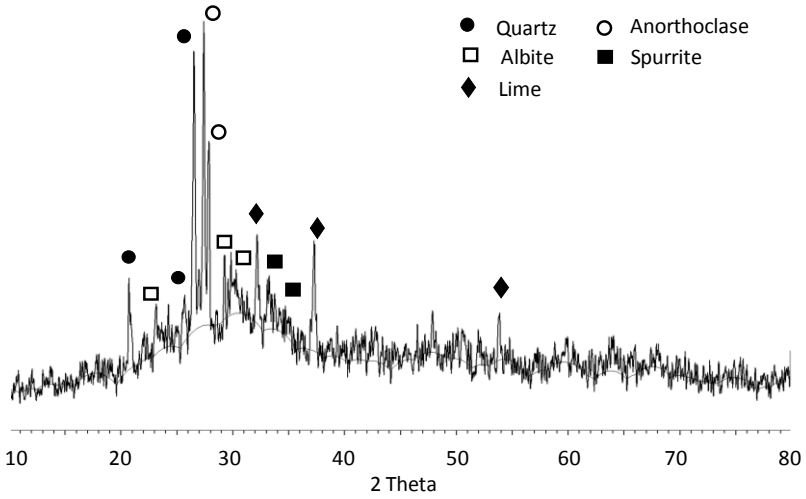

Figure 13. XRD pattern of the alkali aluminosilicate cement.

The particle size distributions of the Portland cement and the alkali aluminosilicate cement, measured using laser granulometry, are presented in Figure 14. The median particle sizes were 9.8 and 7.4 µm for Portland cement and the alkali aluminosilicate cement, respectively.

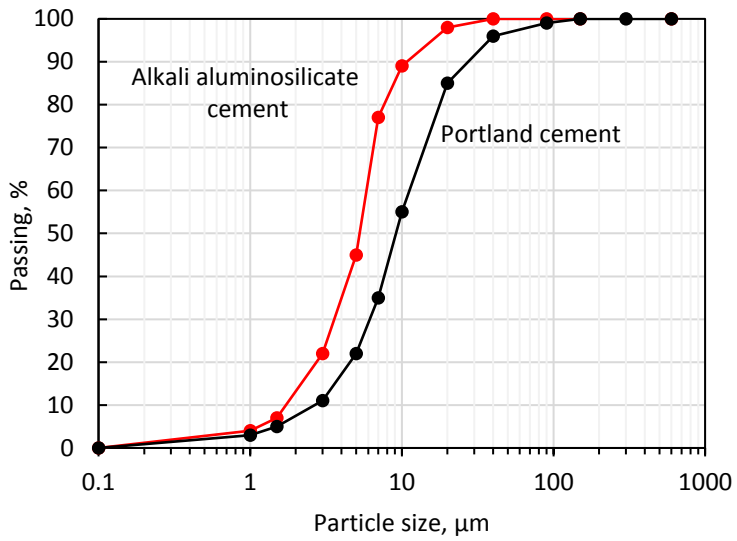

Figure 14. Particle size distributions of Portland cement and the alkali aluminosilicate cement developed in the project.

A number of tests to be performed per ASTM C1157 are performed on mortars prepared with a standard silica sand that meets ASTM C778 requirements [48]. In the case of experiments relating to alkali-silica reactions, highly reactive (sedimentary siliceous) coarse aggregates obtained from Texas DOT were crushed to fine aggregates of millimeter-scale particle size and sieved per ASTM C227 prior to preparation of mortar specimens [49].

3.2.2 Methods Used for Evaluation of Hydraulic Cements

Compressive strength tests were performed per ASTM C109 on 50-mm cubic mortar specimens after 1, 3, 7 and 28 days of curing in sealed condition (>95% relative humidity) at room temperature [50]. These mortar mixtures were prepared with the standard silica sand at a silica sand/cement weight ratio of 2.75. Three specimens were tested, and the average value of compressive strength was recorded. The water-to-cement ratio of mortar mixtures was adjusted to produce a fresh mix flow of 110±5% per ASTM C1437 [51]. The resulting water-to-cement ratios ranged from 0.45 to 0.50. The heat of hydration reactions of cement was measured by

performing the calorimetry test (ASTM C1679 [52]), using an I-cal 2000 HPC calorimeter. For performance of this test, cement was mixed manually with water for 30 seconds at a water/cement ratio of 0.35. The fresh paste was placed inside the calorimeter, and its heat release was monitored over 55 hours. The initial set time of pastes was measured per ASTM C191 using the Vicat needle apparatus [53]. The amount of water mixed with cement for measurement of set time was selected to produce a normal consistency per ASTM C187 [54]. Tests to evaluate expansion caused by alkali silica reaction (ASR) were carried out on mortar specimens per ASTM C227 [49]. Prismatic mortar specimens with 25mm by 25mm by 285mm were prepared at a cement-to-graded aggregate weight ratio of 1:2.25. The amount of mixing water was determined so that it produces the required flow per ASTM C1437 [51]. Three specimens were tested for each hydraulic cement, and the average value was recorded. Autoclave expansion tests were performed on cement paste specimens per ASTM C151 [55]. Cement paste specimens were prepared by mixing the hydraulic cement and sufficient water to produce a paste of normal consistency per ASTM C187 [54]. The fresh paste was used to prepare 25mm by 25mm by 285mm prismatic specimens, and stored in sealed condition. After 24 hours, the specimens were demolded and their initial lengths were measured immediately. The specimens were then subjected to a steam pressure of about 2±0.07 MPa at a temperature of 216˚C for 3 hours. Three specimens were prepared and tested for each hydraulic cement, and the average value of length change was recorded. The mortar bar expansion of prismatic mortar specimens immersed in water was evaluated per ASTM C1038 [56]. The mortar bar specimens of 25mm by 25mm by 285mm dimensions were prepared using the hydraulic cement with graded standard silica sand at cement: sand weight ratio of 1:2.75. The amount of mixing water was adjusted to produce a

flow of 110±5% per ASTM C1437 [51]. The specimens poured inside molds were kept in sealed condition for 24 hours, and were then demolded and placed in water at 23.0±2.0 °C for 30 minutes prior to making the initial length measurement. The specimens were then stored in saturated lime-saturated water. Expansion measurements were taken daily by removing the specimens from water storage, and wiping them with a piece of cloth before length measurement; these measurements were taken up to 21 days. Scanning electronic microscopy (SEM) of the test specimens was performed using a JOEL-5000 instrument on hydrated pastes after 28 days of curing in sealed condition (>95% relative humidity). The unpolished specimens were first coated with gold-palladium alloy using a sputter coater (DESK II), and then imaged in high-vacuum mode at an accelerating voltage of 10 or 15 kV. Thermogravimetric analyses were conducted on hydrated pastes using a Perkin Elmer TGA 4000 with temperature raised from 50 to 950^{o}C at a heating rate of 15˚C/min in nitrogen atmosphere.

3.3 Test Results and Discussion

3.3.1 Compressive Strength

The compressive strength test results for mortar specimens prepared using Type I Portland cement and the alkali aluminosilicate hydraulic cement are presented in Figure 15. The results indicated that the alkali aluminosilicate cement produced compressive strengths exceeding those of Portland cement at all ages considered here (up to 28 days). The compressive strengths obtained with the alkali aluminosilicate hydraulic cement were higher than the minimum values required by ASTM C1157 [39]. Mortars prepared with the alkali aluminosilicate cement (Portland cement) reached 17 (13), 32 (20) and 36 (31) MPa compressive strengths at 3, 7 and 28 days of age, respectively.

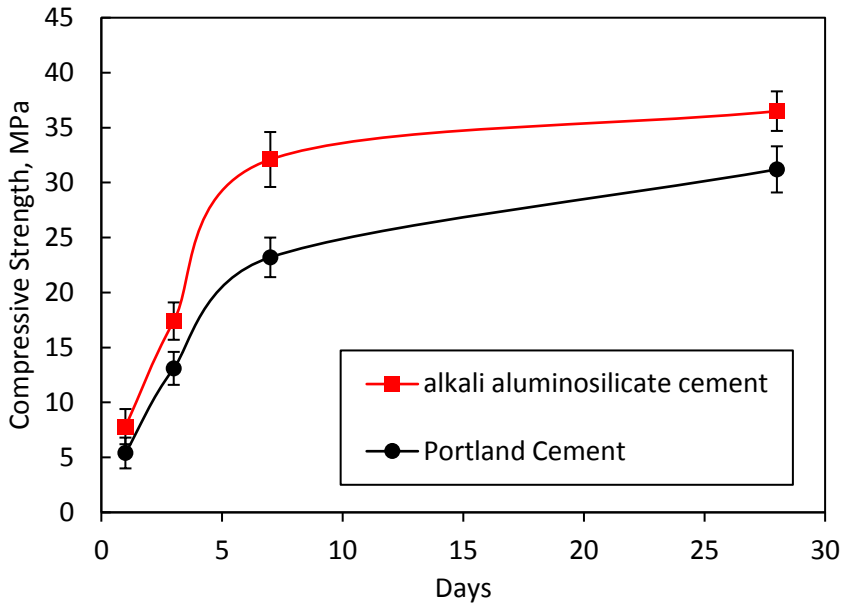

Figure 15. Compressive strength test results for mortar specimens after different curing periods (means & 95% confidence intervals).

3.3.2 Heat of Hydration and Set Time

The heat of hydration and total heat released test results for Portland cement and for the alkali aluminosilicate cement are presented in Figure 16a and Figure 16b, respectively. An instantaneous exothermic peak appeared immediately when water was mixed with both cements. This peak can be attributed to the instant adsorption of the solution on the surface of cement particles, and the dissolution of the highly soluble constituents of cement. This peak is sharper for the alkali aluminosilicate cement when compared with Portland cement, which could be due to the stronger presence of soluble alkalis in the alkali aluminosilicate cement. A second exothermic peak occurred after 2 hours for the alkali aluminosilicate cement, which could be correspond to the exothermic reactions when the alkaline solution is intensively adsorbed, and the OH^- anions begin to attack the Si–O and Al–O bonds in cement particles [25]. For Portland cement, a second broad peak appeared after several hours; this peak (at the so-called

acceleration stage) mainly represents the formation of hydration products, and conversion of ettringite to mono-sulfates [57].

The total heat of hydration test results presented in Figure 16b (represented by the area underneath the rate of heat release curves) suggest that the alkali aluminosilicate cement released more heat of hydration during the first 10 hours. The total heat released by the alkali aluminosilicate cement reached a plateau after about 20 hours; with Portland cement, this plateau was reached after about 40 hours. The total heat released by the alkali aluminosilicate cement after 40 hours was about 30% less than that for Type I Portland cement. ASTM C1157 does not specify a maximum limit for the total heat release of the general use (GU) cement; in the case of low heat of hydration cement, it specifies that the total heat release should not exceed 250 kcal/kg after 7 days [39]. The test results presented in Figure 16b indicate that the alkali aluminosilicate hydraulic cement would meet this requirement. ASTM C150 specify a maximum limit of 315 kcal/kg after 3 days [40], which also seems to be satisfied by the alkali aluminosilicate cement developed in this investigation.

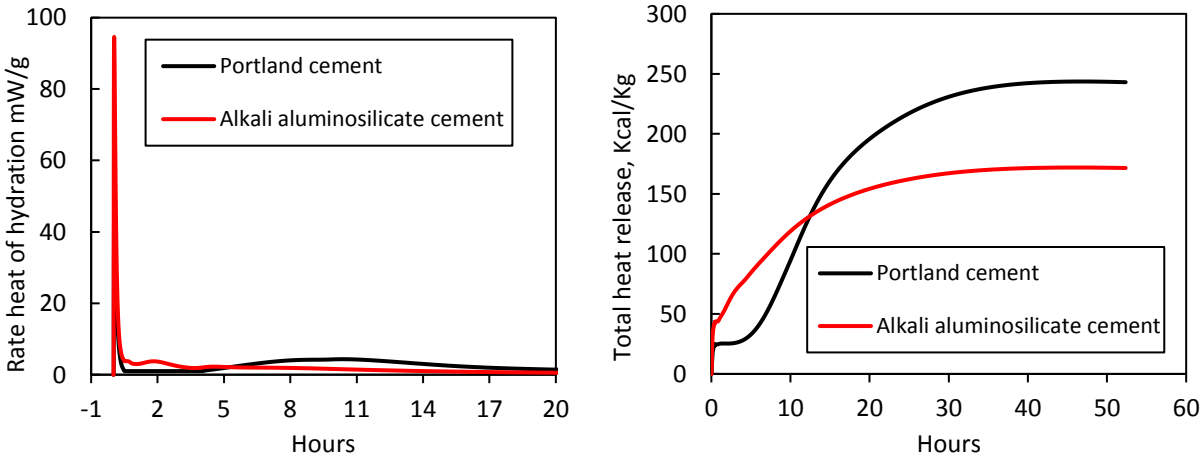

(a) Rate of heat release (b) Total heat release

Figure 16. Heat of hydration test results for Portland cement and the alkali aluminosilicate cement.

Table 8 presents the initial and final set times of Portland cement and the alkali aluminosilicate cement developed in the project. The initial and final set times of the alkali aluminosilicate cement are shorter than those of Portland cement. Both the initial and final set times of the alkali aluminosilicate cement, however, meet the ASTM C1157 requirements [39]. These requirements specify a minimum initial set time of 45 minutes and a maximum final set time of 420 minutes. Rapid setting (and hardening) are some characteristic features of hydraulic cements based on alkali aluminosilicate chemistry. Setting and hardening of these hydraulic cements involves dissolution and polycondensation phenomena that generally takes place at a higher rate than hydration of Portland cement [58, 59].

Table 8. Initial and final set times of Portland cement and the alkali aluminosilicate hydraulic cement.

	Portland cement	Alkali aluminosilicate cement
Initial set time, minutes	132	53
Final set time, minutes	328	84

3.3.3 Alkali-Silica Reactions

Expansions caused by reactions involving the alkaline pore solution of cement hydrates and the reactive constituents of siliceous aggregates can cause premature deterioration of infrastructure systems. ASTM C1157 has an optional requirement for evaluation of expansions caused by alkali-silica reactions per ASTM C227 [49]. For general use (GU) hydraulic cement, the expansion due to alkali-silica reactions should not exceed 0.02% and 0.06% after 14 and 56 days, respectively [39].

Figure 17 presents the length change caused by alkali-silica reactions versus time for Portland cement and the alkali aluminosilicate cement. The expansion for Portland cement specimens

started from the first day at a small rate while the alkali aluminosilicate cement specimens exhibited shrinkage during the first 7 days. Portland cement specimens showed increase of the expansion rate after 2 weeks, while alkali aluminosilicate cement specimens exhibited a gradual rise in expansion over time. At the end of the 14-day exposure period, the mortar specimens prepared with Portland cement and the alkali aluminosilicate cement exhibited expansion of 0.0045% expansion and 0.0021% shrinkage, respectively. After 56 days, mortar specimens prepared with Portland cement and with the alkali aluminosilicate cement reached expansions of 0.028% and 0.0094%, respectively.

Both cements met the ASTM C1157 requirement of less than 0.02% and 0.06% expansion after 14 and 56 days of exposure, respectively. The length change appeared to have stabilized for specimens made with either type of cement. By the end of 70 days, mortar specimens prepared with alkali aluminosilicate cement showed expansion values that were 65% less than those of Portland cement specimens. Alkali-silica reaction in alkali aluminosilicate binders is likely to occur during the original dissolution and condensation polymerization process, while the material is still in gel form. Later-age reactions could be minimized as a dense bond zone forms around each aggregate with progress of curing [60]. Furthermore, the relatively low calcium content present in the alkali aluminosilicate cement compared to Portland cement reduces the possibility of forming expansive sodium-calcium silicate gel [61]. The expansion values measured for Portland cement specimens confirm that the aggregate used in this study is actually prone to deleterious alkali-silica reactions.

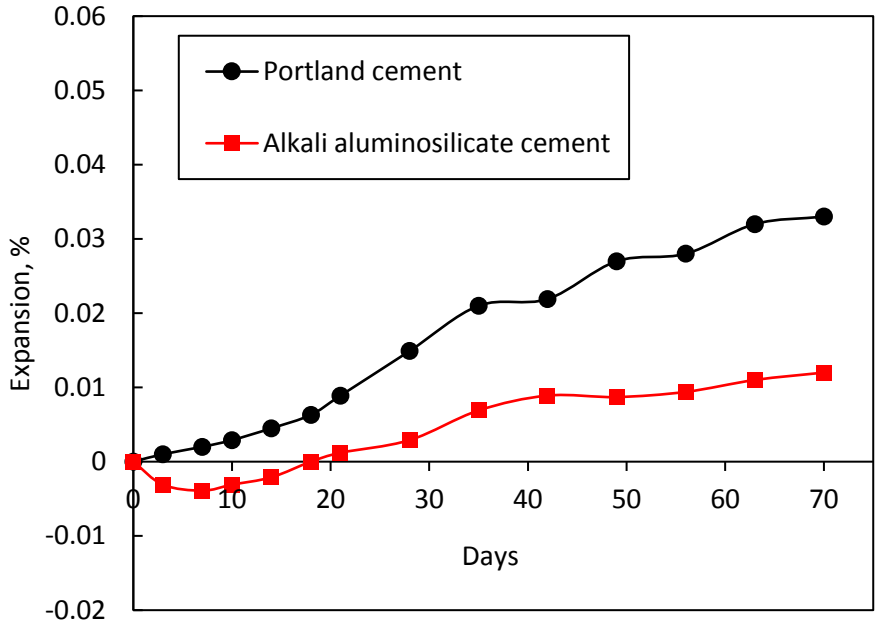

Figure 17. Expansions caused by alkali-silica reactions.

3.3.4 Autoclave Expansion

Autoclave expansion is an accelerated soundness test which determines the potential for deleterious expansion of cement caused by delayed hydration reactions (of any hard-burnt magnesia and calcium oxide present in cement) [62]. This test is conducted under a constant steam pressure and temperature to accelerate hydration reactions which otherwise occur over time.

For general use (GU) cement, ASTM C1157 limits the maximum autoclave expansion (measured per ASTM C151[55]) to 0.8%. The results of the autoclave expansion tests performed on Portland cement and the alkali aluminosilicate cement paste specimens are presented in Table 9. The autoclave expansion of the alkali aluminosilicate cement paste is observed to be significantly lower than that of Portland cement; both meet the ASTM C1157 maximum limit of 0.8%. The reactive nature of the alkali aluminosilicate cement limits the quantities of unhydrated cement

left for delayed hydration that produces expansive tendencies in hardened cement paste. In the case of Portland cement, such delayed hydration reactions are attributed to the presence of hard-burnt magnesia and calcium oxide. The fact that the alkali aluminosilicate cement is processed via input of mechanical energy and not heat at elevated temperatures mitigates formation of hard-burnt species that are prone to delayed hydration reactions.

Table 9. Autoclave expansion test results.

	Autoclave length change, %
Portland cement	0.411
Alkali aluminosilicate cement	0.237

3.3.5 Mortar Bar Expansion

Unbalanced cement chemistries may be prone to chemical reactions which proceed at room temperature to produce crystalline structures that apply internal pressure, and cause swelling and eventual cracking of hydrated cement pastes. In conventional cement chemistry, excess sulfate contents can cause internal sulfate attack which transforms calcium mono-sulfoaluminate hydrate to tri-sulfoaluminate hydrate (ettringite) [63] . The mortar bar expansion test (ASTM C1038 [56]) is devised to assess the potential for such deleterious effects. It monitors expansion of prismatic specimens immersed in lime-saturated water at room temperature. ASTM C1157 specifies a maximum mortar bar expansion of 0.02% after 14 days.

The expansion values versus time for Portland cement and for the alkali aluminosilicate hydraulic cement specimens are presented in Figure 18. After 14 days of immersion, the measured value of expansion for the alkali aluminosilicate hydraulic cement and the Portland cement specimens reached about 0.003% and 0.005%, respectively. The larger expansion of Portland cement specimens could feasibly result from delayed ettringite formation [64]. The measured value of

mortar bar expansion for the alkali aluminosilicate hydraulic cement easily meets the ASTM C1157 requirement. The mechanism causing this minor expansion needs further investigation. This alkali aluminosilicate cement has minor sulfate content (0.53 wt.% SO_3), and provides the potential to incorporate SO_3 into the aluminosilicate gel structure [65].

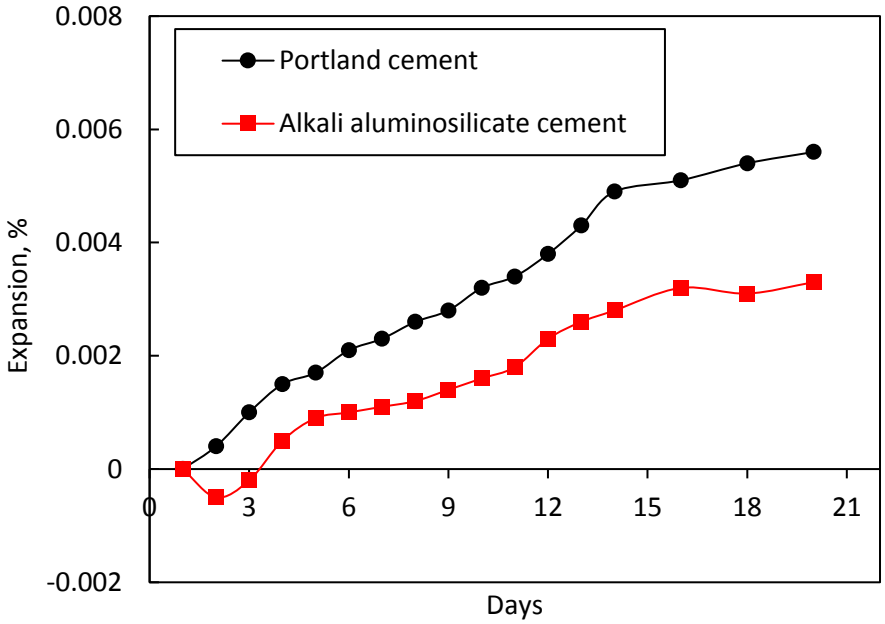

Figure 18. Expansion test results versus time for mortar bar specimens prepared with the alkali aluminosilicate cement and Portland cement.

3.3.6 Microstructure

Figure 19 presents SEM images of the hydrated pastes, at 28 days of age, for Portland cement and the alkali aluminosilicate cement. The primary binder in hydrated Portland cement is calcium silicate hydrated (C-S-H gel). The binder resulting from hydration of the alkali aluminosilicate cement is expected to be an integrated structure comprising sodium aluminosilicate hydrate (N-A-S-H) and calcium aluminosilicate hydrate (C-A-S-H) gels. The hydration products of the alkali aluminosilicate cement appear denser than those of Portland cement in the SEM images presented here.

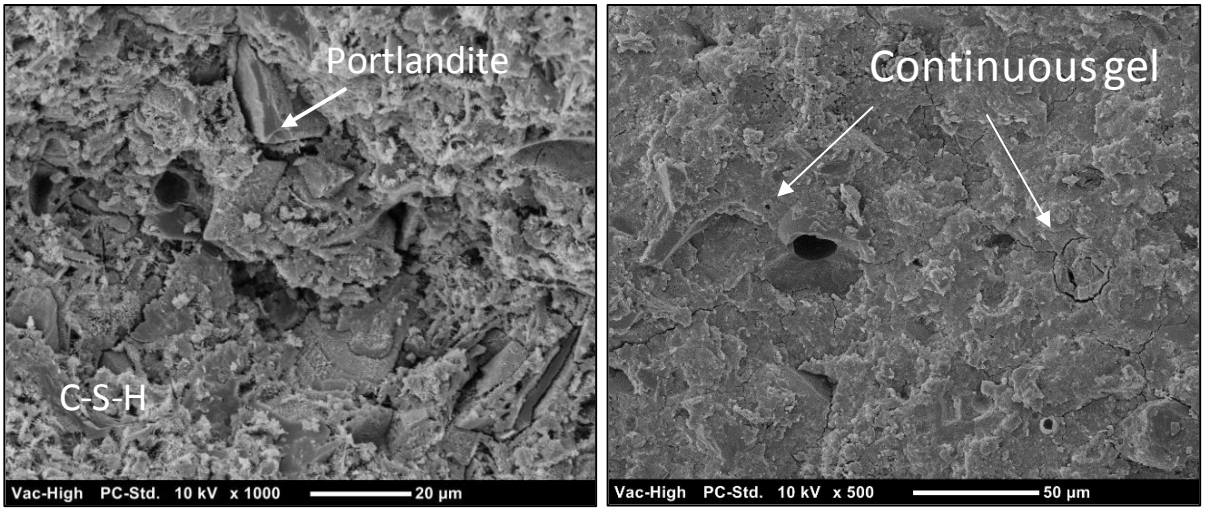

(a) Portland cement (b) Alkali aluminosilicate cement

Figure 19. SEM images of the hydration products of Portland cement and the alkali aluminosilicate cement.

3.3.7 Thermogravimetric Analysis

The TGA/DTA test results are presented in Figure 20 for hydrated pastes of Portland and alkali aluminosilicate cements at different ages. For Portland cement, three main mass loss stages could be recognized in Figure 20a. The first one at about 100^{o}C (Peak 1) can be attributed to the loss of free and physical adsorbed (capillary) water. The second mass loss stage (Peak 2), around 450^{o}C, has been attributed to the decomposition of calcium hydroxide (Portlandite) [66]. The third stage around 750^{o}C (Peak 3) can be partly attributed partly to the decomposition of carbonates that form by carbonation of cement hydrates (primarily Portlandite) in air [67]. The least mass loss is observed for the Portland cement paste at 28 days of age (compared to 7 and 3 days of age). More replicated tests may be needed to distinguish between the TGA/DTA trends at 3 and 7 days of age for Portland cement paste. In the case of the hydrated paste of the alkali aluminosilicate cement (Figure 20b), the trends in mass loss with temperature are distinct from those of Portland cement paste. Most of the weight loss occurs within the 100 to 200^{o}C

temperature range (Peak 1), which can be attributed to the loss of free and physical adsorbed water. Two minor peaks are also observed around 450 (Peak 2) and 700°C (Peak 3), which correspond to the second and third stages of mass loss in hydrated Portland cement paste. Besides this minor peak, a rather continuous mass loss at relatively low rate was observed in the alkali aluminosilicate cement paste 200 and 950°C, which can be attributed to dehydration of the products of hydration [68, 69] and hydrotalcite-like phases [69, 70]. The mass loss beyond 200°C (up to 950°C) for alkali aluminosilicate cement paste was smaller than that of Portland cement paste; the reverse was true up to 200°C. At the later age of 28 days, the overall mass loss of the alkali aluminosilicate cement paste up to 950°C (~18%) was comparable to that of Portland cement paste at a similar age. At younger ages, however, the total mass loss of the alkali aluminosilicate cement paste was smaller than that of Portland cement paste. Alkali aluminosilicate hydrates are known for their high-temperature stability [71]. The observed mass loss of the alkali aluminosilicate cement paste from 200 to 950°C was about half the corresponding mass loss of Portland cement paste, which could point at the greater high-temperature stability of the alkali aluminosilicate cement paste.

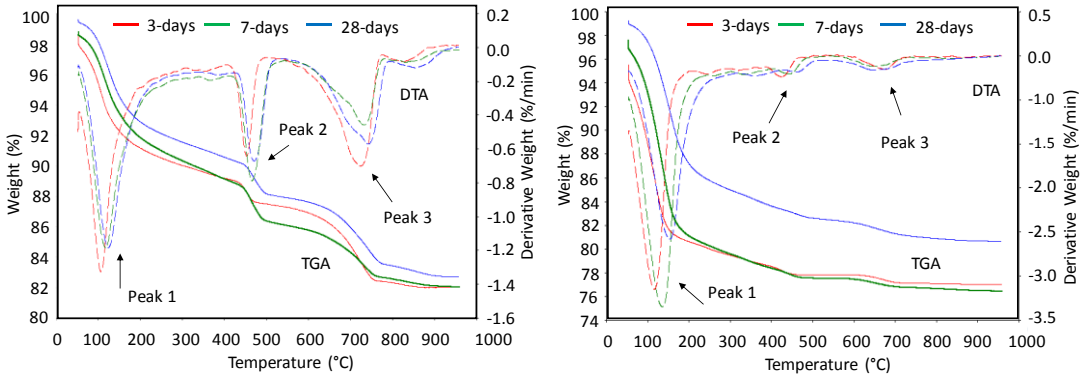

(a) Portland cement paste (b) alkali aluminosilicate cement paste

Figure 20. TGA/DTA test results for hydrated pastes of Portland and alkali aluminosilicate cements of different ages.

3.4 Conclusions

A new class of hydraulic cement was developed as a more sustainable and higher-performance alternative to the now prevalent Portland cement. The new cement relies primarily upon alkali aluminosilicate hydrates. This cement was developed and tested against the performance requirements of general use (GU) cement in ASTM C1157. A conventional Type I Portland cement was used as control. The following primary conclusions were derived based on the data generated in this experimental work.

- The strength development potential of the alkali aluminosilicate cement was greater than that of Portland cement. The alkali aluminosilicate cement also exhibited a higher rate of strength gain within the first few days of hydration at room temperature.
- The heat of hydration test results indicate that the alkali aluminosilicate cement undergoes rapid hydration reactions, with the bulk of exothermic heat release occurring within the first 24 hours. The rate of exothermic heat release was slower for Portland cement, but took place over extended time periods. The total heat released by hydration of Portland cement was larger than that of the alkali aluminosilicate cement which met the ASTM C1157 requirements for low heat of hydration cement.
- The initial and final set times of the alkali aluminosilicate cement were smaller than those for Portland cement, but still met the ASTM C1157 requirements for general use (GU) cement.
- In spite of the higher alkalinity of the alkali aluminosilicate cement, its expansion caused by alkali-silica reaction was significantly smaller than that of Portland cement. This could be attributed to the lower calcium content of the alkali aluminosilicate cement, and the

probability that alkali-silica reactions with potentially beneficial effects occur largely in the course of hydration and not after hardening of the cement paste when alkali-silica reactions produce deleterious expansive effects.

- Some aspects of the long-term chemical stability of cement hydrates are measured using the mortar bar and autoclave expansion experiments. The alkali aluminosilicate cement performed favorably in these two tests, exhibiting significantly reduced expansions when compared with Portland cement.
- The hydration products of the alkali aluminosilicate cement appeared denser than those of Portland cement in scanning electron microscopic analysis of hydrated cement pastes. The extent of hydration which rendered desired binding effects appeared to be less in the alkali aluminosilicate hydraulic cement than Portland cement.
- Thermogravimetric analyses indicated that the mass loss trends of the alkali aluminosilicate cement with temperature rise were different from those of Portland cement. The alkali aluminosilicate cement paste experienced more mass loss up to 200^{o}C; the reverse was true above 200^{o}C up to 950^{o}C which was the highest temperature considered in this investigation. The significantly lower mass loss of the alkali aluminosilicate cement paste (when compared with Portland cement paste) above 200^{o}C could point at its desired high-temperature stability.
- The process developed for production of a hydraulic cement avoids elevated temperature and involves milling of a blend of raw materials at room temperature. Scaled-up implementation of the process is projected to require reduced capital investment when compared with Portland cement production plants. The fact that elevated temperatures

are not required in production of this hydraulic cement benefits its energy-efficiency, and limits carbon dioxide emissions associated with energy use and also high-temperature decomposition of carbonates. Finally, the robust chemistry of this cement enables increased use of abundant industrial byproducts as raw materials, which also benefits its sustainability.

Chapter 4

Freeze Thaw and Deicer Salt Scaling Resistance of Concrete Prepared with Alkali Aluminosilicate Cement

4.1 Introduction

In cold climates, concrete faces two primary durability challenges that involve physical deterioration mechanisms: (i) general deterioration of concrete exposed to freeze-thaw cycles in the presence of moisture; and (ii) scaling of the concrete surface exposed to deicer salt. The freeze-thaw damage is usually manifested as cracking and spalling of concrete, which are caused by progressive expansion of the cement paste under repeated cycles of freezing and thawing [72]. The combination of freeze-thaw cycles and deicer salt application has particularly damaging effects on concrete [73, 74]. The cumulative damage to concrete under these two effects compromises the moisture barrier qualities of concrete, and magnifies the susceptibility of concrete to freeze-thaw attack and other mechanisms of deterioration (e.g., corrosion of reinforcing steel) [75, 76].

Alkali activated aluminosilicate binders have been found to experience minor deterioration when exposed to freeze-thaw cycles [77]; their resistance to chloride ion diffusion is also found to be high [78]. There is, however, very limited literature on the deicer salt scaling resistance of these binders. Alkali aluminosilicate hydrates are highly complex, and encompass diverse structural qualities which are poorly understood. The availability of limited data on the long-term durability of alkali-activated binders, including their deicer salt scaling resistance, is an important factor hindering their commercial success in spite of their favorable performance, cost and sustainability attributes [79-81]. The work reported herein was inspired by our background field

investigations which pointed at the susceptibility of the conventional (two-part) alkali-activated binders to deicer salt scaling. Figure 21 shows the extensive deicer salt scaling experienced by a sidewalk after six months (covering one full winter) of exposure to freeze-thaw cycles and deicer salt in mid-Michigan (USA). The damage to this sidewalk seemed to be limited to its surface.Figure 21. (a) Picture of the sidewalk cast in summer; and (b) the extensive deice salt scaling experienced after six months.

(a) (b)

Figure 21. (a) Picture of the sidewalk cast in summer; and (b) the extensive deice salt scaling experienced after six months.

4.2 Materials and Methods

4.2.1 Materials

The alkali aluminosilicate cement used in this investigation was developed via mechanochemical processing described in the previous work of the same authors [82]. The aluminosilicate precursors used in the mechanochemical process were coal fly ash, ground granulated blast furnace slag, and albite. The (dry) alkalis used as raw materials were sodium hydroxide, sodium silicate, and calcium oxide. Sodium tetra-borate (Borax) was also added to the cement formulation to increase its set time. Portland cement (Lafarge Type I/ASTM C150) was used as control for comparative assessment of the new hydraulic cement. The chemical compositions

and the Blaine fineness of Portland cement and alkali aluminosilicate cement are presented in Table 10. When compared with Portland cement, the alkali aluminosilicate cement has lower calcium and higher silicon, aluminum and alkali metal (Na & K) contents.

Table 10. Chemical compositions (wt.%) and Blaine fineness (BF) of the Portland cement and the alkali aluminosilicate (AAS) cement

	SiO_2	CaO	Al_2O_3	Fe_2O_3	MgO	K_2O	Na_2O	SO_3	BF, cm^2/g
AAS cement	35.2	28.1	13.6	4.03	3.73	1.14	8.89	0.53	3960
Portland cement	20.1	64.2	5.31	2.86	2.65	0.10	0.02	2.14	3870

The particle size distributions of the Portland cement and the alkali aluminosilicate cement, measured using laser granulometry, are presented in

Figure 22. The median particle sizes were 9.8 and 7.4 µm for Portland cement and the alkali aluminosilicate hydraulic cement, respectively.

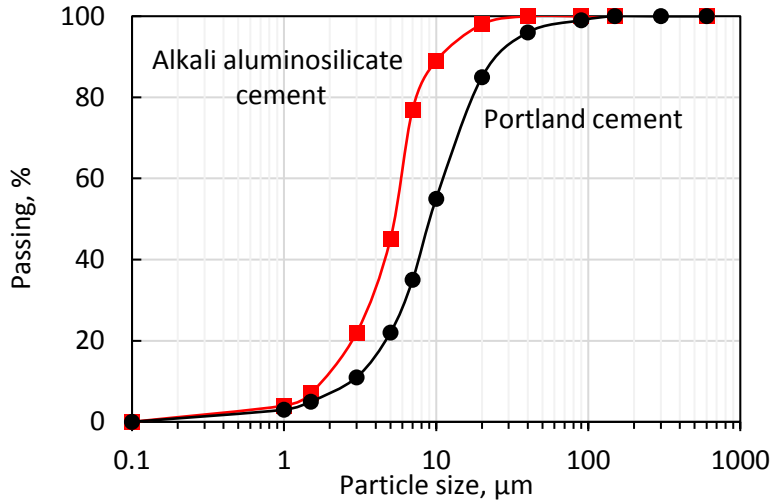

Figure 22. Particle size distributions of Portland cement and for the alkali aluminosilicate hydraulic cement.

Natural sand with maximum particle size of 4.75 mm was used as fine aggregate. Limestone with a maximum particle size of 12.5 mm was used as coarse aggregate. The particle size distributions

of the coarse and fine aggregates are presented in Figure 23. The fineness modulus of the blend of coarse and fine aggregates used for proportioning of concrete was 4.3.

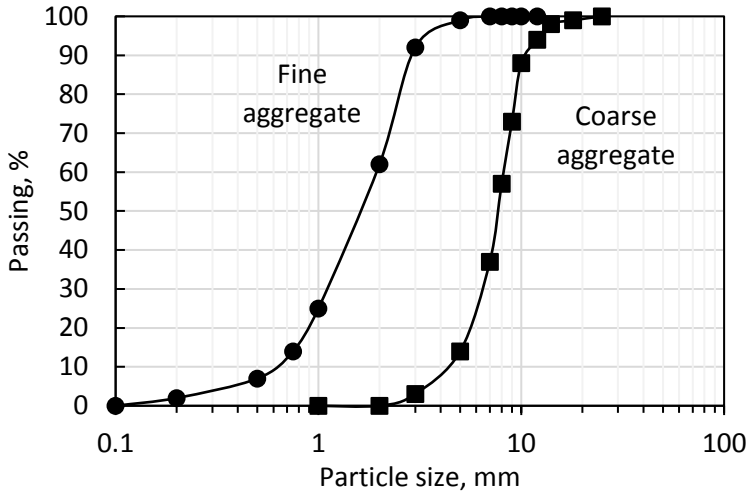

Figure 23. Particle size distributions of fine and coarse aggregates.

In order to improve the resistance of concrete to deicer salt scaling, several additives were used in concrete. The additives and their dosages are summarized below.

Commercial air-entrancing agent (MasterAir AE 90) was used at a dosage of 1.5 ml per kg of cement. This dosage was used to produce a fresh concrete mixture with air content of 5-7 percent measured using the pressure method per ASTM C231. It should be noted that, at the same dosage of air entraining agent, the air contents of Portland cement concrete and the alkali aluminosilicate cement concrete were 7.2 and 5.2%, respectively. The difference could be due to the absorption of the air-entraining agent by the organic carbon that was present in fly ash and survived the mechanochemical process of transforming fly ash and other raw materials into hydraulic cement [83]. The differences in the chemistry of Portland versus the alkali aluminosilicate cement could have also influenced the performance of the admixture that has been developed for use with Portland cement. Polyethylene glycol (PEG) powder (purchased

from sigma Aldrich) with molecular weight of 600 was used at 2.5 % by weight of cement. Polyethylene glycol can improve the deicer salt scaling resistance of concrete primarily by lowering affinity of concrete pores to water, and altering the pore structure of cement hydrates. It has been reported that the presence of Polyethylene glycol increases the fraction of pores within the 0.1–1.0 μm size range for which the capillary force is much lower than in smaller capillaries [84]. A combination of sodium benzoate and triisopropanolamine was added to concrete as recommended in the literature at 2 and 0.4%, respectively, by weight of cement [85]. Tartaric acid (polyvalent organic oxyacid) powder (purchased from sigma Aldrich) was used at 0.5% by weight of cement. Tartaric acid is a common generic foaming agent used for plaster and cement compositions [86]. This dosage was used after trial and adjustment to achieve a viable balance of compressive strength and set time. Calcined clay with chemical compositions comprising mainly (SiO_2 of 52 wt.%) and Al_2O_3 (46 wt.%) was used at 5 wt.% by weight of cement to reduce the Si-to-Al ratio of the hydrates of the alkali aluminosilicate cement. Kaolin (purchased from sigma Aldrich) was calcined at 750°C in a laboratory furnace (Neytech Benchtop Muffle Furnaces) for 12 hours with a heating rate of 15°C/minute.

4.2.2 Methods

A 19 L planetary mixer (Hobart A-200, Lombard) was used to prepare the concrete mixture presented in Table 11. With the mixer operating, the hydraulic cement was added first flowed by water, and mixing was continued for 2 minutes. Any additives were then added, and mixing was continued for an extra 2 minutes. Fine and coarse aggregates were then added, and 3 more minutes of mixing produced a homogeneous fresh concrete mixture. The fresh mix was placed inside molds, and consolidated via vibration at medium intensity for 2 minutes. The molded

specimens were sealed and stored at room temperature for 24 hours; they were then demold and kept in sealed condition at room temperature and 95±2% relative humidity for the required period of curing (typically 7 days, as described for each test procedure).

Table 11. Mix design for the concrete used in this investigation.

Material	Quantity, kg/m^3
Cement	400
Fine aggregate	910
Coarse aggregate	1100
Water-to-cement ratio*	0.45-0.55

*water-to-cement ratio was adjusted so that fresh concrete produced a slump of 60±10 mm.

The ASTM C1585 sorptivity test was used as a simple and rapid method of determining the tendency of concrete to absorb water by capillary suction. Duplicate cylindrical specimens (cured in sealed condition for 7 days) with 100 mm diameter and 50 mm height were used for this purpose. The concrete specimens were dried in an oven at 105 ± 2°C to reach a constant mass prior to starting the test. Density, void content, and water absorption capacity of concrete specimens were also measured following the ASTM C642 test procedures. The void space in concrete largely results from the use of water beyond that needed for the hydration process; evaporation of this excess water leaves the capillary pore space. There are also entrapped air voids in concrete due to its imperfect consolidation.

Freeze-thaw tests were conducted per ASTM C 666 (Procedure A: rapid freeze-thaw under wet conditions, (as shown in Figure 24a). Freeze-thaw tests were performed on cylindrical specimens of 75 mm diameter and 150 mm height, that had been cured for 7 days in sealed condition at room temperature. One freeze–thaw cycle involves lowering the temperature of specimen from 6 to -16 ˚C, followed by raising temperature from -16 to 6 ˚C. One cycle lasts 3.2 hours, which

comprises 1.8 hours of freezing 1.4 hour of thawing as shown in Figure 24b; approximately 7 cycles of freezing and thawing were per day.

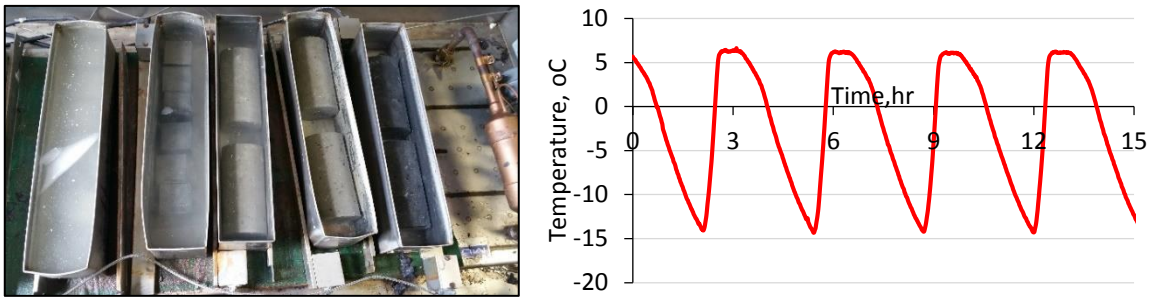

(a) (b)

Figure 24. Freeze and thaw test set up (a), and cycles of freezing and thawing (b).

Weight loss and ultrasound pulse velocity were measured after exposure of concrete specimens to repeated freeze-thaw cycles. E-METER resonance frequency tester was also performed for measurement of the resonant frequency and the dynamic modulus of elasticity (Figure 25Figure 25). The percent change in dynamic elastic modulus (P_c) was determined after application of freeze-thaw cycles:

$$P_c = \frac{n_c^2}{n^2} \times 100$$

Where, c is the number of cycles of freezing and thawing, n_c is the resonant frequency after c cycles, and n is the initial resonant frequency (at zero cycles).

Figure 25. The dynamic modulus of elasticity test set up.

ASTM C672 was followed to evaluate the scaling resistance of concrete surfaces exposed to freezing-and-thawing cycles in the presence of deicing chemicals. In this test, the water-to-cement ratio of concrete was selected to produce a concrete with slump of 75 mm (ASTM C672). Plain concrete was cast in rectangular metal molds of 150 mm by 200 mm planar dimensions with 50 mm depth (Figure 26Figure 26a). Fresh concrete was poured into molds in two layers, rodded for consolidation, leveled with three passes of a wood strike-off board, and brushed with a medium-stiff brush as a final finishing operation per ASTM C672. After final finishing, concrete specimens were stored in moist condition for 14 days at 23 ± 2°C temperature and 95±3 % relative humidity, and then stored for 14 days at 23±2°C temperature and 50±5% relative humidity. For the purpose of assessing deicer salt scaling resistance, 4% calcium chloride solution was pond on the top surface of the test specimens (Figure 26Figure 26b). To maintain a pond on the top surface, a flexible plastic material was adhered to the specimen along the perimeter using a silicone based glue.

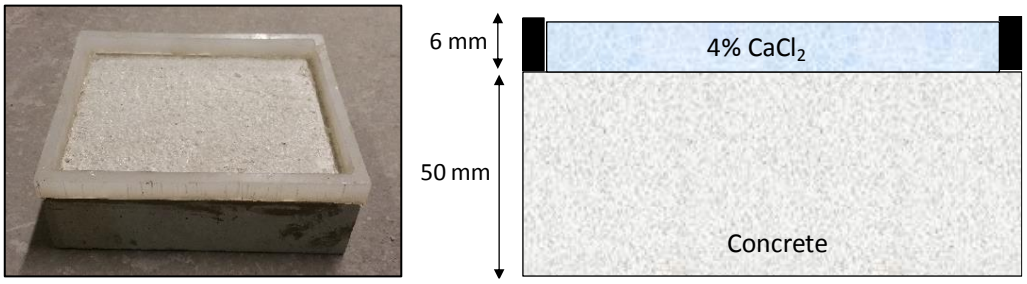

(a) Test specimen (b) Schematics of the ASTM C672 test

Figure 26. Deicer salt scaling resistance test setup.

At the age of 28 days, the specimens were placed in a freezing environment for 16 hours at -18 ±2°C temperature. At the end of this time, specimens were removed from the freezer and placed in laboratory air at 23±2°C temperature and 50±5% relative humidity for 6 hours. Water was added between cycles as required in order to maintain the proper depth of solution on the top

surface of specimens. After making a visual examination, the solution was replaced, and the test was continued. Visual rating of the surface was made after each cycle in accordance with the rating scale presented in Table 12.

Table 12. Rating of the deicer salt scaling damage to concrete surface per ASTM C 672.

Rating	Condition of surface
0	no scaling
1	very slight scaling (3 mm depth max, no coarse aggregate visible)
2	slight to moderate scaling
3	moderate scaling (some coarse aggregates visible)
4	moderate to severe scaling
5	severe scaling (coarse aggregates visible over entire surface)

In addition to the visual rating of the concrete surfaces, the surface scaling residues were collected and weighed at the end of each cycle as a measure of deterioration (Figure 27Figure 27). The weight of scaled-off residues can be considered a good quantitative way to evaluate surface deterioration [87, 88]. It is well known that visual rating is highly subjective, and depends on the operator; it cannot, therefore, be used for a precise assessment of deterioration due to deicer salt scaling.

(a) (b)

Figure 27. Removal of scaled residues (a), and the scaled-off residues (b).

To evaluate the effects of additives on the concrete compressive strength, 50-mm concrete cubes were cast for each mix, cured in sealed condition at 23±2°C temperature and 95±2% relative humidity. Compressive strength tests were performed using a Forney test equipment with 2,227 kN force capacity at 3, 7 and 28 days of age. Three specimens were tested at each age, and the average value of compressive strength was recorded. Bulk density, voids ratio and water absorption capacity were also measured for the cube specimens per ASTM C642 at 28 days of age.

Scanning electronic microscopy (SEM) was performed using a JEOL-5000 on hydrated cement pastes after 28 days of curing in sealed condition. The SEM sample was first coated with a gold-palladium alloy using a sputter coater (DESK II), and then imaged in high-vacuum mode at an accelerating voltage of 10 kV. Optic microscope images were taken using an AM Scope microscope for concrete specimens used in the freeze-thaw and deicer salt scaling tests to better understand the corresponding damage conditions, including surface deterioration and debonding at aggregate-paste interfaces.

4.3 Results and Discussion

4.3.1 Density, Void Content, and Water Absorption Capacity

Table 13 presents the density, void content, and water absorption capacity test results for Portland cement concrete and the alkali aluminosilicate cement concrete. The density and void content of the alkali aluminosilicate cement concrete are slightly higher than those of Portland cement concrete, and its water absorption capacity is somewhat lower. These results could indicate that the average density of the alkali aluminosilicate cement hydrates is higher than that of the Portland cement hydrates. The SEM images presented later also support this hypothesis.

The extended primary bond structure of alkali aluminosilicate hydrates and their distinct pore system characteristics resembling zeolitic structures are probably responsible for this observation. The reduced water absorption capacity of the alkali aluminosilicate cement concrete would benefit its long-term durability.

Table 13. Density, voids content, and water absorption capacity test results.

	Density	Voids (%)	Absorption (%)
Portland cement concrete	2.28	12.25	6.17
Alkali aluminosilicate cement concrete	2.30	14.07	5.74

4.3.2 Sorptivity and Microstructure

Figure 28 presents the capillary sorption test results for concrete materials prepared with Portland cement and the alkali aluminosilicate cement. The sorptivity test results indicate that the concrete prepared using the alkali aluminosilicate cement produces significantly reduced capillary sorption rate sorption capacities when compared with the concrete prepared with Portland cement. The distinct pore structure and the relatively high density of hydrates in the alkali aluminosilicate cement hydrates (Figure 29) could be responsible for these highly favorable features. The alkali aluminosilicate cement hydrates Figure 29b) seem to form denser structures with lower porosity when compared with the Portland cement hydrates (Figure 29a).

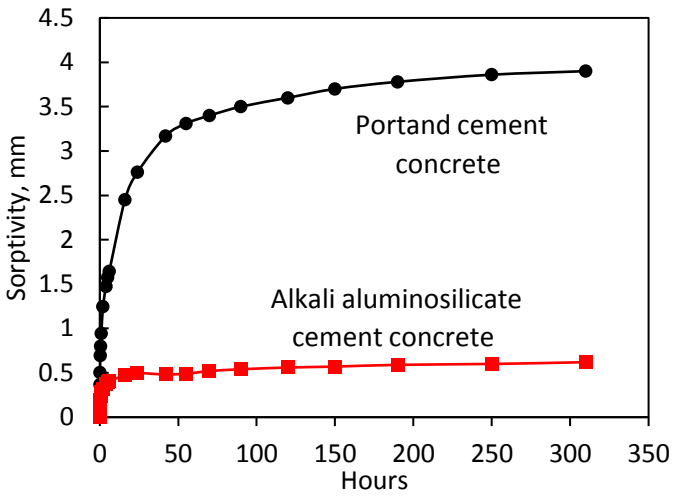

Figure 28. Capillary sorption test results for Portland cement and the alkali aluminosilicate cement concrete materials.

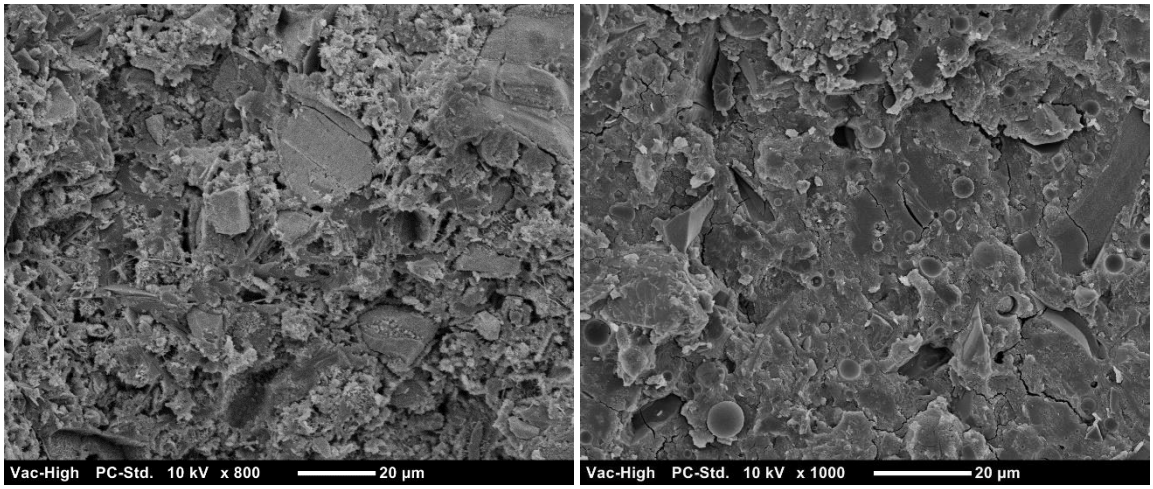

(a) Portland cement paste (b) Alkali aluminosilicate cement paste

Figure 29. SEM images the hydration products of Portland cement and the alkali aluminosilicate cement.

ASTM C1585 provides guidelines for analyzing the sorptivity test results. This analysis yields the initial rate of water sorption (defined as the slope of the best linear fit to the sorption curve versus the square root of time over the first 6 h), and the secondary rate of water sorption (defined as the slope of the best linear fit to sorption plotted against the square root of time using all the test data collected from 1 to 7 days). Table 14 presents the calculated values of the

initial and the secondary sorptivities for the Portland cement and the alkali aluminosilicate cement concrete materials. The initial and secondary sorptivities of the alkali aluminosilicate cement concrete are observed to be approximately 75 and 85%, respectively, lower than those of Portland cement concrete. These findings further highlight the desired resistance of alkali aluminosilicate cement concrete to moisture sorption, which has major durability and life-cycle economic benefits.

Table 14. Initial and secondary sorptivity values ($mm.s^{-1/2}$).

	Initial sorptivity	Secondary sorptivity
Portland cement concrete	10.1	1.32
Alkali aluminosilicate cement concrete	2.36	0.20

4.3.3 Freeze-Thaw Durability

4.3.3.1 Visual Observations

Figure 30 compares images of non-air-entrained Portland cement and alkali aluminosilicate cement concrete specimens after exposure to repeated cycles of freezing and thawing. After 15 freeze-thaw cycles, the Portland cement concrete specimens exhibited minor signs of surface damage; the alkali aluminosilicate cement concrete showed some surface damage. Portland cement concrete did not show any further signs of damage after 30 and 60 cycles, whereas there was some increase in the surface scaling of the paste in the alkali aluminosilicate cement concrete. After 100 cycles, severe damage was noticed in the Portland cement concrete specimen resulting in spalling of 3-5 mm paste thickness from the concrete surface. By the end of 150 cycles, the Portland cement concrete specimen experienced severe internal damage with separation 1-2 cm concrete pieces. alkali aluminosilicate cement concrete, on the other hand, exhibited significant stability after exposure to 150 freeze-thaw cycles, exhibiting only some

surface scaling. These observations indicate that the alkali aluminosilicate cement concrete (without air entrainment) provides inherently high resistance to repeated cycles of freezing and thawing, distinguishing it from Portland cement concrete that is inherently susceptible to severe freeze-thaw damage (without air entrainment). However, the potential for initial surface scaling of the alkali aluminosilicate cement concrete under about 30 freeze-thaw cycles needs further investigation.

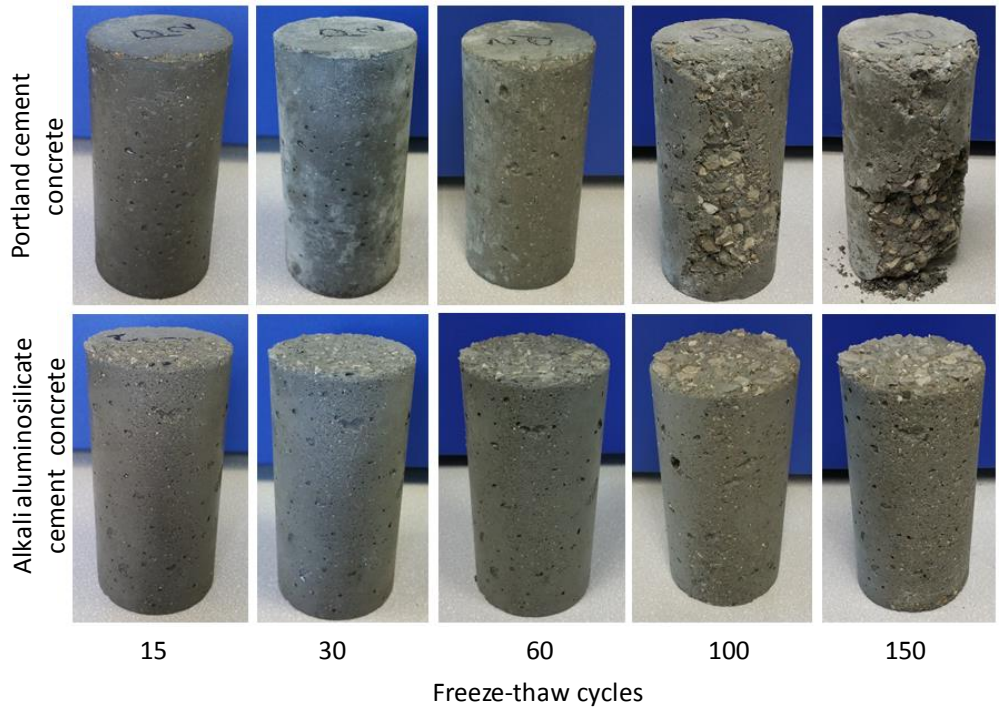

Figure 30. Concrete specimens made with the alkali aluminosilicate cement and Portland cement subjected to freeze-thaw cycles.

4.3.3.2 Drop in Mass, Resonant Frequency and Dynamic Modulus

Figure 31 presents the effects of freeze-thaw cycles on the concrete remaining mass (Figure 31a), relative resonant frequency (Figure 31b), and dynamic modulus (Figure 31c). Portland cement concrete experienced mass gain after exposure to 60 freeze-thaw cycles; the mass of alkali aluminosilicate cement concrete was stable under freeze-thaw cycles. The rise in Portland

cement concrete mass at early stages of freeze-thaw damage could be attributed to initial microcracking and cracking that raise the water absorption capacity of concrete without breakout of solid mass. Portland cement concrete experienced 4% mass loss after exposure to 100 freeze-thaw cycles, and 89% mass loss after 150 cycles. The alkali aluminosilicate cement concrete experienced a minor mass loss of about 3% after exposure to 150 cycles of freezing thawing. The trends in mass loss under freeze-thaw cycles for the two types of concrete support the findings based on visual observations of concrete specimens (see Figure 30).

Figure 31b indicates that the losses of resonant frequency under freeze-thaw cycles are smaller for the alkali aluminosilicate cement concrete when compared with Portland cement concrete. The losses in resonant frequency after 15 and 100 freeze-thaw cycles were 4.3% and 12%, respectively, for Portland cement concrete. After 150 cycles, Portland cement concrete specimens were severely damaged, and their resonant frequency could not be measures. For the alkali aluminosilicate cement concrete, the loss of resonant frequency was only 7% after exposure to 150 cycles of freezing and thawing. Similar trends were observed with the dynamic modulus of the two concrete materials under exposure to cycles of freezing and thawing (Figure 31c). Portland cement concrete experienced a continuous drop in dynamic modulus under freeze-thaw cycles, which was 22% after 100 cycles compared to only 6% for the alkali aluminosilicate cement concrete. After 150 cycles, the dynamic modulus of Portland cement concrete could not be measured since the specimens were severely damaged, whereas the alkali aluminosilicate cement concrete exhibited only 13% loss of dynamic elastic modulus after exposure to 150 cycles of freezing and thawing. These findings obtained with a hydraulic cement based on alkali aluminosilicate chemistry are compatible with the excellent freeze-thaw

durability of two-part alkali-activated fly ash binders reported in the literature [89]. The highly desired inherent freeze-thaw durability of the alkali aluminosilicate cement concrete (without air-entrainment), when compared with Portland cement concrete, may be attributed to its: (i) relatively low water/cement ratio for achieving desired fresh mix workability (0.45 for the alkali aluminosilicate cement concrete versus 0.50 for Portland cement concrete), noting that lower water/cement ratios reduce the connectivity of capillary pores due to the development of self-desiccation [90]; (ii) the symmetric, close-grained and dense (Table 14) nature of the alkali aluminosilicate cement hydrates, which tend to be cemented densely and lack massive hydration products like $Ca(OH)_2$ that forms among the Portland cement hydrates (see SEM images of Figure 29Figure 19) [91]; and (iii) discontinuous nature of the pores formed among the alkali aluminosilicate cement hydrates, which benefit the moisture barrier qualities of the hydration products of the alkali aluminosilicate cement.

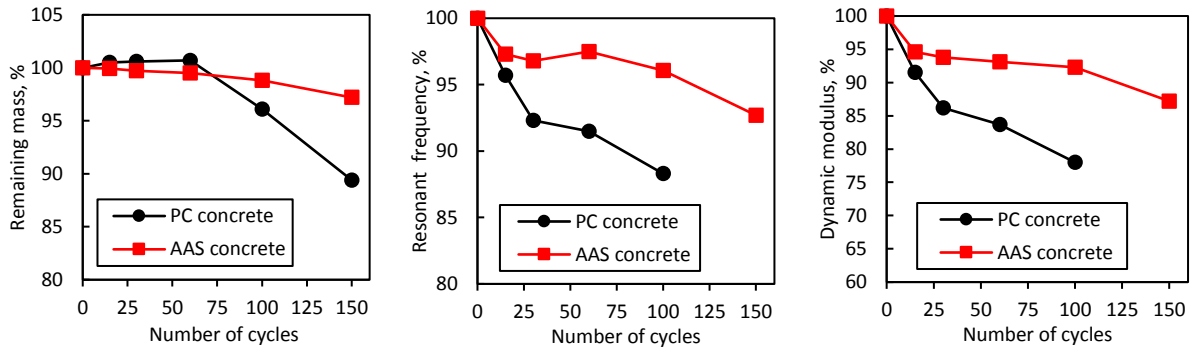

(a) (b) (c)

Figure 31. Effects of freeze-thaw cycles on the remaining mass (a), resonant frequency (b), and dynamic modulus (c) of the alkali aluminosilicate cement (AAS) versus Portland cement (PC) concrete.

4.3.3.3 Microstructure

Figure 32 shows optic microscope images taken from cut sections of concrete specimens after 150 freeze-thaw cycles. In the case of Portland cement concrete, microcracks were observed

within the paste, across aggregates, and at the paste-aggregate interfaces, producing networked microcrack systems. It has been reported that a relative modulus of less than 75% reflects the presence of networked and continuous microcrack systems [92]. These trends seem to be supported by the results generated in this work. The alkali aluminosilicate cement concrete, on the other hand, did not experience any notable microcracking or debonding of aggregates from paste after exposure to 150 cycles of freezing and thawing (Figure 32b).

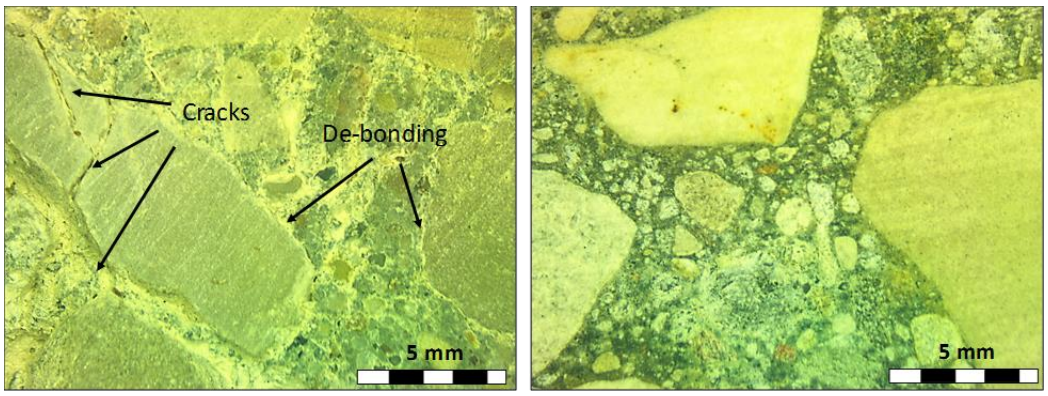

(a) Portland cement concrete (b) Alkali aluminosilicate cement concrete

Figure 32. Optic microscopy images of Portland cement and the alkali aluminosilicate cement concrete cross sections after exposure to 150 cycles of freezing and thawing.

Figure 33 shows SEM images Figure 33for representative paste pieces taken from the interior of concrete specimens exposed to 100 freeze-thaw cycles. The SEM images for Portland cement (Figure 33a) indicate that the freeze-thaw damage also occurred within the hydrated paste. This damage was in the form of networked microcracks with widths approaching 5 µm. The alkali aluminosilicate cement paste (Figure 33b) exhibited far less damage in the form of fine, discontinuous microcracks with widths less than 1 µm. Spherical coal fly ash particles could be identified among the hydration products of the alkali aluminosilicate cement. They seemed to have blocked the propagation of microcracks within the alkali aluminosilicate cement hydrates. It has been reported that the high-modulus (glassy) fly ash particles can favorably influence the

structure and damage mechanisms of cementitious binders [93]. The interactions of carbon dioxide in air with the solution formed in the course of hydration, which incorporates relatively high concentrations of sodium cation is a concern. These interactions can form sodium carbonate. Release of calcium cations to the solution during the hydration process would thus produce a tendency towards precipitation of calcium carbonate and gaylussite [94, 95]. The resulting solution would be rich in sodium, aluminum and silicon, which favors formation of zeolitic structures [95]. In the absence of carbon dioxide, calcium would be incorporated into the aluminosilicate hydrate structures, yielding calcium aluminosilicate hydrates [96].

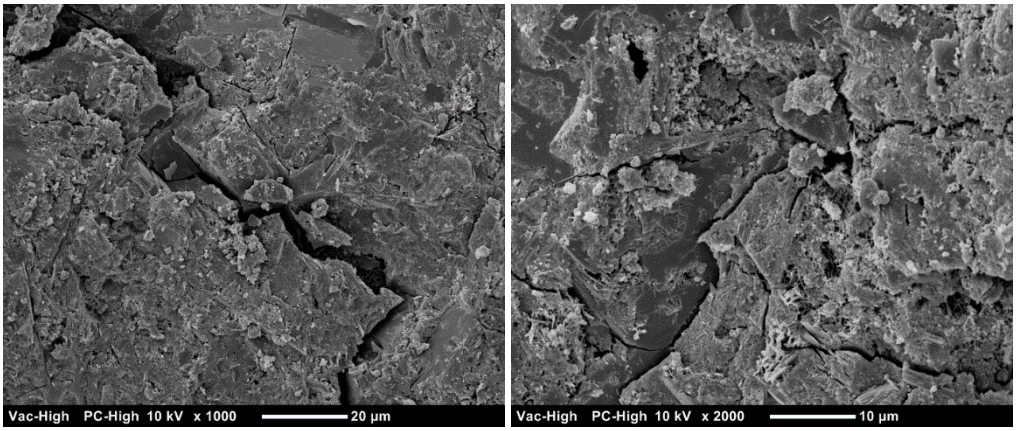

(a) Portland cement paste

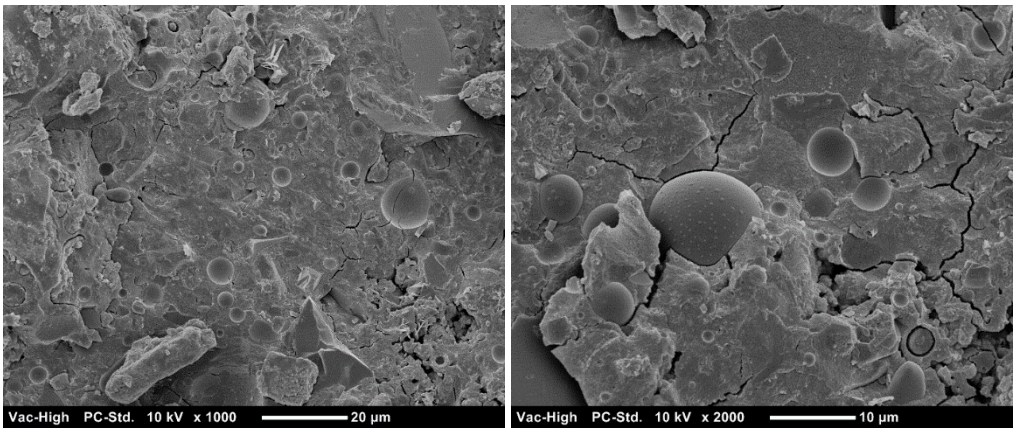

(b) Alkali aluminosilicate cement paste

Figure 33. SEM images of non-air-entrained Portland and alkali aluminosilicate cement pastes after exposure to 100 freeze-thaw cycles.

4.3.4 Deicer Salt Scaling Resistance

4.3.4.1 Effect of air entrainment

Figure 34 presents pictures of the concrete top surfaces after exposure to several cycles of freezing and thawing in presence of deicer salt. Non-air-entrained Portland cement concrete exhibited good deicer salt scaling resistance up to 2 freeze-thaw cycles. The non-air-entrained alkali aluminosilicate cement concrete experienced only minor damage (damage rating of 1) after two cycles of freezing and thawing in the presence of deicer salt. Slight scaling damage (damage rating of 1) was noticed in the Portland cement concrete after 4 freeze-thaw cycles; the non-air-entrained alkali aluminosilicate cement concrete experienced spalling of paste (damage rating of 3) after 4 freeze-thaw cycles in the presence of deicer salt. After 6 freeze-thaw cycles, the non-air-entrained Portland cement concrete experienced some spalling (damage rating of 2) whereas the non-air-entrained alkali aluminosilicate cement concrete experienced moderate damage that still corresponded to a damage rating of 3. After 8 freeze-thaw cycles, moderate scaling was noted on the Portland cement concrete surface (with a damage rating of 3); the damage to non-air-entrained alkali aluminosilicate cement concrete was more pronounced, with some visible coarse aggregates and a damage rating of 4. This surface deterioration of Portland cement concrete could be due to the formation of significant amounts of Friedel's salt and ettringite on the exposed surface [97]. The resulting crystallization pressure could contribute to weakening of the concrete surface and its spalling [98]. Furthermore, the presence of deicer salt on the upper surface of concrete produces a high osmotic pressure, with a consequent movement of water toward the colder surface where freezing takes place and aggravates scaling. Exposure of concrete to freeze-thaw cycle and deicer salt solution yields C-S-H structures of lower the Ca/Si

ratio (due to the leaching of Ca^{2+} to the deicer solution). It has been reported that Ca^{2+} can also leach from the AF_m and Af_t phases to raise the Al/Ca ratios [99, 100]. These chemical changes in cement paste lead to weight loss and visually notable deterioration of Portland cement concrete. The literature on deicer salt scaling of alkali activated aluminosilicate binders is very limited, with the available information pointing at their relatively low deicer salt scaling resistance when compared with Portland cement-based binders. This could be explained by the microstructural differences of the two binders. It has been reported that the presence of Cl^- and H^+ ions accelerates deterioration of alkali-activated aluminosilicate binders [101]. There are indications in the literature that finer pore structures can restrict ionic movements due to the electric double layer effect [102]. The tendency of moisture to move towards the upper surface with higher salt concentration could have more damaging effects on alkali-activated aluminosilicate binders.

The pore system in Portland cement binder is saturated with respect to $Ca(OH)_2$ [103]; Portlandite supplies relatively large concentrations of Ca^{2+} and OH^- ions into the Portland cement paste pore solution. Unlike Portland cement binders, the pore solution of alkali aluminosilicate binders tends to be rich in sodium and silicon, with lower concentrations of calcium cations [104]. Considering that calcium chloride is the popular deicer salt (which is also used in standard salt scaling tests), the sodium-rich pore solution of alkali aluminosilicate cement [105] generates a tendency towards cation-exchange phenomena that yield sodium chloride together with calcium cations. The consumption of Na from the pore solution reduces the alkalinity, thus destabilize the hydrates in the alkali aluminosilicates binder. This chemical destabilizing effect associated with the application of deicer salt exacerbates the deleterious physical effects associated with deicer

salt application. The concentration gradient of sodium could also produce an osmotic pressure that would not have existed in the case of calcium-rich Portland cement solution.

Air entrainment of Portland cement and alkali aluminosilicate cement concrete materials was noted to improve their deicer salt scaling resistance. In the case of air-entrained Portland cement concrete, minor scaling (damage rating of 1) was noted after 6 freeze-thaw cycles in the presence of deicer salt. Severe deicer salt scaling damage (with a damage rating of 4) was observed after 8 cycles of freezing and thawing in the presence of deicer salt. Air-entrained alkali aluminosilicate cement concrete also exhibited similar trends; minor scaling (damaging rating of 1) was noted after 4 cycles of freezing and thawing in the presence of deicer salt. Moderate damage was observed (with damage rating of 3) on the air-entrained alkali aluminosilicate concrete surface after 8 cycles of freezing thawing in the presence of deicer salt (compared to 4 cycles for non-air-entrained alkali aluminosilicate cement concrete).

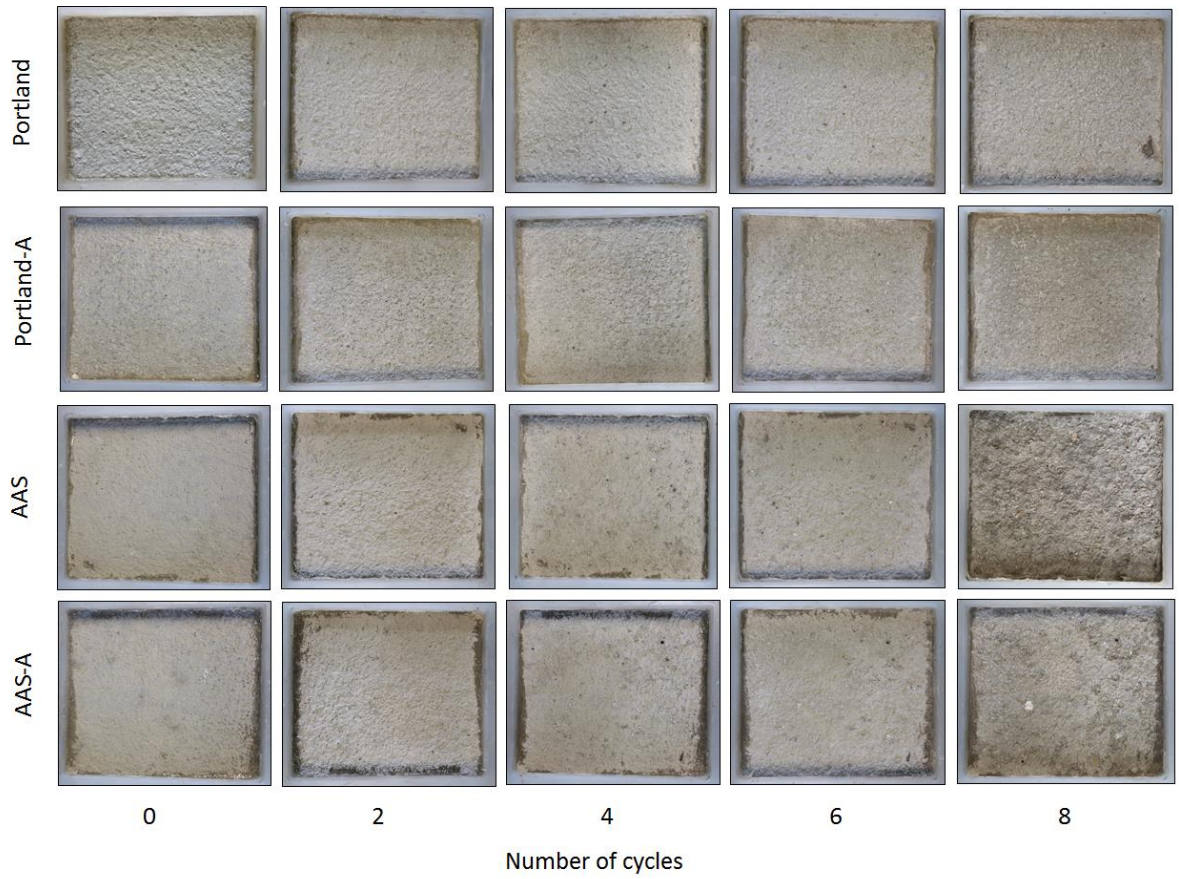

Figure 34. Surface appearances of Portland cement and alkali aluminosilicate cement (AAS) concrete specimens after exposure to different cycles of freezing and thawing in the presence of deicer salt (A: air entrained).

Figure 35 compares optic images taken of concrete surfaces after exposure to 2 freeze-thaw cycles in the presence of deicer salt. In the case of non-air-entrained Portland cement concrete, which exhibited desired resistance under visual inspection at this stage of aging, spalling of small pieces of paste (1-3 mm in dimensions) together with minor cracking could be detected under microscope. Minor signs of scaling were also noticed in the air-entrained Portland cement concrete with less damage (spalling of 0.5-1 mm pieces) when compared with non-air entrained Portland cement concrete. The scaling damage in alkali aluminosilicate cement after 2 cycles of freezing and thawing in the presence of deicer salt was more pronounced under microscope;

cracks were detected, and paste was noted to scaled-off of aggregates. Air-entrained alkali aluminosilicate cement concrete exhibited only minor signs of scaling damage when compared with its non-air-entrained counterpart. The optic microscope observations provide further support for the significant benefits of air entrainment towards improvement of the scaling resistance of alkali aluminosilicate cement concrete as well as Portland cement concrete.

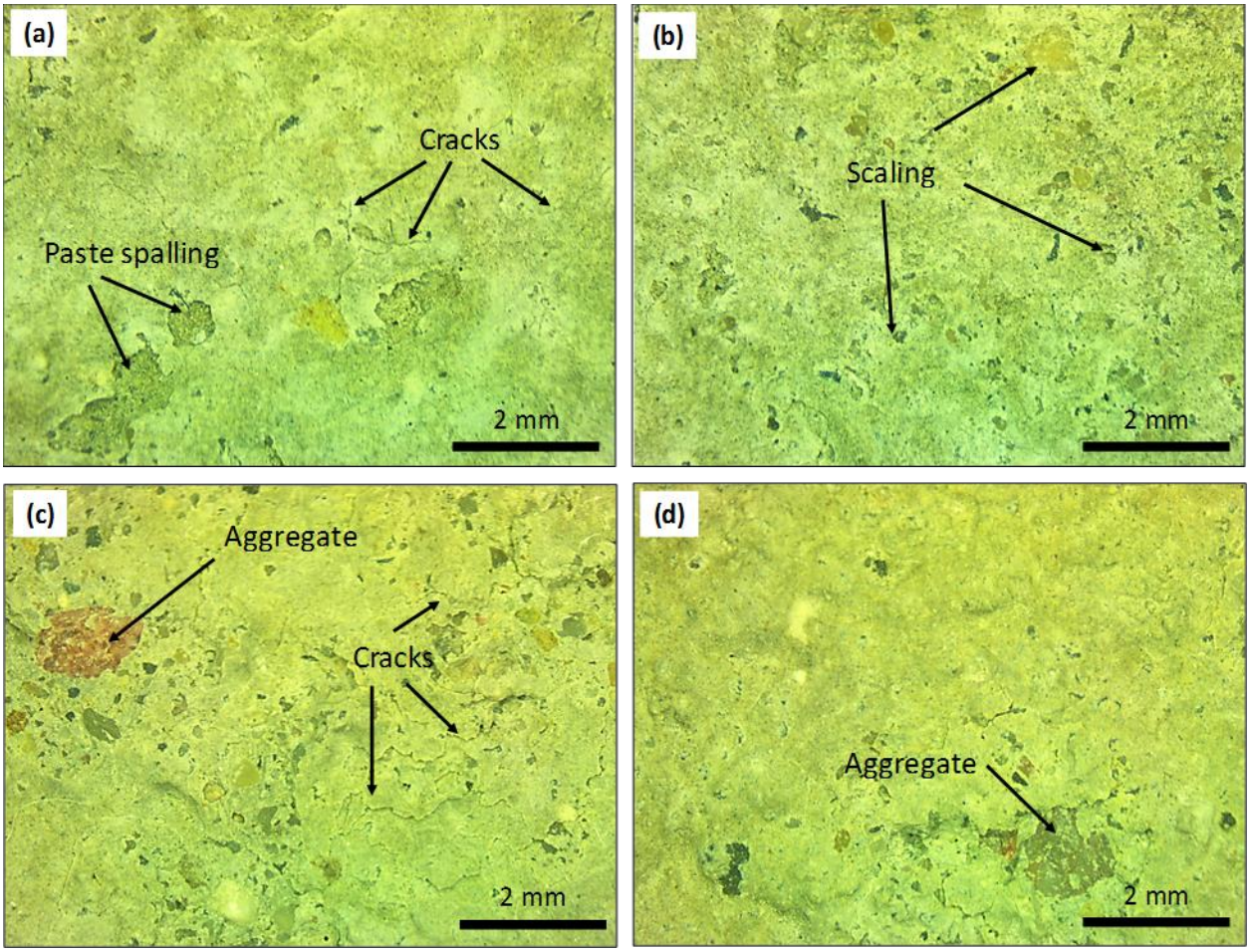

Figure 35. Optic microscope images concrete surfaces after 2 freeze-thaw cycles in the presence of deicer salt: (a) non-air-entrained Portland cement concrete; (b) air-entrained Portland cement concrete; (c)non-air-entrained alkali aluminosilicate cement concrete; and (d) air-entrained alkali aluminosilicate cement concrete.

Entrained air voids with spacing smaller than the material-specific threshold significantly improve the resistance of concrete to internal freeze-thaw damage [106]. An excellent correlation has

also been found between deicer salt scaling resistance and the volume of entrained air voids with less than 300 µm diameter [107]. These findings have led to the suggestion that internal frost action is the cause of scaling damage [108]. However, the presence of salt reduces the amount of ice formed [109]. Therefore, if internal frost action just beneath the surface were the cause of scaling, the most damaging solution applied on concrete would be pure water. Air voids may also protect the surface by providing a location where the crystals can grow into without exerting stress on the paste. Perhaps more importantly, entrained air voids reduce bleeding (Figure 36) and thereby enhance the strength of the concrete surface, which improves scaling resistance [98].

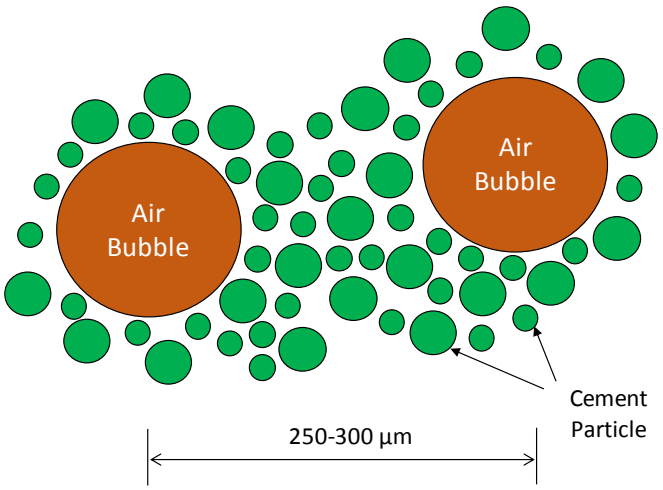

Figure 36. Schematic depiction of air bubbles making nearby cement particles more buoyant.

4.3.4.2 Effects of Additives

Figure 37 shows the effects of different additives on the deicer salt scaling resistance of the alkali aluminosilicate cement concrete. The addition of polyethylene glycol (PEG) to the alkali aluminosilicate cement concrete significantly improved its resistance to deicer salt scaling; no signs of damage were observed on the concrete surface after 2 freeze-thaw cycles. By the end of the fourth cycle, minor scaling damage was observed (with damage rating of 1), and moderate

scaling damage occurred on the surface after 6 freeze-thaw cycles (with damage rating of 3). The addition of PEG to the concrete mixture reduces the surface tension of liquid water filling the capillary pore [84, 110]. Furthermore, PEG , as a viscosity modifying admixture, comprises of polymers that could improve the paste flexibility and thus enhance its resistance to internal pressure [111]. The addition of PEG to concrete has also been noted to increase its water retention capacity due to hydrophilic conversion of the capillary pore surfaces [112, 113]; this provides for more effective curing which yields a denser hydrated gel.

The addition of tartaric acid was found to slightly enhance the deicer scaling resistance of the alkali aluminosilicate cement concrete. Minor scaling was observed (with damage rating of 1) after 2 freeze-thaw cycles, and slight to moderate scaling after 4 cycles (with damage rating of 2). After 6 freeze-thaw cycles, moderate scaling was noticed with some coarse aggregates exposed on the surface (damage rating of 3). This effect of tartaric acid can be attributed to the formation of air bubbles within aluminosilicate hydrates that can have effects similar to those of air entraining agents. Tartaric acid can have retarding effects on cement hydration by chemically interacting with cement phases to form calcium tartrate hydrate which covers cement grains and hinder the hydration process [114]. This reaction can also chemically bind Ca^{+2} within the aluminosilicate structure, thus reducing its leaching which aggravates the deicer salt (calcium chloride) deleterious effects.

The addition of a combination of sodium benzoate and triisopropanolamine was found to significantly improve the scaling resistance of the alkali aluminosilicate cement concrete. Minor scaling was noticed after 2 freeze-thaw cycles (damage rating of 1), and the extent of deicer salt scaling was moderate after of 8 cycles, (versus only 3 cycles for the non-modified alkali

aluminosilicate cement concrete. Sodium benzoate has been used as a corrosion inhibitor in Portland cement concrete, which acts by reducing the diffusion coefficient of concrete [115, 116]. Other investigations have used a combination of sodium benzoate and triisopropanolamine in alkali aluminosilicate binders as freeze-thaw stabilizers [85]. It has been proposed that triisopropanolamine improves the mechanical properties of hydrated cement paste by strengthening the interfacial transition zone between the cement paste and aggregates [117]. The improvement in the interfacial transition zone could be explained by the effect of triisopropanolamine on promoting the hydration of limestone [118]. Other investigations have indicated that the improvements in concrete properties by the addition of triisopropanolamine could be not only be due to enhancement of the interfacial transition zone, but also due to a rise in the degree of hydration of cement paste [119]. The presence of triisopropanolamine in the pore solution was reported to leach Fe^{3+} and Al^{3+} from cement, thereby accelerating the dissolution rate and thus the hydration reactions [120]. Also, triisopropanolamine reportedly improves the reaction of aluminosilicates via (i) accelerating the silicate reactions; and (ii) accelerating the dissolution of aluminosilicates under highly alkaline conditions [121].

The addition of calcined clay lowered the deicer salt scaling resistance of the alkali aluminosilicate cement concrete. The damage started on the specimen surface after 1 freeze-thaw cycle as minor paste spalling (with damage rating of 2). After 2 freeze-thaw cycles, major damage with coarse aggregates clearly exposed (damage rating of 4). Severe damage was observed after 6 freeze-thaw cycles (damage rating of 5). Previous work on incorporating metakaolin in alkali activated fly ash indicated that metakaolin enhances the progress of hydration (alkali-activation) by forming a desired aluminosilicate chemistry in the solution to advance the polycondensation step

[122]. Calcined clays (similar to metakaolin), however, require elevated temperatures to achieve higher solubility and improve the microstructure of the resultant alkali aluminosilicate hydrates [123, 124]. This could explain the adverse effect of calcined clay on the deicer salt scaling resistance of the alkali aluminosilicate cement concrete noted in this investigation.

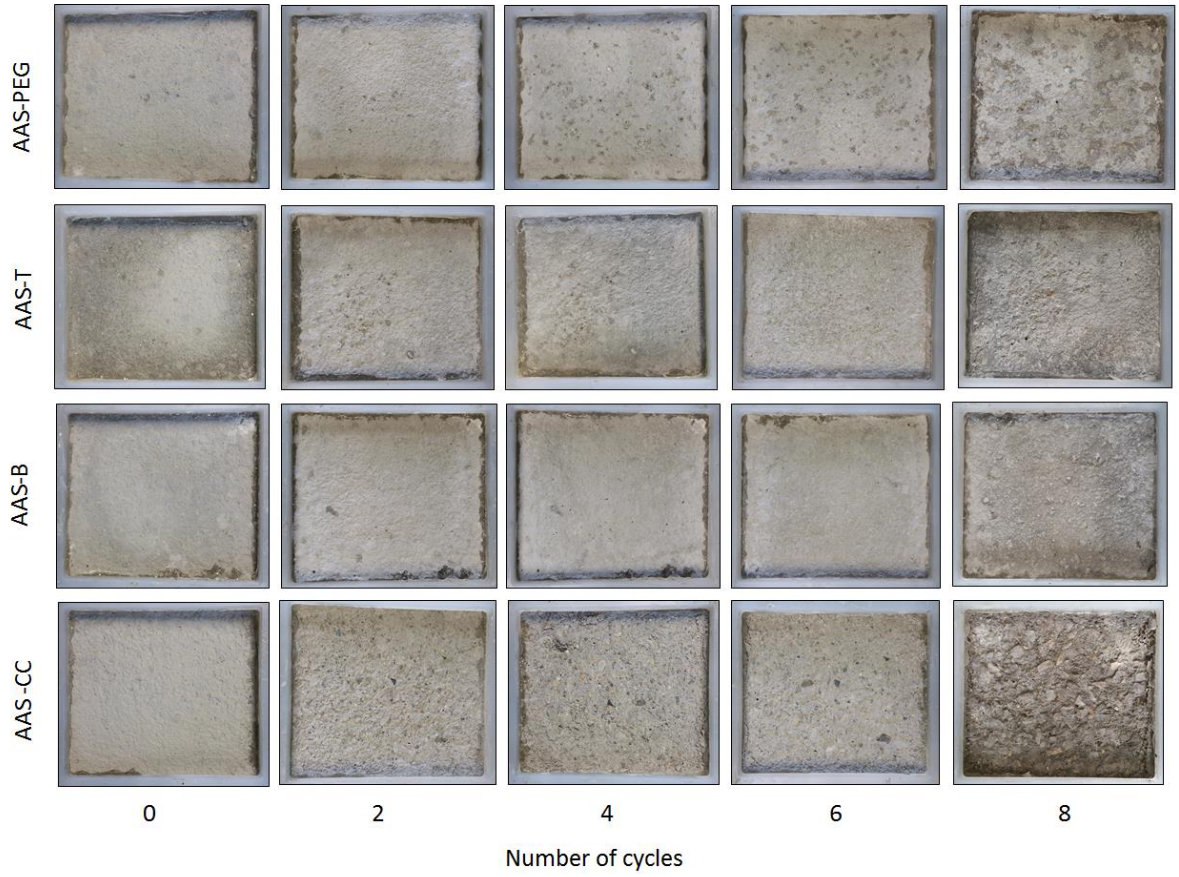

Figure 37. Visual appearances of the surfaces of alkali aluminosilicate cement (AAS) concretes with different modifications after exposure to repeated cycles of freezing and thawing in the presence of deicer salt, (PEG: polyethylene glycol, T: tartaric acid, B: sodium benzoate and triisopropanolamine, CC: calcined clay).

Figure 38 presents optic microscope images of the alkali aluminosilicate cement concrete surfaces prepared with different additives after 2 freeze-thaw cycles in the presence of deicer salt. No indications of damage were found on the alkali aluminosilicate cement concrete surface with 2.5 wt.% PEG (Figure 38a). Surfaces of the alkali aluminosilicate cement concrete with 1%

tartaric acid (Figure 38b) exhibited minor microcracking with no signs of scaling. The addition sodium benzoate and triisopropanolamine to the alkali aluminosilicate cement concrete was found to reduce the microcracking tendency of cement paste and produce more homogenous surfaces with very fine microcracks (Figure 38c). Significant damage was observed on the surfaces of alkali aluminosilicate cement concrete modified with 5% calcined clay (Figure 38d) where aggregates were visible on the surface.

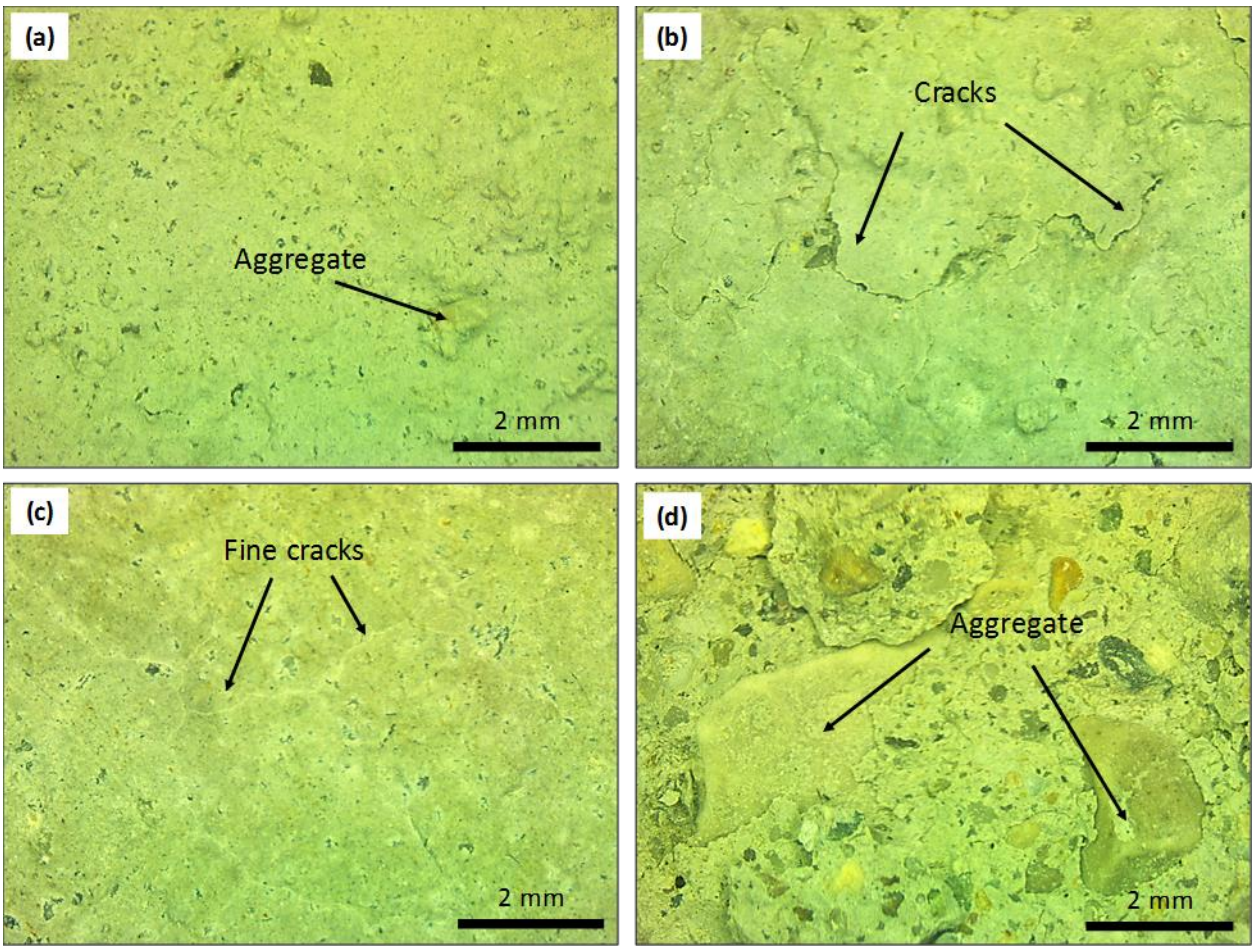

Figure 38. Optic images for alkali aluminosilicate cement concrete surface after 2 cycles with: (a) 2.5% PEG; (b) 1% tartaric acid; (c) 2% sodium benzoate and 0.4% triisopropanolamine and (d) 5% calcined clay.

Figure 39 compares the cumulative masses of the scaled-off residues from concrete surfaces after exposure to freeze-thaw cycles in the presence of deicer salt. The air-entrained and non-air entrained Portland cement concrete materials exhibited minor mass loss during the first 4 freeze-thaw cycles, with cumulative mass losses that were less than 0.005 kg/m^2. Non-air and air entrained alkali aluminosilicate cement concrete materials, on the other hand, experienced mass losses of 0.21 and 0.09 kg/m^2, respectively, after 4 freeze-thaw cycles. Negligible mass loss was recorded for the alkali aluminosilicate cement concrete with sodium benzoate and triisopropanolamine additives after 4 freeze-thaw cycles, where the cumulative scaled-off mass was less than 0.01 kg/m^2. The cumulative mass loss for the alkali aluminosilicate cement concrete with PEG and tartaric acid were less than 0.1 kg/m^2. The addition of calcined clay (as noted earlier) significantly reduced the deicer salt scaling resistance of the alkali aluminosilicate cement concrete; the scaled-off mass increased rapidly under exposure to freeze-thaw cycles, and reached 1 kg/m^3 after 4 cycles. From a mass loss point of view, the combination of sodium benzoate and triisopropanolamine was most effective, reducing the alkali aluminosilicate cement concrete mass loss due to deicer salt scaling after 8 freeze-thaw cycles by 80%. The use of PEG or tartaric acid reduced the mass loss after 8 freeze-thaw cycles by 60%. The desired deicer salt scaling resistance of Portland cement concrete points at the stability of calcium silicate hydrate under this particular aggressive exposure condition [88]. The quantitative data presented in Figure 39 are consistent with the qualitative visual observations of deicer salt scaling presented earlier based on visual observations (Figure 34 and Figure 37) per ASTM C672 and optic microscope images (Figure 35 and Figure 38).

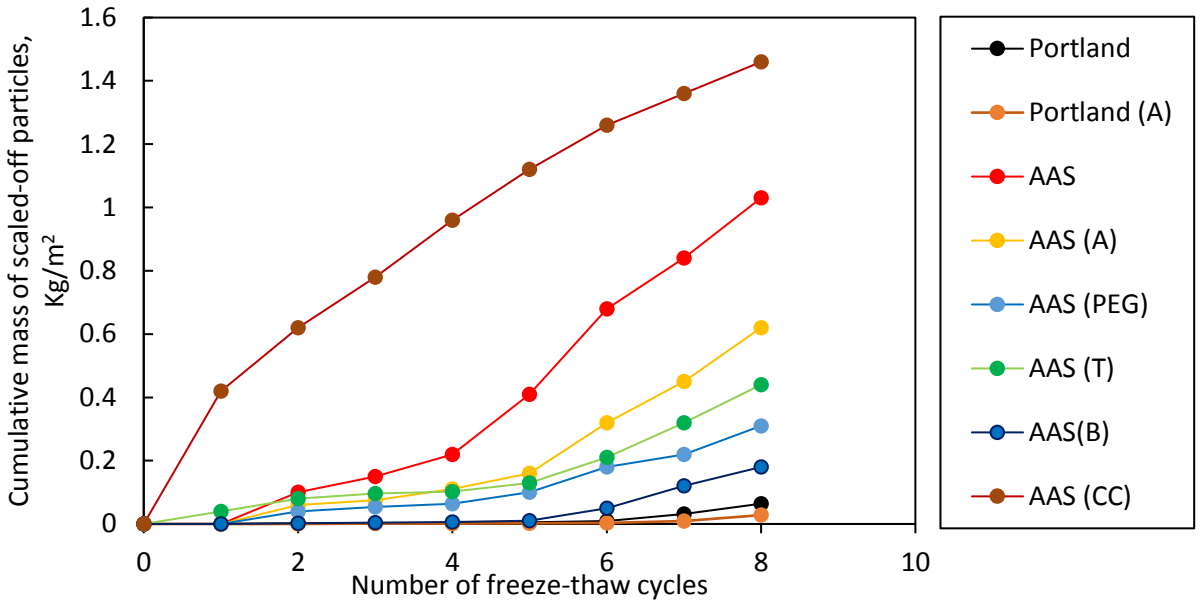

Figure 39. Cumulative mass of scaled-off residues of concrete prepared using Portland cement and alkali aluminosilicate cement (AAS) after exposure to freeze-thaw cycles in the presence of deicer salt (A: Air entrained, PEG: polyethylene glycol, B: sodium benzoate and triisopropanolamine, T: tartaric acid, CC: calcined clay).

The trends in compressive strength development for non-air entrained and air-entrained Portland cement concrete and also for the alkali aluminosilicate cement concrete without and with different additives (used primarily for enhancement of deicer salt scaling resistance) are shown in Figure 40. Air entrainment of Portland cement concrete reduced its compressive strength at all ages; this loss of compressive strength was about 8% at 28 days of age. Air entrainment of the alkali aluminosilicate cement concrete lowered its compressive strength by about 10% at 3 and 7 days of age, but increased its compressive strength by 5% at 28 days. The addition of PEG slightly reduced the compressive strength of the alkali aluminosilicate cement concrete. This could be due to some hindering of the alkali aluminosilicate cement hydration in the presence of PEG [125]. The use of tartaric acid initially reduced the values of compressive strength at 3 and 7 days of age. At 28 days, however, it increased compressive strength

significantly to more than 50 MPa, which represents a 30% rise in the 28-day compressive strength of the alkali aluminosilicate cement concrete. The use of tartaric acid in the alkali aluminosilicate cement formulation leads to the formation of calcium tartrate hydrate at early stages of hydration, which coats the cement particles and hinders their hydration reactions (rendering retardation effects) [114]. The significant improvement in the compressive strength at later ages can be explained by the role of tartaric acid in facilitating the extraction of ions (such as Si and Al) from the amorphous cement powder [126]. The resulting rise in the concentration of cations in solution further advances the hydration reactions and could yield hydrates with more favorable structures. The addition of sodium benzoate and triisopropanolamine to the alkali aluminosilicate cement formulation was found to raise the compressive strength of the alkali aluminosilicate cement concrete at all ages. This could be attributed to: (i) reduction of water/cement ratio by 15% for achieving similar slump when sodium benzoate and triisopropanolamine was used in the alkali aluminosilicate cement formulation, which is because clustering of particles is reduced (by lowering the attractive forces within them) and the water locked within clusters if released to render lubricating effects [127]; and (ii) strengthening of the interfacial transition zone between cement hydrates and aggregates [117] by promoting hydration of limestone [118] and enhancing the degree of hydration of cement paste [119]. The addition of calcined clay lowered the alkali aluminosilicate cement concrete strength. Calcined clay did not notably compromise the 3-day compressive strength of the alkali aluminosilicate cement concrete, but lowered its compressive strength by about 35% at 28 days of age. As noted earlier, it is feasible that room-temperature curing did not allow calcined clay to favorably alter the ionic concentrations of the solution.

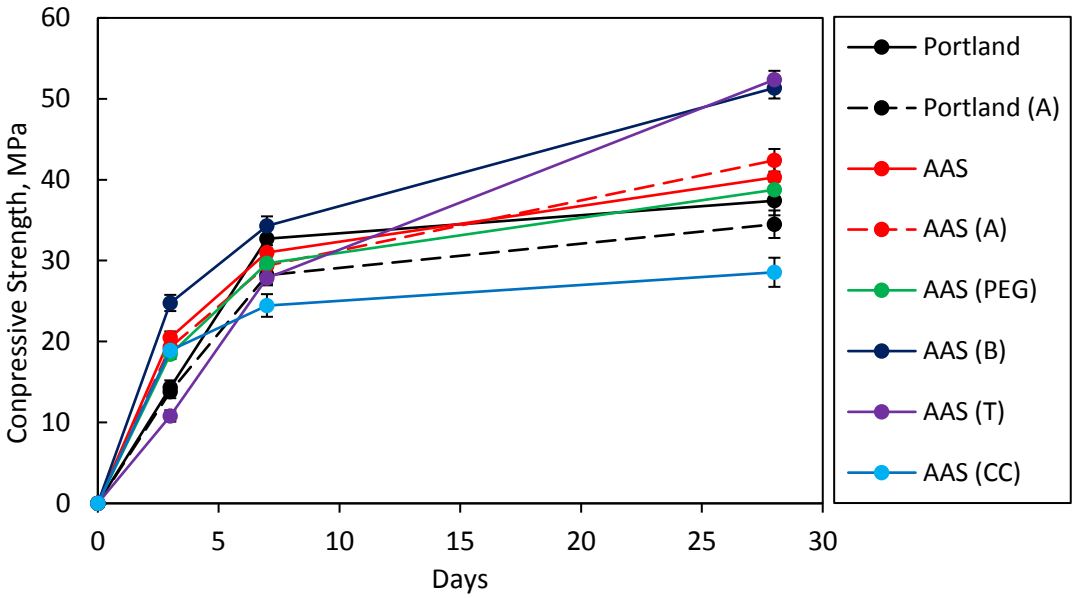

Figure 40. Compressive strength test results for concrete materials prepared using Portland cement and alkali aluminosilicate cement (AAS) with different modification, (A: Air entrained, PEG: polyethylene glycol, B: sodium benzoate and triisopropanolamine, T: tartaric acid, CC: calcined clay).

The density, voids content and water absorption test results for the alkali aluminosilicate cement concrete with different modified cement formulations are presented in Figure 41. The addition of PEG raised the alkali aluminosilicate cement concrete density, and lowered its voids content and water absorption capacity. These effects could have resulted from the greater retention of the original mixing water in the alkali aluminosilicate cement concrete incorporating PEG [84, 110], which enhances the extent of hydration of cement and binding of water. The increase in the density and lowering the voids content and water absorption did not increase the compressive strength of the alkali aluminosilicate binder; this could be due to hindering effect of PEG. Tartaric acid slightly increased the density of the alkali aluminosilicate cement concrete, and also decreased its voids content and water absorption capacity. These effects of tartaric acid can be attributed to its ability to raise the cationic concentration of the solution which can increase

the extent of hydration and the resulting structure of cement hydrates [126], which lead to the improvement of the compressive strength values at later ages (as shown in Figure 40). The effect of sodium benzoate used in combination of triisopropanolamine on the alkali aluminosilicate cement concrete density was small; the corresponding effects towards lowering the voids content and the water absorption capacity of the alkali aluminosilicate cement concrete, on the other hand, were significant. Similar to the corresponding effects on the deicer salt scaling resistance and the compressive strength of alkali aluminosilicate cement concrete, these favorable effects can also be attributed to the plasticizing effect [127] and the improvement of the interfacial transition zone [117], activation of limestone [118] and enhancement of the degree of hydration [119] of the alkali aluminosilicate cement concrete in the presence of sodium benzoate and triisopropanolamine. The density, voids content and water absorption capacity test results corroborate the deicer salt scaling and the strength test results presented earlier for alkali aluminosilicate cement concrete materials prepared with different modified cement formulations.

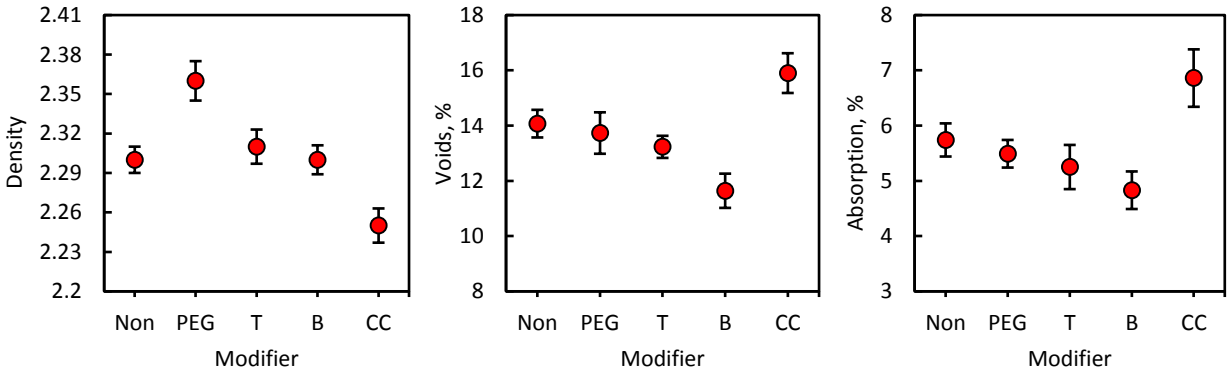

Figure 41. Density, void content, and absorption capacity test results for alkali aluminosilicate cement concrete materials prepared with different modified cement formulations, (PEG: polyethylene glycol, T: tartaric acid, B: sodium benzoate and triisopropanolamine, CC: calcined clay).

Figure 42 presents the SEM images of the alkali aluminosilicate cement paste prepared with different modified cement formulations. A denser microstructure with reduced microcracks and was observed in the presence of PEG (Figure 42a); some air voids the interior surfaces of which were coated PEG could also be found among the cement hydrates. Integration of the PEG polymer into the inorganic binder structure could benefit its strain capacity. A dense microstructure with minimal microcracking and limited presence of unreacted fly ash particles was observed with tartaric acid incorporated into the cement formulation (Figure 42b). These observations confirm the positive effects of tartaric acid on the extent of hydration of the alkali aluminosilicate cement over time. With a combination of sodium benzoate and triisopropanolamine introduced into the cement formulation, the resulting hydrates exhibited a dense microstructure; some finer fly ash particles were also observed among the cement hydrates (Figure 42c). Finally, the introduction of calcined clay into the alkali aluminosilicate cement formulation produced significant microcracking with a networked microcrack structure (Figure 42d). The SEM images are consistent with the effects of various modifiers on the physical and mechanical characteristics produced by the hydration products of the alkali aluminosilicate cement.

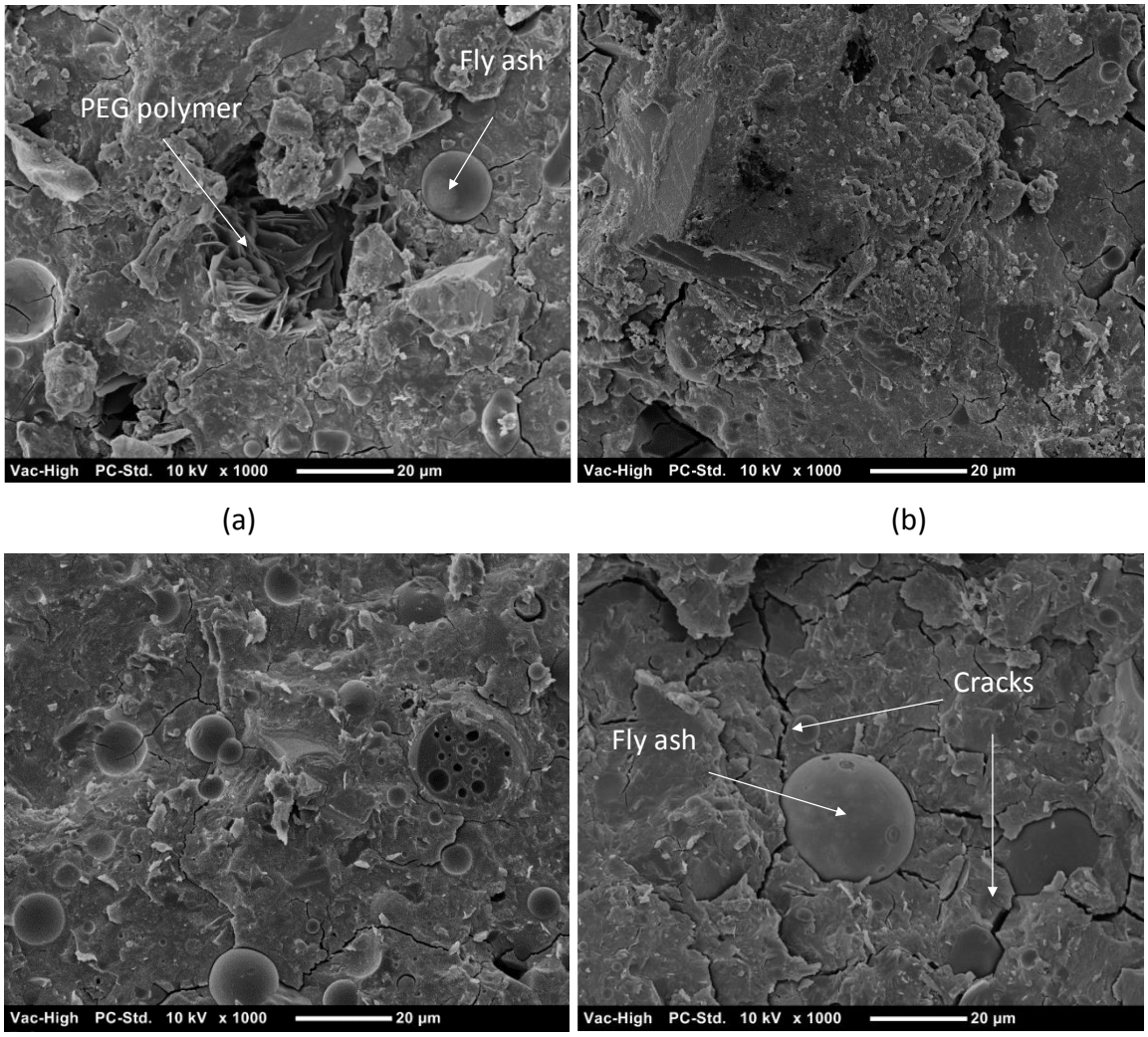

Figure 42. SEM images of the hydration products of the alkali aluminosilicate cement modified with: (a) 2.5% PEG; (b) 1% tartaric acid; (c) 2% sodium benzonate and 0.4% triisopoplnene; and (d) 5% calcined clay.

4.4 Conclusions

Concrete specimens were prepared with a cement of alkali aluminosilicate chemistry which embodies elements of alkali-activated aluminosilicates, and their moisture transport and durability characteristics were evaluated. The following primary conclusions were derived based on the experimental data generated in this investigation.

- Capillary sorptivity test results indicated that concrete prepared with the alkali aluminosilicate cement offers reduced sorption rates and capacities when compared with Portland cement concrete. Hydration products of the alkali aluminosilicate cement were found in scanning electron microscope images to be denser and with reduced capillary pores when compared with the Portland cement hydrates.
- Concrete prepared with the alkali aluminosilicate cement produced concrete materials with significantly improved inherent freeze-thaw durability (without air-entrainment) when compared with Portland cement concrete. Visual observations, and measurements of mass loss and dynamic elastic modulus compared the inherent stability of the hydration products of the alkali aluminosilicate cement when exposed to repeated cycles of freezing and thawing in water. Optic and scanning electron microscope images indicated that the aggregate-paste interface was resistant to freeze-thaw damage, and the hydrated cement paste exhibited minor microcracking.
- The base alkali aluminosilicate cement produced concrete materials with relatively low deicer salt scaling resistance when compared with Portland cement concrete. Several alternatives were evaluated for improving the deicer salt scaling resistance of the Portland cement concrete, including air entrainment, and incorporation of polyethylene glycol (PEG), tartaric acid, a combination of sodium benzoate and triisopropanolamine, and calcined clay into the alkali aluminosilicate cement formulation. Air entrainment improved the deicer salt scaling resistance of the alkali aluminosilicate cement concrete; the corresponding improvement in the deicer salt scaling resistance of Portland cement concrete was more significant. Use of PEG and tartaric acid at relatively low

concentrations enhanced the deicer salt scaling resistance of the alkali aluminosilicate cement concrete. Significant improvements in deicer salt scaling resistance were brought about by the use of a combination of sodium benzoate and triisopropanolamine in the alkali aluminosilicate cement formulation. The use of calcined clay compromised the scaling resistance of the alkali aluminosilicate cement concrete.

- Scanning electron microscopic analyses of the hydrates of alkali aluminosilicate cements with different modified formulations indicated that modified cement formulations incorporating tartaric acid and benzoate triisopropanolamine produced dense hydrates with minimal microcracking of the hydration products. A similar trend was noted with PEG where polymer coating of the interior void surfaces was also observed. Extensive microcracking of cement hydrates were noted in the presence of calcined clay.
- Modified alkali aluminosilicate cements which produced hydrated of dense microstructure with minimal cracking produced also produced concrete materials of high compressive strength. This was particularly true for the combination of sodium benzoate and triisopropanolamine which raised the early-age and long-term strength of the alkali aluminosilicate cement concrete, with about 35% gain in the 28-day compressive strength. Tartaric acid lowered the early-age strength of the alkali aluminosilicate cement concrete, but significantly improved its 28-day strength. The beneficial effects of the combination of sodium benzoate and triisopropanolamine, tartaric acid and PEG on the structure and properties of the alkali aluminosilicate cement concrete were explained based on the beneficial effects of these modifiers on the hydration process and the interfacial bonding of the alkali aluminosilicate cement.

Chapter 5

Plastic Shrinkage Cracking and Bleeding of Alkali Aluminosilicate Cement Concrete

5.1 Introduction

Cracking of concrete compromises its barrier qualities, and accelerates weathering attack on concrete and also corrosion of the reinforcing steel embedded in concrete. Cracking of concrete also compromises the structural performance of the concrete-based infrastructure. Internal and/or external restraint of the concrete shrinkage movements is an important cause of concrete cracking. The shrinkage movements of concrete when it is still in semi-fluid (plastic) state is referred to as plastic shrinkage [128]. Plastic shrinkage cracking generally occurs on the exposed concrete surfaces which, due to more rapid drying, undergo greater plastic shrinkage movements when compared with the body of concrete. Internal restraint of the surface plastic shrinkage can thus cause cracking of concrete surfaces between the time of placement and the final setting of concrete [129]. Exposure of concrete surfaces to windy surfaces in relatively warm and dry conditions encourage plastic shrinkage cracking.

Research into the plastic shrinkage mechanisms of concrete have generally concluded that capillary stresses near the exposed concrete surfaces, caused by the imbalance between the rates of bleeding and water evaporation, are the primary drivers of plastic shrinkage movements [130, 131]. Plastic settlements have also been found to influence plastic shrinkage of concrete [132]. These mechanisms of plastic shrinkage are largely physical [131, 133]; chemical phenomena have minimal effects on the early-age (plastic) shrinkage of concrete.

Figure 43 explains the process of capillary pressure buildup and plastic shrinkage in cement paste [134]. After casting, the solid particles in fresh concrete settle and water moves towards and accumulates at the surface (a phenomenon referred to as bleeding) (Figure 43A). The space between cement particles is largely filled with water throughout this process.

Due to evaporation or in certain materials also due to self-desiccation, the thickness of the water film at the concrete surface is reduced. With evaporation of the water film accumulated on the concrete surface, eventually the particles at the surface are no longer covered by water. Because of adhesive forces and surface tension, water menisci are formed between solid particles (Figure 43B). The curvature of the water surface causes a negative pressure in the capillary water. This pressure is inversely proportional to the main radii of the water surface, and also depends upon the surface tension of water. This pressure acts on the solid particles, resulting in contraction of the still plastic material [135]. The pores between particles get smaller under the action of capillary pressure, and more pore water is drawn towards the surface. Since a part of the pressure is counteracted by the repulsive forces between solid particles, the amount of water transported to the surface is not enough to completely relieve the pressure. The latter is nearly uniformly distributed near the surface where evaporation takes place. Hydrostatic pressure differences are small when compared with the occurring capillary pressure. The ongoing evaporation at the surface causes a continuing reduction of the main radii of the menisci (Figure 43Figure 43C), resulting in a rise in the absolute capillary pressure and the corresponding shrinkage strain. After reaching a certain pressure, the main radii of the water menisci are too small to bridge all the spaces between particles occurring at the surface. If the pressure reaches this limit, air penetrates the pore system, starting at the largest pores. The system becomes unstable and a relocation of

water takes place. The capillary pressure ‘‘breaks through” locally, and the pores are no longer completely filled with water (Figure 43D). At this stage, solid particles would remain interconnected by water sleeves [131].

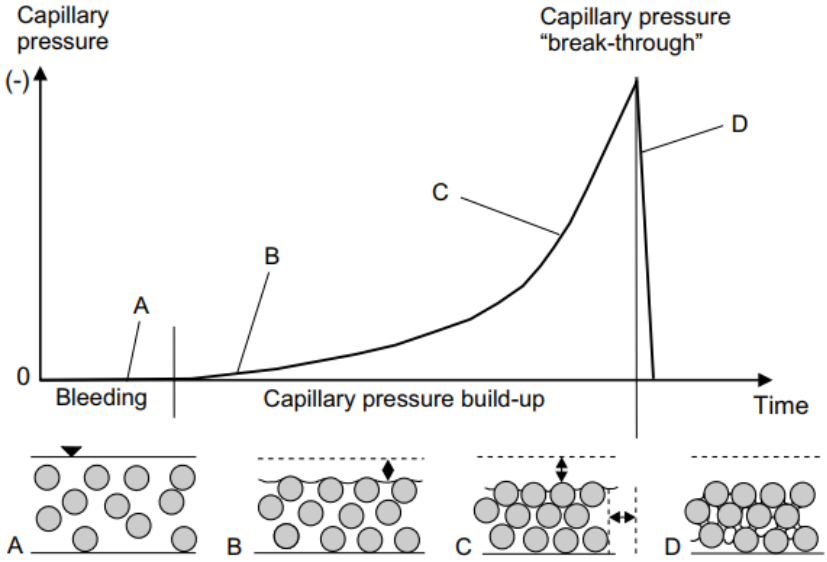

Figure 43. Capillary pressure buildup in a drying suspension of solid particles.

Control of plastic shrinkage cracking of concrete has been subject of several investigations. Plastic shrinkage reducing admixtures have been developed to reduce the affinity of particle (and pore) surfaces to water [136, 137], thereby reducing the buildup of capillary pressure. Cellulose-based stabilizers [138] or superabsorbent polymers [139] have also been used to reduce the evaporation rate and thus the potential for plastic shrinkage cracking of concrete. Different types of fibers, especially fibrillated polypropylene fibers, have been employed to reduce the extent of plastic shrinkage cracking [140, 141]. At the construction site, measures to prevent plastic shrinkage cracking include spraying of water or curing compounds on the concrete surface [142], or minimizing the evaporation of water by applying protective cover sheets [143]. Plastic shrinkage cracking remains a concern, particularly in large surface area placements like slabs on grade, thin surface repairs, patching, tunnel linings, etc. [144, 145]. In these applications, the

exposed surface area per unit volume of the overlay material is relatively large, and the old concrete substrate or the subgrade surface offers a high degree of restraint. Efforts to develop new classes of hydraulic cement should address the concerns with plastic shrinkage cracking and the related material properties of concrete.

The work reported herein investigated the plastic shrinkage cracking resistance of alkali aluminosilicate cement concrete. The bleeding and rheological attributes of alkali aluminosilicate cement pastes were also measured. Portland cement paste, and concrete were tested as control materials. The distinctions between the alkali aluminosilicate and Portland cement were identified, and were explained based on the experimental results.

5.2 Materials and Methods

5.2.1 Materials

The alkali aluminosilicate cement used in this investigation was produced via mechanochemical processing as reported in the previous work of same authors [146]. Portland cement (Type I per ASTM C150 acquired from Lafarge-Holcim) was used as control. Chemical compositions and Blaine fineness for the Portland cement and the alkali aluminosilicate cement used in this investigation are presented in Table 15.

Table 15. Chemical compositions (wt.%) and Blaine finesses (BF) of the Portland cement and the alkali aluminosilicate (AAS) cement used in this investigation.

	SiO_2	CaO	Al_2O_3	Fe_2O_3	MgO	K_2O	Na_2O	SO_3	BF, cm^2/g
AAS cement	35.2	28.1	13.6	4.03	3.73	1.14	8.89	0.53	3960
Portland cement	20.1	64.2	5.31	2.86	2.65	0.10	0.02	2.14	3870

The particle size distributions of the Portland cement and the alkali aluminosilicate cement are presented in Figure 44 .The median particle sizes were 9.8 and 7.4 µm for Portland cement and the alkali aluminosilicate cement, respectively.

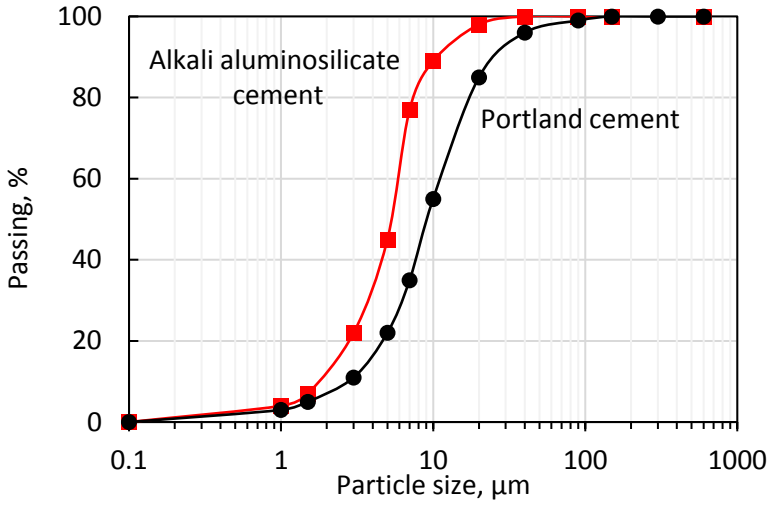

Figure 44. Particle size distributions of the Portland cement and the alkali aluminosilicate cement used in this investigation.

Natural sand with maximum particle size of 4.75 mm, was used as fine aggregate. Crushed limestone with a maximum particle size of 19 mm was used as coarse aggregate. The particle size distributions of the coarse and fine aggregates are presented in Figure 45.

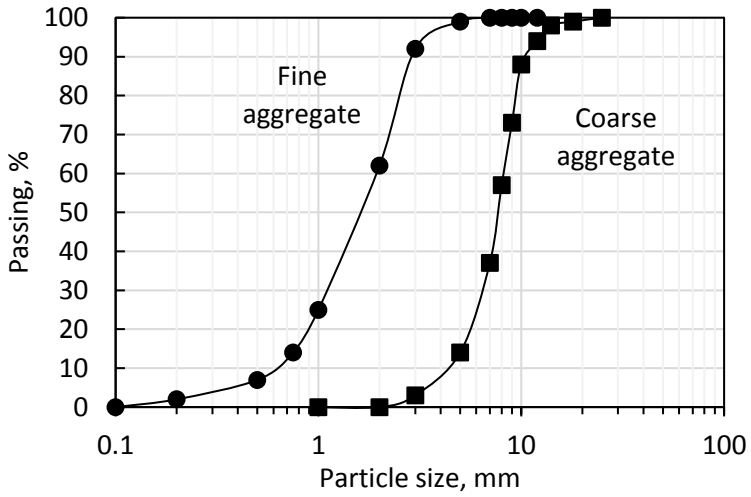

Figure 45. Particle size distributions of the fine and coarse aggregates used in this investigation.

5.2.2 Methods

Plastic shrinkage crack resistance of concrete was measured per ASTM C1579. A 19 L planetary mixer (Hobart A-200, Lombard) was used to prepare the concrete mixture with the mix proportions presented in Table 16.

Table 16. Mix design for the concrete used in this investigation.

Material	Quantity, kg/m^3
Cement	400
Fine aggregate	910
Coarse aggregate	1100
Water-to-cement ratio*	0.45-0.55

*water cement ratio was adjusted so that concrete produce similar fresh mix workability (slump of 60±10 mm).

The hydraulic cement was added first to the operating mixer followed by water, and mixing was continued for 2 minutes. Fine and coarse aggregates were then added, and mixing was continued for another three minutes until a homogeneous fresh concrete mixture was produced. The fresh concrete was placed in the plastic shrinkage mold (Figure 46Figure 46), consolidated using rods, and finished with a trowel.

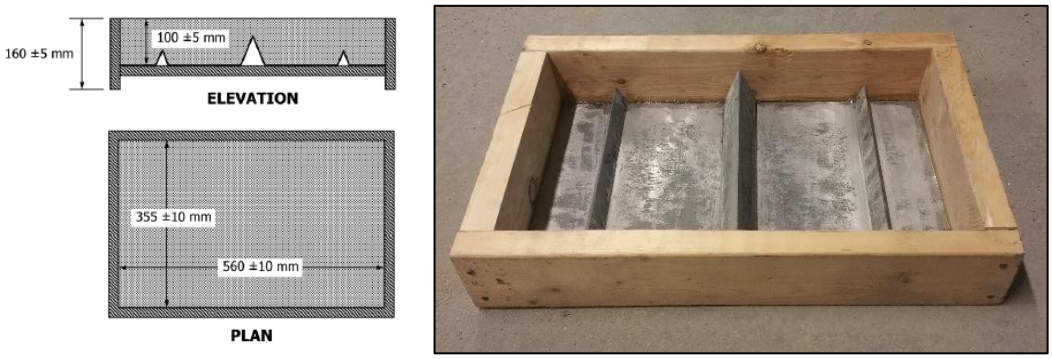

(a) (b)

Figure 46. Schematics of the plastic shrinkage mold with stress risers (a), and picture of the mold with stress risers used in this investigation (b).

Twenty-five minutes after the addition of water to cement, the specimens were placed in an environmental chamber with a temperature of 36±3 °C, relative humidity of 30±2%, and wind velocity of 24±2 km/h (Figure 47Figure 47). Pictures of the concrete surfaces were taken after 2, 4 and 6 hours. The fans were turned off after 6 hours, and the specimens were exposed to the chamber temperature and humidity for an additional 18 hours during which surface cracking was monitored at 1-hour time intervals. The specimens were removed from the environmental chamber after 24±2 hours, and inspected visually in order to evaluate plastic shrinkage cracking and surface condition. Water loss with exposure time was also monitored during the first 6 hours of testing.

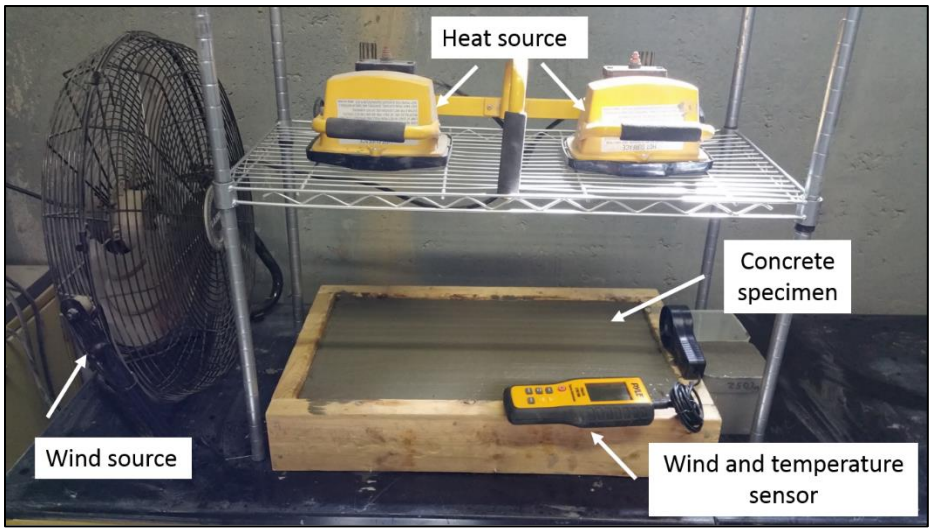

Figure 47. Plastic shrinkage test set-up

Bleeding tests were performed on fresh concrete specimens per ASTM C232 (Method-B For a sample consolidated by vibration). Fresh concrete (mix design presented in Table 2) was filled into a metal container with 150 mm diameter and 150 mm height in two layers, with each layer vibrated for 10 seconds on a vibrating table at medium speed. The container was then placed on a level platform free from vibration, and covered with a film to prevent the evaporation of water.

A pipette was used to draw off the bleed water at 10-minute intervals during the first 70 minutes, and at 30-minute intervals thereafter until cessation of bleeding. The bleeding test set up is shown in Figure 48.

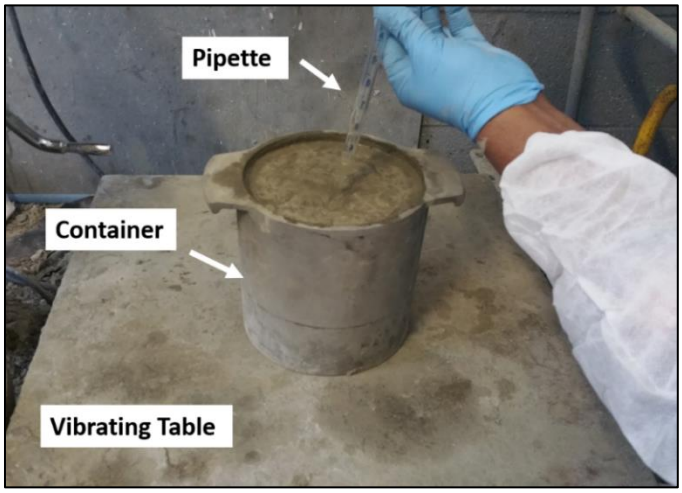

Figure 48. Bleeding test set up.

The rheological features of fresh (Portland and alkali aluminosilicate cement) pastes were measured using a digital rheometer (DV-III ULTRA) with stress control and data acquisition capabilities (Figure 49). The fresh mix was placed in a sample holder comprising an external sleeve and an internal rotator. The dimensions of the internal rotator and the external sleeve can be selected based on the rheological properties of the fresh mix. The stress controller controls the torque of the internal rotator. If the relationship between torque and rotational speed is linear, the linearity coefficients are preoperational to the Bingham constants of the fluid. The water-to-cement ratio considered here was 0.35 for both cement pastes.

Figure 49. Rheometer

5.3 Results and Discussion

5.3.1 Plastic Shrinkage

Figure 50 shows the images taken from the top surfaces of concrete specimens (and zoomed images of any cracks) after 2, 4, and 6 hours of exposure; the measured values of plastic shrinkage crack areas are presented in Table 17.

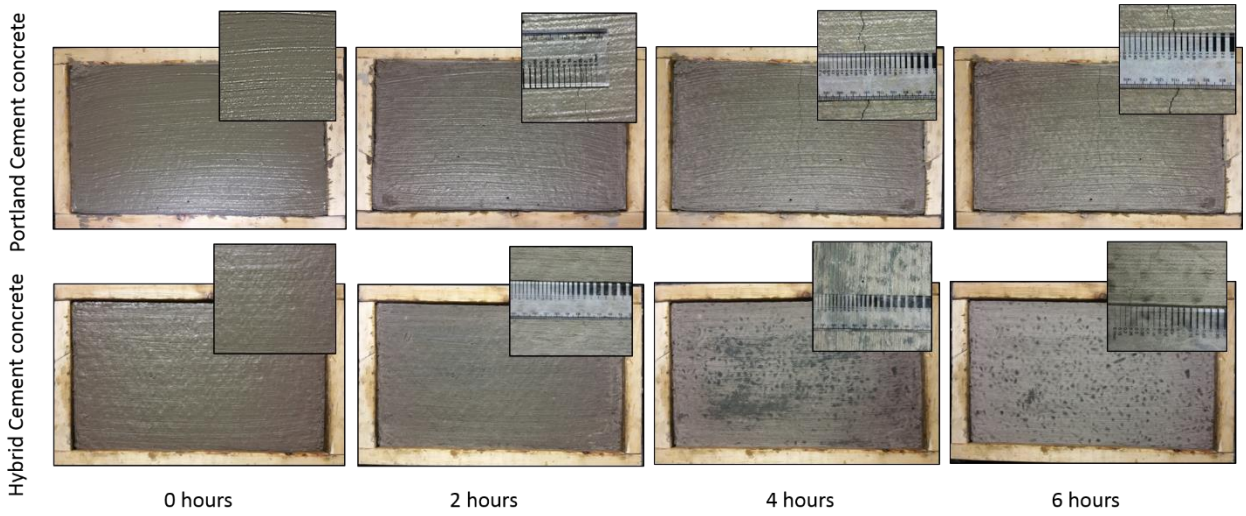

Figure 50. Visual appearance of the concrete specimen at different exposure time.

Small cracks with total area of 8 mm^2 started to appear on the Portland cement concrete surface after 1 hour. The cracks were more visible after 2 hours of exposure (as shown in Figure 50) with total area of 28 mm^2. Substantial increase in the crack area was observed after 3 and 4 hours of

exposure with areas of 93 and 138 mm^2, respectively. By the end of 6 hours, large cracks were observed with total crack area of 190 mm^2. Alkali aluminosilicate cement concrete, on the other hand, did not exhibit any signs of cracking after 2 hours of exposure. After 3 and 4 hours, microcracks were hardly detected with total area of less than 5 mm^2. By the end of 6 hours, small cracks were noted on the top surface of alkali aluminosilicate cement concrete with total area of 10 mm^2. These results indicate that the alkali aluminosilicate cement concrete provided significantly more resistance to plastic shrinkage cracking when compared with Portland cement concrete.

Table 17. Total plastic shrinkage crack areas (mm^2) versus time of exposure for Portland cement and alkali aluminosilicate cement concrete materials.

	Exposure time, hours						
	0	1	2	3	4	5	6
Portland cement concrete	0	8.2	28.1	92.7	138.4	177.8	190.2
Alkali aluminosilicate cement concrete	0	0	0	1.2	4.8	8.8	9.6

Figure 51 presents the measured values of cumulative water loss versus time from the Portland cement and alkali aluminosilicate cement concrete specimens under exposure to drying conditions over 6 hours. Portland cement concrete exhibited greater water loss with exposure time, which reached about 2% of the initial mass of the specimen by the end of 4 hours, after which the rate of moisture loss was smaller and reached 2.2% of the initial mass after 6 hours. The rate and extent of moisture loss from concrete specimens were significantly smaller for the alkali aluminosilicate cement concrete. Moisture loss was 0.3% of the initial weight of the concrete specimen after 1 hour of exposure. After 6 hours, the total moisture loss was 0.5%. These minimal values of moisture loss point at minimal bleeding of the alkali aluminosilicate

cement concrete; rapid setting of the alkali aluminosilicate cement concrete partly explains these observations.

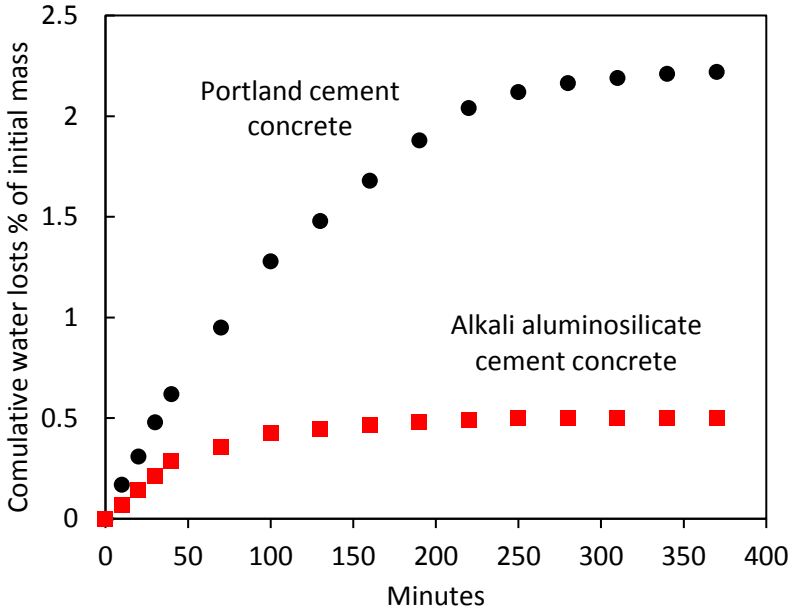

Figure 51. Cumulative water loss of the alkali aluminosilicate cement and Portland cement concrete materials versus time under exposure to drying conditions.

Figure 52 presents top and side views of the alkali aluminosilicate and Portland cement concrete surfaces after 24 hours. A continuous crack was observed on the Portland cement concrete surface whereas no notable cracks were observed on the alkali aluminosilicate cement concrete surface. This observation could be explained partly by the thicker layer of cement paste formed on the Portland cement concrete surface, which exacerbates moisture loss and thus the plastic shrinkage and consequent cracking. While the coarse aggregates were not visible on the surface of Portland cement concrete, they could be observed on the surface of the alkali aluminosilicate cement concrete. This observation pointed at the relatively small thickness of the cement paste formed on the alkali aluminosilicate cement concrete surface. The heavy presence of coarse aggregates on the top surface of the alkali aluminosilicate cement concrete lowers the plastic

shrinkage values and raises the resistance to plastic shrinkage cracking. These effects seem to more than compensate for the adverse effects of the reduced bleeding of the alkali aluminosilicate cement concrete versus Portland cement concrete (presented later).

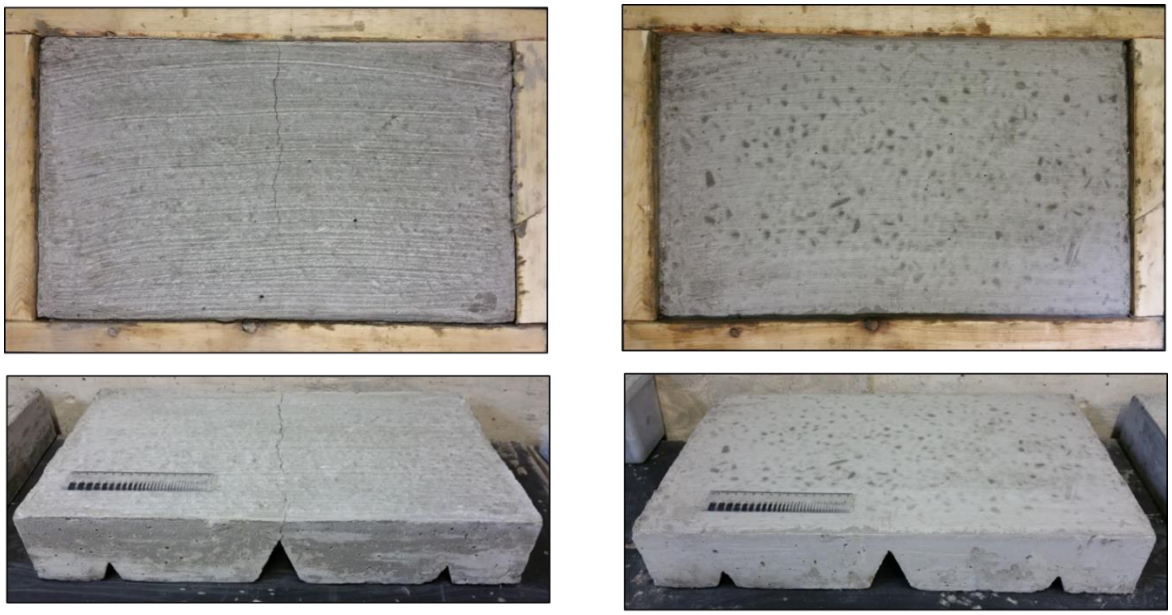

Portland cement concrete Alkali aluminosilicate cement concrete

Figure 52. Top and side views of the Portland and alkali aluminosilicate cement concrete specimens after 24 hours.

Figure 53 compares the optic microscope images taken from concrete surfaces after 24 hours of drying. Portland cement concrete was noted to exhibit networked microcracking which covered most of its surface area. Only fine and discontinuous microcracks could be observed on the alkali aluminosilicate concrete surface. The optic microscope images also indicated that the aggregate-paste interfaces were denser in the alkali aluminosilicate cement concrete when compared with the Portland cement concrete. The rapid moisture loss from the Portland cement concrete surface could reduce the degree of hydration at the surface, compromise the quality of aggregate-paste interfaces, and made the surfaces more vulnerable to plastic shrinkage cracking [147].

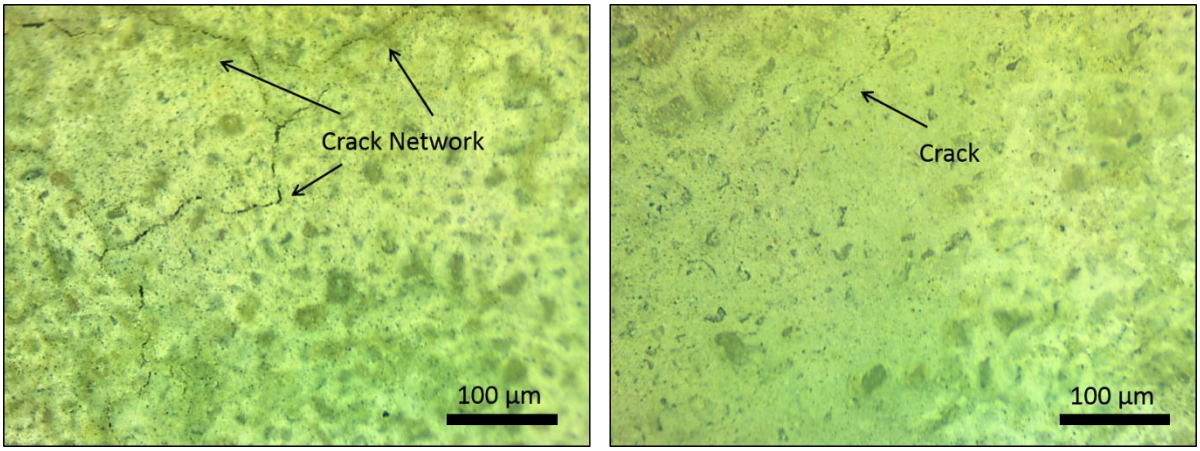

(a) Portland cement concrete (b) Alkali aluminosilicate cement concrete

Figure 53. Optic microscope images of Portland and alkali aluminosilicate cement concrete surfaces exposed to drying conditions.

5.3.2 Bleeding

Bleeding has mixed effects on concrete properties. It could raise the water content of the exposed concrete surface that experienced strong weathering effects. At the same time, in conditions that accelerate moisture loss from the concrete surface, it could have beneficial effects towards mitigating plastic shrinkage cracking of the concrete surface by restoring the moisture lost to evaporation. Excess bleeding could also signal segregation tendencies of fresh concrete mixtures [148].Figure 54 compares the cumulative bleed water of Portland and alkali aluminosilicate cement concrete materials. Bleeding of the alkali aluminosilicate cement concrete is observed to be negligible when compared with that of Portland cement concrete. Alkali aluminosilicate cements generally exhibit rapid setting and distinct rheological attributes (discussed later). These features could be used to explain the minimal bleeding of the alkali aluminosilicate cement concrete measured in this investigation. Bleeding generally benefits the resistance of concrete to plastic shrinkage cracking. In spite of its low bleeding, the alkali aluminosilicate cement concrete was observed to exhibit high resistance to plastic shrinkage

cracking. As noted earlier, this could be because some favorable features of the alkali aluminosilicate cement concrete, including its high aggregate content at the surface and reduced rates of moisture evaporation, more than compensate for its reduced bleeding as far as the effects on plastic shrinkage cracking are concerned.

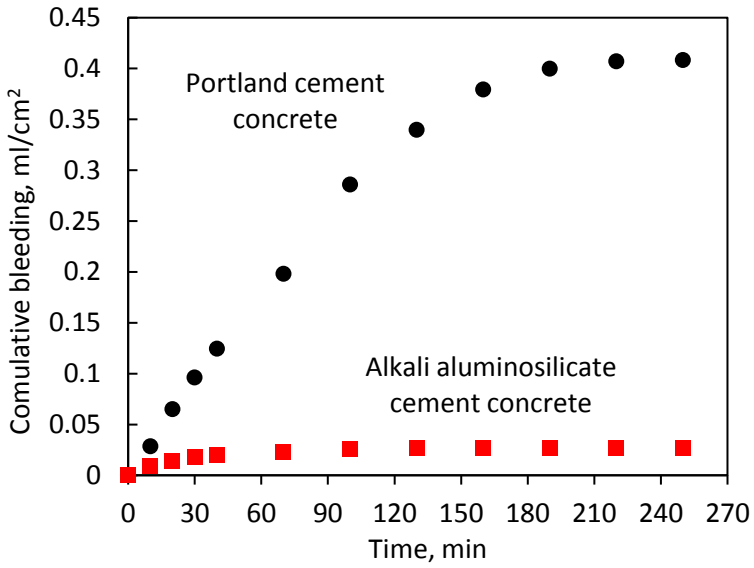

Figure 54. Cumulative bleeding versus time for Portland and alkali aluminosilicate cement concrete materials.

Figure 55 shows cross sections of the Portland and alkali aluminosilicate cement concrete specimens after performing the bleeding test. Three layers could be identified in Portland cement concrete (Figure 55a): (i) a thin paste layer of cement paste with about 8 mm thickness on top; (ii) a mortar layer of about 4 cm thickness; and (iii) concrete. The alkali aluminosilicate cement concrete (Figure 55b) was homogeneous, and coarse aggregates could be detected on the surface. As schematically depicted in Figure 56, the formation of the layered structure with the top cement paste (or mortar) layer that does not benefit from the stabilizing effect of aggregates exacerbates the potential for plastic shrinkage cracking. It seems that the distinctly high viscosity and the relatively high yield stress of the alkali aluminosilicate cement concrete (when compared

with Portland cement concrete), discussed in the next section, produced a segregation-resistant concrete mix which mitigated settlement of aggregates and bleeding of water to the surface. Finally, it should be noted that (barring notable evaporation of surface moisture) bleeding raises the moisture content of the concrete surface, and thus raises its water/cement ratio and lowers its quality [149]. Furthermore, the formation of a network of capillary pores due to the movement of bleeding water towards the surface also reduces the durability of concrete in this zone [150].

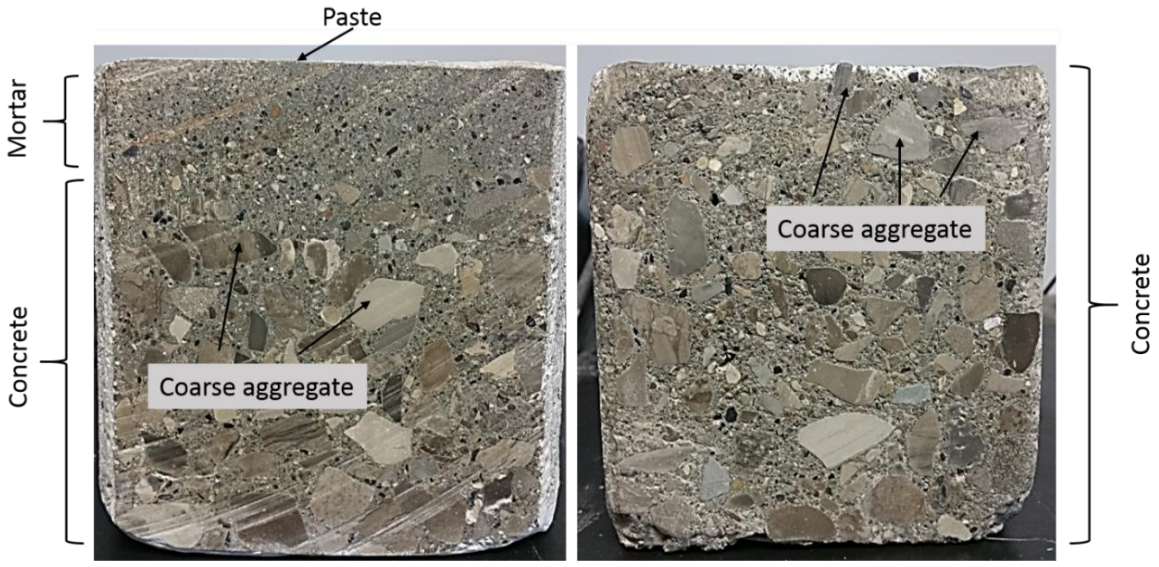

(a) Portland cement concrete (b) Alkali aluminosilicate cement concrete

Figure 55. Cross sections of the Portland and alkali aluminosilicate cement bleed test specimens.

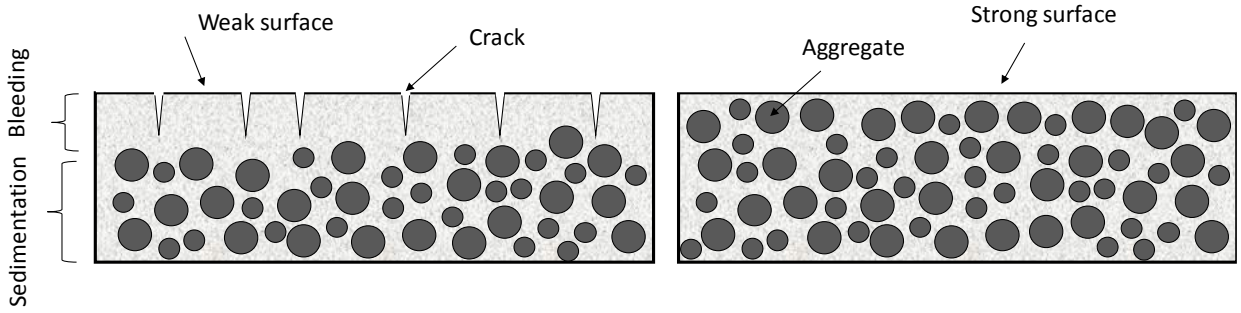

(a) Portland cement concrete (b) alkali aluminosilicate cement concrete

Figure 56. Schematics of the surface composition and cracking in Portland and alkali aluminosilicate cement concrete materials.

5.3.3 Rheological Characteristics

Figure 57 shows the viscosity-shear rate and the shear stress-shear rate relationships for Portland cement and the alkali aluminosilicate cement pastes. These test results suggest that the alkali aluminosilicate cement paste has a higher viscosity when compared with the Portland cement paste. The test results on viscosity-shear rate relationships were analyzed in order to determine if the rheological behavior of the two pastes follow the Bingham model. The resulting shear stress-shear rate relationships presented Figure 57b indicate that application of the Bingham model to these pastes is appropriate. Linear regression analyses of these relationships produced the yield stress and viscosity values summarized in Table 18. These results indicate that the yield stress of the alkali aluminosilicate cement paste is about 30% higher than that of the Portland cement paste. The plastic viscosity of the alkali aluminosilicate cement paste is two times that of the Portland cement paste.

The relatively higher viscosity and yield stress of alkali aluminosilicate cement paste could also explain the lower bleeding of the alkali aluminosilicate cement concrete when compared with Portland cement concrete. The higher attractive forces in the viscous paste could hinder settlement of particles which causes upward movement (bleeding) of water. This is actually the concept used in development of viscosity-enhancing admixtures which enhance the segregation resistance of fresh (e.g., self-consolidating) Portland cement concrete [151].

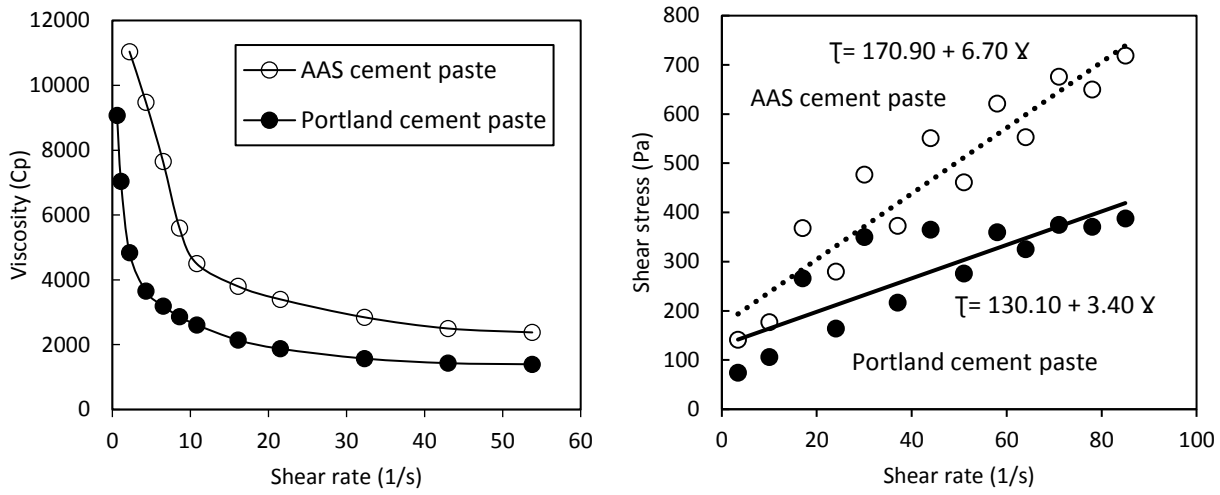

Figure 57. Apparent Viscosity test results for Portland and alkali aluminosilicate (AAS) cement pastes (a), and the shear stress-shear rate relationships (b).

Table 18. Yield stress and viscosity of Portland and alkali aluminosilicate cement pastes.

	Yield stress, Pa	Viscosity, Pa.S
Portland cement paste	130.1	3.40
Alkali aluminosilicate cement paste	170.9	6.70

5.4 Conclusions

Concrete specimens prepared using an alkali aluminosilicate cement with predominantly alkali aluminosilicate chemistry and also with Portland cement were tested for plastic shrinkage, bleeding and rheological characteristics. The following primary conclusions were derived based on the data generated in this experimental work.

- The alkali aluminosilicate cement concrete exhibited significantly higher resistance to plastic shrinkage cracking when compared with Portland cement concrete. Moisture evaporation from the alkali aluminosilicate cement concrete was distinctly low when compared with Portland cement concrete.

- Bleeding of the alkali aluminosilicate cement concrete was negligible when compared with that of Portland cement concrete. Viscosity of the fresh alkali aluminosilicate cement paste was, at comparable water/cement ratio, twice that of Portland cement paste. Yield stress of the fresh alkali aluminosilicate cement paste was also relatively high when compared with Portland cement paste.
- Cross-sectional comparisons of the alkali aluminosilicate and Portland cement concrete materials indicated that the surface of Portland cement concrete exhibited indications of segregation where a surface layer that was rich in Portland cement paste formed, and the coarse aggregate content increased with depth. alkali aluminosilicate cement concrete did not exhibit such segregation; it did not have a notable compositional gradient with respect to depth, and coarse aggregates were present at the surface; they were visible on the top surface.
- The relatively high viscosity and yield stress of the fresh alkali aluminosilicate cement paste seems to have reduce settlement of particles which cause upward movement (bleeding) of water. The reduced bleeding of the alkali aluminosilicate cement concrete can be used to explain its reduced moisture evaporation when exposed to drying conditions. Finally, the presence of aggregates near the surface of the alkali aluminosilicate cement concrete has a stabilizing effect as far as plastic shrinkage movements and cracking potential are concerned. These effects seem to more than compensate for the reduced bleeding of alkali aluminosilicate cement concrete which could delay drying and thus improve the plastic shrinkage cracking of the alkali aluminosilicate concrete surface. In conditions which do not cause rapid drying of the

concrete surface, reduce bleeding could also lower the water/cement ratio and thus improve the quality of the alkali aluminosilicate concrete surface.

Chapter 6

Acid Resistance and Corrosion Protection Potential of Concrete Prepared with Alkali Aluminosilicate Cement

6.1 Introduction

Ordinary Portland Cement is the most widely used hydraulic binder in concrete construction. Portland cement concrete is generally considered to be a durable material requiring minor maintenance efforts. The growing emphasis on the life-cycle economy of infrastructure systems has led to a greater scrutiny of the concrete performance under aggressive exposures. The resistance of concrete to chemical attacks such as acids [152], and its ability to protect the reinforcing steel against corrosion [153] have been identified as some key aspects of concrete durability that could benefit from further improvement. The environmental impacts and energy use associate with concrete (especially Portland cement) production also represent growing concerns [154].

Alkali activated binders are produced by activating aluminosilicate precursors with alkaline activators; this class of binder benefit significantly from thermal curing [59, 155, 156]. When compared with Portland cement, alkali activated binders offer advantages in terms of sustainability, moisture barrier qualities and durability characteristics [157-159]. There is limited existing knowledge of the durability characteristics and the corrosion protection potential of alkali activated binders cured at room temperature [160, 161]. This is a key obstacle against large-scale use of alkali activated binder in concrete construction [162].

The work reported herein investigated the acid resistance and corrosion protection capabilities of concrete prepared with alkali aluminosilicate cement. Concrete cylinders were prepared and

exposed to an acid solution for 28 days, and their stability under acid attack was evaluated. The potential of this concrete to protect embedded steel reinforcing bars against corrosion was also evaluated under exposure to wetting and drying cycles. These qualities of alkali aluminosilicate cement concrete were compared with those of Portland cement concrete.

6.2 Materials and Methods

6.2.1 Materials

The alkali aluminosilicate cement used in this investigation was produced via mechanochemical processing [163]. Portland cement (Type I per ASTM C150 acquired from Lafarge-Holcim) was used as control. Chemical compositions and Blaine fineness for the Portland cement and the alkali aluminosilicate cement used in this investigation are presented in Table 19.

Table 19. Chemical compositions (wt.%) and Blaine fineness (BF) of the Portland cement and the alkali aluminosilicate (AAS) cement used in this investigation.

	SiO_2	CaO	Al_2O_3	Fe_2O_3	MgO	K_2O	Na_2O	SO_3	BF, cm^2/g
Portland cement	20.1	64.2	5.31	2.86	2.65	0.10	0.02	2.14	3870
AAS cement	35.2	28.1	13.6	4.03	3.73	1.14	8.89	0.53	3960

The particle size distributions of the Portland cement and the alkali aluminosilicate cement are presented in Figure 58. The median particle sizes were 9.8 and 7.4 μm for Portland cement and the alkali aluminosilicate cement, respectively.

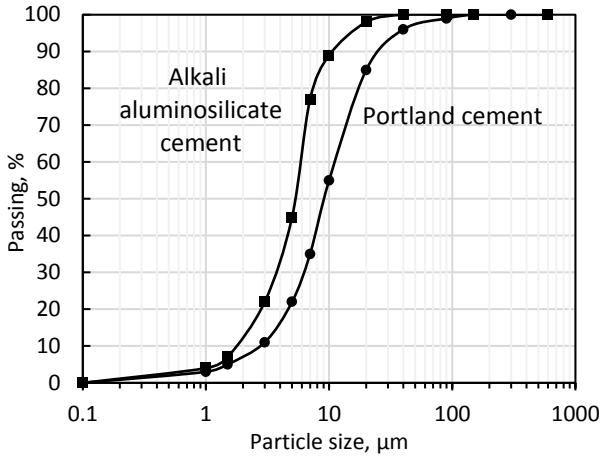

Figure 58. Particle size distributions of the Portland cement and the alkali aluminosilicate cement used in this investigation.

Natural sand with maximum particle size of 4.75 mm, was used as fine aggregate. Crushed limestone with a maximum particle size of 19 mm was used as coarse aggregate. The particle size distributions of the coarse and fine aggregates are presented in Figure 59.

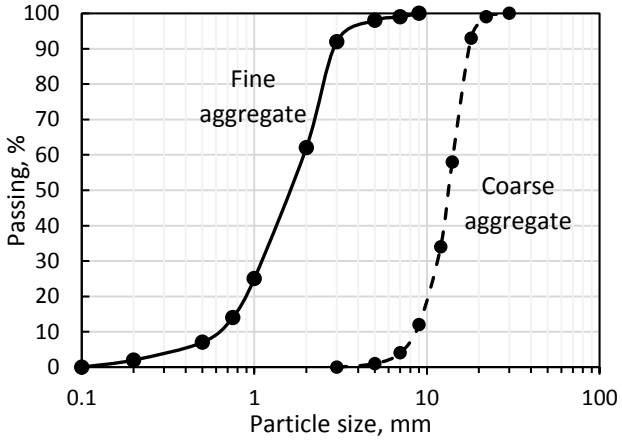

Figure 59. Particle size distributions of the fine and coarse aggregates used in this investigation.

6.2.2 Methods

Table 20 presents the concrete mix proportions used to prepare the concrete specimens for acid and corrosion resistance A 19 L planetary mixer (Hobart A-200, Lombard) was used to prepare the concrete mixture.

Table 20. Mix design for the concrete used in this investigation

Material	Quantity, kg/m^3
Cement	400
Fine aggregate	910
Coarse aggregate	1100
Water-to-cement ratio*	0.45-0.55

*water cement ratio was adjusted so that concrete produce similar fresh mix workability (slump of 60±10 mm).

Acid resistance was assessed by immersing the concrete specimens that were cured at room temperature for 28 days in 5% sulfuric acid solution [164]. The choice of acid and the acid concentration in solution were made to represent the exposure conditions of concrete in sanitary sewer pipes. The pH of acid solution was retained at 1.0, and a solution-to-specimen volumetric ratio of 4 was used in this investigation. Cylindrical (75mm × 150mm) concrete specimens were kept fully immersed in acid solution for a duration of 28 days. Acid resistance was evaluated on a weekly basis through visual inspection and measurement of the change in mass and compressive strength. SEM images were also taken of cement pastes after 28 days of immersion in acid solution. Portland cement concrete specimens were also prepared using the same mix design, and subjected to similar exposure in order to produce a basis for relative assessment of the alkali aluminosilicate cement performance.

Corrosion tests were performed following the procedures described in ASTM C878. Concrete cylindrical specimens (100mm×200mm) were cast with a 16-mm diameter uncoated reinforcing steel bar embedded at their center (Figure 60). The specimens were cured for 28 days at room temperature, and were then subjected to accelerated cycles of wetting and drying. These cycles comprised 2 hours of wetting at room temperature followed by the drying at 40°C over 2 hours.

Figure 60. Corrosion test specimens subjected to wet-dry cycles.

A high impedance voltmeter was used to measure to corrosion potential of the reinforcing bars embedded in concrete specimens. The high impedance voltmeter had two terminals, one of which was connected to the steel bar embedded in concrete, with the other connected to a copper/copper sulfate reference cell with porous sponge. In weekly measurements, the copper/copper sulfate electrode was moved with a sponge over the surface of the concrete specimen, and the high impedance voltmeter readings were recorded over the 12-week period of the accelerated corrosion test. The high impedance voltmeter used in this investigation had a variable input impedance ranging from 10 to 200 MΩ. At the conclusion of the corrosion test, the concrete specimens were split, and visual observations were made of the corrosion conditions of the embedded reinforcing bar. SEM images were taken for the hydrated cement paste samples occurring at the rebar-matrix interface in concrete specimens. In order to evaluate the alkalinity of concrete, freshly fractured concrete surfaces were sprayed with phenolphthalein solution [165], used as pH indicator; the specimens were then inspected visually. The solution comprised 1% phenolphthalein in ethanol [166].

6.3 Results and Discussion

6.3.1 Acid Resistance

6.3.1.1 Visual Appearance

Figure 61 compares the visual appearances of concrete specimens prepared with Portland cement and with the alkali aluminosilicate cement after immersed in 5% sulfuric acid solution for 28 days. Portland cement concrete experienced minor surface deterioration after 3 and 7 days of exposure to acid solution. The alkali aluminosilicate cement concrete experienced negligible damage up to 7 days of exposure to acid attack. After 14 days, a layer of a white mixture was noted to form on the surface of Portland cement concrete. The alkali aluminosilicate cement concrete experienced minor surface damage after 14 days of exposure. Between 14 of 28 days of exposure, a more notable white and mushy mixture formed on the Portland cement concrete surface; it then began to dissolve, exposing sand grains on the concrete surface and producing a rough surface. Subsequently, the surface layer became loose and powdered, and then pulpified and softened. After 28 days of exposure, the Portland cement concrete surface exhibited expansive cracks that could have been caused by sulfate attack and ettringite formation [167]. The alkali aluminosilicate cement concrete, on the other hand, displayed less visible surface deterioration up to 28 days of exposure. These observations point at the stable chemistry and the desired barrier qualities of the alkali aluminosilicate cement concrete when compared with Portland cement concrete.

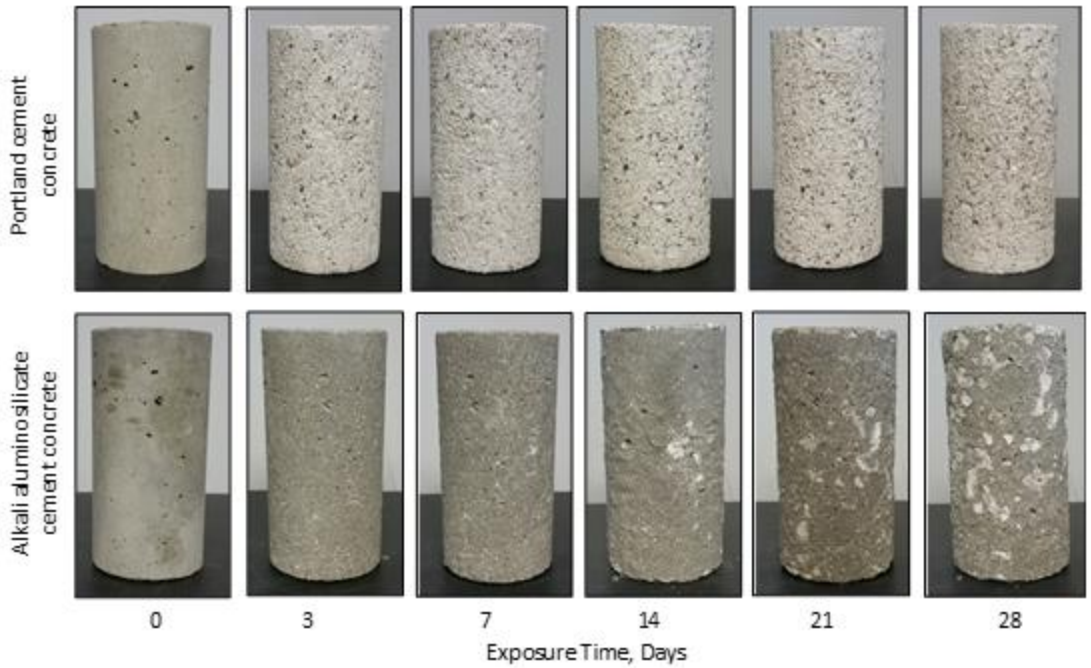

Figure 61. Visual appearances under acid attack of Portland cement concrete versus alkali aluminosilicate cement concrete.

6.3.1.2 Mass and Strength Loss

The remaining mass and the residual compressive strength of concrete specimens versus immersion duration are presented in Figure 62a and Figure 62b respectively. While there was hardly any mass loss after 28 days of immersion in acid solution in the case of the alkali aluminosilicate cement concrete (less than 1%), Portland cement concrete experienced about 3% mass loss after this period of immersion in acid solution. This finding confirms that the alkali aluminosilicate cement considered here, similar to other alkali activated binders, provides high resistance to acid attack when compared with the Portland cement-based binder. The low concentrations of calcium hydroxide and calcium sulfoaluminate, and the low Ca/Si ratio in the alkali (calcium/sodium) aluminosilicate hydrate provide for improved acid resistance.

The residual compressive strength test results indicate that the alkali aluminosilicate cement concrete retains its compressive strength better than Portland cement concrete. Initially,

Portland cement concrete experienced a gain in compressive strength, that could be due to further moist curing of the concrete. After 14 days of immersion in acid solution, the alkali aluminosilicate cement concrete experienced hardly any loss of compressive strength while normal Portland cement concrete lost about 15% of its initial compressive strength. After 28 days of immersion in acid solution, the alkali aluminosilicate cement concrete experienced 7% loss of compressive strength compared to 23% loss for Portland cement concrete. The stable, crosslinked aluminosilicate structure of the alkali aluminosilicate cement concrete with hydrates of relatively low calcium content as well as its very fine pore structure which is not amenable to capillary sorption of the acidic solution could be used to explain its superior acid resistance. The severe acid attack on Portland cement can be attributed to the susceptibility to acid attack of the calcium hydroxide, calcium sulfoaluminate and Ca-rich calcium silicate hydrate constituents of the Portland cement hydration products [168].

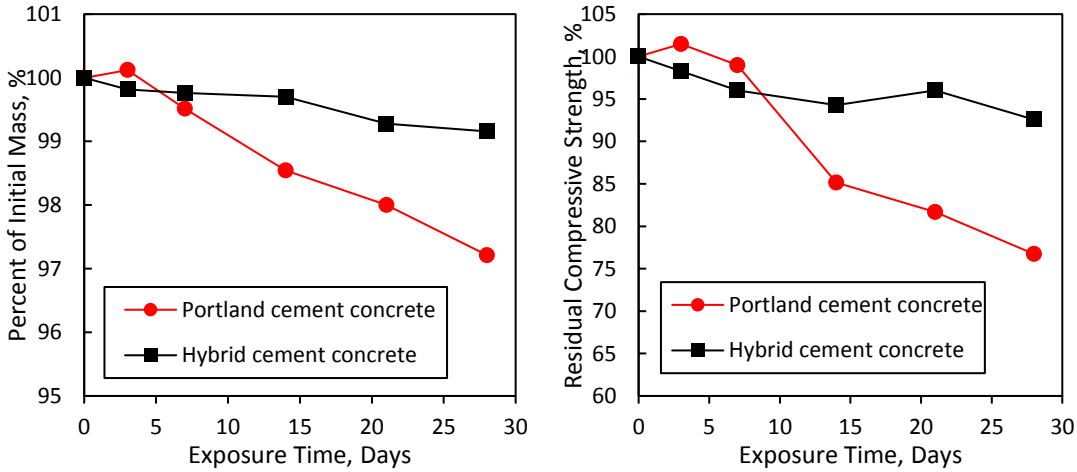

(a) Mass (b) Compressive strength

Figure 62. Measured values of the remaining mass and the residual compressive strength of concrete specimens versus time of immersion in acid solution.

6.3.1.3 SEM Observations After Immersion in Acidic Solution

Figure 63 SEM images of the hydrated paste in Portland cement concrete and the alkali aluminosilicate cement concrete after 28 days of immersion in acid solution. In general, with progress of sulfuric acid attack, calcium silicate hydrate (C–S–H) and calcium aluminosilicate hydrate (C–A–S–H) tend to decalcify, thus assuming lower Ca/Si molar ratios [168]. Ca-rich gels such as C–S–H (which is prevalent among the Portland cement hydrates) could experience more pronounced deterioration under acid attack (Figure 63a) when compared with, say, sodium aluminosilicate hydrate (N-A-S-H) or even calcium aluminosilicate hydrate (C-A-S-H) with lower Ca/Si ratios, which are some key hydrates of alkali aluminosilicate cement. The SEM image of Portland cement paste could point at decomposition of C–S–H which, at this point, is difficult to identify. Furthermore, some club-shaped crystals (probably $Ca_SO_4.2H_2O$) of different sizes could be identified; the formation of gypsum, accompanied with reduction of calcium hydroxide, induces expansive forces that can cause cracking [169, 170]. The alkali aluminosilicate cement paste subjected to acid attack (Figure 63b), on the other hand, exhibited a denser and more homogeneous microstructure with minimal indications of deterioration or any crystal formation. This finding confirms those of other researchers who found that alkali activated binders provide better resistant to acid attack than Portland cement binders [171, 172].

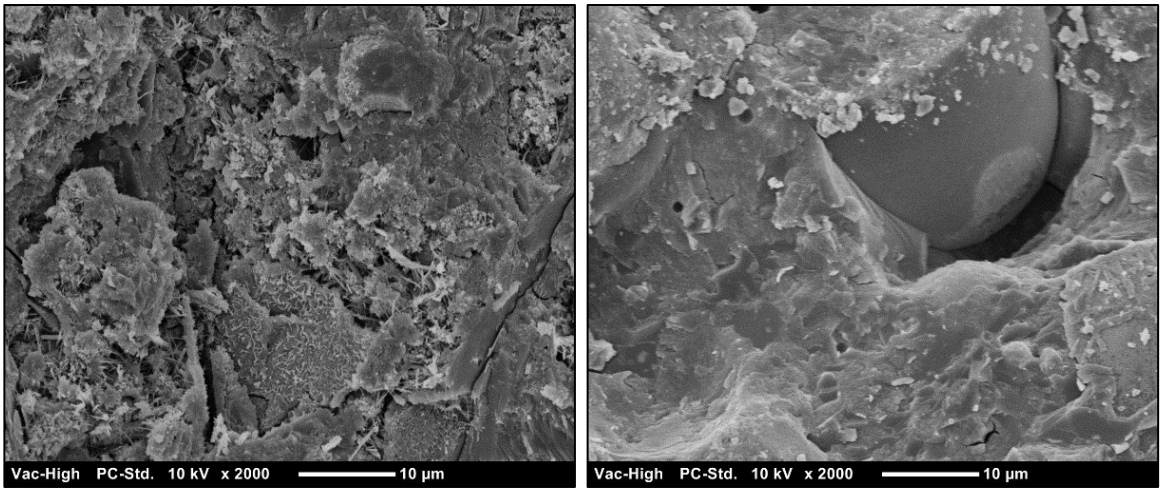

(a) Portland cement paste (b) Alkali aluminosilicate cement paste

Figure 63. SEM images of the hydrated pastes of Portland cement and the alkali aluminosilicate cement after 28 days of immersion in acid solution.

6.3.2 Corrosion Resistance

6.3.2.1 Corrosion Potential

Figure 64 presents the corrosion potential for the steel rebar embedded in concrete specimens prepared with Portland cement and with the alkali aluminosilicate cement. The corrosion potential in Portland cement concrete was observed to be slightly greater than that in the alkali aluminosilicate cement concrete, especially after longer exposure periods. This observation points at the better protection of the embedded steel bar against corrosion by the alkali aluminosilicate cement when compared with Portland cement. The higher alkalinity of the alkali aluminosilicate cement and the desired barrier qualities of its hydrates could be used to explain its corrosion protection potential.

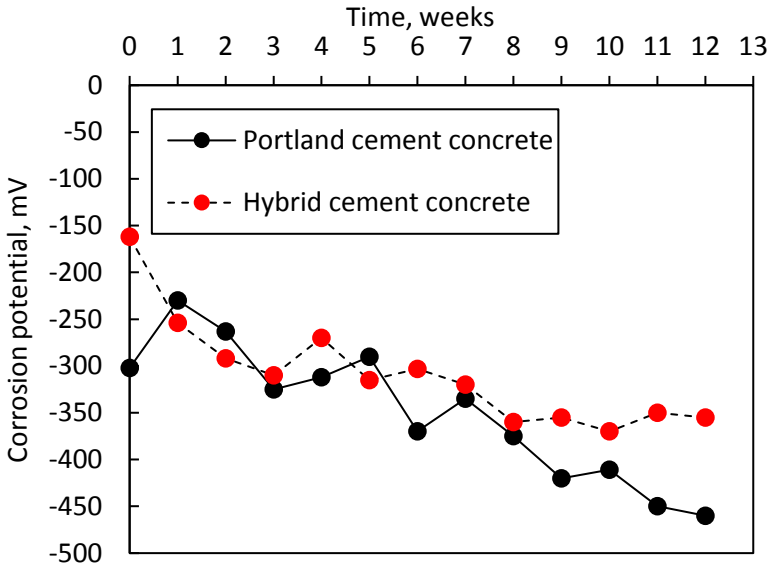

Figure 64. corrosion potential for the steel bar embedded in concrete specimens over the time of exposure to cycles of wetting and drying.

6.3.2.2 Visual Assessment of The Reinforcing Bars After Exposure to Repeated Wet-Dry Cycles

Photographs of the embedded rebars after 12 weeks of wet-dry cycles are presented in Figure 65. The rebar embedded in Portland cement concrete exhibited some signs of corrosion (Figure 65a) at both ends of the concrete specimens (Region 1 and Region 2). The rebar embedded in the alkali aluminosilicate cement concrete, on the other hand, showed clean threads with no signs of corrosion at both ends of the concrete specimen (Figure 65b). This indicates that the alkali aluminosilicate cement paste retained its alkaline nature, and provide conditions which favor passivation of the steel reinforcement surfaces [173]. Steel corrodes at pH values drop below 10–11, with the exact initiation point depending on the presence or absence of other ions in the pore solution. This is due to the breakdown of the passive oxide layer that forms in highly alkaline conditions [174].

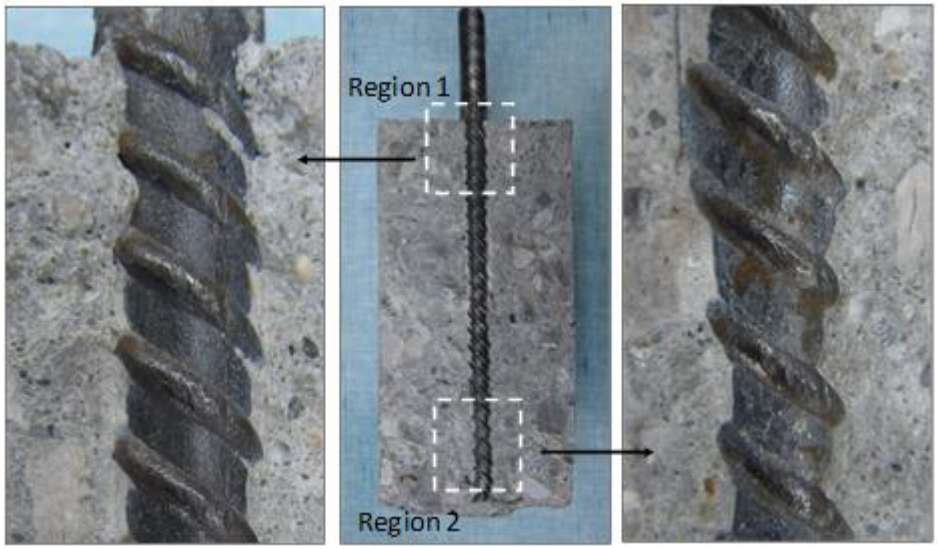

(a) Rebar embedded in Portland cement concrete

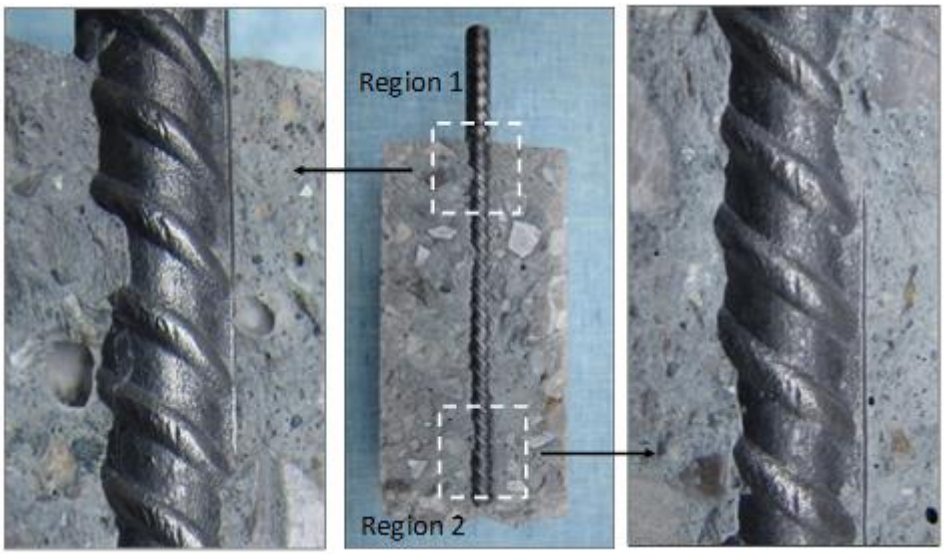

(b) Rebar embedded in the alkali aluminosilicate cement concrete

Figure 65. Visual appearances of the reinforcing bars embedded in Portland cement concrete and the alkali aluminosilicate cement concrete after 12 weeks of exposure to repeated wet-dry cycles.

6.3.2.3 Alkalinity of Freshly Fractured Concrete Surfaces

Figure 66 sows freshly fractured concrete surfaces after spraying with phenolphthalein. Both concrete surfaces assumed a purple color, pointing at the alkaline nature of both binders. The concrete surface for the alkali aluminosilicate binder (Figure 66b) prepared slightly darker than

the concrete with Portland binder (Figure 66a), reflecting the higher alkalinity of the alkali aluminosilicate binder. This higher alkalinity of the alkali aluminosilicate binder benefits the stability of the protective passive oxide film that forms on the rebar surface, further reducing its corrosion potential in alkali aluminosilicate cement concrete [175].

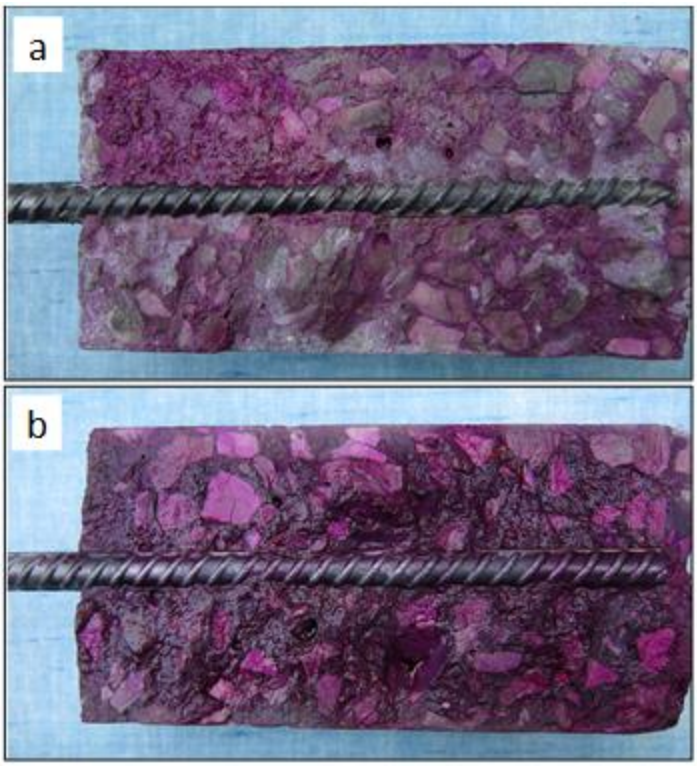

Figure 66. Visual appearance of concrete specimens sprayed with phenolphthalein: (a) Portland cement concrete, and (b) alkali aluminosilicate cement concrete.

6.3.2.4 SEM Observations of The Interface Regions After Accelerated Corrosion

Figure 67 and Figure 68 show SEM images at two magnifications taken of hydrated cement pastes occurring at the rebar-matrix interface at the conclusion of the accelerated corrosion tests for the Portland cement binder and the alkali aluminosilicate cement binder. The hydrated Portland cement binder was observed to exhibit a microstructure of relatively low density (Figure 67 a) which compared with the alkali aluminosilicate cement binder (Figure 11a). The magnified SEM image for Portland cement (Figure 68b) showed a disturbed structure with loosely held crystals

in size range of 1-3 micrometer. These crystals could be the Iron oxide/hydroxide crystals formed at different stages of steel corrosion [176]. The alkali aluminosilicate cement binder, on the other hand, showed a homogeneous microstructure with denser hydration products and no signs of iron crystals formation (Figure 11b).

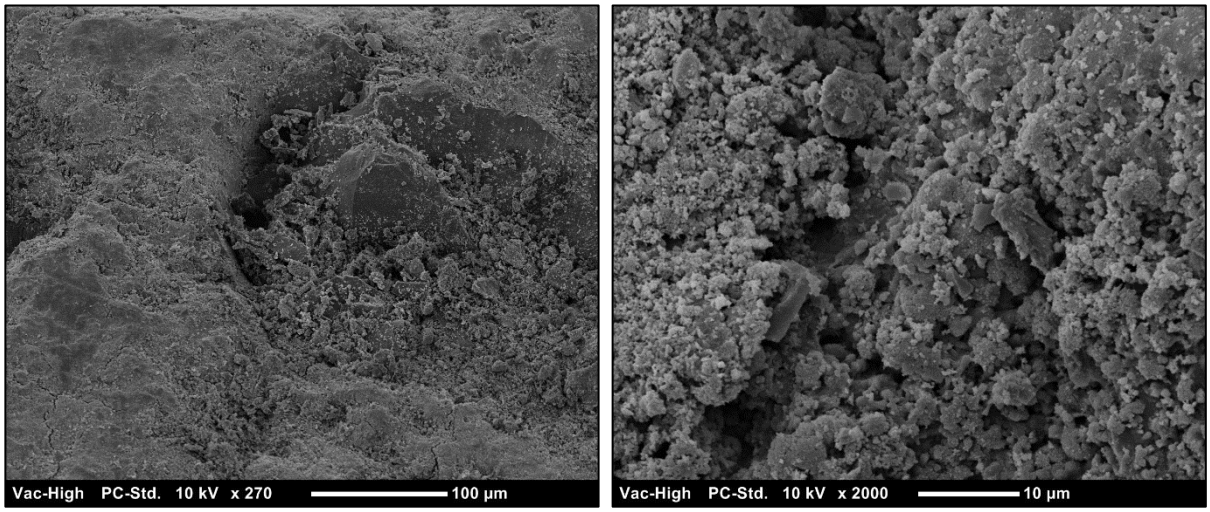

(a) 270X (b) 2000X

Figure 67. SEM images for Portland cement binder at the rebar-matrix interface after accelerated corrosion tests.

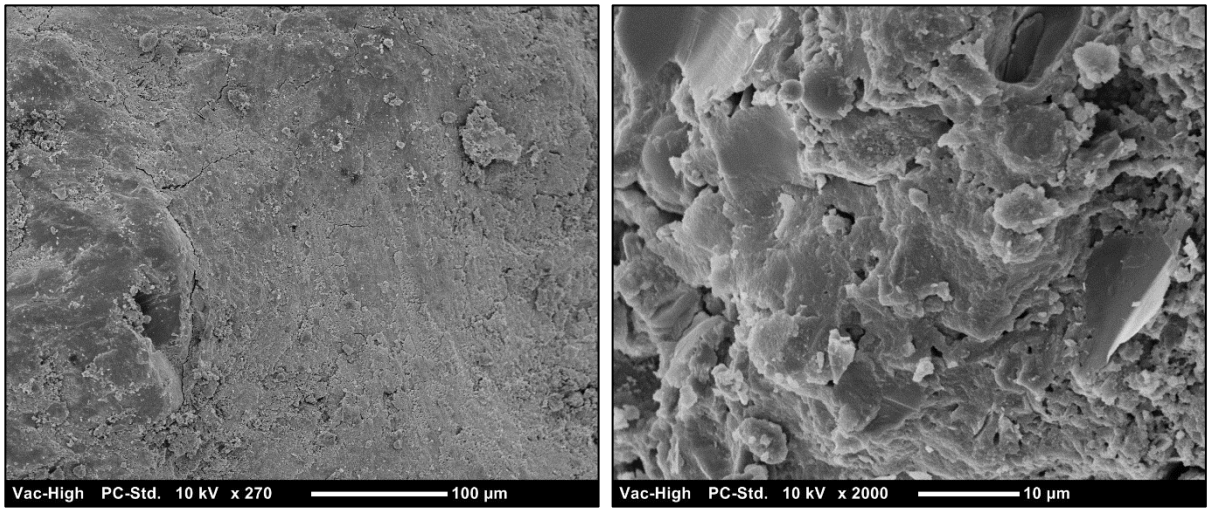

(a) 270X (b) 2000X

Figure 68. SEM images for the alkali aluminosilicate cement binder at the rebar-matrix interface after accelerated corrosion tests.

6.4 Conclusions

Concrete specimens prepared using an alkali aluminosilicate cement with predominantly alkali aluminosilicate chemistry and also with Portland cement were tested for acid resistance and protection of embedded steel against corrosion. The following conclusions were derived based on a comparative study of test results.

- The alkali aluminosilicate cement concrete exhibited significantly higher resistance to acid attack when compared with Portland cement concrete. Portland cement concrete exhibited more notable surface deterioration when immersed in acid solution. The alkali aluminosilicate cement concrete also experienced less losses of mass and compressive strength over time of immersion in acid solution. SEM images pointed at the highly stable nature of the hydrates of the alkali aluminosilicate cement, when compared with Portland cement, after prolonged exposure to acid attack.
- Corrosion test results indicated that the alkali aluminosilicate cement concrete provided the embedded steel bars with improved protection against corrosion when compared with Portland cement concrete. The measured value of electrochemical potential that correlates with the corrosion rate of the embedded steel was lower in the alkali aluminosilicate cement concrete when compared with Portland cement concrete. Visual observations also indicated that the extent of corrosion after prolonged exposure to cycles of wetting and drying was more pronounced in Portland cement concrete when compared with the alkali aluminosilicate cement concrete. The alkali aluminosilicate binder exhibited higher alkalinity when compared with the Portland cement binder; the higher alkalinity of the alkali aluminosilicate binder benefits the stability of the passive

oxide film that protects rebars from corrosion in concrete. The microstructure of hydrates in the alkali aluminosilicate binder at the rebar-matrix interface at the conclusion of accelerated corrosion tests were found to be denser and more homogenous when compared with the Portland cement binder.

- The hydration products of alkali aluminosilicate cements offer desired chemical stability complemented with a favorable pore structure for resisting the sorption and diffusion of moisture and aggressive solution. The pore solution of alkali aluminosilicate hydrates tends to be more alkaline than that of Portland cement. These features of alkali aluminosilicate cement could be used to explain its improved acid resistance and protection of embedded steel against corrosion.

Chapter 7

Carbon Dioxide Integration into Alkali Aluminosilicate Cement Particles for Achievement of Improved Properties

7.1 Introduction

The consumption of concrete, estimated at 30 billion tons per year, is second only to that of water. The desired balance of performance and cost offered by concrete has led to its prominent position as the most widely used material of construction [177]. Concrete is the defining feature of the vast infrastructure that supports economic and societal activities on earth. While the structural performance and economics of concrete have led to its prevalent role in the infrastructure for more than two centuries, the sustainability of concrete is subject of growing scrutiny. Production of Portland cement relies heavily upon phase reactions occurring at elevated temperatures in a rotary kiln [178]. This key step accounts for the bulk of energy use and carbon emissions associated with production of cement [179]. Decomposition of limestone at elevated temperatures is another major cause of carbon emissions during Portland cement production [180]. Close to 5% of energy use, 10% of anthropogenic CO_2 emissions and 30 billion tons/year consumption of valuable natural resources worldwide are associated with production of Portland cement [177, 181]. Lowering the carbon footprint and energy content of cement and concrete, and increased use of market-limited industrial wastes in their production have emerged as key priorities of the cement and concrete industries [182-185].

Partial replacement of Portland cement with supplementary cementitious materials is a widespread practice with positive impacts on the sustainability of concrete production [186]. Coal fly ash is by far the most widely used supplementary cementitious material, followed by

ground granulated blast furnace slag and natural pozzolans [187]. In addition, silica fume, metakaolin and rice husk ash have found applications in high-performance concrete [188, 189].

The alkaline environment of concrete and the prevalence of calcium hydroxide among cement hydrates have inspired efforts towards chemical binding of carbon dioxide during concrete production [1-3]. These efforts [190] have laid the technological basis for launching commercial activities. The focus of these activities is on energy-efficient acceleration of the curing of concrete products via carbonation reactions; these reactions chemically bind carbon dioxide into the cementitious binder of concrete [191, 192]. Existing methods of using carbon dioxide towards accelerated curing of concrete, however, employ CO_2 delivery methods with some inherent technical and economic drawbacks [193, 194] which limit their commercial prospects. Existing methods of CO_2 sequestration into concrete lower the alkalinity of the concrete pore solution [195], which compromises the long-term stability of cement hydrates [196] and their ability to effectively protect the steel reinforcement in concrete against corrosion [197]. The methods adopted for delivering of CO_2 to concrete require capital investment refurbish the concrete production facilities, limit the effective depth of carbonation reactions, and are viable only for the niche dry-cast segment of the precast concrete production [198, 199]. Minor efforts have been devoted to the delivery of CO_2 in liquid form to concrete [200]. Technical and cost constraints limit the resulting concentration of the chemically bound CO_2 in concrete to levels that minimize any value realized in terms of CO_2 sequestration or improvement of concrete properties.

Carbon capture and storage is considered by many to be a crucial component of any U.S. strategy for addressing the climate change problem [201]. The approach developed in the work reported

herein enables value-added and large-volume use of carbon dioxide as a raw material in production of cement. This approach can selectively capture carbon dioxide directly from combustion emissions. Storage of carbon dioxide in geologic formations [202], and its permanent binding into some abundant minerals via carbonation reactions [203] have been subject of major research and development efforts. [204, 205]. Extensive research has been conducted on mineral carbonation where the emphasis is on chemical binding of carbon dioxide into some abundant minerals [203, 206-210].

Mechanical activation (via milling) of certain silicates and complex oxides in the presence of carbon dioxide has been found to induce penetration of carbon dioxide into the structurally perturbed silicate (oxide) matrices in the form of distorted carbonate groups [211-218]. This mechanism of forming carbonate-containing glassy phases is closely related to the formation of structural defects and plastic flow. The accelerated transport of carbon dioxide into the volume of particles is likely facilitated by the deformation mixing of the system components at molecular level, and diffusion along crystalline boundaries. The density of the network of boundaries increases with increasing duration of milling in the presence of carbon dioxide [216].

This investigation evaluated the potential for integration of carbon dioxide into an alkali aluminosilicate cement. The new cement chemistry embodies reactive carbonates and abundant aluminosilicates which undergo synergistic hydration and carbonation reactions upon addition of water to yield a high-performance inorganic binder for concrete production and other applications.

7.2 Materials and Methods

7.2.1 Materials

The materials used in this investigation were ground granulated blast furnace (GGBF) slag, which was used as aluminosilicate precursor. In addition, sodium hydroxide powders and calcium oxide were used as sources of alkali metal. These raw materials used for production of cement and simultaneous capture of carbon dioxide are introduced in the following.

The GGBF slag used in this study is iron slag powder (Nucem100) obtained from Lafarge cement. The slag has a specific gravity of 2.90 and bulk density of 1,225 kg/m^3. The chemical composition of the slag, given in Table 21, was determined by x-ray fluorescence (XRF) spectroscopy. The silicon and calcium oxides constitute about 75% of the total mass, and the weight ratio of silicon to calcium oxide is about 1. Low amounts (les s than 1 wt.%) of alkalis are also present; the loss on ignition of the slag is 0.2%. It should be emphasized that the slag used here was received in milled condition. Sodium hydroxide (NaOH) and calcium oxide were purchased in powder form with 97%-98% purity from Sigma Aldrich. The particle size distribution of the as-received slag is presented in Figure 1.

Table 21. Chemical composition of the GGBF slag.

Oxide Formula	SiO_2	Al_2O_3	Fe_2O_3	CaO	MgO	Na_2O	K_2O	LOI
Mass Percentage	37.53	9.54	0.47	40.78	10.85	0.25	0.45	0.2

Granite aggregate with 8.5 mm maximum size was used as coarse aggregate; this selection minimizes the introduction of carbonates by coarse aggregates. Natural sand was used as fine aggregate. The fineness modulus of the blend of coarse and fine aggregates was 4.3. The particle size distributions of the coarse and fine aggregates are presented in Figure 69.

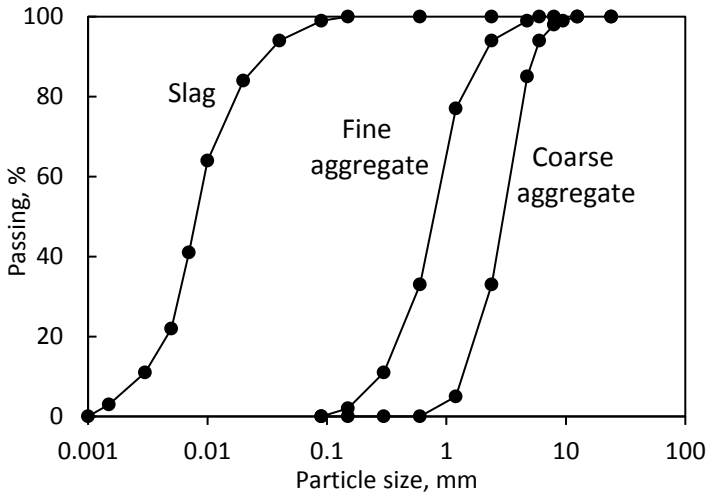

Figure 69. Particle size distributions of the as-received slag powder, and the coarse and fine aggregates used in the project.

7.2.2 Methods

The raw materials introduced above were processed via milling in both air and in CO_2 environment at room temperature and atmospheric pressure to produce a hydraulic cement.

The hydraulic cements considered in this investigation were formulated ground granulated blast furnace slag. The formulation comprised slag: quick lime: NaOH 80: 16: 4 weight ratios. This blend was selected, via trial experimental studies, to produce a desired balance of strength, set time and moisture stability. The mechanochemical effects [47] were relied upon to incorporate carbon dioxide into the hydraulic cement particles. The simultaneous transformation of raw materials into hydraulic cement and capture of carbon dioxide was accomplished by milling of the blend of raw materials in a carbon dioxide environment over a period of two hours at room temperature and atmospheric pressure.

The captured CO_2 was in the cement particles evaluated using Fourier Transform Infrared (FTIR) Spectroscopy, Thermogravimetric Analysis (TGA) and X-ray diffraction (XRD).

FTIR spectroscopy was carried out using a JASCO FTIR Spectrophotometer. The wavenumber considered covered the range of 400 to 4000 cm^{-1}. The spectra were recorded after 50 scans with a spectral resolution of 4 cm^{-1}. Specimens (made with Potassium bromide) were pressed directly against the diamond crystal. FTIR spectroscopy was used to assess the presence of bonds associated with the chemically reacted or physically adsorbed carbon dioxide in the mechanochemically processed hydraulic cement.

Thermogravimetric analyses were conducted using a Perkin Elmer TGA 4000 at a heating rate of 15˚C/min from 50 to 950^{o}C in a nitrogen atmosphere. The difference in the carbonate peak between cement processed in air and in CO_2 was used to quantify the CO_2 uptake.

The mineralogy of the hydraulic cement and its hydrates were assessed using the x-ray diffraction (XRD) technique. A Bruker D8 diffractometer equipped with Cu x-ray radiation operating at 40 kV and 40 mA was used for XRD analysis. Peak intensities were obtained by counting with the Lynxeye detector every 0.05^{o} 2θ /min; the test was carried out at a reflection angle range of 2θ =10−80°. The degree of crystallinity was determined using the EVA software; it was calculated as the ratio of the area under all peaks to the total area under the curve. ^{13}C NMR spectra for cement paste were collected on a 400 MHz Bruker Advance spectrometer using a Chemagnetics probe configured for 7.5 mm (o.d.) rotors. Samples were spun at 3 kHz, and the spectra were collected for 4000 (air) and 7000 (CO_2) acquisitions using a pulse delay of 20 s and a pulse sequence designed to suppress most of the background signal from the probe housing. Scanning electron microscopic (SEM) observations and energy dispersive X-rays spectroscopy (EDX) were used to analyze the hydraulic cement pastes at 28 days of age. A JEOL JSM-6610LV scanning electron microscope was used in this investigation. Unpolished specimens were coated with a 20-nm thick

platinum layer in an Emscope sputter coater Model Sc-500 purged with Argon gas. Vickers microhardness tests were conducted to measure the microhardness of hydrated cement paste. Microhardness testing was carried out on cement pastes at 28 days of age; these pastes were prepared with hydraulic cements cured in air or in CO_2. Ten measurements were made for each sample with 625 mm^2 area and 5 mm thickness. The Microhardness test procedure (ASTM E384) specifies a range of light loads, one of which would be applied on a diamond indenter to make an indentation which is measured and converted to a hardness value. A load of 20 N was applied in this investigation for 15 seconds before taking the reading. Figure 70 shows a typical impression made on the paste surface in this test.

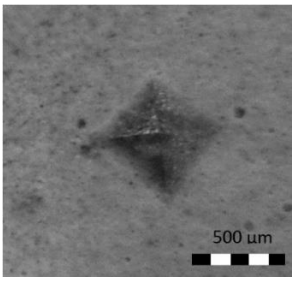

Figure 70. A typical impresion made on the cement paste surface in the Vickers hardness test.

The hydraulic cement was also used to produce concrete specimens for compressive strength testing. A 20 Quart planetary mixer (Hobart A-200) was used to prepare concrete mixtures; the concrete mix design is presented in Table 22.

Table 22. The hydraulic cement concrete mix design.

Material	Quantity, kg/m3
cement	400
Fine aggregate	810
Coarse Aggregate	1125
Water (w/c 0.45)	180

7.3 Results and Discussion

7.3.1 Cement Characteristics

7.3.1.1 Fourier Transform Infrared (FTIR) Spectroscopy

Figure 71 compares FTIR spectra of the cements processed mechanochemically in air and in CO_2. The cement processed in CO_2 exhibited an intense carbonate peak near 1409 cm^{-1}, corresponding to the stretching mode of the CO_3^{2-} group [219]. A new band also appeared around 895 cm^{-1}, corresponding to the out-of-plane bending of CO_3^{2-} group in aragonite [220]. Another small peak around 2370 cm^{-1} appeared when processing of cement was performed in CO_2, which points at the formation of new carbonates.

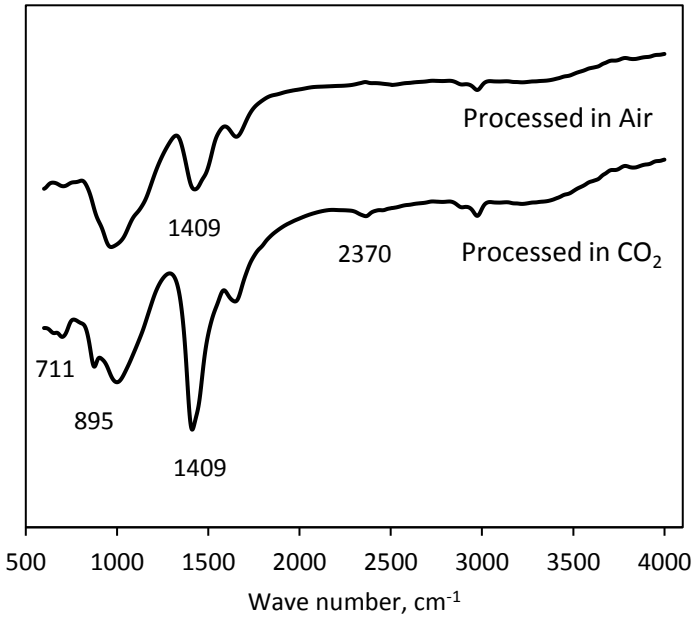

Figure 71. FTIR spectra for the cement processed in air and in CO_2.

7.3.1.2 Thermogravimetric Analysis

Figure 72 presents the TGA/DTA test results for cements processed in air and in CO_2. A mass loss was observed to occur within the 50-200°C range, which corresponds to the loss of moisture.

Relatively low rates of mass loss were observed between 200 and 500°C for both cements, with a DTA peak at 400°C corresponding to the decomposition of calcium hydroxide [221]; this peak was observed to be more pronounced in the cement processed in air, pointing at the stronger presence of Portlandite. The rate of mass loss after 500°C increased notably for the cement processed in CO_2 when compared with the cement processed in air. Carbonates generally decompose within the 500-950°C temperature range [222]. Therefore, mass loss within this range was used to estimate the CO_2 uptake when processing of cement was performed in carbon dioxide. The cement processed in air experienced a mass loss of 1 wt.% while the cement processed in CO_2 experienced a mass loss of 4% within the 500-950°C temperature range. Therefore, the net CO_2 uptake associated with processing in carbon dioxide can be estimated at 3 wt.%.

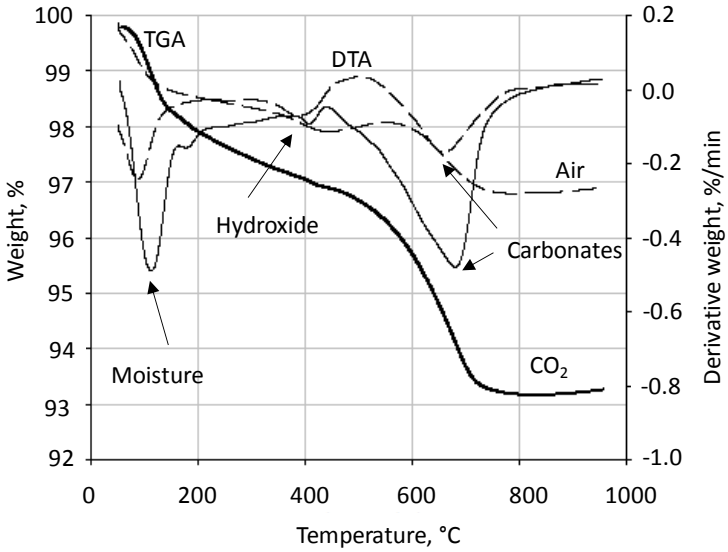

Figure 72. TGA/DTA test results for cements processed in air and in CO_2

7.3.1.3 X-Ray Diffraction

Figure 73 presents the XRD spectra for the slag-based hydraulic cement formulation processed in air and in CO_2. Both spectra point at the strong presence of Portlandite and lime crystals. In

the case of processing in CO_2, the calcite peak observed at 2θ=29° was more pronounced. The degree of crystallinity increased slightly from 44% to 46% when processing was performed in CO_2 (versus in air).

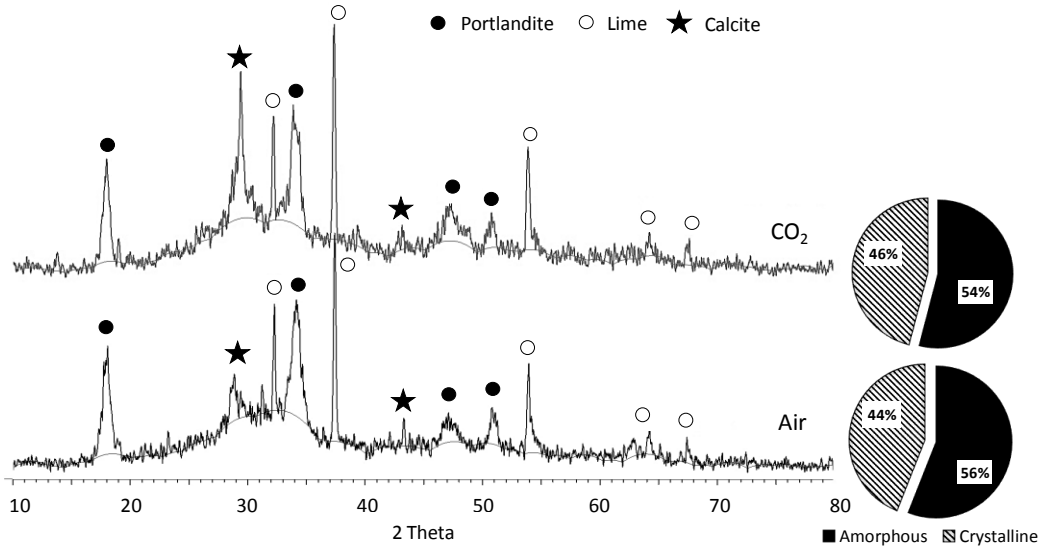

Figure 73. XRD spectra for cements processed in air and in CO_2.

The hypotheses developed to explain the role of CO_2 as a raw material in production of hydraulic cement rely upon a strong presence of metastable carbonates among the amorphous constituents of the hydraulic cement processed via milling in carbon dioxide. In order to test this hypothesis, hydraulic cements milled in CO_2 were heated to facilitate crystallization of amorphous carbonates, which were then identified via XRD spectroscopy. Past experience has indicated that heating amorphous carbonates to 350^oC enables conversion of amorphous carbonates to form crystalline carbonate structures [223]. Figure 74 schematically depicts the stages of amorphous calcium carbonate (ACC) dehydration and Calcite crystallization (left), and a comparison of the scanning electron microscope (SEM) images of amorphous versus crystalline carbonates (right). Figure 75 compares the XRD spectra of the hydraulic cement processed via milling in CO_2 prior to and after heating to 350^oC. After heating, the calcite peak got more

pronounced and sharper at 2θ=30°, and other calcite peaks appeared more clearly at 2θ=38° and 49°. The degree of crystallinity increased from 46% to 57% upon heating. These findings provide critical support for the hypothesis that the mechanochemical effects associated with processing of hydraulic cement via milling in CO_2 incorporate carbon dioxide as metastable carbonates into the amorphous constituents of the resultant hydraulic cement.

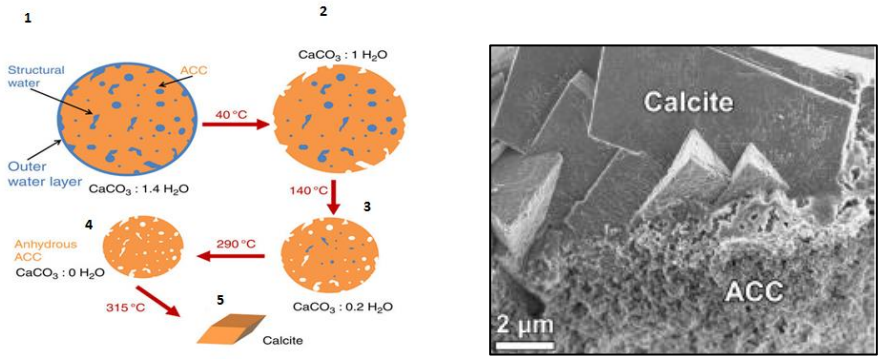

Figure 74. Schematic depiction of the stages involved in amorphous calcium carbonate (ACC) dehydration and crystallization for form calcite with temperature rise.

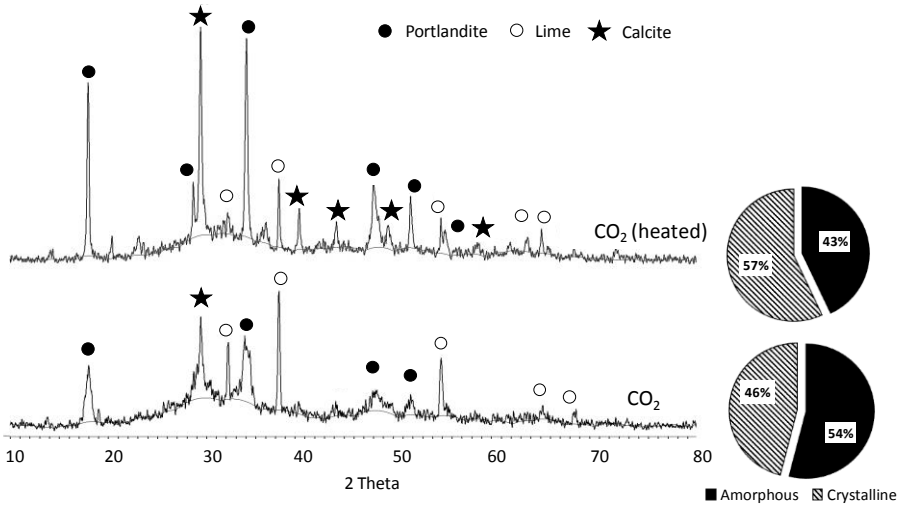

Figure 75. XRD spectra for the hydraulic cement processed via milling in CO_2 prior to and after heating to 350°C.

7.3.2 Structures and Properties Obtained After Cements Hydration

7.3.2.1 Compressive Strength

Figure 76 presents the concrete compressive strength test results obtained with the mechanochemically processed hydraulic cements. The concrete prepared with the cement processed in CO_2 produced higher compressive strengths at all ages when compared with that prepared with the cement processed in air. Significant improvement of the compressive strength was noted over time for the cement processed mechanochemically in CO_2. After 28 days of room-temperature curing, the cement processed in air produced less than 10 MPa compressive strength compared with 25 MPa for the cement processed in CO_2.

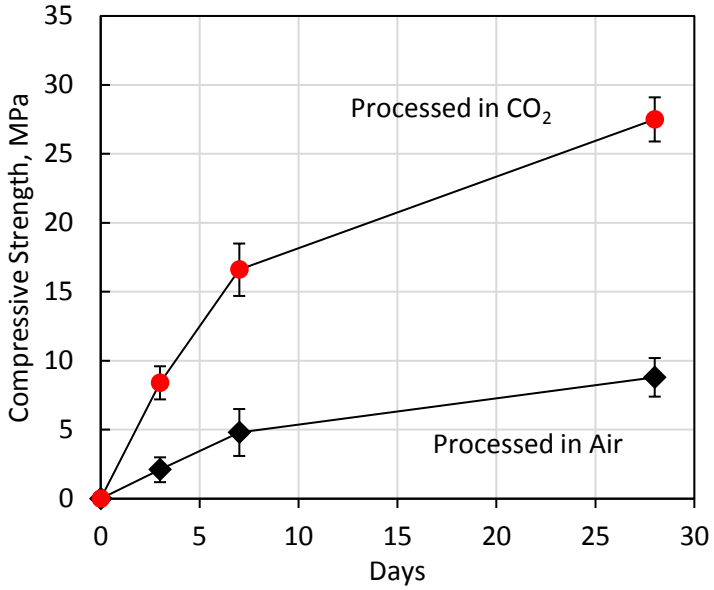

Figure 76. Compressive strength test results for thr concrete specimen prepared with cements processed in air and in CO_2.

7.3.2.2 X-Ray Diffraction

The hypotheses developed to explain the strength development qualities of the concrete prepared with cement processed in CO_2 imply that carbonate anions are released to the solution together with other species from cement particles, and precipitate fine crystalline carbonate

grains parallel with hydration products. The integrated structure comprising fine carbonate crystallites and amorphous hydrates provides the resulting inorganic binder with desired strength, barrier, durability and dimensional stability attributes. In order to test these hypotheses, XRD spectra were produced for hydrated cement pastes prepared with hydraulic cements processed via milling in air versus CO_2. The resulting spectra presented in Figure 77 indicate that the paste made with the cement processed in CO_2 exhibited carbonate peaks such as hydrotalcite at 2θ=12, gaylussite at different angles, and calcite at 2θ=40° and 48°. The paste prepared with the hydraulic cement processed in air, on the other hand, exhibited a strong presence of Portlandite, and a minor peak associated with calcite. These observations support the hypothesis that the hydraulic cement processed in CO_2 has captured carbon dioxide in the form of metastable carbonates that are largely in disordered (amorphous) state. In the course of hydration of cement, these disordered carbonates form carbonate crystallites which benefit the binding qualities of the resultant hydrated cement paste.

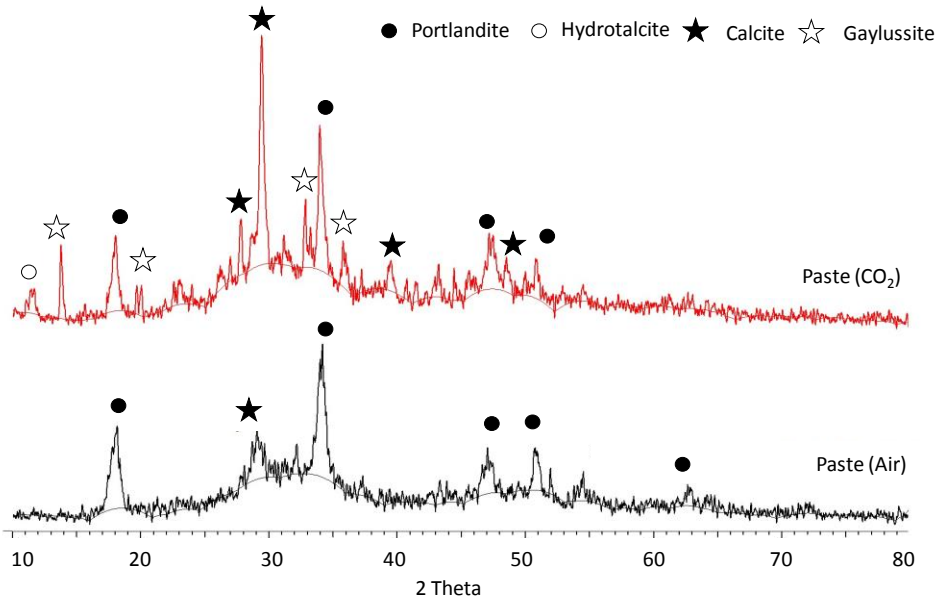

Figure 77. XRD spectra for hydrated cement pastes made with hydraulic cements processed in CO_2 and in air.

7.3.2.3 Microstructure and Hardness

While the XRD spectra of the hydration products of cement processed mechanochemically in CO_2 provide clear indications of the presence of various crystalline carbonates, one cannot identify large crystalline products among cement hydrates. This implies that carbonates exist among hydrates as fine crystallites with high specific surface area and viable binding qualities. The SEM images and the EDX spectrum presented in Figure 78 point at the distributed nature of carbon within cement hydrates. After significant search with the scanning electron microscope, one crystalline carbonate grain could be identified with dimensions of about 2 micrometers, which was well-integrated within the matrix of alkali aluminosilicate hydrates. Otherwise, the crystalline carbonate grains could not be identified, indicating that they are largely of sub-micrometer dimensions.

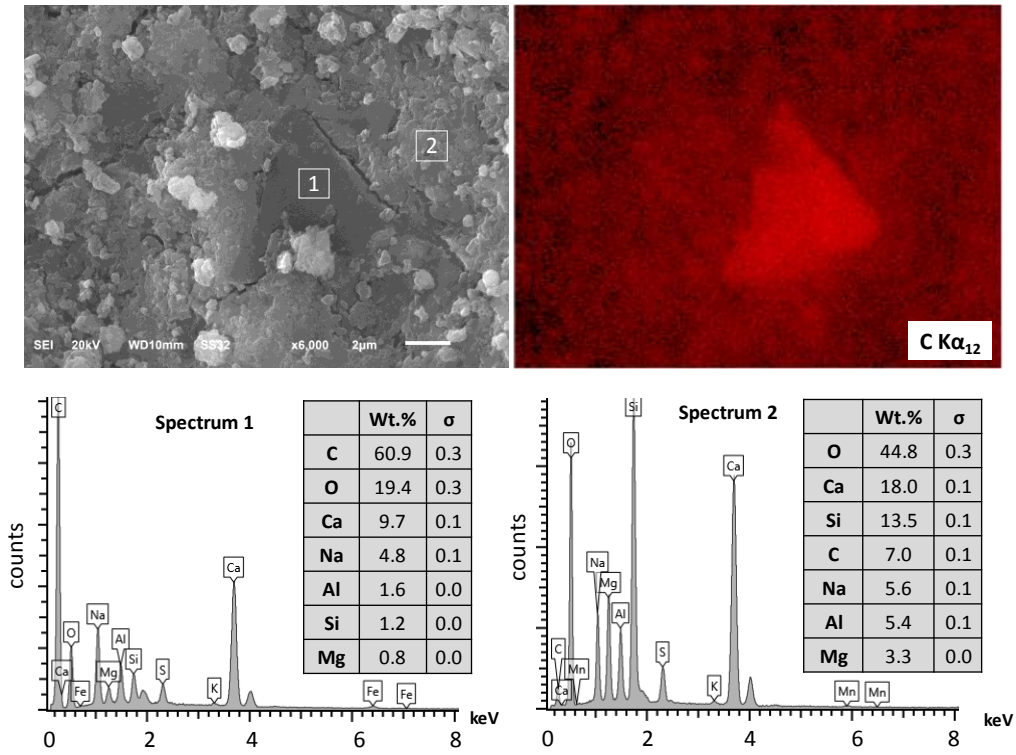

	Wt.%	σ
C	60.9	0.3
O	19.4	0.3
Ca	9.7	0.1
Na	4.8	0.1
Al	1.6	0.0
Si	1.2	0.0
Mg	0.8	0.0

	Wt.%	σ
O	44.8	0.3
Ca	18.0	0.1
Si	13.5	0.1
C	7.0	0.1
Na	5.6	0.1
Al	5.4	0.1
Mg	3.3	0.0

Figure 78. SEM image and an EDX spectrum for the hydrates of the cement processed in CO_2.

The hardness values measured for the pastes prepared with cements processed in and in air and in CO_2 (Table 23) point at the presence of hard carbonates [224] within the relatively soft hydrates. The hardness of the paste prepared with the cement processed in CO_2 was 43% higher than that for the paste prepared with the cement processed in air

Table 23. Vickers hardness test results for pastes prepared with cements processed in air and in CO_2.

	HV, GPa
Paste (Air processed)	0.180
Paste (CO2 Processed)	0.258

7.3.2.4 NMR

Figure 79 shows the ^{13}C NMR spectra obtained for hydrated pastes prepared with cements processed in air and in CO_2. These spectra have been scaled vertically to identical intensity from the PTFE (teflon) background at ~112 ppm to compare the carbonate intensities. The ^{13}C NMR collected for the paste prepared with the cement processed in air did not produce any peak in the carbonate region at ~170 ppm. The paste prepared with the cement processed in CO_2, on the other hand, produced two peaks at 169.3 and 171.5 ppm which probably correspond to calcite and aragonite, respectively [225]. The NMR results provide further support for the presence of carbonates within the hydrated alkali aluminosilicate binders.

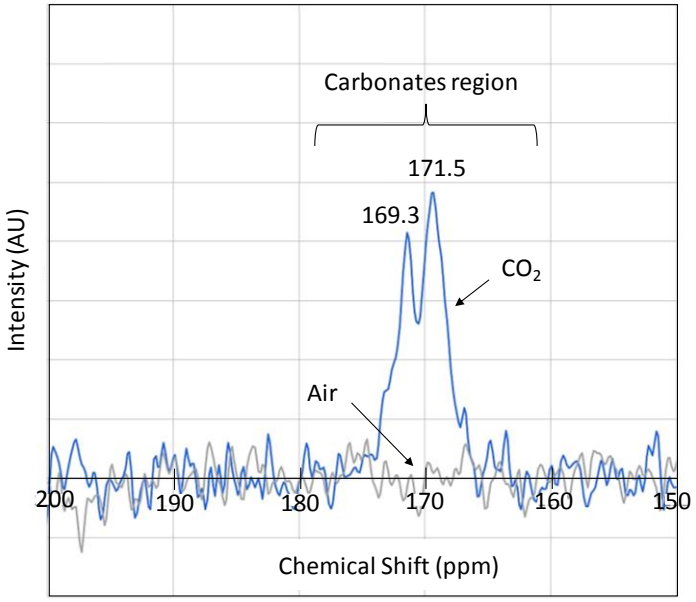

Figure 79.^{13}C Single Pulse (SP) NMR spectra for hydrated pastes prepared with cements processed in air and in CO_2

7.4 Conclusions

Carbon dioxide was integrated into alkali aluminosilicate cement, formulated primary with slag, by input of mechanical energy at ambient temperature and atmospheric pressure. Fundamental investigations were conducted in order to identify the form of captured carbon dioxide in cement. The value offered by carbon dioxide towards enhancing the binding qualities of the resultant cement was investigated. The following conclusions were derived based on the outcomes of this investigation.

- The hydraulic cement formulation with slag processed in CO_2 exhibited FTIR and DTA peaks that pointed at the presence of carbonate complexes. The XRD spectra of this cement, however, did not point at the formation of crystalline carbonates. The combination of FTIR, XRD, TGA and SEM/EDX data generated in the project suggested that the carbon dioxide captured by the hydraulic cement existed largely in a metastable (non-crystalline) state.

- Concrete materials prepared with the hydraulic cement processed in CO_2 had significantly improved engineering properties when compared with those prepared with the cement processed in air. The SEM/EDX, XRD and NMR data generated in this investigation indicated that the non-crystalline (metastable) carbonates formed during processing of the hydraulic cement in CO_2 undergo reactions that form carbonate crystallites which supplement the binding effects of amorphous hydrates. The fine carbonates were found to be well integrated with the alkali aluminosilicate hydrates.

Chapter 8

Scaled-Up Production of an Alkali Aluminosilicate Hydraulic Cement in the Presence of Carbon Dioxide for Concrete Construction

8.1 Introduction

Production of ordinary Portland cement releases close to 1.5 Gt/yr of CO_2, that is approximately 8% of the total anthropogenic CO_2 emissions [28]. This is in spite of the improvements made by the Portland cement industry in enhancing the efficiency of the production process. The projected rise in Portland cement production, from 3.4 Gr in 2015 to about 4.0 Gt by 2050 is expected to raise the percentage of global CO_2 emissions associated with the production of Portland cement [226]. Close to half of the CO_2 emissions in production of Portland cement result from the decomposition of limestone and elevated temperature. This is a defining feature of the Portland cement chemistry, which cannot be resolved by improving the energy-efficiency of its production process. A departure from the established (calcium silicate-based) chemistry of Portland cement would be needed in order to make qualitative gains towards reduction of the carbon footprint (and energy content) of the hydraulic cements used for concrete production [227]. An alternative hydraulic cement based on sodium/calcium aluminosilicate chemistry, which has abundant natural counterparts, provides a viable basis for development of sustainable hydraulic cements of high performance characteristics [171, 228-230]. This chemistry, however, has produced solid binders via heat treatment of a blend of alkaline solutions and aluminosilicate precursors [12, 14]. Further investigations are needed to develop hydraulic cements based on this chemistry, which can cure in a solid binder at room temperature after simple mixing with water.

The work reported herein is an extension of laboratory investigations undertaken by the authors towards development of a hydraulic cement based on sodium/calcium aluminosilicate chemistry [80, 155, 231]. The objective of this work is to demonstrate the scalability of the production process of this hydraulic cement, and its compatibility with industrial-scale methods of concrete production and field construction methods. Scale-up of the hydraulic cement production process was based on equivalency of energy input in laboratory- and pilot-scale production methods. The data generated at pilot scale was used to assess the competitive sustainability merits of the new class of hydraulic cements versus Portland cement.

8.2 Materials and methods

8.2.1 Materials

The approach adopted in the project involves mechanochemical processing of aluminosilicate precursors in the presence of sodium/calcium compounds and carbon dioxide to produce a hydraulic cement. This process induces physicochemical effects in a solid-gas medium [47]. The input of mechanical energy to the blend of solid raw materials in the presence of combustion emissions can be accomplished via ball-milling. The raw materials and processing conditions of the alkali aluminosilicate cement have been introduced in the previous work of the same authors [82]. The aluminosilicate precursors used in in this investigation were coal fly ash, ground granulated blast furnace slag, and albite. The (dry) alkalis used as raw materials in mechanochemical processing of the hydraulic cement were sodium hydroxide, sodium silicate, and calcium oxide. Sodium tetra-borate (Borax) was also added to the raw materials formulation in order to raise the set time of the resulting hydraulic cement.

Concrete materials were produced with crushed limestone of 19.5 mm maximum particle size as coarse aggregate, and natural size with 4.75 mm maximum particle size as fine aggregate. The particle size distributions of the alkali aluminosilicate cement, coarse and fine aggregates, and the standard silica sand are presented in Figure 80. Coarse and fine aggregates were used in oven-dried condition.

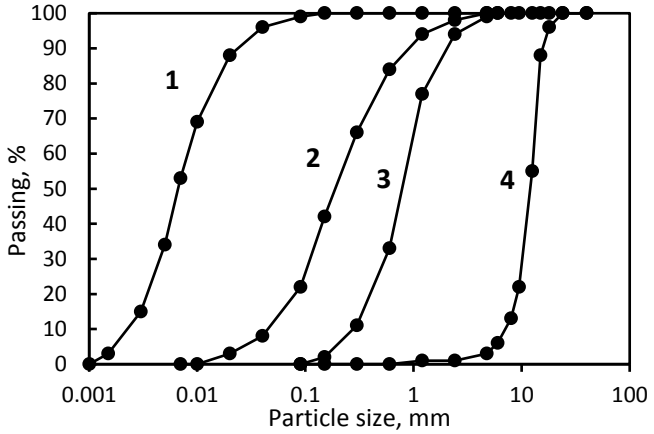

Figure 80. Particle size distributions of the alkali aluminosilicate cement (1), coarse (4) and fine (3) aggregates, and the standard silica sand (2) used in this investigation.

8.2.2 Methods

Pilot-scale production of the hydraulic cement was launched after successful production and characterization of the cement at laboratory scale. This cement was shown to meet the ASTM C1157 requirements for 'General Use' hydraulic cement [82]. The purpose of the pilot-scale studies reported herein was to verify the scalability of the production process of the hydraulic cement. The pilot-scale production process was designed to input similar energy as the laboratory-scale production process. The hydraulic cements produced at pilot scale was used for industrial-scale production of concrete materials that were used in a field construction project. The pilot-scale production conditions of the hydraulic cement also provided a basis for estimation of its carbon footprint, energy content and cost.

8.2.2.1 Pilot-Scale Production of The Hydraulic Cement

A pilot-scale ball mill was installed in the T.B. Simon power plant located in mid-Michigan (Figure 81a). The pilot-scale mill had a diameter of 610 mm diameter and a length of 914 mm, providing a total volume of 255 liter (compared to the 5.6-liter capacity of the laboratory-scale ball mill used in earlier investigations). The T.B. Simon power plant combusts natural gas for power generation; the concentration of CO_2 gas in its combustion emissions is close to 7% (that is notably lower than that in coal combustion emissions [232]). Carbon dioxide is used as a raw material in the production process of the hydraulic cement.

Arrangements were made in the power plant in order to divert a fraction of the combustion emissions from the stack to run through the pilot-scale ball mill at a flow rate of 20-30 CFM. The emission reached room temperature as it flew through the piping (Figure 81b) to reach the mill. Otherwise, the emission was not treated; mechanochemical processing of raw materials was relied upon to selectively capture carbon dioxide from the combustion emission. After stripping of the emission from carbon dioxide in the mill, the resultant gas was returned to the stack for emission to the atmosphere.

The pilot-scale ball mill installed in the power plant is shown in Figure 81c. The ball mill used steel balls ranging in diameter from 9 to 50 mm, and the weight ratio of steel balls to raw materials was 10. Thermocouples were installed inside the mill and on its exterior wall in order to monitor its temperature during the milling process.

The effects of the pilot-scale milling duration were investigated; samples were obtained from the mill after 30, 60, 120 and 240 minutes for experimental evaluation of the hydraulic cement. The

cement was characterized using FTIR, TGA, laser particle size analysis techniques, pH, total dissolved solids and compressive strength development.

FTIR spectroscopy was carried out using a JASCO FTIR Spectrophotometer. The wavenumber ranges considered covered 400 cm^{-1} to 3000 cm^{-1}.

Thermogravimetric analysis was performed to evaluate the CO_2 uptake using a Perkin Elmer TGA 4000 at a heating rate of 15˚C/min from 50 to 950oC under nitrogen atmosphere. Particle size distribution of the cement was evaluated using a Horiba laser LA-920 laser particle size analyzer. The pH and total dissolved solids (TDS) were evaluated by adding the cement to deionized water at 1% concentration by mass in a vial, and placing the solution on shaking table for 1 hour. A pH meter (ORION STAR A215) was used to determine the pH and TDS of solutions.

Compressive strength tests were performed per ASTM C109 on 50-mm cubic mortar specimens after 1, 3, 7 and 28 days of curing in sealed condition (>95% relative humidity) at room temperature. These mortar mixtures were prepared with the standard silica sand at a silica sand/cement weight ratio of 2.75. Three specimens were tested, and the average value of compressive strength was recorded. The water-to-cement ratio of mortar mixtures was adjusted to produce a fresh mix flow of 110 ± 5% per ASTM C1437.

(a) T.B. Simon power plant

(b) Piping of emissions

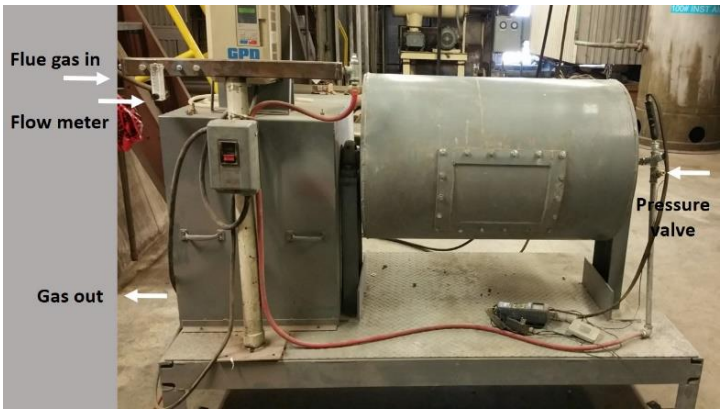

(c) Pilot-scale ball mill

Figure 81. Pilot-scale implementation of the technology in the T.B. Simon power plant in mid-Michigan.

8.2.2.2 Theoretical Considerations in Scale-Up of The Mechanochemical Process

Ball-mills are used commonly for the purpose of size reduction of minerals (including hydraulic cements); the same mills can be used to render mechanochemical effects. In addition, ball-mills can be modified easily at low cost to allow for flow of combustion emissions (or other gases) during milling. Ball-mills subject the material to impact and frictional forces produced by the tumbling steel or ceramic balls. The ball charge is typically close to 30 vol.% of the mill [233].

Most ball-mill chambers have smaller diameters than lengths; typical length-to-diameter (aspect) ratios range from 1.5 to 2.5. Industrial-scale ball-mills have even higher aspect ratios, and are operated in a continuous manner where the feed is input to the chamber continuously, and a separated (operated using air flow) is used to remove particles that are finer than a set size from the chamber. Ball-mills are used commonly in production of Portland cement, noting that high-temperature processing (in a rotary kiln) is the primary step in transforming the raw materials into Portland cement (clinker). Ball-milling is used in the process for size reduction in order to raise the specific surface area of Portland cement for more thorough and timely interactions with water molecules.

The background work of authors validated the process of concurrently capturing carbon dioxide from combustion emissions and transforming the raw materials into a high-performance hydraulic cement using a laboratory-scale ball mill with a chamber of 203 mm diameter and 280 mm length. The pilot-scale mill employed for scaled-up implementation of the technology had a diameter of 610 mm and length of 914 mm.

Depending on speed and other factors, the movement of balls within jar during the ball-mill operation can be sliding (Figure 82a), cascading (Figure 82b), or centrifugal (Figure 82c). In the approach adopted here, the ball-mill operation conditions were selected to produce a cascading movement of balls. The critical rotational speed of the jar that is just adequate to centrifuge the balls away from the pile without cascading is dependent mainly on the jar diameter, and can be calculated using the following equation; the optimum rotational speed of a jar ranges from 65% to 82% of the critical speed [24].

$$\mathrm{n_c} = \frac{42.3}{\sqrt{Dm}}$$

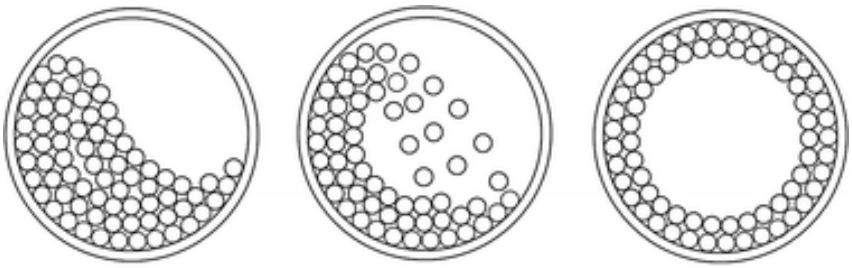

(a) Sliding (b) Cascading (c) Centrifugal (rotating)

Figure 82. Sliding, cascading and centrifugal movements of balls in a ball mill operated at different speeds.

The theory used for scale-up of the milling process from laboratory- to pilot-scale seeks to input similar mechanical energies to the blend of raw materials. In this theory, scale-up of the horizontal ball-mills was accomplished by producing similar instantaneously applied and cumulative mechanical energies. The impact energy, Ei, applied by a contacting ball was calculated as:

$$Ei = \frac{1}{2}mv^2$$

where, *v* represents the relative velocity of the ball at the moment when it comes into contact with another ball or the drum wall (Figure 83). The impact energy generated within a certain time interval has a statistical distribution which depends upon the size and operating conditions of the mill. The impact energy per unit time, i.e. the power P, is defined as the total kinetic energy of the contacting balls per unit time. It can be calculated for all balls considering the average number of contacts (k) per unit time:

$$P = \sum_{0}^{k} Ei = \sum_{0}^{k} \frac{1}{2}\, mv^2$$

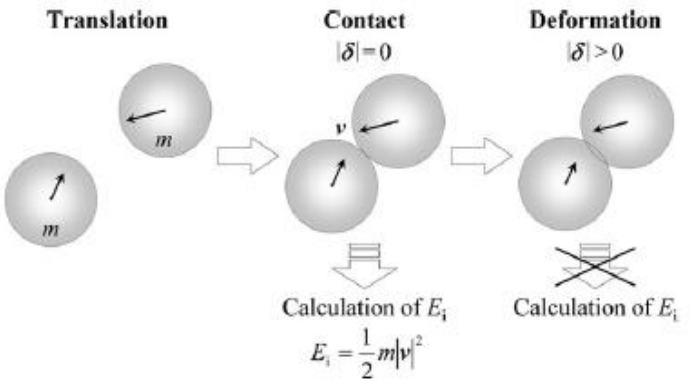

Figure 83. Collision of balls and the resultant impact energy.

In scale-up of the ball-milling process, the products obtained in the larger-sized mill should have the same properties as those obtained in the smaller-sized (laboratory-scale) mill. In order to meet this requirement, the amount of the impact energy applied to the raw materials per unit mass, that is the specific energy, should be the same in both larger and smaller mills. The specific energy depends on a number of parameters, including the input power and the milling time. Analysis of the impact energy distribution would allow for calculation of power, based on which the operation conditions of the larger-sized mill can be determined based on those used with the smaller-sized (laboratory-scale) mill. These considerations yield the following equation for calculating the ratio of the milling durations (t/t_0) in terms of the inverses of their relative rotational speeds with respect to their corresponding critical speeds (N_0/N), chamber depth-to-diameter ratio (β_0/β), ratio of the raw materials volume to the chamber capacity, and ratio of the raw materials in the large mill to the raw materials in the small mill (X):

$$\frac{t}{t_0} = \frac{No}{N}^{1.3} X.\frac{\beta o}{\beta}^{-0.2} \frac{So}{S}^{-1.2}$$

In order to verify the above theoretical findings, the energy transferred from steel balls to raw materials per unit time was calculated. The following expressions yield the milling energy

transferred per unit time to raw materials (E_p) for the cascading motion of balls [234]; as presented in the following equations:

$$E_{p=\frac{N}{m_p}}$$

$$N = 0.864\ \frac{G}{\phi}\ \sqrt{D\psi^3}\ \left[9(1-K^4) - \frac{16\ \psi^4}{3}\ (1-K^6)\right] kW$$

where, G = weight of balls (kg); D = drum diameter (m); ψ = rotation rate which is the ratio of the drum rotational speed to the critical speed; φ = loading rate of drum which is ball-to-drum volume ratio; k = a parameter relating to the speeding rate and the loading rate; and m_p = weight of raw materials (kg).

8.2.2.3 Concrete Mix Design Considerations

The alkali aluminosilicate cement produced in pilot-scale processing was used to develop a concrete mix design for field evaluation and demonstration. The mix design was developed to achieve a desired balance of water film thickness and paste film thickness for achieving high levels of compressive strength complemented with desired fresh mix workability. In this work, viable ranges of water film thicknesses for achieving desired fresh mix workability and effective binding of aggregates were identified. These criteria provided the basis for development of a systematic approach to design of the alkali aluminosilicate hydraulic cement concrete.

Water plays a lubricating role in fresh concrete. All (cement and aggregate) particles in fresh mix should receive a continuous coating of water. The water film thickness formed on particles is a key factor determining the fresh mix workability [235]. In normal- and high-strength concrete materials, the available water fills the void space between particles, and also forms a continuous

film on the particle surfaces (Figure 84a). An optimum water film thickness should provide adequate workability without excessively separating the particles which would increase porosity and thus lower the compressive strength of the resulting concrete [236-238] .

Given the brittle nature of the cementitious paste, it needs to fully coat the aggregates in order to render binding effects. The paste should fill the void space between fine and coarse aggregates before it can effectively coat the aggregate particles. The excess paste theory views the thickness of the excess paste beyond that required for filling of voids between fine and coarse aggregates (Figure 84b) as a parameter influencing the fresh mix and the hardened material qualities.

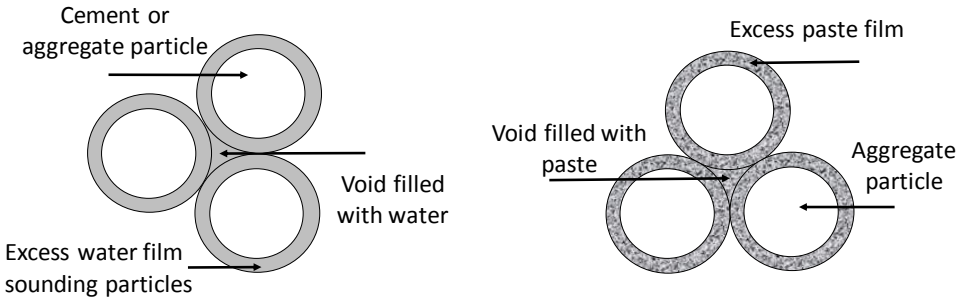

(a) (b)

Figure 84. The excess water film thickness (a), and the excess paste film thickness (b) principles.

The conventional approach to calculation of water film thickness considers the 'excess" water film thickness covering the surfaces of all granular matter, neglecting the amount of water required to fill the voids between granules [128, 239]. For this purpose, the packing density of particles, Φ, needs to be calculated, based on which the voids ratio between the packed particles, μ, can be derived following equation [240]:

$$\mu = \frac{1 - \Phi}{\Phi}$$

The excess water ratio (μ_w'), beyond that required to fill the void space, can thus be calculated as following [241]:

$\mu_w' = \mu_w - \mu$

where, μ_w is the total volume of water divided by the volume of all solid particles. The excess water film thickness, WFT, can then be calculated as following

$$WFT = \frac{\mu w'}{As}$$

where,

$A_s = \sum_{k=1}^{n} R_k . A_k$

where, k refers to each of the n granular solids in the mix, R_k is the volumetric ratio of the k^{th} granular matter, and A_k is the specific surface area of the k^{th} granular matter. Given the energetic preference of water to adsorb onto hydrophilic surfaces, we assumed that water is present only as the film adsorbed on particle surfaces, and does not fill the voids between them. Hence, the water film thickness (WFT) can be calculated as the following equation:

$$WFT = \frac{\mu w}{As}$$

Concrete mixtures were prepared with Portland cement and also with the hydraulic cement produced at pilot scale. The above equations were used to compare with excess water film and paste thickness required with either type of cement.

In concrete mix design, the coarse-to-fine aggregate ratio was kept constant at 55:45 by weight. Water-to-cement ratio was adjusted for each mix to produce the same fresh mix workability characterized by a slump of 100 mm. Different cement contents were considered in order to cover the normal range encountered in common Portland cement concrete mixtures. Concrete mixtures were prepared initially using a rotary drum mixer of 0.035 m^3 capacity. Cylindrical specimens with 75 mm diameter and 150 mm height were cast, cured at room temperature in

sealed condition, and tested at 1, 3, 7 and 28 days of age. The preferred concrete mix design selected based on this laboratory work was then produced at industrial scale in a ready-mixed concrete truck.

8.2.2.4 Field Construction

A total of 630 kg of the cement was produced at pilot scale, and was added to a ready-mixed concrete truck in lieu of Portland cement. Water, and fine and coarse aggregates were batched into the truck using the conventional practices of the ready-mixed concrete plant in industrial-scale production of concrete. The concrete mix proportions used in the field project are presented in Table 24.

Table 24. The alkali aluminosilicate cement concrete mix design.

Material	Quantity, Kg/m^3
Alkali aluminosilicate cement	360
Coarse aggregate	1100
Fine aggregate	910
Water-to-cement ratio	0.45

The ready-mixed concrete truck transported the concrete over a distance of about 10 kilometers, and the alkali aluminosilicate cement concrete was used for construction of a sidewalk. Conventional concrete placement, consolidation and finishing procedures and tools were used for construction of the sidewalk. The fresh mix workability was measured per ASTM C143 slump test method. The initial and final set times were measured following the ASTM C403 penetration test procedure. Cylindrical specimens of 75 mm diameter and 150 mm height were prepared from the concrete prepared in the ready mixed concrete truck, and consolidated via external vibration at medium intensity over 2 minutes. The molded specimens were kept in sealed

condition, demolded after 24 hours, and then kept in sealed (>95% relative humidity) condition at room temperature for performance of compression tests at 1, 3, 7 and 28 days of age.

8.3 Results and Discussion

8.3.1 Pilot-Scale Implementation

8.3.1.1 Mill Temperature

A fraction of the impact temperature during milling transforms into thermal energy, which produces a temperature rise. The recorded values of temperature are presented in Figure 85. The highest temperature reached inside the mill was about 39^{o}C after 4 hours of milling. Temperature rise reportedly improves the mechanochemical reaction rates [242]. The rate of temperature rise was observed to slow down after about two hours of milling. It should be noted that one factor in mechanochemical reactions is the local temperature rise at contact points, which is expected to be far greater than the average temperatures recorded here [243].

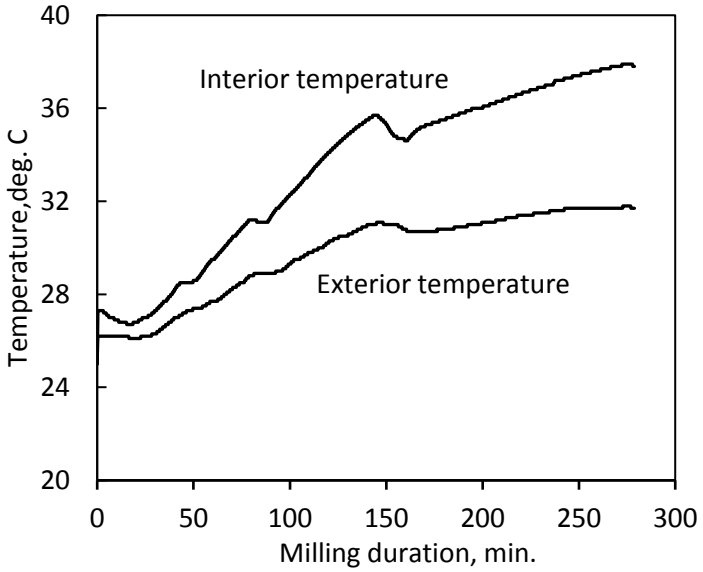

Figure 85. Temperature versus milling duration recorded inside and outside of the pilot-scale mill.

8.3.1.2 Particle Size Analysis

The particle size distributions presented in Figure 86 indicate that continued milling from 30 minutes to 1 hour produced a notable reduction in particle size, with the median particle size decreasing from 10.5 to 7 µm. Longer milling durations beyond 1 hour produced limited change in particle size distribution. The median particle size after 4 hours of milling was 6.5 µm.

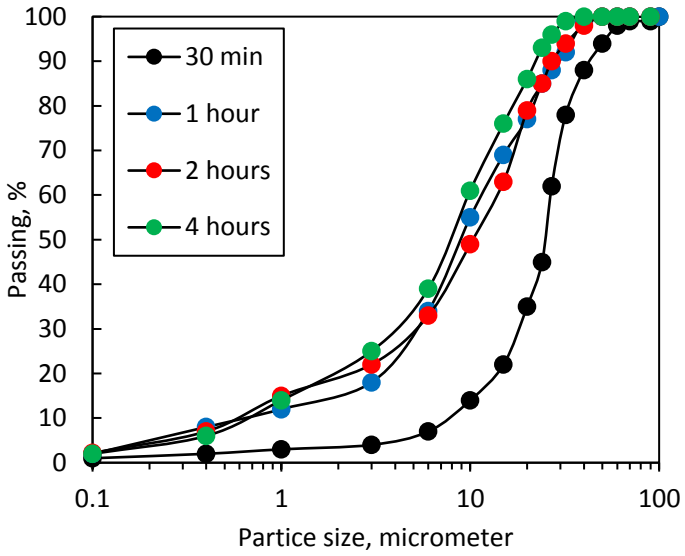

Figure 86. Particle size distributions of hydraulic cements produced at pilot scale after different durations of milling in flue gas.

8.3.1.3 CO_2 Uptake

Figure 87 presents the TGA/DTA test data for the hydraulic cement raw materials and the cement produced after 30 min, 1, 2 and 4 hours of at pilot scale. A notable rise in CO_2 uptake is observed as the milling duration increased from 30 minutes to 1 hour. Three main regions of mass loss were observed associated with moisture, hydroxide and carbonate DTA peaks at 160°C, 400°C and 700°C, respectively. Milling the raw materials for 30 minutes was observed to increase the moisture content of the resultant cement; this could be due to the moisture introduced by the flue gas. Increasing the milling duration to 60 minutes reduced the moisture content of the

resultant cement, which could be explained by the partial loss of moisture due to heat rise within the mill. After 4 hours of milling, however, the moisture peak was more intense and occurred at a higher temperature (170°C compared 150°C for raw materials), pointing at the formation of minor hydrates. These hydrates could lower the hydraulic activity of the resultant cement, but benefits its CO_2 uptake. The carbonate peak increased with increasing milling duration, producing a CO_2 uptake of about 3% after 4 hours of milling.

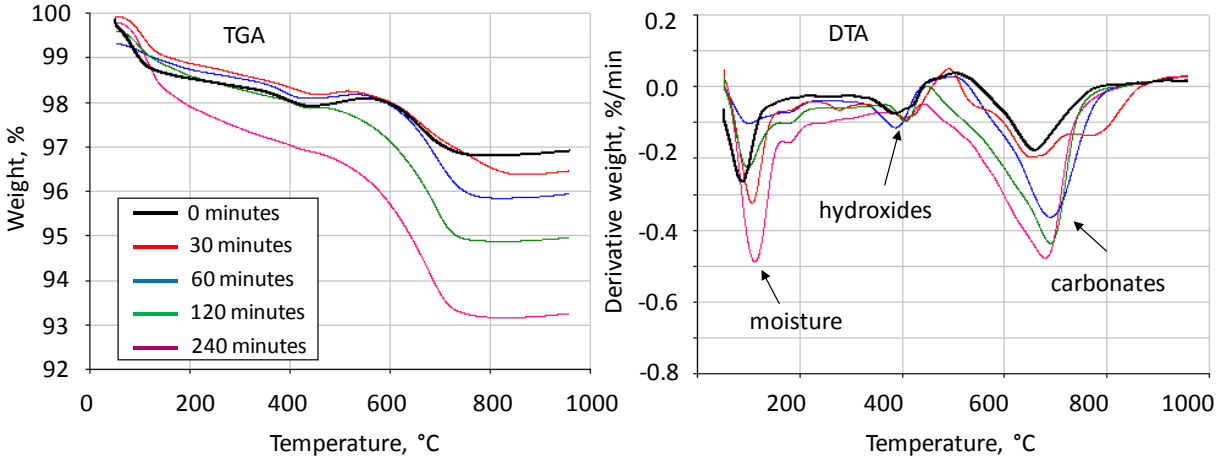

Figure 87. TGA/DTA test data for hydraulic cements produced after different milling durations.

8.3.1.4 FTIR Analysis

Figure 88 compares the FTIR spectra of the hydraulic cement raw materials and the hydraulic cements produced via pilot-scale milled in combustion emissions for different durations. Increasing the milling duration enhances the intensity of the peak at 1414 cm^{-1}, which is a typical carbonate peak. Appearance of new peaks around 720 and 870 cm^{-1} may also point at the presence of carbonates. The FTIR results support the conclusions derived based on the TGA test results as far as the effects of milling duration on the CO_2 uptake are concerned.

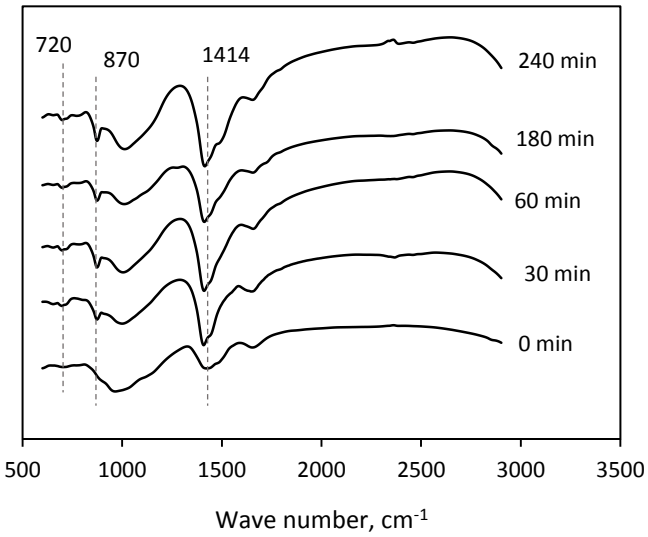

Figure 88. FTIR Spectra of the blend of raw materials (0 min milling) and the hydraulic cements produced via pilot-scale milling in combustion emissions for different durations.

8.3.1.5 pH and Total Dissolved Solids

Figure 89 presents the effect of the duration of milling in CO_2 on the pH and total dissolved solids (TDS) of the resultant hydraulic cements. Milling of the raw materials in the presence of flue gas for 30 minutes raised both the pH and TDS values. Further milling for 1 hour did not cause any notable change in these values. Continued milling beyond 1 hour actually lowered the pH and TDS values. The initial rise in pH and TDS could be attributed to particle size reduction and the mechanochemical effects which raise the specific surface area and produce soluble/activated compounds. The eventual drop in pH and TDS could be attributed to the CO_2 capture which lowers the pH value, and the consequent formation of insoluble carbonates which lowers the TDS value. These observations are in line with those made based on the TGA and FTIR results.

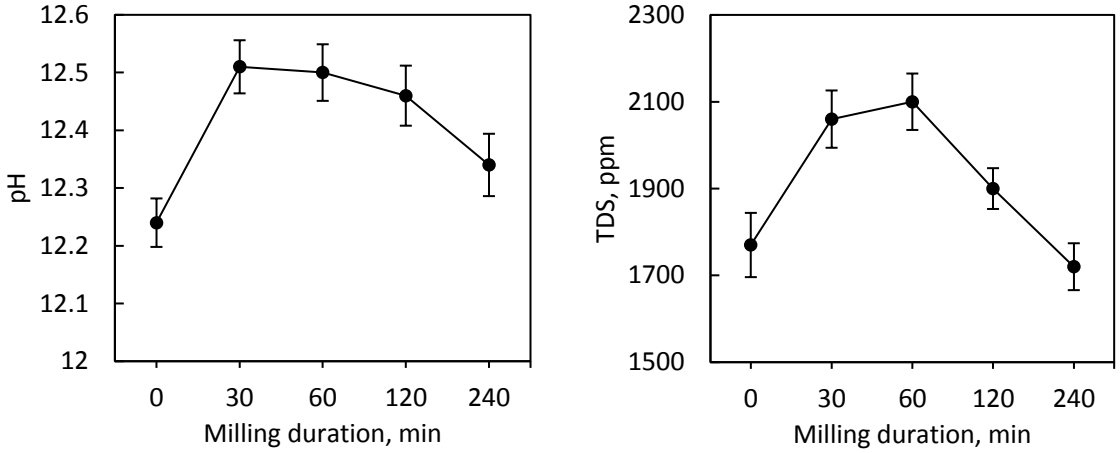

Figure 89. pH and total dissolved solids test results.

8.3.1.6 Mechanical Properties

Figure 90 compares the compressive strength test results for mortar specimens prepared with the cement milled (using the scaled-up mill) for different durations, and with the cement milled for 2 hours using small mill [82]. The cement milled for 30 minutes produced strength levels that are comparable with those produced using the small mill. Increasing the scaled-up milling duration beyond 30 minutes is observed to produce lower compressive strengths. Increasing the milling duration, as noted before, lowered the alkalinity of the resultant cement, which could comprise the hydration reactions that benefit from the higher alkalinity of the solution.

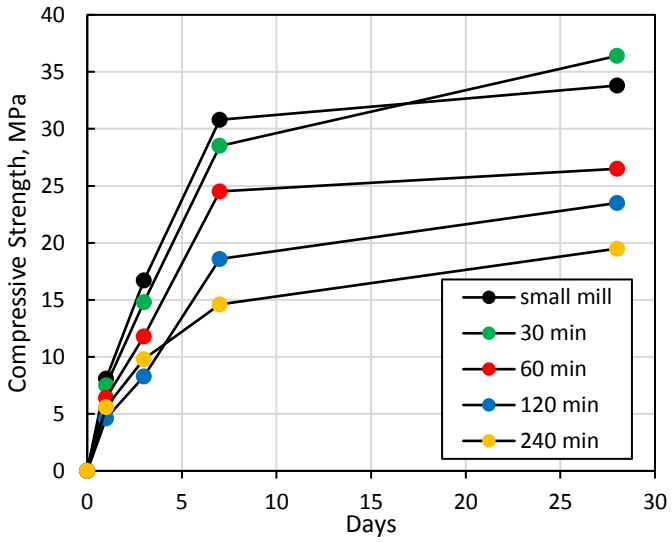

Figure 90. Compressive strength test results obtained with the hydraulic cements processed using the scaled-up mill over different time periods, and using the small mill over 2 hours.

8.3.2 Energy Inputs of Laboratory- and Pilot-scale Millings

The critical and optimum rotational speeds of the laboratory- and pilot-scale mills are presented in Table 25 together with the actual rotational speeds of the mills.

Table 25. Critical, optimum and actual rotational speeds of the laboratory- and pilot-scale ball mills.

Mill	Jar Diameter, m	Critical Speed (n_c), rpm	Optimum Speed (65-85% of n_c), rpm	Test speed (n), rpm
Laboratory-Scale	0.28	86	56-71	57
Pilot-Scale	0.61	54	35-44	40

The depth-to-diameter ratios were 1.2 and 1.5 for the laboratory- and pilot-scales mills, respectively, and the ratio of raw materials in the large mill to those in the small mills was 10 in this investigation. Both mills rotated at about 70% of their critical speeds.

The milling duration established for the laboratory-scale mill based on test data was 120 minutes. This optimum milling duration minimized the input of energy for producing hydraulic cements of

desired quality. Table 26 shows that, considering the theoretical considerations noted above, the pilot-scale mill would input the same amount of energy to raw materials over a milling duration of only 18.2 minutes as the laboratory-scale mill would do over 120 minutes.

Table 26. Milling duration for laboratory and pilot-scale mills required for input of comparable energy to raw materials.

Mill Type	Milling duration, min
Laboratory-Scale	120
Pilot-Scale	18.2

Supporting calculations were done to affirm the equivalency of the mechanical energy input to raw materials in laboratory- and pilot-scale mills using an alternative theory. Table 27 presents the milling parameters and the resulting energy inputs to raw materials per unit time for the laboratory- and pilot-scale ball mills used in this investigation. These results indicate that the energy transferred per unit time from the steel balls to raw materials in the pilot-scale mill is about 5.8 times that in the laboratory-scale mill. This ratio is close to the ratio of the required durations of milling in the laboratory-scale mill to that in pilot-scale mill (6.7) calculated earlier using the original theory. The similarity of these two ratios indicates that the two theories yield similar results.

Table 27. Mill parameters and calculated values of the energy transferred to raw materials per unit time.

Mill Type	Balls weight, kg	Rotation rate, ψ	Loading rate	Energy of balls, N (kW)	Input energy, Ep(J/s.g)
Pilot-Scale	100	0.74	0.087	1037	104
Laboratory-Scale	10	0.58	0.213	18.9	18.9

8.3.3 Mix Design of the Alkali Aluminosilicate Cement Concrete

Concrete mixtures were prepared with different excess water film thicknesses using both Portland cement and the alkali aluminosilicate cement in order to make a comparative assessment of the optimum water film thickness for the two types of cement. Cement content was changed in these mixtures, and the water content was adjusted to produce a targeted slump of 100 mm. Figure 91 compares the visual appearances of the cross-sections of concrete materials made with different alkali aluminosilicate cement contents. At a relatively low cement content, fine aggregates were exposed with minimum paste coating (Figure 91a). A medium cement content produced a dense structure with relatively small aggregate spacing (Figure 91b). With high cement content, the spacing between coarse aggregates was relatively large, which had to be filled with the mortar that is rich in hydrated cement paste (Figure 91c)

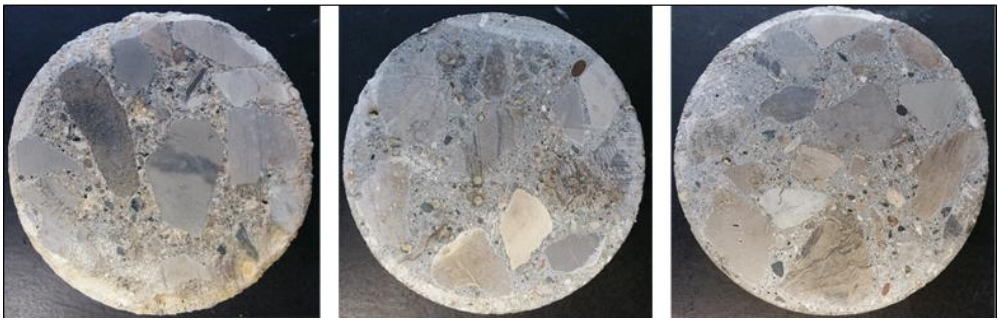

(a) Low cement content (b) medium cement content (c) high cement content

Figure 91. Cross sections of concrete specimens with different of cement contents.

Figure 92 presents the compressive strength test results at 1, 3, 7 and 28 days of age. After 1 day, the concrete prepared with the alkali aluminosilicate cement produced about double the compressive strength of the concrete prepared with Portland cement. The difference between the compressive strengths of the two concrete mixtures decreased with increasing curing time up to 7 days. After 28 days, the alkali aluminosilicate cement concrete again produced notable

improvements in compressive strength when compared with Portland cement concrete of comparable water film thickness. The trends in the effects of water film thickness on compressive strength were similar in Portland and alkali aluminosilicate cement concrete materials. The optimum water film thickness was about 2 micrometers in both cases. These results indicate that the mix design procedures established for Portland cement concrete could be applicable to the alkali aluminosilicate cement concrete, noting that the compressive strength values would be somewhat higher in the case of the alkali aluminosilicate cement concrete.

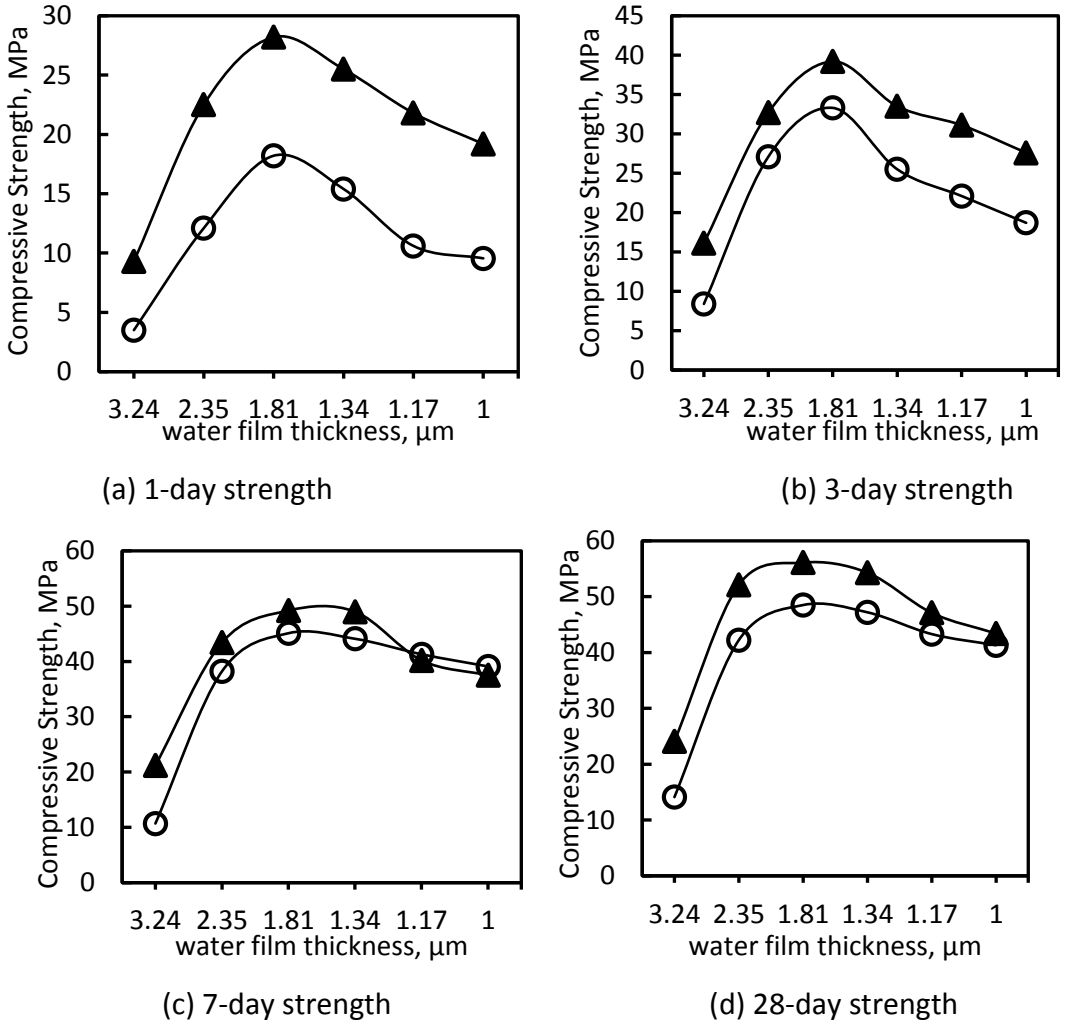

Figure 92. Compressive strength test results for concrete materials prepared with Portland cement (circle) and the alkali aluminosilicate hydraulic cement (triangle).

8.3.4 Field Evaluation and Demonstration

Figure 93 shows the visual appearance of a sample of the alkali aluminosilicate cement, and the method used for addition of the cement to a ready-mixed concrete truck. Figure 94 shows placement and finishing of the alkali aluminosilicate concrete in field.

Figure 93. The visual appearance of the cement, and loading of the cement into the concrete truck.

Figure 94. Placement and finishing of the alkali aluminosilicate cement concrete in field.

The fresh mix slump and the initial set time were measured for the fresh concrete mixture produced at industrial scale (Figure 95). The results presented in Table 28 point at the desired fresh mix workability and set time of the concrete produced with the alkali aluminosilicate cement.

Figure 95. Slump test.

Table 28. Slump and initial set time test results for the concrete produced using industrial facilities with the alkali aluminosilicate cement.

	Slump, inch	Initial set time, min
Measured Value	3.2	54

The compressive strength test results presented in Figure 96 point at successful achievement of relatively high strength levels with the alkali aluminosilicate cement.

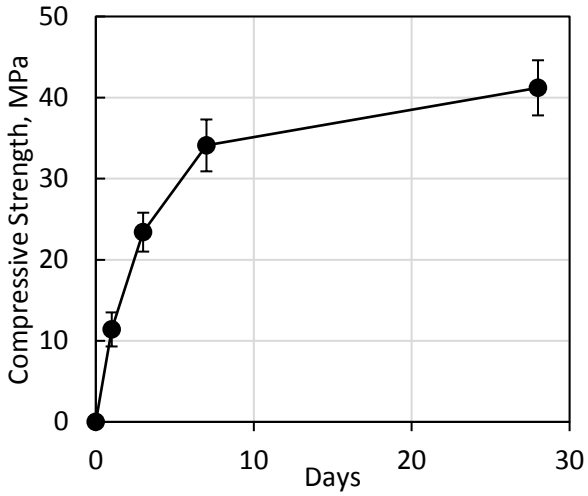

Figure 96. Compressive strength for the specimens taken from the concrete truck.

8.3.5 Competitive Analysis of Cost, Carbon Footprint and Energy Content

A key consideration in this development effort is to produce an end-product (hydraulic cement) that meets application requirements at competitive cost. The carbon footprint and energy content of the resultant hydraulic cement would also influence their market appeal. A desired balance of carbon cost, carbon footprint and energy content would significantly enhance the commercial prospects for the approach to carbon sequestration developed in this project. It is worth mentioning that the chemistry and processing methods adopted in this project are inherently sustainable even with synthetic raw materials [244]. Competitive analyses were conducted on the initial carbon footprint, cost and energy content of the hydraulic cement developed in the project versus Portland cement. These analyses are reviewed in the following.

8.3.5.1 Cost

Initial cost is a primary factor governing successful transition of new technologies to commercial markets. Sustainability advantages and energy savings can benefit commercialization efforts as far as new products do not constitute an initial cost burden (or preferably yield initial cost savings). A comparative cost analysis was conducted on Portland cement versus the new hydraulic binder developed in the project.

Table 29 presents the cost of the raw materials used to prepare the hydraulic cement. Processing (energy) cost is another consideration in evaluating the production cost of hydraulic binders. Energy calculations indicated that 20 minutes of pilot-scale milling produces results that are equivalent to 2 hours of laboratory-scale milling. Ball-milling at pilot scale consumes about 17 kWh of energy (5.67 kW in 20 minutes) per ton of the resultant hydraulic binder. Assuming a

reasonable cost of $0.18 per kWh, the energy costs of producing the hydraulic binder can be calculated at $1.02 per ton.

Table 30 presents the formulation of raw materials and the costs associated with the raw materials and production energy of the hydraulic cement. The total cost of the hydraulic cement makes it competitive against Portland cement. Recent statistical study showed that one tone of Portland cement cost about 111$ in 2016 in the united states (Source: https://www.statista.com/statistics/219339/us-prices-of-cement) where alkali aluminosilicate cement produced in this investigation costs less than $50 per ton.

Table 29. Cost per ton the raw materials used in production of the hydraulic binder complexed with CO_2.

Material	Cost $/ton
Coal fly ash [245]	20
Sodium hydroxide [79]	200
sodium silicate [246]	180 - 250
Granulated blast furnace slag [247]	35
Calcium oxide [248]	90
Albite [249]	50
Borax (set retarder): https://www.alibaba.com/product-detail/Price-sodium-borate-borax-powder-price_1932292319.html	130

Table 30. Costs associated with the raw materials and processing energy of the hydraulic binder.

Ingredient	Quantity, kg/ton of hydraulic binder	Cost ($)
Coal fly ash	450	7.0
Calcium oxide	40	3.6
Blast furnace slag	250	8.75
Sodium silicate	70	15.0
Sodium hydroxide	30	6.0
Albite	150	7.5
Borax	10	1.30
Processing energy	-	1.02
Total		49.67

8.3.5.2 Carbon Footprint

Reduction of CO_2 emissions is an important feature of the hydraulic binder complexed with carbon dioxide that is subject of this development effort. The chemistry of the hydraulic binder that is subject of this development effort, even when processed with synthetic raw materials at elevated temperatures, has a lower carbon footprint than Portland cement [250], noting that close to 0.8 tons of carbon dioxide are emitted to the atmosphere for production of each ton of Portland cement. Figure 97 presents the percent CO_2 emissions associated with the raw materials and production of Portland cement.

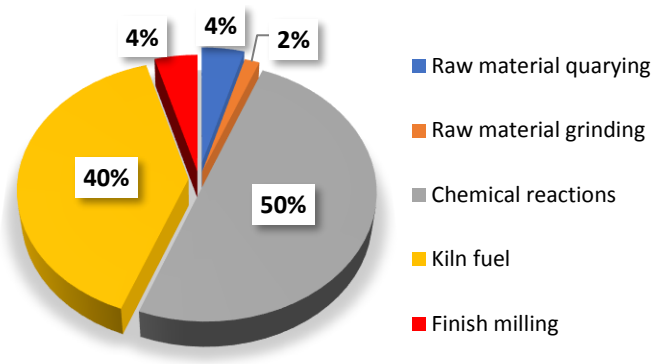

Figure 97. CO_2 emissions associated with production of Portland cement

The hydraulic binder developed in this project is formulated with coal fly ash and slag as the primary raw materials, and is complexed with CO_2 which constitutes another key raw material. The conventional coal ash used in processing of the new hydraulic cement are by-products of power generation. They are not processed synthetically, and thus account for minor CO_2 emissions (and energy use) [251]. Sodium tetra borax was used at 1 wt.% concentration, hence the impacts on the CO_2 and energy were negligible. Table 31 presents the carbon footprint of the raw materials used in the production of the hydraulic binder that is subject of this development effort.

Table 31. Carbon footprints of raw materials.

Material	Kg CO_2 /ton
Sodium hydroxide [252]	500
Sodium silicate [252]	110
Calcium oxide	540
Slag [253]	60
Coal fly ash	-

The CO_2 emissions of slag, an industrial by-product, are associated with its shipment. The 17 kWh energy use in mechanochemical processing of the hydraulic cement translates into 0.6 CO_2

emissions of 0.6 kg of CO_2 emissions [254]. For the required 20 minutes of milling, this energy use translates into 3.4 kg of CO_2 emission per ton of hydraulic cement. Table 32 presents the CO_2 emissions per ton of hydraulic cement associated with its raw materials and processing energy. This hydraulic binder is observed to have a very minor carbon footprint of about 32 kg/ton compared to carbon footprint of about 800 kg per ton for Portland cement [255].

Table 32. Cement ingredients and the CO_2 released

Ingredient	Quantity, kg/tone cement	CO_2, kg
Coal fly ash	450	-
Calcium oxide	40	+21.6
Blast furnace slag	250	+15.0
Sodium silicate	70	+7.7
Sodium hydroxide	30	+15
Mechanochemical processing	-	+3.4
Total CO_2 Released by one ton of cement		+62.7
CO_2 uptake by the hydraulic cement	-	-30
Total		+32.7

8.3.5.3 Energy Content

Manufacturing of Portland cement is an energy-intensive process, accounting for 4 GJ of energy consumption per ton of cement [256]. Figure 98 shows the relative contributions of various steps in manufacturing of cement to the energy content of cement.

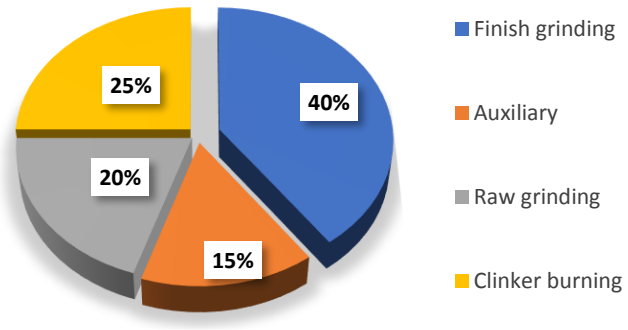

Figure 98. Relative contributions of different processing steps to the energy content of Portland cement [257].

The hydraulic cement processed mechanochemically in flue gas uses aluminosilicates precursors and emissions of fossil fuel combustion emissions as the primary raw materials, without any pretreatment.

Table 33 presents the energy content of the supplementary raw materials used in production of the hydraulic cement. Table 34 presents the cement formulation and the contributions to energy content of raw materials and mechanochemical processing. It was assumed that mechanochemical processing of 1 ton of the hydraulic cement formulated with landfilled ash consumes 17 KWh of energy [254]. Production of 1 ton of the hydraulic cement embodying carbon dioxide is observed to require 1.0 GJ of energy, which is 75% less than the energy required to produce 1 ton of Portland cement.

Table 33. Energy contents of supplementary raw materials.

Material	GJ /ton
Sodium hydroxide [258]	12
Sodium silicate [258]	5.0
Calcium oxide [259]	3.2

Table 34. Cement formulation and the corresponding CO_2

Ingredient	Quantity, kg/ton of cement	Energy, GJ
Coal fly ash	450	-
Calcium oxide	40	0.127
Blast furnace slag	25	-
Sodium silicate	70	0.35
Sodium hydroxide	30	0.36
Mechanochemical processing	-	0.17
Total		1.00

Figure 99 summarizes the differences between Portland cement and the alkali aluminosilicate cement on the cost, energy and carbon dioxide.

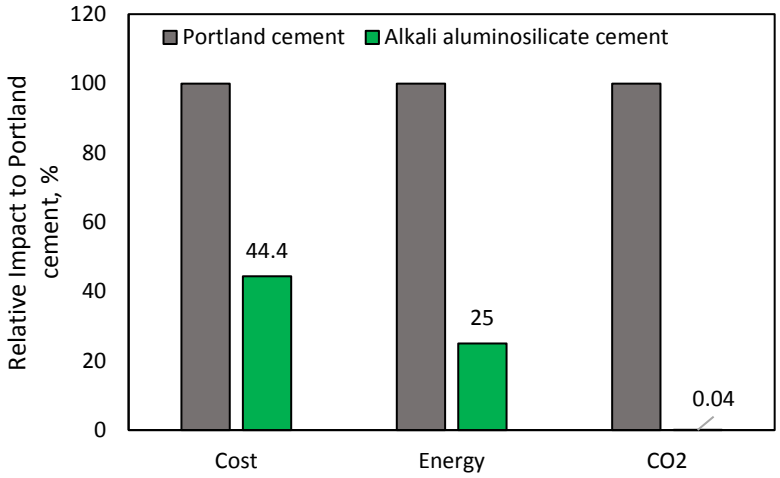

Figure 99. The life-cycle cost, energy and CO_2 associated with one tone of cement (relative to Portland cement)

8.3.5.4 Competitive Life-Cycle Analysis

The alkali aluminosilicate cement concrete developed in the project using mechanochemically processing of aluminosilicate waste/by-product solids complexed with CO_2 is based on a chemically stable binder of 3D networked alkali aluminosilicate hydrates integrated with crystalline carbonates. This inorganic binder provides highly desired barrier qualities and

durability characteristics under weathering and chemical attack as noticed in previous chapters. Table 35 and Figure 100 summarizes the durability attributes of the alkali aluminosilicate hydraulic cement concrete developed in the project against those of Portland cement concrete

Table 35. Barrier and durability characteristics of alkali aluminosilicate cement concrete versus Portland cement concrete.

	Portland cement concrete	Alkali aluminosilicate cement concrete
Sorptivity (initial/secondary) (μm/s$^{1/2}$)	10.1/1.32	2.36/0.2
Residual strength after 28 days of acid attack	77%	93%
Residual mass after 28 days of acid attack	97%	99%
Expansion due to alkali silica reactions (%)	0.033	0.012
Mortar bar expansion (%)	0.0055	0.0033
Autoclave expansion (%)	0.411	0.237

(a) (b) (c)

Figure 100. Visual appearance of concrete specimens after exposing to (a) freeze-thaw cycles, (b) acidic solution and (c) accelerated corrosion test.

Based on the durability test results presented, one can estimate that the service life of the new hydraulic cement concrete is more than 50% greater than that of normal Portland cement concrete in application to infrastructure systems subjected to severe weathering and chemical exposures. Considering an average service life of 50 years for Portland cement concrete-based

infrastructure systems [260], use of alkali aluminosilicate cement concrete in lieu of Portland cement concrete can provide these infrastructure systems with service lives of about 75 years. It is worth mentioning that 50% gain in service life is a conservative estimate compared to those reported in the literature for alkali aluminosilicate-based hydraulic cement concrete materials [261].

The enhanced service life of the alkali aluminosilicate cement concrete structures provides them with favorable life-cycle environmental, cost and energy positions. A 150-year was used for the purpose of life-cycle analysis in this comparative investigation. During this period, infrastructure systems made with alkali aluminosilicate cement concrete (offering 75-year of service life) must be demolished and reconstructed one time. Similar Portland cement concrete infrastructure systems with 50 years of service life, on the other hand, have to be demolished and reconstructed twice during the 150-year period of life-cycle analysis. Therefore, assuming comparable inflation and interest rates, the initial advantages of the alkali aluminosilicate cement concrete over Portland cement concrete would be magnified by 1.5 when viewed from a life-cycle point of view. The initial cost, energy content and carbon footprint of the alkali aluminosilicate cement were found in previous section (considering only the raw materials contributions) to be 55%, 75% and 101%, respectively, less than those of Portland cement concrete.

From a life-cycle point of view, therefore, alkali aluminosilicate cement concrete based on mechanochemically processed aluminosilicates complex with CO_2, offers 85%, 131% and 203% net cost, energy content and carbon emission savings when compared with Portland cement. While these benefits relate only to the raw materials used in concrete, neglecting mixing, transportation and construction impacts, they still reflect the significant life-cycle environmental,

economic and energy benefits that can be realized by market introduction of the new hydraulic cement concrete.

8.4 Conclusions

Mechanochemical production of alkali aluminosilicate cement in carbon dioxide environment was investigated at pilot scale. A comparative investigation was performed on the effects of milling duration at pilot versus laboratory scale. A theoretical model was used to guide the scale-up effort based on the primary principle that the mechanical energy input to the raw materials subjected to mechanochemical processing should be comparable at different scales. A field construction project was implemented using the cement produced at pilot scale in order to verify the compatibility of the mechanochemically processed alkali aluminosilicate cement with the conventional concrete production and construction practices. The following conclusions were derived based on the outcomes of the project.

- With proper selection of the ball-milling parameters, scale-up of the mechanochemical approach to processing of alkali aluminosilicate hydraulic cement (in dilute carbon dioxide environment) is feasible at different scales with comparable inputs of mechanical energy to raw materials. The rise in the rate of mechanical energy input at larger scales lowers the required milling duration and thus raises the throughput of cement production. Hydraulic cements produced at different scales exhibited comparable structures and engineering properties.
- The mechanochemical approach to processing of alkali aluminosilicate cement enables selective capture of carbon dioxide from flue gas, allowing for capture of CO_2 at about 3% by weight of cement. This phenomenon together with the large-volume use of abundant

industrial byproducts as raw materials, and the energy-efficiency and low carbon footprint of the mechanochemical process led to production of a new class of hydraulic cement with highly favorable energy content, carbon footprint and economics.

- The mix design procedures developed for Portland cement concrete are applicable to concrete materials prepared with the mechanochemically processed alkali aluminosilicate cement. The fresh mix rheology and the set time of the resulting concrete were adequate for industrial-scale mixing, transportation, placement and finishing using conventional concrete construction practices and time schedules.

Chapter 9

Theoretical Evaluation of the Fate of Captured Carbon dioxide in Alkali Aluminosilicate Cements

9.1 Introduction

9.1.1 Thermodynamic Modeling

The software package Geochemist's Workbench uses the thermodynamic database thermos.com to identify the more stable compounds that form for different combinations of raw materials. Simulations were carried out for a hydraulic cement formulation while suppressing the mineral and aqueous phases which cannot form as a result of hydration and carbonation reactions.

The hydraulic cement considered in simulation of the hydration process comprised coal ash: slag: CaO: NaOH: sodium silicate at 65: 20: 5: 5: 5 weight ratios.

The oxide compositions of coal ash and slag are listed in Table 36. Curing (hydration) temperatures were set at 25℃ or 40℃. To compare hydrated phases with different CO_2 uptakes during milling, CO_2 contents of 0%, 5%, 10%, 15%, 20% and 25% (by weight of cement) were considered.

Table 37 presents the input data on reactants with different amounts of captured CO_2. An example water-to-cement ratio of 0.35 was considered. The hydrated phase assemblage is presented in Table 38

Table 36. Oxide compositions of coal ash and slag.

Material	SiO_2	Al_2O_3	Fe_2O_3	CaO	MgO	K_2O	Na_2O	SO_3	LOI
Coal fly ash	28.17	11.67	17.14	28.12	2.5	2.33	2.6	4.35	2.72
slag	37.53	9.54	0.47	40.78	10.85	0.45	0.25	0.20	.01

Table 37. Input data on reactants.

CO_2 Content	SiO_2	Al_2O_3	Fe_2O_3	CaO	MgO	K_2O	Na_2O	SO_3	Na_2SiO_3	CO_2
0	220.6	94.9	112.4	31.4	38.0	16.0	56.2	28.3	50.0	0
5%	216.6	91.1	107.8	301.7	36.4	15.4	53.9	27.1	48.0	48.0
10%	206.7	87.0	102.9	287.9	34.8	14.7	51.4	25.9	45.8	91.6
15%	197.7	83.1	98.4	275.3	33.2	14.1	49.2	24.8	43.8	131.4
20%	189.4	79.7	94.3	263.8	31.8	13.5	47.1	23.7	42.0	167.8
25%	181.7	76.5	90.5	253.1	30.6	12.9	45.2	22.8	40.3	201.3

Table 38. Hydrated phase assemblage of the mechanochemically processed hydraulic cement with different CO_2 uptakes at 25℃ and 40℃.

Mineral	25℃						40℃					
	0	5%	10%	15%	20%	25%	0	5%	10%	15%	20%	25%
Grossular: $Ca_3Al_2(SiO_4)_3$	√	√	√	√	--	--	√	√	√	√	--	--
Brucite: $Mg(OH)_2$	√	√	√	--	--	--	√	√	√	--	--	--
Andradite: $Ca_3Fe_3^{+2}(SiO_4)_3$	√	√	√	√	√	√	√	√	√	√	√	√
Mirabilite: $Na_2SO_4•10(H_2O)$	√	√	√	√	√	√	√	--	--	--	--	--
Gibbsite: $Al(OH)_3$	√	√	√	√	√	Minor	-	--	--	√	√	--
Kalsilite: $KAlSiO_4$	√	√	√	√	√	√	√	√	√	√	√	√
$Ca(OH)_2$(c)	√	√	--	--	--	--	√	√	--	--	--	--
Calcite		√	√	√	√	√		√	√	√	√	√
Clinochl-14A: $(Mg,Fe^{++})5Al(Si_3Al)O10(OH)_8$	-	--	√	√	√	√	-	--	√	√	√	√
Saponite-Na: $(Ca/2,Na)0,3(Mg,Fe^{++})_3(Si,Al)_4O_{10}(OH)_2.4(H_2O)$	-	--	--	√	--	√	-	--	--	Minor	√	√
Prehnite: $Ca_2Al_2Si_3O_{10}(OH)_2$	-	--	--	√	--	√	-	--	Minor	√	--	√
Muscovite: $KAl_2(Si_3Al)O10(OH,F)_2$	-	--	--	√	√	--	-	--	--	√	√	--
Analcime: $NaAlSi2O_6•(H_2O)$	-	--	--	√	√	√	-	--	--	√	√	√
Nepheline: $(Na,K)AlSiO_4$	-	--	--	√	--	--	-	--	--	√	√	√
Gaylussite: $Na_2Ca(CO_3)_2•5(H_2O)$	-	--	--	√	√	--	-	--	--	--	--	--
Hematite/Fe_2O_3	-	--	--	--	√	√	-	--	--	--	√	√
Dawsonite/$NaAl(CO_3)(OH)_2$	-	--	--	--	√	--	-	--	--	--	--	--
Nontronit-Na: $Na0.3Fe^{+++}2(Si,Al)_4O10(OH)_2•n(H_2O)$	-	--	--	--	--	Minor	-	--	--	--	--	Minor
Paragonite: $NaAl_2(Si_3Al)O10(OH)_2$	-	--	--	--	--	Minor	-	--	--	--	Minor	Minor
Phengite: $K(AlMg)_2(OH)_2(SiAl)_4O_{10}$	-	--	--	--	--	√	-	--	--	--	--	√
Epidote: $Ca2(Fe^{+++},Al)_3(SiO_4)_3(OH)$	-	--	--	--	--	Minor	-	--	--	--	--	Minor

9.1.2 Diffusion-Controlled Modeling

A key consideration in this research is CO_2 capture via physicochemical processes occurring in a solid-gas system upon mechanical activation at room temperature [262]. In an effort to simulate this process, a theoretical model was developed based on the assumption that the process is diffusion-controlled. Thermodynamic calculations were used to verify the approach based on the energetics of carbonation reactions, and the effects of activators on these reactions.

The mean number of monolayers of CO_2 gas molecules, N_m, passed through the unit surface area of ash particles due to the consumption of a mechanochemical energy dose D_e (MJ/g solid substance) is [263]:

$$N_m = G_o \frac{D}{N_s}$$

where, G_o is the number of gas moles passed into the bulk of solid phase per unit surface area upon supply of a unit dose of mechanical energy (mol g)/(MJ m^2), and N_s is the surface concentration of the adsorbed CO_2 gas molecules, mol/m^2. A simplified kinetic approach was developed, which considers two regimes of mechanically induced interactions between solid and gas: cleavage and friction. Cleavage, which is more prevalent at early stages of milling, produces fresh surfaces with input of mechanical energy; CO_2 molecules are then chemisorbed on these fresh surfaces. The rate of carbon dioxide adsorption via cleavage is proportional to the rate of formation of active sites (i.e., the rate of increase in specific surface area, S_{sp}). As the total surface area of particles increases, the share of active sites forming due to friction of particle surfaces also rises to the point that it governs the mechanochemical process of CO_2 incorporation into ash and other particles.

The FTIR and XRD data generated in the project indicate that physically adsorbed CO_2 is practically absent, and introduction of carbon dioxide molecules at active surface sites forms CO_3^{2-} groups due to interactions with oxygen anions. Subsequently, carbonate anions diffuse relatively slowly into the particle (tribodiffusion [264]), which controls the rate of CO_2 incorporation into ash and other particles. In this case, the rate of carbon dioxide absorption, W=dM/dτ, is a function of the total surface area of ash particles, S:

$$W = f_{fr}(S)$$

Using Fick's diffusion law in application to semi-bounded solids, the rate of mechanically activated sorption (one-dimensional diffusion) can be expressed as:

$$W = \frac{K_{MSC}.S^2}{M}$$

where, K_{MSC} is the mechanosorption coefficient characterizing the ability of ash and other raw materials to absorb CO_2 during mechanochemical activation ($g^2\ m^{-4}\ min^{-1}$) [265]. Transformation of the right hand side of above equation, considering the variation in S over time, yields the following expressions for calculating the M and S values [266]:

$$M = 0.01\frac{C.q}{1-0.01C}$$

$$S = S_{sp}\frac{q}{1-0.01C}$$

where, q is the mass of ash (or other raw materials), and C is the content of carbon dioxide in mechanochemically activated particles (wt.%). The above three equations can be used to derive the following relationship:

$$-dln\,(1-0.01C) = 10^2 K_{MSC}\frac{S_{sp}^2}{C}.dt$$

Integration of above equation within a time interval from t_0 to t_1 yields the expression:

$$-ln\ (1 - 0.01C_{t1} + \ln(1 - 0.01\ C_{t0}) = 10^2 K_{MSC}$$

The mechanosorption coefficient K_{MSC} in above equation was derived empirically, as described in the following sections, by measuring the CO_2 content and the specific surface area of ash particles versus time in representative mechanochemical activation (milling) conditions and CO_2-rich environments which simulate flue gas. The mechanosorption coefficient K_{MSC} is expected to be dependent upon the raw material (ash, slag, etc.) type, the specifics of the mechanical action, and the environment. The required milling duration is estimated as:

$$e^{-b_2 t} + b_3 e^{-b_4 t}$$

9.2 Experimental Investigations to Support the Mechanosorption Theory

Experimental studies were conducted on a hydraulic cement prepared mechanochemically with a blend of raw materials comprising coal ash, slag and albite as the primary aluminosilicate precursors at 45:25:15 weight ratios, with 7wt.% Na_2SiO_3, 3wt.% NaOH and 4 wt.% CaO used as activators. This blend of raw materials was ball-milled in CO_2 over different time periods. Samples were taken for experimental evaluation every 15 minutes in the first hour, and every 30 minutes after that, with total milling duration of 240 minutes. The CO_2 uptake was assessed using the thermogravimetry method. The specific surface area of the cement was measured using the permeability-based Blaine fineness test method.

9.3 Outcomes of Thermodynamic Modeling

9.3.1 Effects of CO_2 Uptake on the Mineralogical Composition of the Hydrated Binder

Figure 101 presents the results of calculations for hydration of cements with different CO_2 uptakes at 25℃. The amount of $Ca(OH)_2$ is observed to be reduced, and the amount of calcite is

raised with increasing amounts of CO_2 uptake. $Ca(OH)_2$ disappears and Clinochl-14A appears as CO_2 uptake exceeds 5%. With less than 10% CO_2 uptake, the types of phases are similar; further rise in CO_2 uptake delays the appearance of gibbsite and reduces the amounts of gibbsite and brucite formed. With CO_2 uptake exceeding 15%, the variety of phases is increased, and brucite disappears. As the CO_2 uptake exceeds 20%, grossular disappears and hermatite appears.

9.3.2 Effects of the Elevated Curing Temperature and CO_2 Content on the Mineralogical Composition of the Hydrated Binder

Figure 102 presents the results of calculations on the mineral composition of the hydrated binder with different CO_2 uptakes at 40℃. Compared to the results obtained at 25℃, mirabilite and gaylussite almost disappear from the hydrated phase at 40℃, gibbsite appears in the hydrated paste with CO_2 uptakes of 15% and 20%; the amount of gibbsite is still lower than that produced at 25℃. With increasing CO_2 uptake, the variety of minerals formed upon hydration increases at 40℃ as is the case at 25℃.

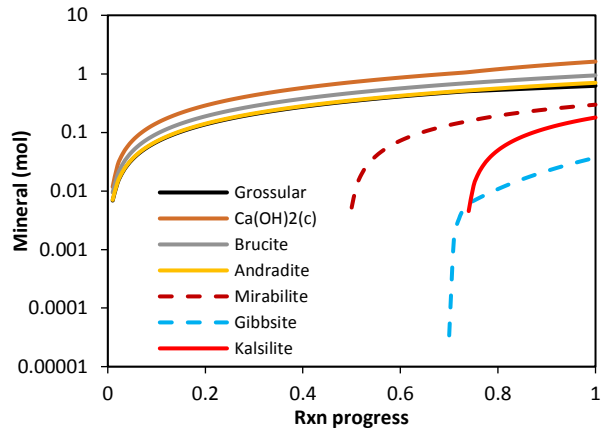

0% CO_2

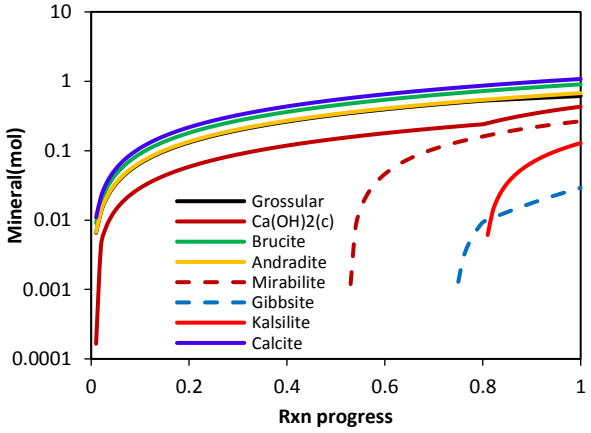

5% CO_2

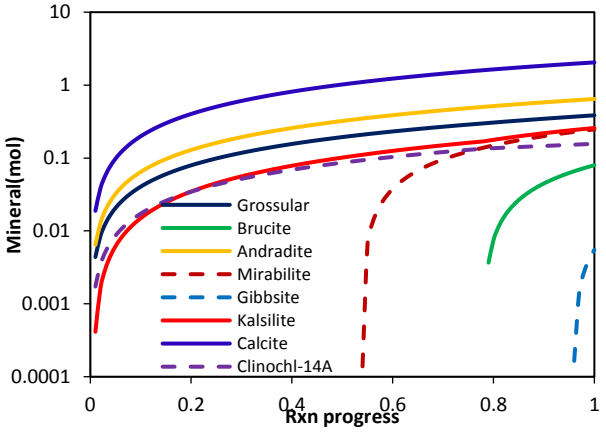

10% CO_2

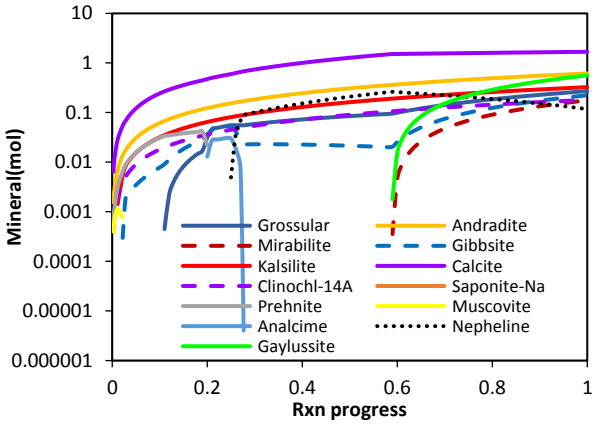

15% CO_2

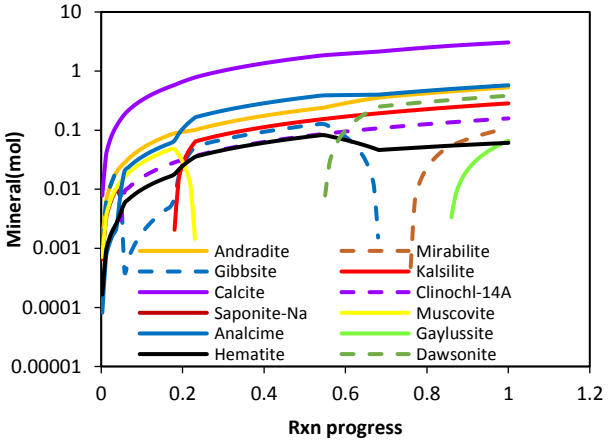

20% CO_2

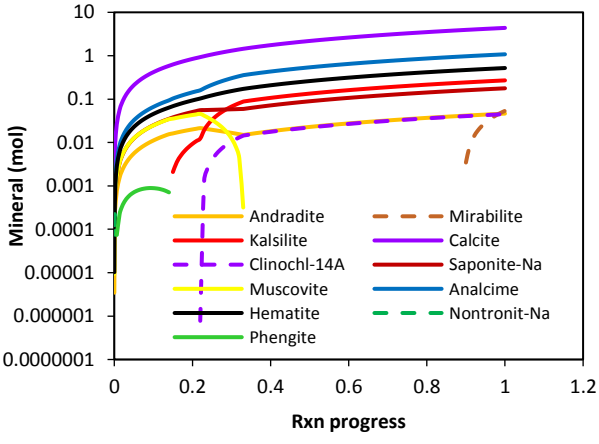

25% CO_2

Figure 101. Mineral products versus Rxn progress without CO_2 and with CO_2 at different concentrations.

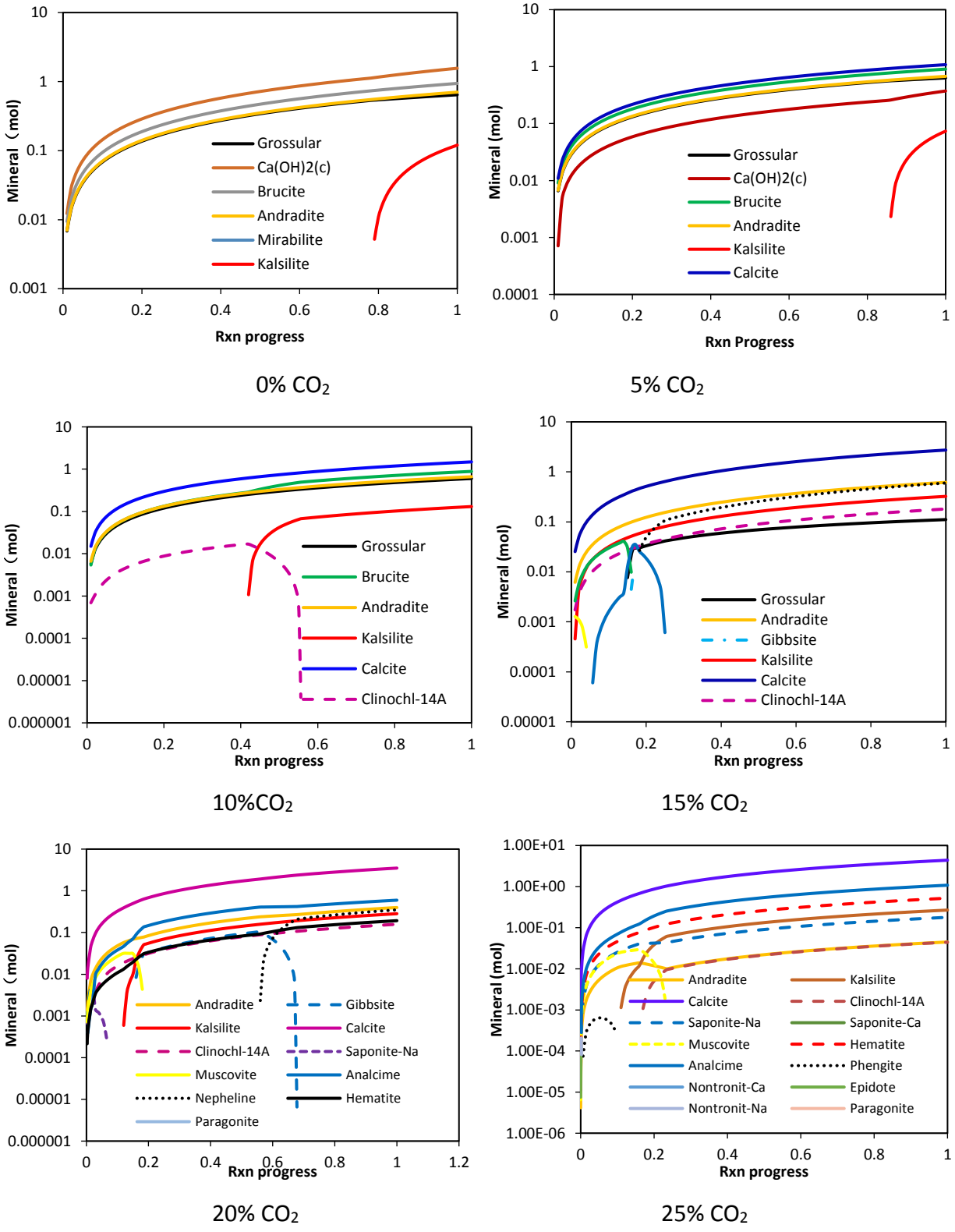

Figure 102. Mineral products versus Rxn progress without and with different concentrations of CO_2 at 40°C curing temperature.

9.4 Outcomes of Diffusion-Controlled Modeling

9.4.1 Theoretical Principles

As the total surface area of particles increases, the fraction of active sites forming due to the friction of particle surfaces also rises. As a result of the enhancement of aggregation processes, the specific surfaces area increases with the milling time (Figure 103). In the first period (less than 60 minutes), rapid increase in the surface area where the mechanical energy was spent predominantly for the formation of fresh surfaces on active sites of which CO_2 molecules are chemisorbed. The rate of carbon dioxide absorption in the regime of cleavage is proportional to the rate of formation of active sites and, hence, to the rate of surface growth [267]. After 60 minutes, the rate of surface area increase was observed to decrease.

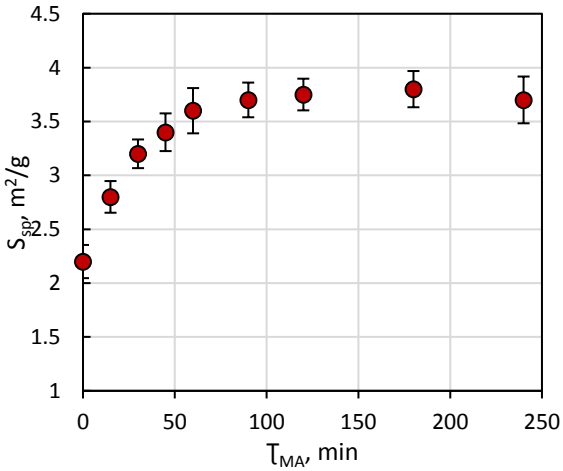

Figure 103. The specific surface area of the mechanochemically processed hydraulic cement versus the milling duration.

Figure 104 presents the accuracy of representing the S^2_{sp}/C value using the equations presented earlier for calculation of the parameters of the kinetic model of CO_2 mechanosorption, which are presented in Table 39. The values of mechanosorption coefficient derived based on the experimental results as a function of the duration of milling. The mechanosorption coefficient is

observed to increase rapidly in the first hours and slow down after that. This rapid rise can be attributed to the mechanically induced damage and disordering of the blend of raw materials and probably the mechanochemical effects of milling on carbon dioxide. The fact that the mechanosorption coefficient increased rapidly within the first hour of milling support the theoretical milling duration that suggests of about 20 minutes of milling could be suitable for this application.

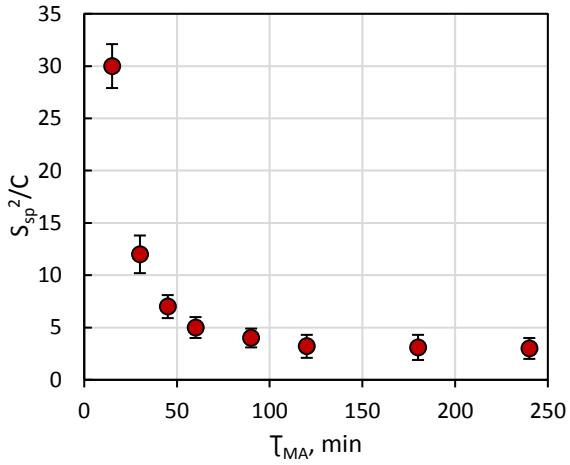

Figure 104. Dependence of the S^2_{sp}/C value on the duration of mechanochemical processing in carbon dioxide.

Table 39. Coefficient bi (i=0, 1, …, 3), and parameters k0 and I of the kinetic model of CO_2 mechanosorption.

Coefficient	Value
b_0, m^4g^{-2}	2.3
b_1, m^4g^{-2}	1200
b_2, min^{-1}	0.05
b_3, m^4g^{-2}	1180
$b_4\times10^2$, min^{-1}	0.05
$K_0\times10^6$, $g^2m^{-4}min^{-1}$	0.42
$k\times10^6$, $g^2m^{-4}min^{-2}$	0.18

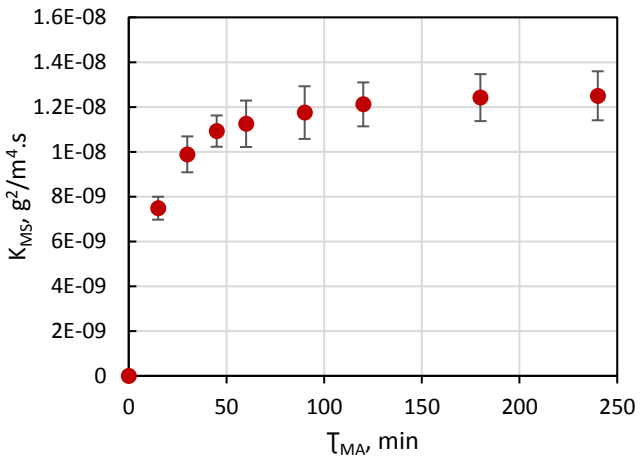

Figure 105. The empirical value of CO_2 mechanosorption coefficient (K_{MS}) versus milling time.

9.5 Thermodynamics of CO_2 Uptake and Reaction Mechanisms

The fact that mechanochemical uptake of CO_2 by the blends of raw materials does not produce crystalline carbonates but metastable complexes complicates applications of thermodynamic principles to the process. Eventually, however, the metastable carbonate complexes transform into stable crystalline carbonates. In order to gain further insight into the carbonation mechanisms, the changes in free energy associated with possible carbonation reactions were calculated using the HSC chemistry software. The mineral compounds found in coal combustion residues include: lime (CaO), anhydrite ($CaSO_4$), gehlenite ($Ca_2Al_2SiO_7$), mullite ($2Al_2O_3.SiO_2$), anorthite ($CaAl_2Si_2O_8$), quartz (SiO_2), hydroxyl ellestadite ($Ca_{10}(SiO_4)_3(SO_4)_3(OH)_2$) and hematite ($Fe_2O_3$) . Carbonation reactions involving some of these minerals are listed below together with the corresponding changes in free energy (at 20°C).

① $CaO+CO_2(g) \rightarrow CaCO_3$ $\Delta G = -31.363\ kJmol^{-1}$

② $2CaO*Al_2O_3*SiO_2 + 2CO_2(g) \rightarrow 2CaCO_3 + Al_2O_3 + SiO_2$ $\Delta G = -28.856\ kJmol^{-1}$

③ $CaO*Al_2O_3*2SiO_2 + CO2(g) \rightarrow CaCO_3 + Al_2O_3 + 2SiO_2$ $\Delta G = -6.608\ kJmol^{-1}$

Since for reactions ①, ② and ③ the change in free energy is negative (ΔG <0), these reactions can occur spontaneously.

Various activators were used to enhance mechanochemical uptake of CO_2. An example of such activators is sodium silicate (Na_2SiO_3). The carbonation reactions that could occur with sodium silicate added to coal ash are presented below together with the corresponding changes in free energy (at 20^oC).

④ $CaO+Na_2SiO_3+2CO_2(g) \rightarrow CaCO_3+SiO_2+Na_2CO_3$ $\Delta G = -41.758\ kJmol^{-1}$

⑤ $*2CaO*Al_2O_3*SiO_2 + 3CO_2(g)+Na_2SiO_3 \rightarrow 2CaCO_3 + A_{l2}O_3 + 2SiO_2+Na_2CO_3$ $\Delta G = -39.251\ kJmol^{-1}$

⑥ $CaO*Al2O_3*2SiO_2 + 2CO_2(g) +Na_2SiO_3 \rightarrow CaCO_3 + Al_2O_3 + 3SiO_2+Na_2CO_3$ $\Delta G = -17.002\ kJmol^{-1}$

Reactions④, ⑤ and ⑥ are also observed to be spontaneous (ΔG <0), with changes in free energy that are greater (in absolute value) than those obtained without the addition of sodium silicate.

Calculations of free energy were also conducted for above reactions occurring at different temperatures. The resulting values of free energy are presented in Figure 106. These results confirm that the above carbonation reactions are spontaneous, and that introduction of sodium silicate to the milling process enhances the thermodynamics of carbonation reactions. This finding supports the contributions of sodium silicate to the mechanochemical uptake of CO_2 observed in experimental studies conducted in the project.

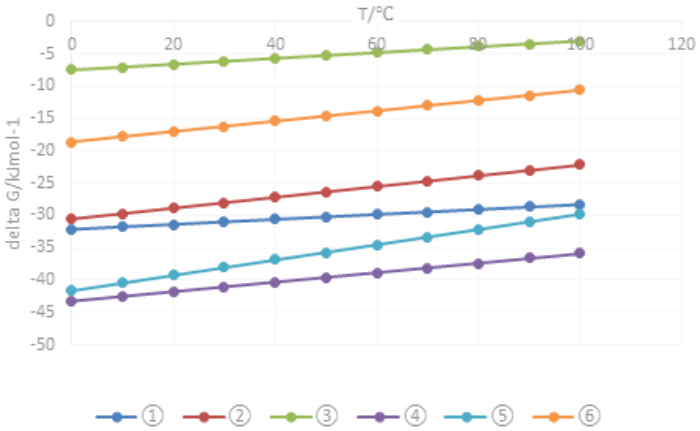

Figure 106. The change in free energy as a function of temperature for different carbonation reactions without and with introduction of sodium silicate.

9.6 Conclusions

The Geochemist's Workbench and the HSC Chemistry software were used to gain insight into the thermodynamically feasible products of the hydration processes of cements developed in the project with different carbon dioxide contents.

A theoretical model was developed for the incorporation of carbon dioxide into the hydraulic cements particles based on the assumption that the process is diffusion-controlled. Thermodynamic calculations were also conducted in order to gain insight into the energetics of carbonation reactions, and the effects of activators on these reactions. The mechanosorption theory developed in the project relates the CO_2 uptake to the specific surface area of cement (which increases with milling duration) and a mechanosorption coefficient which characterizes the ability of alkali aluminosilicate cement to absorb CO_2 during mechanochemical activation.

Experimental studies were conducted in order to measure the CO_2 uptake and the evolution of the specific surface area of cement as a function of the milling duration. The results were input into the equations developed based on the mechanosorption principles in order to calculate the mechanosorption coefficient of cement. The results indicated that the CO_2 mechanosorption

coefficient increases rapidly during the first hour of milling, and slows down thereafter with further input of mechanical energy.

REFERENCES

REFERENCES

1. Monkman, S. and R. Niven, Integration of Carbon Dioxide Curing into Precast Concrete Production. 2010, Halifax.

2. NIVEN, R., G.S. MONKMAN, and D. FORGERON, *CARBON DIOXIDE SEQUESTRATION IN CONCRETE ARTICLES*. 2012, WO Patent 2,012,079,173.

3. Shao, Y., S. Monkman, and A.J. Boyd. Recycling carbon dioxide into concrete: a feasibility study. 2010.

4. Lancellotti, I., et al., Inorganic polymers from alkali activation of metakaolin: Effect of setting and curing on structure. Journal of Solid State Chemistry, 2013. **200**: p. 341-348.

5. Davidovits, J., *Geopolymers and geopolymeric materials.* Journal of Thermal Analysis, 1989. **35**(2): p. 429-441.

6. Provis, J.L. and S.A. Bernal, *Geopolymers and related alkali-activated materials.* Annual Review of Materials Research, 2014. **44**: p. 299-327.

7. Davidovits, J. and J.L. Sawyer, *Early high-strength mineral polymer*. 1985, Google Patents.

8. Davidovits, J., *Geopolymers.* Journal of thermal analysis, 1991. **37**(8): p. 1633-1656.

9. Duxson, P. and J.L. Provis, *Designing precursors for geopolymer cements.* Journal of the American Ceramic Society, 2008. **91**(12): p. 3864-3869.

10. Nematollahi, B., J. Sanjayan, and F.U.A. Shaikh, *Synthesis of heat and ambient cured one-part geopolymer mixes with different grades of sodium silicate.* Ceramics International, 2015. **41**(4): p. 5696-5704.

11. Chindaprasirt, P., et al., Effect of SiO2 and Al2O3 on the setting and hardening of high calcium fly ash-based geopolymer systems. Journal of Materials Science, 2012. **47**(12): p. 4876-4883.

12. Feng, D., J.L. Provis, and J.S. Deventer, *Thermal Activation of Albite for the Synthesis of One-Part Mix Geopolymers.* Journal of the American Ceramic Society, 2012. **95**(2): p. 565-572.

13. Koloušek, D., et al., Preparation, structure and hydrothermal stability of alternative (sodium silicate-free) geopolymers. Journal of Materials Science, 2007. **42**(22): p. 9267-9275.

14. Peng, M.X., et al., Synthesis, characterization and mechanisms of one-part geopolymeric cement by calcining low-quality kaolin with alkali. Materials and Structures, 2015. **48**(3): p. 699-708.

15. Ye, N., et al., *Synthesis and strength optimization of one-part geopolymer based on red mud.* Construction and Building Materials, 2016. **111**: p. 317-325.

16. Sturm, P., et al., *Synthesizing one-part geopolymers from rice husk ash.* Construction and Building Materials, 2016. **124**: p. 961-966.

17. Temuujin, J., R. Williams, and A. Van Riessen, *Effect of mechanical activation of fly ash on the properties of geopolymer cured at ambient temperature.* Journal of Materials Processing Technology, 2009. **209**(12): p. 5276-5280.

18. Djobo, J.N.Y., et al., Mechanical activation of volcanic ash for geopolymer synthesis: effect on reaction kinetics, gel characteristics, physical and mechanical properties. RSC Advances, 2016. **6**(45): p. 39106-39117.

19. Guo, X., et al., A review of mechanochemistry applications in waste management. Waste management, 2010. **30**(1): p. 4-10.

20. Baláž, P., et al., *Mechanochemistry in the preparation of advanced materials.* Acta Montanistica Slovaca, 2006. **11**(2): p. 122-129.

21. Boldyrev, V., *Mechanochemical modification and synthesis of drugs.* Journal of materials science, 2004. **39**(16-17): p. 5117-5120.

22. Hadi, P., et al., Sustainable development of a surface-functionalized mesoporous aluminosilicate with ultra-high ion exchange efficiency. Inorganic Chemistry Frontiers, 2016. **3**(4): p. 502-513.

23. Van Jaarsveld, J., J. Van Deventer, and G. Lukey, *The characterisation of source materials in fly ash-based geopolymers.* Materials Letters, 2003. **57**(7): p. 1272-1280.

24. Deniz, V., The effect of mill speed on kinetic breakage parameters of clinker and limestone. Cement and concrete research, 2004. **34**(8): p. 1365-1371.

25. Yao, X., et al., Geopolymerization process of alkali–metakaolinite characterized by isothermal calorimetry. Thermochimica Acta, 2009. **493**(1): p. 49-54.

26. Rahier, H., et al., *Reaction mechanism, kinetics and high temperature transformations of geopolymers.* Journal of materials science, 2007. **42**(9): p. 2982-2996.

27. Jackson, M.D., et al., *Material and elastic properties of Al-tobermorite in ancient Roman seawater concrete.* Journal of the American Ceramic Society, 2013. **96**(8): p. 2598-2606.

28. Worrell, E., et al., *Carbon dioxide emissions from the global cement industry.* Annual review of energy and the environment, 2001. **26**(1): p. 303-329.

29. Oss, H.G. and A.C. Padovani, *Cement manufacture and the environment: part I: chemistry and technology.* Journal of Industrial Ecology, 2002. **6**(1): p. 89-105.

30. Aïtcin, P.-C., *Cements of yesterday and today: concrete of tomorrow.* Cement and Concrete research, 2000. **30**(9): p. 1349-1359.

31. Jolicoeur, C. and M.-A. Simard, *Chemical admixture-cement interactions: phenomenology and physico-chemical concepts.* Cement and Concrete Composites, 1998. **20**(2-3): p. 87-101.

32. Shi, C., A.F. Jiménez, and A. Palomo, *New cements for the 21st century: the pursuit of an alternative to Portland cement.* Cement and concrete research, 2011. **41**(7): p. 750-763.

33. Phair, J.W., *Green chemistry for sustainable cement production and use.* Green Chemistry, 2006. **8**(9): p. 763-780.

34. C1157, A., Standard Performance Specification for Hydraulic Cement. 2011.

35. Provis, J., Alkali-activated binders and concretes: the path to standardization, in Geopolymer Binder Systems. 2013, ASTM International.

36. Hicks, J.K., M.A. Caldarone, and E. Bescher, *Opportunities from Alternative Cementitious Materials.* Concrete International, 2015. **37**(4): p. 47-51.

37. Hajimohammadi, A. and J.S. van Deventer, *Characterisation of One-Part Geopolymer Binders Made from Fly Ash.* Waste and Biomass Valorization: p. 1-9.

38. Hajimohammadi, A. and J.S. van Deventer, *Solid Reactant-Based Geopolymers from Rice Hull Ash and Sodium Aluminate.* Waste and Biomass Valorization: p. 1-10.

39. ASTM, *Standard Performance Specification for Hydraulic Cement.* ASTM International, 2011. **C1157**(West Conshohocken, PA, USA).

40. ASTM, *Standard Specification for Portland Cement* ASTM International, 2015. **C150**(West Conshohocken, PA, USA).

41. ASTM, *Standard Specification for Blended Hydraulic Cements.* ASTM International, 2005. **C595**(West Conshohocken, PA, USA).

42. ASTM, Standard Test Method for Length Change of Hydraulic-Cement Mortars Exposed to a Sulfate Solution. ASTM International, 2015. **C1012**(West Conshohocken, PA, USA).

43. Wu, W., et al., Influence of admixtures on rheological properties and heat of hydration of alkali aluminosilicate cement. Advances in Cement Research, 2017: p. No. 1600181.

44. Wu, W., et al., Influence of admixtures on rheological properties and heat of hydration of alkali aluminosilicate cement. Advances in Cement Research, 2017: p. 1-7.

45. De Weerdt, K., et al., Hydration mechanisms of ternary Portland cements containing limestone powder and fly ash. Cement and Concrete Research, 2011. **41**(3): p. 279-291.

46. Lawrence, P., M. Cyr, and E. Ringot, *Mineral admixtures in mortars: effect of inert materials on short-term hydration.* Cement and concrete research, 2003. **33**(12): p. 1939-1947.

47. Matalkah, F., et al., Mechanochemical synthesis of one-part alkali aluminosilicate hydraulic cement. Materials and Structures, 2017. **50**(1): p. 97.

48. ASTM, *Standard Specification for Standard Sand.* ASTM International, 2013. **C778**(West Conshohocken, PA, USA).

49. ASTM, Standard Test Method for Potential Alkali Reactivity of Cement-Aggregate Combinations (Mortar-Bar Method). ASTM International, 2010. **C227**(West Conshohocken, PA, USA).

50. ASTM, Compressive Strength of Hydraulic Cement Mortars (Using 2-in. or [50-mm] Cube Specimens). ASTM International, 2013. **C109**(West Conshohocken, PA, USA).

51. ASTM, *Standard Test Method for Flow of Hydraulic Cement Mortar.* ASTM International, 2013. **C1437**(West Conshohocken, PA, USA).

52. ASTM, Standard Practice for Measuring Hydration Kinetics of Hydraulic Cementitious Mixtures Using Isothermal Calorimetry`. ASTM International, 2014. **C1679**(West Conshohocken, PA, USA).

53. ASTM, Standard Test Methods for Time of Setting of Hydraulic Cement by Vicat Needle. ASTM International, 2013. **C191**(West Conshohocken, PA, USA).

54. ASTM, Standard Test Method for Amount of Water Required for Normal Consistency of Hydraulic Cement Paste. ASTM International, 2011. **C187**(West Conshohocken, PA, USA).

55. ASTM, *Standard Test Method for Autoclave Expansion of Hydraulic Cement.* ASTM International, 2015. **C151**(West Conshohocken, PA, USA).

56. ASTM, Standard Test Method for Expansion of Hydraulic Cement Mortar Bars Stored in Water. ASTM International, 2014. **C1038**(West Conshohocken, PA, USA).

57. Scrivener, K.L. and A. Nonat, *Hydration of cementitious materials, present and future.* Cement and concrete research, 2011. **41**(7): p. 651-665.

58. Lee, W. and J. Van Deventer, The effect of ionic contaminants on the early-age properties of alkali-activated fly ash-based cements. Cement and Concrete Research, 2002. **32**(4): p. 577-584.

59. Davidovits, J. Properties of geopolymer cements. in First international conference on alkaline cements and concretes. 1994.

60. Gourley, J. and G. Johnson. Developments in geopolymer precast concrete. in World Congress Geopolymer. 2005.

61. Fernández-Jiménez, A., I. Garcia-Lodeiro, and A. Palomo, *Durability of alkali-activated fly ash cementitious materials.* Journal of Materials Science, 2007. **42**(9): p. 3055-3065.

62. Chatterji, S., Mechanism of expansion of concrete due to the presence of dead-burnt CaO and MgO. Cement and Concrete Research, 1995. **25**(1): p. 51-56.

63. Fu, Y., J. Ding, and J. Beaudoin, *Expansion of Portland cement mortar due to internal sulfate attack.* Cement and Concrete Research, 1997. **27**(9): p. 1299-1306.

64. Miller, F.M., et al., Assessing the distribution of sulfate in Portland cement and clinker and its influence on expansion in mortar. Cement, concrete and aggregates, 1999. **21**(2): p. 212-216.

65. Desbats-Le Chequer, C. and F. Frizon, Impact of sulfate and nitrate incorporation on potassium-and sodium-based geopolymers: geopolymerization and materials properties. Journal of materials science, 2011. **46**(17): p. 5657-5664.

66. Dweck, J., et al., *Hydration of a Portland cement blended with calcium carbonate.* Thermochimica Acta, 2000. **346**(1): p. 105-113.

67. Galan, I., C. Andrade, and M. Castellote, *Thermogravimetrical analysis for monitoring carbonation of cementitious materials.* Journal of thermal analysis and calorimetry, 2012. **110**(1): p. 309-319.

68. Abdulkareem, O.A., et al., Effects of elevated temperatures on the thermal behavior and mechanical performance of fly ash geopolymer paste, mortar and lightweight concrete. Construction and building materials, 2014. **50**: p. 377-387.

69. Gruskovnjak, A., et al., Quantification of hydration phases in supersulfated cements: review and new approaches. Adv Cem Res, 2011. **23**(6): p. 265-275.

70. Kanezaki, E., Thermal behavior of the hydrotalcite-like layered structure of Mg and Al-layered double hydroxides with interlayer carbonate by means of in situ powder HTXRD and DTA/TG. Solid State Ionics, 1998. **106**(3): p. 279-284.

71. Fernández-Jiménez, A., et al., *New Cementitious Materials Based on Alkali-Activated Fly Ash: Performance at High Temperatures.* Journal of the American Ceramic Society, 2008. **91**(10): p. 3308-3314.

72. Shang, H., Y. Song, and J. Ou, *Behavior of air-entrained concrete after freeze-thaw cycles.* Acta Mechanica Solida Sinica, 2009. **22**(3): p. 261-266.

73. Harnik, A., U. Meier, and A. Roesli, Combined influence of freezing and deicing salt on concrete—Physical aspects, in Durability of building materials and components. 1980, ASTM International.

74. Deja, J., *Freezing and de-icing salt resistance of blast furnace slag concretes.* Cement and Concrete Composites, 2003. **25**(3): p. 357-361.

75. Yang, Z., W.J. Weiss, and J. Olek, *Water transport in concrete damaged by tensile loading and freeze–thaw cycling.* Journal of materials in civil engineering, 2006. **18**(3): p. 424-434.

76. Wang, Z., et al., Corrosion of rebar in concrete under cyclic freeze–thaw and Chloride salt action. Construction and Building Materials, 2014. **53**: p. 40-47.

77. Škvára, F., T. Jílek, and L. Kopecký, *Geopolymer materials based on fly ash.* Ceram.-Silik, 2005. **49**(3): p. 195-204.

78. Muntingh, Y., Durability and diffusive behaviour evaluation of geopolymeric material. 2006, Stellenbosch: University of Stellenbosch.

79. McLellan, B.C., et al., Costs and carbon emissions for geopolymer pastes in comparison to ordinary portland cement. Journal of Cleaner Production, 2011. **19**(9): p. 1080-1090.

80. Van Deventer, J.S., J.L. Provis, and P. Duxson, *Technical and commercial progress in the adoption of geopolymer cement.* Minerals Engineering, 2012. **29**: p. 89-104.

81. Duxson, P., et al., *The role of inorganic polymer technology in the development of 'green concrete'.* Cement and Concrete Research, 2007. **37**(12): p. 1590-1597.

82. Matalkah, F. and P. Soroushian, Synthesis and characterization of alkali aluminosilicate hydraulic cement that meets standard requirements for general use. Construction and Building Materials, 2018. **158**: p. 42-49.

83. Freeman, E., et al., Interactions of carbon-containing fly ash with commercial air-entraining admixtures for concrete. Fuel, 1997. **76**(8): p. 761-765.

84. Palacios, M. and F. Puertas, Effect of shrinkage-reducing admixtures on the properties of alkali-activated slag mortars and pastes. Cement and concrete research, 2007. **37**(5): p. 691-702.

85. Beraldo, S., N. Montagner, and A. Dal Bo, Alkali-activated aluminosilicate binder with superior freeze-thaw stability. 2016, Google Patents.

86. Jost, L., S. Gerhart, and Z. Albert, *Foaming agent for plaster and cement compositions*. 1975, Google Patents.

87. Şahmaran, M. and V.C. Li, De-icing salt scaling resistance of mechanically loaded engineered cementitious composites. Cement and Concrete Research, 2007. **37**(7): p. 1035-1046.

88. Nili, M. and M. Zaheri, *Deicer salt-scaling resistance of non-air-entrained roller-compacted concrete pavements.* Construction and Building Materials, 2011. **25**(4): p. 1671-1676.

89. Škvára, F. Alkali Activated Material–Geopolymer. in International Conference Alkali Activated Materials–Research, Production and Utilization, Česká rozvojová agentura, Praha. 2007.

90. Aıtcin, P., *The durability characteristics of high performance concrete: a review.* Cement and concrete composites, 2003. **25**(4): p. 409-420.

91. Fu, Y., L. Cai, and W. Yonggen, *Freeze–thaw cycle test and damage mechanics models of alkali-activated slag concrete.* Construction and Building Materials, 2011. **25**(7): p. 3144-3148.

92. Yang, Z., Assessing cumulative damage in concrete and quantifying its influence on life cycle performance modeling. Purdue Univ., West Lafayette, IN, 2004.

93. Zhang, M.-H., Microstructure, crack propagation, and mechanical properties of cement pastes containing high volumes of fly ashes. Cement and Concrete Research, 1995. **25**(6): p. 1165-1178.

94. Xu, H., et al., *Characterization of aged slag concretes.* ACI Materials Journal, 2008. **105**(2): p. 131-139.

95. Bernal, S.A., et al., Gel nanostructure in alkali-activated binders based on slag and fly ash, and effects of accelerated carbonation. Cement and Concrete Research, 2013. **53**: p. 127-144.

96. Bernal, S.A., et al., Role of carbonates in the chemical evolution of sodium carbonate-activated slag binders. Materials and Structures, 2015. **48**(3): p. 517-529.

97. Valenza, J.J. and G.W. Scherer, *Mechanisms of salt scaling.* Materials and Structures, 2005. **38**(4): p. 479-488.

98. Valenza, J.J. and G.W. Scherer, *Mechanism for salt scaling of a cementitious surface.* Materials and structures, 2007. **40**(3): p. 259-268.

99. Kawamura, M., K. Takeuchi, and A. Sugiyama, *Mechanisms of expansion of mortars containing reactive aggregate in NaCl solution.* Cement and concrete research, 1994. **24**(4): p. 621-632.

100. Shi, X., et al., Freeze–thaw damage and chemical change of a portland cement concrete in the presence of diluted deicers. Materials and Structures, 2010. **43**(7): p. 933-946.

101. Provis, J.L. and J.S.J. Van Deventer, Geopolymers: structures, processing, properties and industrial applications. 2009: Elsevier.

102. Yates, D.E., S. Levine, and T.W. Healy, *Site-binding model of the electrical double layer at the oxide/water interface.* Journal of the Chemical Society, Faraday Transactions 1: Physical Chemistry in Condensed Phases, 1974. **70**: p. 1807-1818.

103. Thomas, J.J., et al., Effect of hydration temperature on the solubility behavior of Ca-, S-, Al-, and Si-bearing solid phases in Portland cement pastes. Cement and Concrete Research, 2003. **33**(12): p. 2037-2047.

104. Nedeljkovic, M., et al. Physical properties and pore solution analysis of alkali-activated fly ash-slag pastes. in Proceedings pro113: International RILEM Conference Materials Systems and Structures in Civil Engineering (MSSCE 2016) on Concrete with Supplementary Cementitious Materials. 2016.

105. Szklorzová, H. and V. Bílek. Influence of alkali ions in the activator on the performance of alkali-activated mortars. in 3rd International Symposium on Non-traditional Cement and Concrete. Brno: Czech Republic. 2008.

106. Pigeon, M., R. Pleau, and P.-C. Aitcin, Freeze-thaw durability of concrete with and without silica fume in ASTM C 666 (Procedure A) test method: internal cracking versus scaling. Cement, concrete and aggregates, 1986. **8**(2): p. 76-85.

107. Bruere, G., 'Mechanisms by which Air-Entraining Agents Affect Viscositites and Bleeding Properties of Cement Pastes. Australian J. Appl. Sci, 1958. **9**(2): p. 349-359.

108. Sommer, H., The precision of the microscopical determination of the air-void system in hardened concrete. Cement, Concrete and Aggregates, 1979. **1**(2): p. 49-55.

109. Marchand, J., et al., Influence of chloride solution concentration on deicer salt scaling deterioration of concrete. Materials Journal, 1999. **96**(4): p. 429-435.

110. Łaźniewska-Piekarczyk, B., The influence of selected new generation admixtures on the workability, air-voids parameters and frost-resistance of self compacting concrete. Construction and Building Materials, 2012. **31**: p. 310-319.

111. Ong, F., Method of delivery of agents providing freezing and thawing resistance to cementitious compositions. 2008, Google Patents.

112. Venkateswarlu, M., et al., *Study on Durability Characteristics of Conventional Concrete With PEG-600 as Self Curing Compound.* European Journal of Advances in Engineering and Technology, 2015. **2**(12): p. 47-52.

113. Kumar, M.J., M. Srikanth, and K.J. Rao, *Strength characteristics of self-curing concrete.* Issue, 2012. **1**: p. 51-57.

114. Rai, S., N. Singh, and N. Singh, Interaction of tartaric acid during hydration of Portland cement. 2006.

115. Craig RJ, W.L., Effectiveness of corrosion inhibitors and their influence on the physical properties of Portland cement mortars. Highway Research Records, 1970. **328**(77).

116. Ormellese, M., et al., Effect of corrosion inhibitors on the initiation of chloride-induced corrosion on reinforced concrete structures. Materials and Corrosion, 2008. **59**(2): p. 98-106.

117. PEREZ, J.-P., et al. Influence of triisopropanolamine on the physico-chemical and mechanical properties of pure cement pastes and mortars. in Annales de chimie. 2003. Lavoisier.

118. Ichikawa, M., M. Kanaya, and S. Sano. Effect of triisopropanolamine on hydration and strength development of cements with different character. in Proceedings 10th International Congress on the Chemistry of Cement, Gothenburg (Edited by H Justnes), Sweden. 1997.

119. Sandberg, P.J. and F. Doncaster, *On the mechanism of strength enhancement of cement paste and mortar with triisopropanolamine.* Cement and concrete research, 2004. **34**(6): p. 973-976.

120. Gartner, E. and D. Myers, *Influence of tertiary alkanolamines on Portland cement hydration.* Journal of the American Ceramic Society, 1993. **76**(6): p. 1521-1530.

121. Huang, H., X.-r. Li, and X.-d. Shen, *Hydration of ternary cement in the presence of triisopropanolamine.* Construction and Building Materials, 2016. **111**: p. 513-521.

122. Matalkah, F., et al., *Use of non-wood biomass combustion ash in development of alkali-activated concrete.* Construction and Building Materials, 2016. **121**: p. 491-500.

123. Muñiz-Villarreal, M., et al., The effect of temperature on the geopolymerization process of a metakaolin-based geopolymer. Materials Letters, 2011. **65**(6): p. 995-998.

124. Rovnaník, P., Effect of curing temperature on the development of hard structure of metakaolin-based geopolymer. Construction and Building Materials, 2010. **24**(7): p. 1176-1183.

125. Lamanna, G., et al. Mechanical characterization of hybrid (organic-inorganic) geopolymers. in Key Engineering Materials. 2013. Trans Tech Publ.

126. Crisp, S. and A.D. Wilson, Reactions in glass ionomer cements: V. Effect of incorporating tartaric acid in the cement liquid. Journal of Dental Research, 1976. **55**(6): p. 1023-1031.

127. Katsioti, M., et al., Characterization of various cement grinding aids and their impact on grindability and cement performance. Construction and Building Materials, 2009. **23**(5): p. 1954-1959.

128. Powers, T.C., The properties of fresh concrete. 1969.

129. Holt, E. and M. Leivo, *Cracking risks associated with early age shrinkage.* Cement and Concrete Composites, 2004. **26**(5): p. 521-530.

130. Ravina, D. and R. Shalon. Plastic shrinkage cracking. in Journal Proceedings. 1968.

131. Wittmann, F., *On the action of capillary pressure in fresh concrete.* Cement and Concrete Research, 1976. **6**(1): p. 49-56.

132. Weyers, R., J. Conway, and P. Cady, *Photoelastic analysis of rigid inclusions in fresh concrete.* Cement and Concrete Research, 1982. **12**(4): p. 475-484.

133. Radocea, A., A study on the mechanism of plastic shrinkage of cement-based materials. 1992: Chalmers University of Technology.

134. Slowik, V., M. Schmidt, and R. Fritzsch, *Capillary pressure in fresh cement-based materials and identification of the air entry value.* Cement and Concrete composites, 2008. **30**(7): p. 557-565.

135. Slowik, V., E. Schlattner, and T. Klink, *Experimental investigation into early age shrinkage of cement paste by using fibre Bragg gratings.* Cement and Concrete Composites, 2004. **26**(5): p. 473-479.

136. Mora-Ruacho, J., R. Gettu, and A. Aguado, *Influence of shrinkage-reducing admixtures on the reduction of plastic shrinkage cracking in concrete.* Cement and Concrete Research, 2009. **39**(3): p. 141-146.

137. Bentz, D.P., M.R. Geiker, and K.K. Hansen, *Shrinkage-reducing admixtures and early-age desiccation in cement pastes and mortars.* Cement and concrete research, 2001. **31**(7): p. 1075-1085.

138. Lin, S.-T. and R. Huang, Effect of viscosity modifying agent on plastic shrinkage cracking of cementitious composites. Materials and structures, 2010. **43**(5): p. 651-664.

139. Dudziak, L. and V. Mechtcherine, Enhancing early-age resistance to cracking in high-strength cement-based materials by means of internal curing using super absorbent polymers. Additions improving properties of concrete, RILEM Proceedings PRO, 2010. **77**: p. 129-139.

140. Soroushian, P., F. Mirza, and A. Alhozajiny, *Plastic shrinkage cracking of polypropylene fiber reinforced concrete.* Materials Journal, 1993. **92**(5): p. 553-560.

141. Banthia, N. and R. Gupta, *Influence of polypropylene fiber geometry on plastic shrinkage cracking in concrete.* Cement and Concrete Research, 2006. **36**(7): p. 1263-1267.

142. Slowik, V., et al. Early age cracking and its influence on the durability of concrete structures. in Proceedings of the 8th International Conference on Creep, Shrinkage and Durability of Concrete and Concrete Structures-CONCREEP. 2008.

143. Alsayed, S. and M. Amjad, Effect of curing conditions on strength, porosity, absorptivity, ans shrinkage of concrete in hot and dry climate. Cement and Concrete Research, 1994. **24**(7): p. 1390-1398.

144. Shaeles, C.A. and K.C. Hover, Influence of mix proportions and construction operations on plastic shrinkage cracking in thin slabs. Materials Journal, 1988. **85**(6): p. 495-504.

145. Uno, P.J., *Plastic shrinkage cracking and evaporation formulas.* ACI Materials Journal, 1998. **95**: p. 365-375.

146. Soroushian, F.M.a.P., Development of a Sustainable Hydraulic Cement that Meets Standard Requirements for General Use. Construction and Building Materials, 2017. **Submitted**

147. Abel, J. and K. Hover, *Effect of water/cement ratio on the early age tensile strength of concrete.* Transportation Research Record: Journal of the Transportation Research Board, 1998(1610): p. 33-38.

148. Powers, T.C. The bleeding of potland cement paste, mortar, and concrete. in Journal Proceedings. 1939.

149. Giaccio, G. and A. Giovambattista, *Bleeding: evaluation of its effects on concrete behaviour.* Materials and Structures, 1986. **19**(4): p. 265-271.

150. Deacon, C. and J. Dewar, Concrete durability-specifying more simply and surely by strength. Concrete, 1982. **16**: p. 19-21.

151. Khayat, K.H., *Viscosity-enhancing admixtures for cement-based materials—an overview.* Cement and Concrete Composites, 1998. **20**(2-3): p. 171-188.

152. Chang, Z.-T., et al., Using limestone aggregates and different cements for enhancing resistance of concrete to sulphuric acid attack. Cement and Concrete Research, 2005. **35**(8): p. 1486-1494.

153. Yeau, K.Y. and E.K. Kim, An experimental study on corrosion resistance of concrete with ground granulate blast-furnace slag. Cement and Concrete Research, 2005. **35**(7): p. 1391-1399.

154. Palomo, A., M. Grutzeck, and M. Blanco, *Alkali-activated fly ashes: a cement for the future.* Cement and concrete research, 1999. **29**(8): p. 1323-1329.

155. Duxson, P., et al., *Geopolymer technology: the current state of the art.* Journal of Materials Science, 2007. **42**(9): p. 2917-2933.

156. Hardjito, D., et al., *On the development of fly ash-based geopolymer concrete.* Materials Journal, 2004. **101**(6): p. 467-472.

157. Bakharev, T., J. Sanjayan, and Y.-B. Cheng, *Resistance of alkali-activated slag concrete to acid attack.* Cement and Concrete Research, 2003. **33**(10): p. 1607-1611.

158. Bakharev, T., J. Sanjayan, and Y.-B. Cheng, *Sulfate attack on alkali-activated slag concrete.* Cement and Concrete Research, 2002. **32**(2): p. 211-216.

159. Singh, B., et al., *Geopolymer concrete: A review of some recent developments.* Construction and building materials, 2015. **85**: p. 78-90.

160. Fernández-Jiménez, A., et al., *Steel passive state stability in activated fly ash mortars.* Materiales de Construcción, 2010. **60**(300): p. 51-65.

161. Miranda, J., et al., *Corrosion resistance in activated fly ash mortars.* Cement and Concrete Research, 2005. **35**(6): p. 1210-1217.

162. Roy, D.M., *Alkali-activated cements opportunities and challenges.* Cement and Concrete Research, 1999. **29**(2): p. 249-254.

163. Matalkah, F. and P. Soroushian, Synthesis and Characterization of Alkali Aluminosilicate Hydraulic Cement that Meets Standard Requirements for General Use. Construction and Building Materials, 2017. **In press**.

164. T., B., *Resistance of geopolymer materials to acid attack.* Cement and Concrete Research 2005. **35**: p. 12.

165. Chinchón-Payá, S., C. Andrade, and S. Chinchón, *Indicator of carbonation front in concrete as substitute to phenolphthalein.* Cement and Concrete Research, 2016. **82**: p. 87-91.

166. Sanjuán, M.A. and C. del Olmo, *Carbonation resistance of one industrial mortar used as a concrete coating.* Building and Environment, 2001. **36**(8): p. 949-953.

167. Chen, M.-C., K. Wang, and L. Xie, *Deterioration mechanism of cementitious materials under acid rain attack.* Engineering failure analysis, 2013. **27**: p. 272-285.

168. Ariffin, M.A.M., et al., *Sulfuric acid resistance of blended ash geopolymer concrete.* Construction and Building Materials, 2013. **43**: p. 80-86.

169. Girardi, F. and R. Di Maggio, Resistance of concrete mixtures to cyclic sulfuric acid exposure and mixed sulfates: Effect of the type of aggregate. Cement and concrete composites, 2011. **33**(2): p. 276-285.

170. Bellmann, F., B. Möser, and J. Stark, Influence of sulfate solution concentration on the formation of gypsum in sulfate resistance test specimen. Cement and Concrete Research, 2006. **36**(2): p. 358-363.

171. Bakharev, T., *Resistance of geopolymer materials to acid attack.* Cement and Concrete Research, 2005. **35**(4): p. 658-670.

172. Rangan, B.V., Fly ash-based geopolymer concrete. 2008.

173. Badar, M.S., et al., Corrosion of steel bars induced by accelerated carbonation in low and high calcium fly ash geopolymer concretes. Construction and Building Materials, 2014. **61**: p. 79-89.

174. Broomfield, J.P., Corrosion of steel in concrete: understanding, investigation and repair. 2002: CRC Press.

175. Söylev, T.A. and M. Richardson, *Corrosion inhibitors for steel in concrete: State-of-the-art report.* Construction and Building Materials, 2008. **22**(4): p. 609-622.

176. Kupwade-Patil, K. and E.N. Allouche, *Examination of chloride-induced corrosion in reinforced geopolymer concretes.* Journal of Materials in Civil Engineering, 2012. **25**(10): p. 1465-1476.

177. Mehta, P.K., P.J. Monteiro, and M.-H. Education, *Concrete: microstructure, properties, and materials*. Vol. 3. 2006: McGraw-Hill New York.

178. Karstensen, K.H., *Formation, release and control of dioxins in cement kilns.* Chemosphere, 2008. **70**(4): p. 543-560.

179. Mikulčić, H., et al., The application of CFD modelling to support the reduction of CO 2 emissions in cement industry. Energy, 2012. **45**(1): p. 464-473.

180. Worrell, E., et al., *Carbon dioxide emissions from the global cement industry 1.* Annual Review of Energy and the Environment, 2001. **26**(1): p. 303-329.

181. Bernal, S.A., et al., MgO content of slag controls phase evolution and structural changes induced by accelerated carbonation in alkali-activated binders. Cement and Concrete Research, 2014. **57**: p. 33-43.

182. Bhattacharjee, B., *Sustainability of concrete construction in Indian context.* IndIan ConCreTe Journal, 2010: p. 46.

183. Davidovits, J., Geopolymer, Green Chemistry and Sustainable Development Solutions: Proceedings of the World Congress Geopolymer 2005. 2005: Geopolymer Institute.

184. Bots, P., et al., Mechanistic insights into the crystallization of amorphous calcium carbonate (ACC). Crystal Growth & Design, 2012. **12**(7): p. 3806-3814.

185. Provis, J.L., P. Duxson, and J.S. van Deventer, *Alkali-activated binders to enhance the sustainability of concrete production*. 2011, Advanced Photon Source (APS), Argonne National Laboratory (ANL), Argonne, IL (US).

186. Lothenbach, B., K. Scrivener, and R. Hooton, *Supplementary cementitious materials.* Cement and Concrete Research, 2011. **41**(12): p. 1244-1256.

187. BSI, *Fly Ash for Concrete*. 2012, British Standard Institute. p. 34.

188. Sabir, B., S. Wild, and J. Bai, *Metakaolin and calcined clays as pozzolans for concrete: a review.* Cement and Concrete Composites, 2001. **23**(6): p. 441-454.

189. Sata, V., C. Jaturapitakkul, and K. Kiattikomol, *Influence of pozzolan from various by-product materials on mechanical properties of high-strength concrete.* Construction and Building Materials, 2007. **21**(7): p. 1589-1598.

190. Hutchcroft, C.R. and H.R. Anderson. The Use of Carbon Dioxide to Reduce Efflorescence on Asbestos-Cement Shingles. ACI.

191. Technologies, C. *Carboncure Technologies Inc.* 2014; Available from: http://carboncure.com/.

192. Technologies, S. *Solidia Technologies*. 2014; Available from: http://solidiatech.com/.

193. Klemm, W.A. and R.L. Berger, *Accelerated curing of cementitious systems by carbon dioxide: part I. Portland cement.* Cement and Concrete Research, 1972. **2**(5): p. 567-576.

194. Klem, W. and R.L. Berger, *Accelerated curing of cementitious systems by carbon dioxide.* Cement and Concrete Research, 1972. **2**: p. 567.

195. Naik, T.R. and R. Kumar. Carbonation: An Efficient and Economical Process for CO2 Sequestration.

196. Kobayashi, K., K. Suzuki, and Y. Uno, *Carbonation of concrete structures and decomposition of C□ S□ H.* Cement and Concrete Research, 1994. **24**(1): p. 55-61.

197. Hussain, R.R. and T. Ishida, Critical carbonation depth for initiation of steel corrosion in fully carbonated concrete and development of electrochemical carbonation induced corrosion model. Int. J. Electrochem. Sci, 2009. **4**: p. 1178-1195.

198. Shao, Y., S. Monkman, and S. Wang. Market analysis of CO 2 sequestration in concrete building products. in Second international conference on sustainable construction materials and technologies. Italy: Ancona. 2010.

199. Niven, R., G.S. Monkman, and D. Forgeron, *Carbon dioxide sequestration in concrete articles*. 2011, Google Patents.

200. Inc., C.T. *CarbonCure*. 2014 [cited 2015; Available from: http://carboncure.com/.

201. Ciferno, J., J. Litynski, and S. Plasynski, *DOE/NETL Carbon Dioxide Capture and Storage R&D Roadmap*. 2010, National Energy Technology Laboratory. p. 67.

202. Damiani, D., et al., The US Department of Energy's R&D program to reduce greenhouse gas emissions through beneficial uses of carbon dioxide. Greenhouse Gases-Science and Technology, 2012. **2**(1): p. 9-19.

203. Zevenhoven, R. and I. Kavaliauskaite, *Mineral carbonation for long-term CO2 storage: an exergy analysis.* International Journal of Thermodynamics, 2010. **7**(1): p. 23-31.

204. Rodosta, T., D. Damiani, and Y. Shao. *Beneficial Use of CO2 in Precast Concrete Products*. 2014; Available from: http://www.netl.doe.gov/publications/factsheets/project/FE0004285.pdf.

205. Soroushian, P., J.-P. Won, and M. Hassan, Durability and microstructure analysis of CO< sub> 2</sub>-cured cement-bonded wood particleboard. Cement and Concrete Composites, 2013.

206. Gerdemann, S.J., et al., *Carbon dioxide sequestration by aqueous mineral carbonation of magnesium silicate minerals.* Greenhouse gas technologies. Elsevier Science, Amsterdam, The Netherlands, 2003.

207. Huntzinger, D.N., et al., *Mineral carbonation for carbon sequestration in cement kiln dust from waste piles.* Journal of Hazardous Materials, 2009. **168**(1): p. 31-37.

208. O'Connor, W., et al., *Aqueous mineral carbonation.* Final Report, DOE/ARC-TR-04, 2005. **2**.

209. Sipilä, J., S. Teir, and R. Zevenhoven, *Carbon dioxide sequestration by mineral carbonation Literature review update 2005–2007.* Åbo Akademi Univ., Heat Engineering Lab. report VT, 2008. **1**.

210. White, M.D., et al., Multiphase sequestration geochemistry: Model for mineral carbonation. Energy Procedia, 2011. **4**: p. 5009-5016.

211. Kalinkin, A.M., *Mechanosorption of carbon dioxide by CaTiO3 perovskite: Structure-chemical changes.* Russian Journal of Physical Chemistry A, 2008. **82**(2): p. 263-268.

212. Kalinkin, A.M., The kinetics of sorption of CO2 by perovskite CaTiO3 and the degree of perovskite decomposition with nitric acid after its mechanical activation. Russian Journal of Physical Chemistry A, 2008. **82**(3): p. 401-404.

213. Kalinkin, A.M., Mechanosorption of carbon dioxide by Ca- and Mg-containing silicates and alumosilicates: Kinetic regularities and correlations with the dissolution of CO2 in silicate melts. Colloid Journal, 2009. **71**(2): p. 193-201.

214. Kalinkin, A.M., Kinetics of carbon dioxide mechanosorption by Ca-containing silicates : CCO2 release on heating of mechanically activated samples. Journal of Thermal Analysis and Calorimetry, 2009. **95**(1): p. 105-110.

215. Kalinkin, A.M. Mechanosorption of COinf2/inf by silicates: Mechanism, kinetics and possible applications. in 6th International Conference on Mechanochemistry and Mechanical

Alloying, INCOME 2008, December 1, 2008 - December 4, 2008. 2011. Jamshedpur, India: CSIR-National Metallurgical Laboratory.

216. Kalinkin, A.M. and E.V. Kalinkina, *The mechanosorption of carbon dioxide by magnesium, calcium, and strontium metasilicates.* Russian Journal of Physical Chemistry A, 2010. **84**(9): p. 1585-1591.

217. Kalinkin, A.M., E.V. Kalinkina, and O.A. Zalkind, Mechanosorption of carbon dioxide by Ca- and Mg-containing silicates and alumosilicates. Sorption of CO2 and structure-related chemical changes. Colloid Journal, 2009. **71**(2): p. 185-192.

218. Kalinkin, A.M., et al., Mechanochemical interaction of alkali metal metasilicates with carbon dioxide: 1. Absorption of CO2 and phase formation. Colloid Journal, 2008. **70**(1): p. 33-41.

219. Little, L.H., Infrared spectra of adsorbed species. 1966.

220. Liu, C., et al., Surface Modification and Planar Defects of Calcium Carbonates by Magnetic Water Treatment. Nanoscale research letters, 2010. **5**(12): p. 1982.

221. Goñi, S., et al., Quantitative study of hydration of C3S and C2S by thermal analysis: evolution and composition of C–S–H gels formed. Journal of thermal analysis and calorimetry, 2010. **102**(3): p. 965-973.

222. Huntzinger, D.N., et al., *Carbon dioxide sequestration in cement kiln dust through mineral carbonation.* Environmental Science & Technology, 2009. **43**(6): p. 1986-1992.

223. Koga N., N.Y., Tanaka H., *Crystallization of amorphous calcium carbonate.* Thermochimica acta, 1998. **318**: p. 5.

224. Mo, L., F. Zhang, and M. Deng, Mechanical performance and microstructure of the calcium carbonate binders produced by carbonating steel slag paste under CO 2 curing. Cement and Concrete Research, 2016. **88**: p. 217-226.

225. Sevelsted, T.F., D. Herfort, and J. Skibsted, 13 C chemical shift anisotropies for carbonate ions in cement minerals and the use of 13 C, 27 Al and 29 Si MAS NMR in studies of Portland cement including limestone additions. Cement and Concrete Research, 2013. **52**: p. 100-111.

226. Schneider, M., et al., *Sustainable cement production—present and future.* Cement and Concrete Research, 2011. **41**(7): p. 642-650.

227. Gartner, E. and H. Hirao, A review of alternative approaches to the reduction of CO 2 emissions associated with the manufacture of the binder phase in concrete. Cement and Concrete research, 2015. **78**: p. 126-142.

228. Albitar, M., et al., *Durability evaluation of geopolymer and conventional concretes.* Construction and Building Materials, 2017. **136**: p. 374-385.

229. Kong, D.L. and J.G. Sanjayan, *Effect of elevated temperatures on geopolymer paste, mortar and concrete.* Cement and concrete research, 2010. **40**(2): p. 334-339.

230. Bakri, A., et al., Comparison of Geopolymer Fly Ash and Ordinary Portland Cement to the Strength of Concrete. Advanced Science Letters, 2013. **19**(12): p. 3592-3595.

231. Yaozhong, Y.H.J., The development of geopolymer and its future application in our country [J]. BULLETIN OF THECHINESE CERAMIC SOCIETY, 1998. **2**.

232. Energy, U.S.D.o., Cement Kiln Flue Gas Recovery Scrubber Project: A DOE Assessment. 202.

233. Kawatra, S.K., *Advances in comminution*. 2006: SME.

234. Chen, B., *Grinding principle.* Text Book, 1989.

235. Chandrasekhar, S., et al., Microsilica from rice husk as a possible substitute for condensed silica fume for high performance concrete. Journal of materials science letters, 2002. **21**(16): p. 1245-1247.

236. Kwan, A. and W. Fung, *Roles of water film thickness and SP dosage in rheology and cohesiveness of mortar.* Cement and Concrete Composites, 2012. **34**(2): p. 121-130.

237. Kwan, A., W. Fung, and H. Wong, *Water film thickness, flowability and rheology of cement-sand mortar.* Advances in Cement Research, 2010.

238. Li, L. and A. Kwan, *Mortar design based on water film thickness.* Construction and Building Materials, 2011. **25**(5): p. 2381-2390.

239. Li, L.G. and A.K. Kwan, *Concrete mix design based on water film thickness and paste film thickness.* Cement and Concrete Composites, 2013. **39**: p. 33-42.

240. Graybeal, B., Ultra-high performance concrete. 2011.

241. Yost, J.R., et al., Structural behavior of alkali activated fly ash concrete. Part 2: structural testing and experimental findings. Materials and Structures, 2013. **46**(3): p. 449-462.

242. Užarević, K., et al., Exploring the effect of temperature on a mechanochemical reaction by in situ synchrotron powder X-ray diffraction. Crystal Growth & Design, 2016. **16**(4): p. 2342-2347.

243. Urakaev, F.K. and V. Boldyrev, Mechanism and kinetics of mechanochemical processes in comminuting devices: 1. Theory. Powder Technology, 2000. **107**(1): p. 93-107.

244. Cassagnabèr F., L.M., Escadeillas G,Mouret M, Broilliard P., *lash metakaolin/slag/cement binder: An environmental and performantial alternative for steam-cured mortar for precast use.* Annual Conference of the Transportation Association of Canada, 2010: p. 10.

245. Black, A.P., et al., The Economic Impacts of Prohibiting Coal Fly Ash Use in Transportation Infrastructure Construction. 2011.

246. Horsley, C., *Geopolymer-The Green Cement*. 2015, Worcester Polytechnic Institute.

247. Kalyoncu, R.S., *Slag–iron and steel.* US geological survey minerals yearbook, 2001. **2001**.

248. Kim, M.S., et al., Use of CaO as an activator for producing a price-competitive non-cement structural binder using ground granulated blast furnace slag. Cement and concrete research, 2013. **54**: p. 208-214.

249. Bhagwat, S., et al., Feldspar and quartz from the dunes of Kankakee, Illinois: a preliminary feasibility study. Illinois minerals no. 122, 2001.

250. van Deventer, J.S.J., et al., Chemical Research and Climate Change as Drivers in the Commercial Adoption of Alkali Activated Materials. Waste and Biomass Valorization, 2010. **1**(1): p. 145-155.

251. Kupwade-Patil, K. and E. Allouche, *Effect of alkali silica reaction (ASR) in geopolymer concrete.* World of Coal Ash, 2011.

252. Cheema D., L.N., *Blended Low Calcium Fly Ash Gepolymer Concrete – Environment Friendly Construction Material.* International Conference on Geological and Civil Engineering, 2014. **62**.

253. Valenza, J.J. and G.W. Scherer, *A review of salt scaling: I. Phenomenology.* Cement and Concrete Research, 2007. **37**(7): p. 1007-1021.

254. Huijgen, W.J., *Carbon Dioxide Sequestration by Mineral Carbonation.* Thesis, Energy research Centre of the Netherlands, 2007.

255. Price, L., E. Worrell, and D. Phylipsen, Energy use and carbon dioxide emissions in energy-intensive industries in key developing countries. Lawrence Berkeley National Laboratory, 1999.

256. Ali A., M.V., waste heat recovery power generation for cement production process. IEEE, 2013. **93**: p. 13.

257. Madlool, N.A., et al., *A critical review on energy use and savings in the cement industries.* Renewable and Sustainable Energy Reviews, 2011. **15**(4): p. 2042-2060.

258. McLellan, B.C., et al., Costs and carbon emissions for geopolymer pastes in comparison to ordinary portland cement. Journal of Cleaner Production, 2011. **19**(9-10): p. 1080-1090.

259. Bourton on Dunsmore, R., Warwickshire, , HOW TO CALCULATE THE ENERGY EFFICIENCY OF YOUR LIME BURNING PROCESS
Energy efficiency of lime brining

260. S., R., SERVICE LIFE DESIGN OF CONCRETE STRUCTURES -
A CHALLENGE TO DESIGNERS AS WELL AS TO OWNERS. ASIAN JOURNAL OF CIVIL ENGINEERING (BUILDING AND HOUSING), 2005. **6**(5): p. 23.

261. Allouche, E., High Durability "Green" Inorganic Polymer Binders for Sustainable Construction.

262. Baláž, P. and E. Dutková, Applied mechanochemistry of solids (a review). 2011.

263. Butyagin, P.Y., The role of interfaces in the reactions of low-temperature mechanochemical synthesis. Kolloidnyj Zhurnal, 1997. **59**(4): p. 460-467.

264. Ioan, Ţ. and V. NECULĂIASA, STUDIES ON FUNCTIONING CONDITIONS OF TRIBOSYSTEMS SUBJECTED TO TRIBOCORROSIVE WEAR WITH APPLICATIONS ON MACHINES FROM AGRICULTURE AND FOOD INDUSTRY. 2004.

265. Kalinkin, A., Mechanosorption of carbon dioxide by Ca-and Mg-containing silicates and alumosilicates: Kinetic regularities and correlations with the dissolution of CO 2 in silicate melts. Colloid journal, 2009. **71**(2): p. 193-201.

266. Heinike, G., *Tribochemistry, Berlin: Akademie, 1984.* Google Scholar, 1987: p. 169.

267. Streletskii, A. and P.Y. Butyagin, *MECHANOCHEMISTRY OF QUARTZ SURFACE. 2. ROLE OF FRICTION.* Kinetics and Catalysis, 1980. **21**(3): p. 575-580.